AD-A048 252 STANFORD UNIV CALIF GUIDANCE AND CONTROL LAB F/G 8/5
STUDY TO DEVELOP GRADIOMETER TECHNIQUES.(U)
JUN 77 D B DEBRA, E J PELKA F19628-74-C-0162
UNCLASSIFIED AFGL-TR-76-0297 NL

1 OF 4
AD
AD48252



AD A048252

AFGL-TR-76-0297

STUDY TO DEVELOP GRADIOMETER TECHNIQUES

Daniel B. DeBra
Eugene J. Pelka

Stanford University
Guidance and Control Laboratory
Department of Aeronautics and Astronautics
Stanford, California 94305

DDC
RECEIVED
NOV 4 1977
F

Final Report
July 1975 through June 1976

June 1977

Approved for public release; distribution unlimited.

AIR FORCE GEOPHYSICS LABORATORY
AIR FORCE SYSTEMS COMMAND
UNITED STATES AIR FORCE
HANSCOM AFB, MASSACHUSETTS 01731

AD NO.
DDC FILE COPY

Qualified requestors may obtain additional copies from the Defense Documentation Center. All others should apply to the National Technical Information Service.

SECURITY CLASSIFICATION OF THIS PAGE (When Data Entered)

REPORT DOCUMENTATION PAGE

READ INSTRUCTIONS BEFORE COMPLETING FORM

1. REPORT NUMBER: AFGL-TR-76-0297	2. GOVT ACCESSION NO.
3. RECIPIENT'S CATALOG NUMBER	
4. TITLE (and Subtitle): STUDY TO DEVELOP GRADIOMETER TECHNIQUES.	5. TYPE OF REPORT & PERIOD COVERED: Final Report. Jul[illegible] 1975 - Jun[illegible] 1976.
6. PERFORMING ORG. REPORT NUMBER	
7. AUTHOR(s): Daniel B. /DeBra [illegible] Eugene J. /Pelka	8. CONTRACT OR GRANT NUMBER(s): F19628-74-C-0162
9. PERFORMING ORGANIZATION NAME AND ADDRESS: Stanford University, Guidance & Control Lab., Dept. Aero & Astro, Stanford, Calif., 94305	10. PROGRAM ELEMENT, PROJECT, TASK AREA & WORK UNIT NUMBERS: Work Unit No. 86070201
11. CONTROLLING OFFICE NAME AND ADDRESS: Air Force Geophysics Laboratory, Hanscom AFB, Massachusetts 01731, Monitor/James A. Hammond/LWG	12. REPORT DATE: Jun[illegible]77
	13. NUMBER OF PAGES: 334
14. MONITORING AGENCY NAME & ADDRESS (if different from Controlling Office)	15. SECURITY CLASS. (of this report): unclassified
	15a. DECLASSIFICATION/DOWNGRADING SCHEDULE

16. DISTRIBUTION STATEMENT (of this Report)

Approved for public release; distribution unlimited.

17. DISTRIBUTION STATEMENT (of the abstract entered in Block 20, I[illegible] Report)

61102F

DDC RECEIVED NOV 4 1977 F

18. SUPPLEMENTARY NOTES

19. KEY WORDS (Continue on reverse side if necessary and identify by block number)

Hughes gravity gradiometer, parameter estimation, on-line compensation, Draper Lab, rotating gravity gradiometer (RGG), error model, EU, sensor, Bell Aerospace, output, error

20. ABSTRACT (Continue on reverse side if necessary and identify by block number)

The primary goal of the gravity gradiometer research effort at Stanford University has been to establish the feasibility of operation of a gravity gradiometer in a closed loop mode. A parameter estimation technique will allow for on-line modification (compensation) of the sensor output signal, as well as for trimming of pertinent sensor physical properties so as to improve instrument performance. Gravity gradiometers are required to operate with an accuracy of 1 EU (Eötvös unit). This is so demanding that closed loop mode operation may be essential. Although attention has been focussed

DD FORM 1 JAN 73 1473 EDITION OF 1 NOV 65 IS OBSOLETE S/N 0102-LF-014-6601

SECURITY CLASSIFICATION OF THIS PAGE (When Data Entered)

407 256

exclusively upon the Hughes rotating gravity gradiometer (RGG), the parameter estimation method developed is applicable, in principle, to any instrument subject to dynamically induced errors.

ACCESSION for
NTIS White Section
DDC Buff Section
UNANNOUNCED
JUSTIFICATION
BY
DISTRIBUTION/AVAILABILITY CODES
Dist. SPECIAL
A

TABLE OF CONTENTS

Chapter		Page
	TABLE OF CONTENTS	iii
	List of Figures	ix
	List of Tables	xvii
	List of Symbols	xxi
	English Letters	xxi
	Greek Letters	xxv
	Subscripts	xxvii
	Superscripts	xxiii
	Abbreviations used in Text	xxiii
I.	INTRODUCTION	1
	A. Gravity Gradiometer Background and Applications	1
	B. Purpose of Research	3
	C. Chapter Contents	4
	D. Contributions	6
II.	GRAVITY GRADIOMETERS	7
	A. The Gravitational Field and Its Gradient	7
	B. Some Comments on the Philosophy of Gradient Sensor Design	9
	B.1 Sensor Concepts	9
	C. Gravity Gradiometers Under Development	10
	D. Hughes Rotating Gravity Gradiometer	10
	D.1 Sensor Physical Properties	12
	D.2 Reference Systems	14
	D.3 Rotating Gravity Gradiometer Signal Equation; The Twice Frequency Torque	14
	D.4 Simplified Gradiometer Signal Development. Steady State Operation Approximation	17
	D.5 Rotating Gravity Gradiometer (RGG) Output Equation	20
	D.6 Hughes Gradiometer Signal and Error Torque Levels	21

TABLE OF CONTENTS (Cont)

Chapter		Page
	E. Draper Labs Floated Proof Mass Gravity Gradiometer	21
	E.1 Cylindrical Gradiometer	21
	E.2 Spherical Gradiometer	23
	F. Bell Aerospace Corp. Gradiometer	24
	G. Gradient Tensor Determination	26
	G.1 Measuring the Gravity Gradient With the Hughes RGG Orthogonal Instrument Triad	27
	G.2 Measuring the Gravity Gradient With the Hughes RGG Non-Orthogonal Instrument Triad	31
	G.3 Measuring the Gravity Gradient With the Draper Labs Cylindrical Gravity Gradiometer	49
	G.4 Measuring the Gravity Gradient With the Draper Labs Spherical Gravity Gradiometer	53
	G.5 Conclusions Regarding Gravity Gradient Measurement	70
III.	HUGHES GRAVITY GRADIOMETER ERROR MODEL	75
	A. Introduction	75
	B. Instrument Error Sources	76
	B.1 Linear Acceleration Induced Torque, ϵ_{LA}	77
	B.2 Axial-Torsional Coupling (Yankee Screwdriver Effect) ϵ_{YS}	78
	B.3 Non-principal Axis Spin and Mass Center Offset, ϵ_R	83
	B.4 Elastic/Spin/Principal Axis Misalignment, ϵ_{AM}	85
	B.5 Platform/Sensor Axis System Misalignment, ϵ_{PMA}	89
	B.6 Sum Mode Mismatch Error	91
	B.7 Arm Anisoelastic Error Torque, ϵ_A	97
	B.8 Spin/Elastic Axis Displacement	98
	C. Differential Torque Output Error Summary	101

TABLE OF CONTENTS (Cont)

Chapter		Page
IV.	DEVELOPMENT OF PARAMETERS FOR ESTIMATION	105
	A. Introduction	105
	B. Error Equation Development	105
	B.1 Output Equation Simplification	112
	B.2 Inclusion of Spin/Elastic Axis Misalignment Angles	117
	C. Input for Parameter Identification	120
	C.1 Measurement of Sensor Dynamics	121
	C.2 Parameter Identification Input Selection	121
	D. Error Equation With Specified Inputs	123
	E. Parameter Independence	126
	F. Sensor Input-to-Output Transfer Function	127
	F.1 RGG Spin Rate Selection	134
	G. Effect of Frequency Considerations on Parameter Identification Input	136
	H. A Comment On Parameter Identifiability	136
V.	OUTPUT EFFECTIVE PARAMETER (OEP) ESTIMATION USING PARALLEL FILTERS AND PHASE SENSITIVE SIGNAL DEMODULATION (PSSD)	137
	A. Introduction	137
	B. Parallel Filter Formulation--P_1, P_2 Estimation	138
	B.1 Rate Filter Formulation	141
	B.2 Torque Filter Formulation	145
	B.3 Parameter Estimation	148
	C. Parallel Filter Evaluation of P_{14} and P_{17}	154
	D. Phase Sensitive Demodulation	154
	E. Comments On The Parallel Filter and PSSD Approaches to Output Effective Parameter Estimation	162

TABLE OF CONTENTS (Cont)

Chapter		Page
VI.	OUTPUT CORRELATION	165
	A. Introduction	165
	B. Output Correlation Concept	165
	C. Concept Demonstration	168
	D. The Effects of Correlated Random Input on Estimator Performance	173
	E. The Forced Input Correlator. Definition of the Correlation Function	174
	E.1 The L^2 (Second Order Lag) System: The Basic Forced Input Correlator	175
	E.2 The Frequency Discrimination Filter Correlator	181
	E.3 The IL^2 System (Integrated Second Order Lag)	181
	E.4 Higher Order Filters: The L^6 (Sixth Order Lag) System	183
	F. Platform Input Frequency Selection	186
	F.1 The Correlation Functions	186
	G. Correlation Technique Performance--6th Order System	197
	G.1 Closed Form Solution--P_{14} Estimation	198
	G.2 Correlation Technique Performance--P_1 Estimation	202
	G.3 Correlation Technique Performance--P_{11} Estimation	202
	H. Conclusions Regarding a Correlation Approach to Output Effective Parameter (OEP) Identification	208
	H.1 Pivot Stiffness Knowledge Requirements	209
VII	ACTIVE PARAMETER CONTROL	213
	A. Introduction	213
	B. Selection of a Method of Control	213
	C. Control Law Development	214
	D. Example of Under-Determined Least Squares Parameter Control	217

TABLE OF CONTENTS (Cont)

Chapter		Page
VIII.	EXTENSION OF THE INSTRUMENT MODEL TO A CONTROL COMPATIBLE FORM	221
	A. Introduction	221
	B. Expression of Arm Mass Centers and Inertias In Control Compatible Form	223
	C. Arm Compliance Model Development	226
	D. Axial Arm Compliance Calculation	229
	E. Lateral Arm Compliance Calculation	232
	F. Arm Compliance Calculation	236
	G. OEP Formulation In Control Compatible Form	237
	H. Coarse Control Of Arm Compliances	239
IX.	OUTPUT EFFECTIVE PARAMETER CONTROL USING UNDER-DETERMINED LEAST SQUARES	243
	A. Introduction	243
	B. Control Configuration	243
	C. The Parameter Control Problem	252
	D. Parameter Controllability	252
	E. Digital Simulation	253
	F. General Error Case Tests	265
	F.1 Test Case 4--All Model-Mass Values and Positions Perturbed	266
	F.2 Additional Test Cases	279
	G. Variations In The Nominal Control Mass Values	291
	H. Reduction In the Number of Control Masses	297
	I. Conclusions Regarding The Under-Determined Least Squares Controller	301
X.	CONCLUSIONS AND RECOMMENDATIONS FOR FURTHER STUDY	303
	A. Conclusions	303

TABLE OF CONTENTS (Cont)

Chapter		Page
	B. Recommendations For Further Study	304
	APPENDIX A :	
	THE CONTROL MASS MOTION MECHANISM	305
	APPENDIX B :	
	AN APPROACH TO COMPLIANCE FINE TUNING	309

LIST OF FIGURES

Fig. No.		Page
I-1	EÖTVÖS TORSION BALANCE GRAVITY GRADIOMETER . . .	2
II-1	HUGHES RESEARCH LABS ROTATING GRAVITY GRADIOMETER	11
II-2	HUGHES GRAVITY GRADIOMETER ROTOR ASSEMBLY AS MODELED	12
II-3	SIDE AND AXIAL VIEWS OF HUGHES RGG FOR AXIS SYSTEM DEFINITION	15
II-4	IDEALIZED ROTATING GRAVITY GRADIOMETER UNDER THE INFLUENCE OF THE GRAVITY GRADIENT	16
II-5	SIMPLIFIED SENSOR MODEL DISPLAYING SENSOR TORQUE TO SIGNAL CONVERSION	17
II-6	DUMBELL GRADIOMETER	17
II-7	AXIALLY SYMETRIC CYLINDRICAL FLOATED PROOF MASS GRAVITY GRADIOMETER	22
II-8	DRAPER LABS FLOATED SPHERICAL GRAVITY GRADIOMETER	24
II-9	BELL AEROSPACE HEAVY PROOF MASS ACCELEROMETER GRADIOMETER	25
II-10	BASELINE HUGHES' GRADIOMETER GRADIENT MEASURING SYSTEM	28
II-11	MEASUREMENT REFERENCE SYSTEM ORIENTATIONS FOR THREE ORTHOGONAL RGG	31
II-12	GRADIENT TENSOR ESTIMATE ERROR COST FUNCTION VS SENSOR $2\hat{y}$ AXIS ROTATION NOMINAL	40
II-13	GRADIENT TENSOR ESTIMATE ERROR COST FUNCTION VS SENSOR $2\hat{y}$ AXIS ROTATION NOMINAL	41
II-14	GRADIENT TENSOR ESTIMATE ERROR COST FUNCTION VS SENSOR $2\hat{y}$ AXIS ROTATION NOMINAL	42

LIST OF FIGURES (Cont)

Fig. No.		Page
II-15	GRADIENT TENSOR ESTIMATE ERROR COST FUNCTION VS SENSOR 2$\hat{y}$ AXIS ROTATION FROM NOMINAL	43
II-16	GRADIENT TENSOR ESTIMATE ERROR COST FUNCTION VS SENSOR 2$\hat{y}$ AXIS ROTATION FROM NOMINAL	44
II-17	GRADIENT TENSOR ESTIMATE ERROR COST FUNCTION VS SENSOR 2$\hat{y}$ AXIS ROTATION FROM NOMINAL	45
II-18	GRADIENT TENSOR ESTIMATE ERROR COST FUNCTION VS SENSOR 2$\hat{y}$ AXIS ROTATION FROM NOMINAL	46
II-19	GRADIENT TENSOR ESTIMATE ERROR COST FUNCTION VS SENSOR 2$\hat{y}$ AXIS ROTATION FROM NOMINAL	47
II-20	GRADIENT TENSOR ESTIMATE ERROR COST FUNCTION VS SENSOR 2$\hat{y}$ AXIS ROTATION FROM NOMINAL	48
II-21	DRAPER LABS CYLINDRICAL GRADIOMETER WITH PROOF MASSES REPRESENTED AS POINT MASSES	49
II-22	SIMPLIFIED REPRESENTATION OF DRAPER LABS SPHERICAL GRAVITY GRADIOMETER	53
II-23	THREE SPHERICAL GRAVITY GRADIOMETERS	55
II-24	GRADIENT TENSOR ESTIMATE ERROR COST FUNCTION VS INSTRUMENT $\hat{y}_B$ ROTATION ANGLE. ALL SENSORS ROTATED THROUGH ANGLE β	62
II-25	GRADIENT TENSOR ESTIMATE ERROR COST FUNCTION VS INSTRUMENT $\hat{y}_B$ ROTATION ANGLE. ALL SENSORS ROTATED THROUGH ANGLE β	63
II-26	GRADIENT TENSOR ESTIMATE ERROR COST FUNCTION VS INSTRUMENT $\hat{y}_B$ ROTATION ANGLE. ALL SENSORS ROTATED THROUGH ANGLE β	64

LIST OF FIGURES (Cont)

Fig. No.		Page
II-27	GRADIENT TENSOR ESTIMATE ERROR COST FUNCTION VS INSTRUMENT $\hat{y}_B$ ROTATION ANGLE. ALL SENSORS ROTATED THROUGH ANGLE β. SPHERICAL GRADIOMETER SYSTEM PERFORMANCE COMPARISON	66
II-28	GRADIENT TENSOR ESTIMATE ERROR COST FUNCTION VS $\hat{x}_B$ ANGULAR ROTATION DIFFERENCE BETWEEN SENSORS 2 and 3	69
II-29	GRADIENT TENSOR ESTIMATE ERROR COVARIANCE MATRIX COMPONENTS VS $\hat{x}_B$ ANGULAR ROTATION DIFFERENCE BETWEEN SENSORS 2 and 3	71
II-30	GRADIENT TENSOR ESTIMATE ERROR COVARIANCE MATRIX COMPONENTS VS $\hat{x}_B$ ANGULAR ROTATION DIFFERENCE BETWEEN SENSORS 2 and 3	72
II-31	GRADIENT TENSOR ESTIMATE ERROR COVARIANCE MATRIX COMPONENTS VS $\hat{x}_B$ ANGULAR ROTATION DIFFERENCE BETWEEN SENSORS 2 and 3	73
III-1	SIMPLIFIED ROTATING GRAVITY GRADIOMETER SCHEMATIC DEMONSTRATING THE MOWER REEL MODEL FOR THE AXIAL TORSIONAL COUPLING ERROR	79
III-2	AXIAL-TORSIONAL COUPLING MODEL PIANO STOOL EFFECT	80
III-3	SYSTEM MODEL FOR SUM MODE MISMATCH ERROR DEVELOPMENT	92
III-4	GENERAL CASE OF NON-COINCIDENCE BETWEEN THE SENSOR SPIN AND ELASTIC AXES	99
III-5	END VIEW OF RGG CENTRAL PIVOT SHOWING PARALLEL BUT DISPLACED SPIN ($\hat{z}_S$) AND ELASTIC ($\hat{z}_E$) AXES	99
IV-1	SCHEMATIC DRAWING OF HUGHES ROTATING GRAVITY GRADIOMETER	106

LIST OF FIGURES (Cont)

Fig. No.		Page
IV-2	SCHEMATIC DIAGRAM OF HUGHES' RGG (ROTATING GRAVITY GRADIOMETER TEST BED SYSTEM)	122
IV-3	INPUT-TO-OUTPUT DIFFERENTIAL TORQUE FLOW . .	127
IV-4	PEAK OUTPUT-TO-INPUT AMPLITUDE RATIO FOR DIFFERENTIAL MODE.	130
IV-5	DIFFERENTIAL MODE PHASE ANGLE RELATING INPUT-TO-OUTPUT	131
IV-6	PEAK IN-PHASE ERROR AND PHASE ANGLE AS A FUNCTION OF $(1 - \omega/\omega_n)$.	133
V-1	SCHEMATIC MODEL OF TORQUE FILTER MEASUREMENT GENERATION	145
V-2	SCHEMATIC DRAWING OF A PHASE SENSITIVE SIGNAL DEMODULATOR	155
V-3	EXAMPLE OF INSTRUMENT OUTPUT FOR SINUSOIDAL INPUT HAVING FREQUENCY ν.	156
V-4	IN-PHASE LIMITER SIGNAL AND PSSD OUTPUT SIGNAL .	157
V-5	OUT-OF-PHASE LIMITER SIGNAL AND PSSD OUTPUT SIGNAL	158
V-6	USE OF PSSD FOR RGG P_1 and P_2 ESTIMATION . . .	159
VI-1	IDENTIFICATION OF P_j VIA OUTPUT CORRELATION . .	167
VI-2	IDENTIFICATION OF P_1 VIA OUTPUT CORRELATION . .	171
VI-3	TIME HISTORY OF INTEGRATOR OUTPUT FOR ESTIMATION OF P_1	172
VI-4	P_{14} IDENTIFICATION VIA THE L^2 SYSTEM	176
VI-5	P_{14} ESTIMATION -- ITERATION 1	203
VI-6	P_{14} ESTIMATION -- ITERATION 2	204

LIST OF FIGURES (Cont)

Fig. No.		Page
VI-7	P_{14} ESTIMATION -- ITERATION 3	205
VI-8	P_1 ESTIMATION -- ITERATION ZERO	206
VI-9	P_{11} ESTIMATION -- ITERATION ZERO	207
VIII-1	SIXTEEN MODEL-MASS CONFIGURATION FOR RGG PROOF MASS	222
VIII-2	ISOELASTIC ARM MODEL	227
VIII-3	ISOELASTIC ODD ARM	228
VIII-4	LOAD AND SUPPORT DIAGRAM FOR AXIALLY LOADED ARM	230
VIII-5	SEGMENT e LATERAL GEOMETRY	231
VIII-6	LOAD AND SUPPORT DIAGRAM FOR LATERALLY SUPPORTED ARM	233
IX-1	CONTROL MASS PLACEMENT --ODD ARM	243
IX-2	ODD ARM CONTROL SYSTEM NOMINAL CONFIGURATION	245
IX-3	EVEN ARM CONTROL SYSTEM NOMINAL CONFIGURATION	246
IX-4	POINT OF APPLICATION INCREMENT EXAMPLE	249
IX-5	SIMULATION SUMMARY CHART	254
IX-6	PRECONTROL MASS CENTER AND CONTROL MASS CONFIGURATION FOR P_{11} CONTROL TEST CASE	260
IX-7	CONTROL SYSTEM RESPONSE TO MASS CENTER OFFSET OF NOMINAL INSTRUMENT IN $\hat{x}_s$ DIRECTION	261
IX-8	MODEL MASS PERTURBATIONS FOR TEST CASES 1 TO 4	267
IX-9	MODEL MASS $\hat{z}_s$ PERTURBATIONS FOR TEST CASES 1 TO 4	267
IX-10	MODEL MASS $\hat{x}_s$ PERTURBATIONS FOR TEST CASES 1 TO 4	268

LIST OF FIGURES (Cont)

Fig. No.		Page
IX-11	MODEL MASS ϑ_s PERTURBATIONS FOR TEST CASES 1 TO 4	268
IX-12	OEPs AS A FUNCTION OF CONTROL ITERATION--TEST CASE 4	273
IX-13	ARM CM LOCATION AS A FUNCTION OF CONTROL ITERATION TEST CASE 4	278
IX-14	ARM TO SENSOR ROTATION ANGLES AS A FUNCTION OF CONTROL ITERATION; TEST CASE 4	280
IX-15	OEP AS A FUNCTION OF CONTROL ITERATION. TEST CASE 1	282
IX-16	OEP AS A FUNCTION OF CONTROL ITERATION, TEST CASE 3	283
IX-17	OEP AS A FUNCTION OF CONTROL ITERATION, TEST CASE 3	284
IX-18	ARM CM LOCATION AS A FUNCTION OF CONTROL ITERATION TEST CASE 1	285
IX-19	ARM CM LOCATION AS A FUNCTION OF CONTROL ITERATION TEST CASE 2	286
IX-20	ARM CM LOCATION AS A FUNCTION OF CONTROL ITERATION TEST CASE 3	287
IX-21	ARM TO SENSOR ROTATION ANGLES AS A FUNCTION OF CONTROL ITERATION, TEST CASE 1	288
IX-22	ARM TO SENSOR ROTATION ANGLES AS A FUNCTION OF CONTROL ITERATION, TEST CASE 2	289
IX-23	ARM TO SENSOR ROTATION ANGLES AS A FUNCTION OF CONTROL ITERATION, TEST CASE 3	290
IX-24	OEP AS A FUNCTION OF CONTROL ITERATION, TEST CASE 5	292
IX-25	P_{14} CONTROL VS CONTROL ITERATION FOR TEST CASES 5, 5a, AND 5b.	293

LIST OF FIGURES (Cont)

Fig. No.		Page
IX-26	ITERATION 1 CONTROL MASS MOTION FOR TEST CASES 5, 5a, AND 5b.	294
IX-27	CONTROLLER PERFORMANCE FOR TEST CASE 6 SYSTEM CONFIGURATION. z-AXIS CONTROL REMOVED. . . .	298
IX-28	CONTROL MASS PLACEMENT FOR ODD ARM WITH SYSTEM RECONFIGURED TC 8 CONTROL MASSES PER ARM. . .	299
IX-29	CONTROLLER PERFORMANCE FOR TEST CASE 7 . . .	300
A-1	CLAMPING SEQUENCE FOR INCHWORM MASS MOTION . .	306
A-2	INCHWORM SPECIFICATIONS	307
B-1	HIGH COMPLIANCE PIVOT MODIFIED FOR COMPLIANCE MATCH	310

LIST OF TABLES

No.		Page
II-1	NOMINAL INSTRUMENT DATA	13
II-2	COMPARISON OF THREE HUGHES AND TWO DRAPER LABS DIAGONAL GRADIENT COMPONENT ESTIMATE FOR THE TWO SKEWED MASS SENSOR CASE. GRADIENT ESTIMATION USING MINIMUM NUMBER OF SENSORS.	53
III-1	SENSOR ERROR ANALYSIS INPUT DATA.	102
III-2	DYNAMICALLY INDUCED ERRORS AT $2\omega_s$	103
IV-1	OUTPUT EFFECTIVE PARAMETERS FOR THE CASE WHERE SPIN/ELASTIC AXIS MISALIGNMENTS	116
IV-2	COMPARISON OF OEP WHICH CHANGE WHEN SPIN/ELASTIC MISALIGNMENTS BECOME NON-ZERO	120
IV-3	OUTPUT FREQUENCIES ASSOCIATED WITH THE OUTPUT EFFECTIVE PARAMETERS	125
V-1	STATISTICAL VALUES USED FOR RATE FILTER PERFORMANCE EVALUATION	143
V-2	STEADY STATE RATE FILTER PERFORMANCE	144
V-3	STATISTICAL VALUES APPLIED FOR TORQUE FILTER EVALUATION	147
V-4	STEADY STATE TORQUE FILTER PERFORMANCE . . .	147
V-5	PARAMETER ESTIMATE ERROR EQUATION INPUT . . .	151
V-6	MAXIMUM UNCOMPENSATED OUPUT TORQUE AT $2\omega_s$ DUE TO $\tilde{P}_1$ and $\tilde{P}_2$†	153
V-7	MAXIMUM UNCOMPENSATED OUTPUT TORQUE DUE TO SIGNAL DEMODULATOR 0.01% PARAMETER ESTIMATED ERROR	162
VI-1	FORCED INPUT CORRELATOR MECHANIZATIONS . . .	178
VI-2	SECOND ORDER LAG CORRELATOR FUNCTIONS. . . .	180

PRECEDING PAGE BLANK-NOT FILMED

LIST OF TABLES (Cont)

No.		Page
V[illegible]-3	INTEGRATED SECOND ORDER LAG CORRELATOR FUNCTIONS	182
VI-4	OEP CORRELATION FUNCTIONS.	187
VI-5	SAMPLE CORRELATION FREQUENCIES	188
VI-6	CORRELATED FREQUENCY OUTPUT AS A FUNCTION OF CORRELATION FREQUENCY.	190-196
VI-7	SYSTEM RATE AND ACCELERATION DATA	197
VI-8	COEFFICIENT DEFINITIONS.	198
VI-9	INPUT FREQUENCIES ASSOCIATED WITH P_{14} CORRELATED OUTPUT EQUATION.	199
VII-1	LEAST SQUARES PARAMETER ESTIMATION AND CONTROL DUALITY	218
VIII-1	NOMINAL MASS AND POSITION DATA FOR 16 MODEL-MASS ROTATING GRAVITY GRADIOMETER CONFIGURATION POSITIONS AS SHOWN WITHIN THE MATRICES CORRESPONDING TO MODEL-MASS SUBSCRIPTS	224
VIII-2	PARTIAL DERIVATIVES OF ARM COMPLIANCE WITH RESPECT TO MEMBER WIDTHS w_a AND w_b.	240
IX-1	CONTROL MASS VALUES AND POSITIONS.	244
IX-2	CONTROL VECTOR SPECIFICATION	247
IX-3	IDEAL INSTRUMENT CONFIGURATION	256-257
IX-4	IDEAL INSTRUMENT OEP CALCULATION FROM DIGITAL SIMULATION	258
IX-5	INPUT DATA FOR EVEN ARM MODEL MASS x_s POSITION BIAS POSITION IN MATRIX CORRESPONDS TO MODEL MASS SPECIFICATION	259
IX-6	CM OFFSET TEST INSTRUMENT PHYSICAL PROPERTIES .	262-264

LIST OF TABLES (Cont)

No.		Page
IX-7	CM OFFSET TEST OEP VALUES	265
IX-8	INSTRUMENT ARM MASS AND MASS CENTER DATA PRIOR TO CONTROL	269
IX-9	INSTRUMENT PHYSICAL DATA PRIOR TO CONTROL APPLICATION	270-271
IX-10	COMPARISON OF TEST CASE 4 INPUT DATA WITH ERROR ANALYSIS DATA DEMONSTRATING THE CAPABILITY OF THE SYSTEM TO CONTROL ERRORS IN INSTRUMENT MANUFACTURING WHICH ARE LARGER THAN EXPECTED. . . .	272
IX-11	INSTRUMENT PHYSICAL DATA SUBSEQUENT TO FINAL CONTROL	274-275
IX-12	OEPs AS A FUNCTION OF CONTROL ITERATION . . .	276
IX-13	CONTROL INCREMENTS BY ITERATION NUMBER (m) . .	277
IX-14	PRE- AND POST-CONTROL RGG OUTPUT TORQUE ERROR (N m) FOR TEST CASE 4	281
IX-15	STATISTICAL ANALYSIS OF CONTROL MASS MOTION FOR TEST CASES 5, 5a, AND 5b.	296

LIST OF SYMBOLS

a_j		tangential acceleration of accelerometer j associated with Bell Labs gradiometer
$\bar{a}$		instrument linear acceleration vector
A	Ch. II:G	gradiometer measurements
A	Ch. III:B-2	peak magnitude of linear acceleration
A	Ch. V	coefficient matrix; scalar A
A_j	Ch. IV	maximum magnitude of platform linear acceleration input along jth axis
A_j	Ch. VI	correlation function
A_i, B_i C_i, D_i	Ch. VI:E-4	dummy variables used to define correlator output
b		arm dynamics damping coefficient
B	Ch. VII	weighting matrix
B1, B2, B_3,	Ch. II:G	body referenced measurement systems
c		torque output coefficient
C_a		axial compliance
$C_{E/S}$		transformation to elastic from sensor reference frame
C_ℓ		lateral compliance
$C_{S/P}$		transformation to sensor reference system from platform reference system
d	Ch. II	distance between opposed Bell accelerometers
D_i		structural damping coefficient for ith pivot
$\hat{e}$	Ch. IV	unit vector in the direction of low compliance pivot elastic axis
E		modulus of elasticity
f		force

PRECEDING PAGE BLANK-NOT FILMED

f_c		correlation frequency
F		control mass coefficient matrix
g		magnitude of gravity vector
G	Ch. IV:F	approximate magnitude of vertical gravity gradient
G	Ch. VIII	shear modulus
G(s)		correlator transfer function
h		spin angular momentum
H(s)		sensor signal prefilter
$\mathcal{H}$		Hamiltonian
I		moment of inertia
I_{ij}		ijth component of moment of inertia matrix
I_r		moment of inertia of rotor (case)
$\mathcal{J}$		arm moment of inertia expressed relative to the elastic reference system
$\mathcal{J}_j$		time integral of the product of the correlation function A_j and platform output torque T
J	Ch. II:G	cost function
J	Ch. IV:F	arm polar moment of inertia
J	Ch. VII	cost function
k	Ch. III:B-2	arm lateral bending stiffness
k	Ch. IV:F	effective pivot stiffness
k_j		dummy variables used to define coefficients of correlator output
k_T	Ch. II	pivot stiffness
K		dummy variable used to define correlator output
K_i		stiffness coefficient of ith pivot
K_T		constant of proportionality relating transducer strain to sensor output
K_{YS}		coefficient of axial-torsional coupling error along spin axis

K_0		stiffness of center pivot
K_1, K_2		high compliance pivot stiffness
ΔK		coefficient associated with arm compliances
L		coefficient matrix relating components of gradient tensor to sensor measurements for the Hughes gravity gradiometer
m, M		mass
m	Ch. VI: E-4	dummy variable used to define correlator output
m	Ch. VII	number of controls
$\bar{M}$	Ch. II	torque exerted by gravity gradient
M	Ch. II:G	coefficient matrix relating components of gradient tensor to sensor measurements for Draper Lab spherical gradiometer
M	Ch. VIII	moment
M1, M2, M3		measurement reference systems 1, 2, and 3
n	Ch. III:B	nominal instrument spin rate
n	Ch. VI	order of correlator lag
n	Ch. VII	number of parameters
P		applied load
P_j		jth output effective parameter
P•		sensor model
Q		difference mode quality factor (300 rad/sec)
Q_r		power spectral density matrix for process noise associated with rate filter
Q_t		power spectral density matrix for process noise associated with torque filter
Q_β		sum mode quality factor
r		gradiometer measurement error variance

$\bar{r}$	radius vector
R	difference of (D_i/I_i) for components 1 and 2
R_r	power spectral density matrix for observation noise associated with rate filter
R_t	power spectral density matrix for observation noise associated with torque filter
R_O	difference of (K_i/I_i) for components 1 and 2
s	Laplace domain independent variable
$\hat{s}$	unit vector in direction of spin axis
t	time
t_f	final time
T	torque
$T_{a/b}$	transformation from reference system b to reference system a
T_d	disturbance torque applied to sensor case about $\hat{z}_s$
u	coupling coefficient between platform angular accelerations
U	strain energy
v	sensor noise
v_{jr}	jth component of observation noise vector associated with rate filter
v_{jt}	jth component of observation noise vector associated with torque filter
V	shear force
w_{jr}	jth component of process noise vector associated with rate filter
w_{jt}	jth component of process noise vector associated with torque filter
x	control mass position vector

x_j		correlator output frequencies
$[x[$	Ch. V	state vector
$[x]$	Ch. VI	platform input dynamics vector in sensor reference frame
z_{jt}		jth component of observation vector associated with torque filter
z_{rj}		jth component of observation vector associated with rate filter
$\hat{z}_s$		instrument ideal spin axis unit vector
$[z]$		observation vector

Greek Symbols

α		frequency discrimination filter center frequency error
α	Ch. IV:F	sensor dynamics transfer function amplitude ratio
$\vec{\alpha}$	Ch. III:B-4	rotation of elastic reference system with respect to sensor reference system
α_j		frequency of linear acceleration input along platform jth axis
$\{\alpha,\beta,\gamma\}$	Ch. II:G	Euler rotation sequence
β		ratio of input forcing frequency to sensor natural frequency
β_0		sum mode natural frequency
$\bar{\bar{\Gamma}}$		gravity gradient tensor
ϵ		rotating gravity gradiometer output error signal
ϵ_A		error torque associated with instrument anisoelasticity
ϵ_{AM}		error torque associated with elastic/spin/principal axis misalignment
ϵ_{LA}		error torque associated with the effect of linear acceleration upon the displaced mass center

$\epsilon_{E/S}$	error torque associated with misalignment between sensor and elastic axes
ϵ_{PMA}	error torque associated with platform/instrument axis system misalignment and generated via platform rotational motion
$\epsilon_{P/I\ lin}$	error torque associated with platform/instrument axis system misalignment and generated via platform linear acceleration
ϵ_{R}	error torque due to instrument rotation
ϵ_{SM}	error torque associated with sum mode mismatch
ϵ_{YS}	error torque associated with axial torsional coupling
η_j	system output phase lag along jth axis
θ	angular orientation of instrument with respect to platform
θ_c	angular orientation of the instrument case with respect to the platform
θ_1	angular orientation of the odd arm with respect to the platform
λ	Laplace operator
$\bar{\Lambda}$	angular velocity of rotor with respect to inertial space
$\hat{\mu}$	unit vector extending from origin of sensor axis system to origin of elastic axis system
ν_j	frequency of angular rate input about platform jth axis
ξ_D	damping coefficient of frequency discrimination filter (FDF) denominator
ξ_N	damping coefficient of numerator of FDF
$\vec{\xi}$	rotation of arm principal axis system with respect to sensor axis system
ρ_j	jth component of mass center offset with respect to sensor axis system
σ	standard deviation
τ	integration initiation time

φ	Ch. II	gravitational potential field
φ	Ch. VI	phase angle lag between platform input and sensor output
φ_T		pivot twist angle
φ_x	Ch. V	system output phase lag along sensor x axis associated with P_1 estimation
$\vec{\varphi}$	Ch. III:B-5	axis of rotation defining small angular misalignment between platform and sensor axis system
$\dot{\psi}$	Ch. III:B-2	arm deflection angle due to gravity
ψ	Ch. IV:F	sensor dynamics transfer function phase lag
$\bar{\bar{\psi}}$		arm compliance tensor
ω_b	Ch. VI	frequency contained in correlator output
ω_j		jth component of angular velocity vector
ω_s		instrument spin rate
ω_O		difference mode natural frequency, $2\omega_s$
$\vec{\omega}$		angular velocity vector
Ω		frequency of case disturbance torque
$\bar{\Omega}_j$		maximum magnitude of platform angular rate input about platform jth axis
$[\Omega]_p$	Ch. III:B-5	instrument rate vector in platform reference system
$[\vec{\Omega}_s]$		instrument rate vector in sensor coordinate system

Subscripts

A_x, A_y, A_z	components of the vector A in the direction of the $\hat{x}$, $\hat{y}$, $\hat{z}$ axes
A_1, A_2, A_3	components of the vector A in the direction of the $\hat{1}$, $\hat{2}$, $\hat{3}$ axes
A_i, A_j, A_k	components of the vector A in the direction of the $\hat{i}$, $\hat{j}$, $\hat{k}$ axes
b	body reference system

B	Ch. II	body reference system
B	Ch. III:B-4	body principal axes, single arm
c		case
C		control
e		even arm
E		elastic
IP		in phase
o		odd arm
p		platform
Q		quadrature
s		spin

Superscripts

$\bar{}$ or $\vec{}$	vector
^	unit vector (in the direction of $\bar{A}$)
=	tensor
~	error in estimate of A
•	time rate of change of A

Abbreviations

cm	mass center
EU	Eötvös unit
mag	magnitude
OEP	output effective parameter
PSSD	phase sensitive signal demodulator
RGG	rotating gravity gradiometer

Chapter I

INTRODUCTION

A. GRAVITY GRADIOMETER BACKGROUND AND APPLICATIONS

The earth's gravitational field has been studied for decades and many different mathematical models for it have been proposed. Absolute accuracies of a few parts in 10^9 and recent developments indicate 10^{-8}g and better will be available in future field instruments [Refs. HA-1, SA-1]. Relative measurements of the field have been carried out with accuracies of 1 part in 10^9 [LO-1]. The accuracy with which a gravimeter can provide relative gravity field measurements, from which to get gravity gradient information, depends on the tightly controlled conditions. In order for gradient data of this quality to become generally available, the development of a direct gradient measuring device, the gravity gradiometer, will be necessary.

A gravity gradiometer measures the spatial gradient of the gravitational field in which it is immersed. The first workable gravity gradiometer was built and demonstrated in 1880 by Baron Roland von Eötvös [WI-1]. The instrument was composed of a simple bent beam, two proof masses, and a torsion fiber as shown in Fig. I-1. The Eötvös torsion balance gradiometer provided measurements of the horizontal gravity gradient to an accuracy of 10^{-9} m/sec^2/m, i.e., 10^{-9} (m/sec^2)/m. The 10^{-9} sec^{-2} has become the fundamental unit of gravity gradient measurement and is referred to as the Eötvös Unit (EU). The Eötvös instrument was used within the United States during the early Twentieth Century to aid in geophysical exploration but was eventually replaced by gravimeters which were more "mobile" instruments. However, the limited accuracy

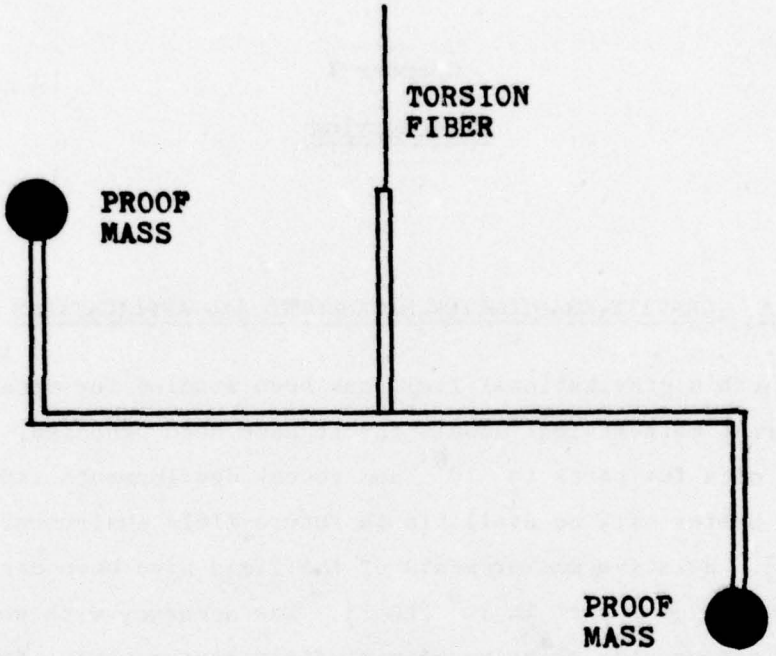


FIG. I-1 EÖTVÖS TORSION BALANCE GRAVITY GRADIOMETER

with which a gradient can be determined by gravimeter measurements has once again caused the gravity gradiometer to be reconsidered for application to geophysical exploration [BE-1].

The potential applications for a gravity gradiometer capable of operation upon a mobile platform such as a spacecraft, aircraft, or ship are numerous. The possible contributions of the gradiometer to earth geodesy are discussed in detail by Metzger [ME-1], Forward [FO-1], and Loomis [LO-1]. A "skyhook" shuttle-borne gradiometer subexperiment has been proposed by Colombo, et. al. [CO-1] for purposes of gravity field mapping by satellite. In addition, the gradiometer also promises to advance the state of the art by inertial navigators. The accuracy of a current, high quality inertial navigation system is limited by unmodeled vertical deflections. Jordan [JO-1] and Britting [BR-1] evaluate the improvement in the performance of an inertial navigator when a gradiometer is used to derive information concerning the local

vertical. Heller [HE-1] develops several different approaches to the gravity gradiometer aided inertial navigation system, and shows that the 1 EU accuracy gradiometer is compatible with such a system. Metzger [ME-2] has shown that a gradiometer aided ship's inertial navigation system can significantly reduce the terminal error of a submarine launched ballistic missile. Forward [FO-2] has discussed gravitational field measurements of the planets via gradiometers. Gradiometers were also considered for Apollo applications in connection with lunar mascon investigations. A lunar orbiting experiment based upon a gravity gradiometer was proposed by DeBra, et. al.[DeB-1] for determination of mascon associated gravity anomalies to within 1% accuracy.

B. PURPOSE OF RESEARCH

Moving base gravity gradiometers have existed in various stages of design and development for more than a decade. While the concept of the moving base gravity gradiometer holds enormous potential with respect to the acquisition of scientific data which cannot be obtained from conventional instruments, the actual development of such a sensor has proven to be a true challenge to the state of the art in both the design and the fabrication of instrument hardware and electronics.

The desired operating accuracy level of gradiometer is 1 EU on a moving base. This is approximately 1/3000th of the earth's vertical gravity gradient. Based upon analysis of one of the instruments currently under development, the Hughes rotating gravity gradiometer (RGG), it is quite possible that any instrument of this type will require, as an integral part of its design, an active parameter estimation and compensation loop. The purpose of the loop is to trim instrument physical properties to within required tolerances at the beginning of operation and then to maintain these tolerances throughout the data gathering period. A simple numerical example lends validity to the need for such a loop. Consider the Kearfott KING II inertial navigation gyro. Based upon physical and performance specifications published by the manufacturer, analysis of the gyro drift characteristics predicts mass center offsets

between 10^{-6}m and 10^{-8}m. For the Hughes rotating gravity gradiometer, a mass center offset equal to 10^{-8}m could result in output errors two orders of magnitude greater than the total allowable instrument error budget. Analysis of the rotating gravity gradiometer clearly indicates that without active compensation, manufacturing and alignment tolerances will be extraordinarily rigid and quite possibly unrealizable.

Three moving base gravity gradiometers are currently under development. To date, none has been successfully operated at the desired 1 EU accuracy level under field conditions. Given this state of development, and the extent to which fabrication of the instrument will test state of the art manufacturing techniques, this research was initiated to establish the feasibility of successful moving base gravity gradiometer operation. A particular instrument, the Hughes rotating gravity gradiometer (RGG) was selected as the "test case" instrument. In this thesis a complete model for the output signal errors induced due to the coupling of RGG instrument dynamics and instrument physical parameters is developed. The problems of parameter estimation, signal compensation, and active parameter trim are analyzed.

C. CHAPTER CONTENTS

In Chapter II the three separate gradiometers under development--Bell Aerospace accelerometer gradiometer, C. Stark Draper Labs' floated proof mass gradiometer, and the Hughes rotating gravity gradiometer--are discussed. The method by which each measures the gradient is described. Sensor orientation requirements for full gradient tensor measurement are developed.

Beginning with Chapter III, discussion is limited to the Hughes RGG and the supportive instrumentation necessary for parameter estimation and control. An instrumented platform/RGG system is defined in Ch. III, and a linear error model developed.

In Chapter IV, the Hughes RGG output error equation is derived. A set of parameters which influences the output error equation is defined. It is pointed out that this set of parameters, the output effective

parameters, must be driven to its nominal condition in order that the dynamics associated error within the instrument output signal to be reduced to zero.

In Chapter V a Kalman Filter approach to output effective parameters (OEP) identification is pursued. Using a two-stage parallel filter approach, a nonlinear time varying coefficient filtering problem, with respect to OEP estimation, is reduced to a problem which is linear with constant coefficients. The parameter identification performance of the parallel filter approach is compared to that of commercially available frequency demodulators.

In Chapter VI a correlation approach to OEP identification is developed. Various modifications to the basic correlation technique are then considered and evaluated. A set of output correlation functions is defined. The effects of various platform input frequencies are evaluated. It is shown that high order, low frequency lags, coupled with known input to the sensors, provide accurate estimates of the OEP.

In Chapter VII an approach to OEP control using the motion of small control masses is suggested. An example of control law operation is given.

In Chapter VIII the OEP are rewritten in such a way as to demonstrate the reachability of each parameter using a control mass repositioning method. A thorough development of the RGG arm compliance equations is included in order to demonstrate reachability of the elasticity related parameters.

In Chapter IX a RGG mass repositioning control system is defined. The digital simulation which was developed to test the system is outlined. Output effective parameter controllability is demonstrated using the simulation. The performance of the parameter control system is studied and variations to the basic controller are considered.

D. CONTRIBUTIONS

The principal contribution of this document is the demonstration that using an active parameter estimation and control system, a 1 EU accuracy, moving base gravity gradiometer can be built given the state of the art in instrument fabrication. The performance of the system developed is adequate for estimation and control of instrument parameters to the extent that uncontrolled instrument signal errors in excess of 6×10^4 EU can be trimmed to approximately 0.4 EU. Current efforts to produce a 1 EU gravity gradiometer are limited to precise control of manufacturing tolerances and preoperational parameter trim performed in the laboratory. An online parameter estimation and control system which is capable of trimming a 60,000 EU error gradiometer to less than 1 EU error adds a completely new dimension to the development effort, significantly increasing the likelihood of successful development of an entirely new class of inertial instruments.

Additional contributions are:

1. A method is developed by which nonlinear, non-constant coefficient systems of a certain class may be analytically evaluated using Kalman filters without iteration;

2. Various relative orientations among the sensors are considered and it is shown that orthogonal sensor output axes provide minimal rms gradient estimate errors in the case of the Hughes and Bell gradiometers. For the Draper Labs spherical gravity gradiometer, it is shown that three sensors having their between-the-weights axes oriented very nearly along the faces of the corner of a cube and bisecting each planar corner provide the best estimate of the components of the gravity gradient tensor.

Chapter II

GRAVITY GRADIOMETERS

A. THE GRAVITATIONAL FIELD AND ITS GRADIENT

A gravitational field is conservative and may be expressed as a scalar function φ of position $\vec{r}$ relative to the attracting body. The gravitational acceleration $\vec{g}$ due to the body, at any point $\vec{r}$, may be written as

$$\vec{g} = \nabla\varphi(\vec{r}) \ . \tag{2.1}$$

Expressing $\vec{g}$ in a set of Cartesian coordinates, (2.1) may be rewritten as

$$[\vec{g}]^T = \begin{bmatrix} \frac{\partial\varphi}{\partial x}, & \frac{\partial\varphi}{\partial y}, & \frac{\partial\varphi}{\partial z} \end{bmatrix} \ . \tag{2.2}$$

The spatial gradient of the gravity vector $\vec{g}$, written in Cartesian coordinates is the second order tensor

$$[\nabla\vec{g}] = \begin{bmatrix} \frac{\partial^2\varphi}{\partial x^2} & \frac{\partial^2\varphi}{\partial x\partial y} & \frac{\partial^2\varphi}{\partial x\partial z} \\ \frac{\partial^2\varphi}{\partial y\partial x} & \frac{\partial^2\varphi}{\partial y^2} & \frac{\partial^2\varphi}{\partial y\partial z} \\ \frac{\partial^2\varphi}{\partial z\partial x} & \frac{\partial^2\varphi}{\partial z\partial y} & \frac{\partial^2\varphi}{\partial z^2} \end{bmatrix} \ . \tag{2.3}$$

In order to determine completely the gravity gradient tensor of (2.3), all of the independent components must be measured. For a conservative gravitational force [KA-1]:

$$\text{A.} \qquad \nabla \times \vec{g} = 0 \; ; \tag{2.4}$$

$$\text{B.} \qquad \nabla \cdot \vec{g} = 0 \; . \tag{2.5}$$

Equation (2.4) demonstrates the symmetry of the gradient tensor. Equation (2.5) is Laplace's equation and requires that the sum of the diagonal components of the gradient tensor is zero. Since the gradient tensor is symmetric, no more than six of its nine components are independent. The scalar Laplace equation (2.5) further reduces the total number of independent elements by one. Hence, only five of the nine elements of the gravity gradient tensor are independent. Complete determination of the gravity gradient tensor at any point requires only five measurements. It will be shown later in this chapter that for any of the gradiometers currently being developed, a set of three instruments is sufficient to determine the gravity gradient, when each instrument is properly oriented with respect to the others. Sensor orientation is discussed in Sect. II-G.

To follow convention, the gradient tensor of (2.3) will be represented by the tensor $\vec{\vec{\Gamma}}$ in the remainder of this document. The gradient tensor of (2.3) is thus expressed as

$$[\vec{\vec{\Gamma}}] = \begin{bmatrix} \Gamma_{xx} & \Gamma_{xy} & \Gamma_{xz} \\ \Gamma_{xy} & \Gamma_{yy} & \Gamma_{yz} \\ \Gamma_{xz} & \Gamma_{yz} & \Gamma_{zz} \end{bmatrix} \tag{2.6}$$

where

$$[\vec{\vec{\Gamma}}] \triangleq [\nabla \vec{g}] \; .$$

B. SOME COMMENTS ON THE PHILOSOPHY OF GRADIENT SENSOR DESIGN

The vertical component of the earth's gravity gradient is approximately 3000 EU.[†] For many applications [e.g., Ref. ME-2], the gradient must be measured to an accuracy of 1 EU, i.e., to an accuracy of about 0.03%. Gradient measurements having this accuracy are more difficult to obtain than might be expected from the 0.03% requirement. For an instrument designed to measure the gravity gradient over a distance of 10 cm, the 1 EU requirement corresponds to measurement of differential accelerations of 10^{-10} m/sec^2 while operating in the presence of 1 g (~ 10 m/sec^2) and vehicle accelerations on the order of 0.1 g. The changing acceleration field in a moving vehicle makes classical gradient measurement techniques unfeasible. In addition, the 1 EU requirement exceeds the state of the art that has been developed for conventional inertial instruments. Brownian noise, which marks a fundamental limit for the performance of any instrument, must be considered as necessary to the stability and drift of instrument parameters.

B.1 Sensor Concepts

There are three moving base gravity gradiometers currently under development. The new designs, all of which propose to achieve the required 1 EU accuracy level, are fundamentally different in design approach. The group includes sensors designed specifically to measure gravity gradient as well as sensors formulated from already existing equipment and used in such a way so as to provide a gradient measurement. Two of the instruments rotate, modulating the information, thereby transferring the gravity gradient signal to a higher frequency, quieter, portion of the spectrum, and separating the signal from some sources of instrument bias. The third sensor uses a gyro float type of suspension to isolate noise from the signal while avoiding errors induced by rotation.

[†] 1 EU is 10^{-9} sec^{-2}.

A rotating instrument which is frequency "tuned" can use resonance to amplify the signal at the signal frequency at the expense of increased phase sensitivity. Instrument rotation involves penalties, however, as well as advantages. Inherent in any rotating system are errors associated with nonuniform rotation due to bearing irregularities, mass unbalance, and drive speed variation. The instrument designer must decide whether better results can be obtained through zero frequency noise reduction or through minimization of the dynamically induced errors associated with a rotating sensor.

C. GRAVITY GRADIOMETERS UNDER DEVELOPMENT

The first moving base gravity gradiometer was proposed by Dr. Robert Forward [BEL-2] of Hughes Research Laboratory. The Hughes instrument is a rotating sensor consisting of hardware designed specifically for the measurement of the gravity gradient. The second of the new gravity gradiometers was designed at the C. Stark Draper Labs by Dr. Milton Traegeser [TR-1]. The Draper Labs' instrument is also one of fundamentally new design. This sensor, however, does not rotate, and nominally senses the gravity gradient at zero frequency. The third of the candidate gradiometers is being developed at Bell Aerospace Corp. under the direction of Mr. E. Metzger [ME-2]. The Bell instrument is a rotating sensor which uses modified Bell Model VII accelerometers in a system approach to sensor development.

Each of the three instruments under development provides measurements of two components, or combinations of the components, of the gravity gradient tensor. The different gradiometers are briefly discussed in the remainder of this chapter.

D. HUGHES ROTATING GRAVITY GRADIOMETER

The rotating gravity gradiometer being developed at Hughes Research Labs measures gravity gradient at a nonzero frequency. The instrument, shown in Fig. II-1, consists primarily of two nonimally

identical arms connected by a flex pivot. The relative torque acting upon the arms strains the pivot and is sensed by a piezoelectric transducer. The torque acting upon the instrument arms due to the gravity gradient is [BEL-1]

$$\Delta T = 2mr^2[\Gamma_{yy} - \Gamma_{xx}]\sin(2\omega t) + 4mr^2[\Gamma_{xy}]\cos(2\omega t) \quad . \tag{2.7}$$

The instrument spin rate ω was selected to be as high as possible so as to maximize information processing capability and instrument ruggedness. With the spin rate optimized in this manner, the sensor was then designed to possess a resonant differential torque output frequency equal to twice the spin frequency. Hence, the gravity gradient signal excites the instrument at its resonant frequency. Each arm acts as a differential specific force sensor. In addition, acting as a pair, the

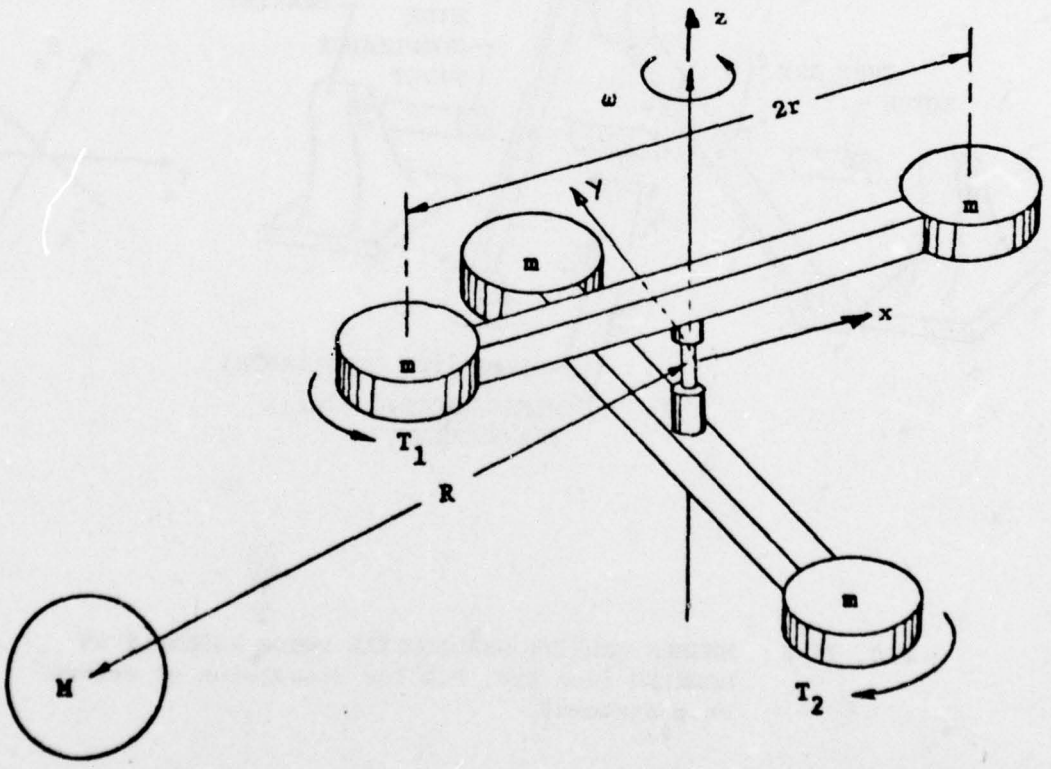


FIG. II-1 HUGHES RESEARCH LABS ROTATING GRAVITY GRADIOMETER

arms provide isolation from case angular acceleration about the spin axis since the instrument is sensitive only to differential torque.

D.1 Sensor Physical Properties

The model used to represent the Hughes gravity gradiometer is shown in Fig. II-2. Nominal physical and operational data associated with the instrument are tabulated in Table II-1.

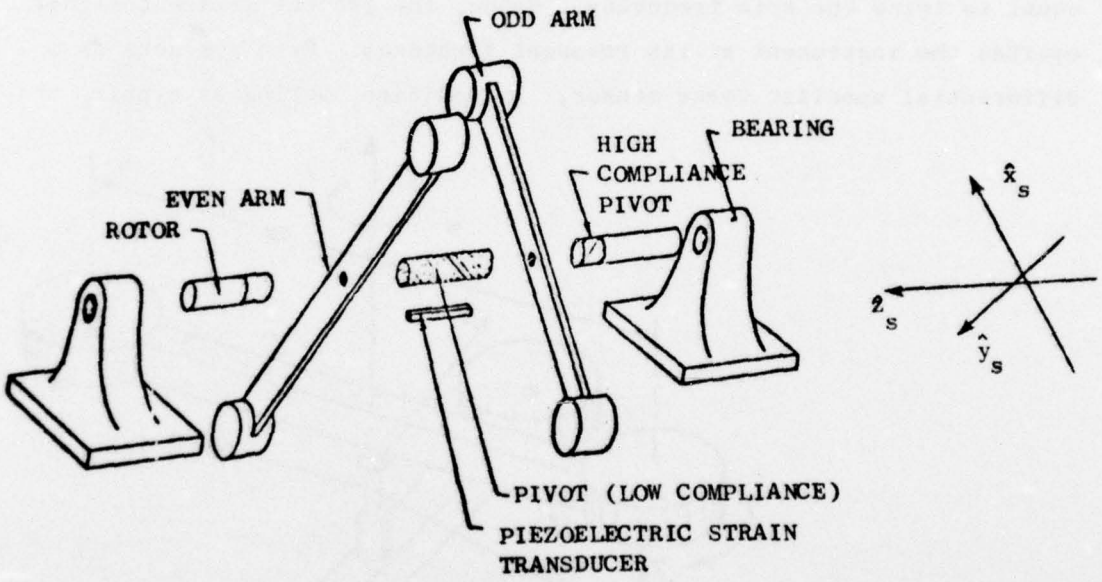


FIG. II-2 HUGHES GRAVITY GRADIOMETER ROTOR ASSEMBLY AS MODELED (see Sec. D.2 for discussion of reference systems).

Table II-1

NOMINAL INSTRUMENT DATA*

Parameter		Value	Units
Odd Arm Mass		1.563	kg
Even Arm Mass		1.563	kg
Odd Arm Moments of Inertia:	I_{xx}	4.990×10^{-4}	kg m^2
	I_{yy}	35.60×10^{-4}	kg m^2
	I_{zz}	35.61×10^{-4}	kg m^2
Even Arm Moments of Inertia:	I_{xx}	35.60×10^{-4}	kg m^2
	I_{yy}	4.990×10^{-4}	kg m^2
	I_{zz}	35.61×10^{-4}	kg m^2
Sensor Spin Rate		110	rad/sec
Difference Mode Resonant Freq., Q		220	rad/sec
Sum Mode Resonant Freq., Q_β		142	rad/sec
Principal Axis Compliances:	ψ_{xx}	3.50×10^{-8}	m/N
	ψ_{yy}	3.50×10^{-8}	m/N
	ψ_{zz}	5.99×10^{-8}	m/N
Low Compliance Pivot Stiffness		63	N m/rad
High Compliance Pivot Stiffness		47	N m/rad

* Data taken from Refs. AM-1 and AM-2

D.2 Reference Systems

Figure II.3 displays side and axial views of the Hughes gradiometer such that the even arm is seen end-on in the side view. The platform reference system is defined as one which remains fixed with respect to the platform upon which the sensor is mounted. The $\hat{z}_p$ axis points along the nominal rotor spin vector. Vector x_p forms the platform norma in the direction of $\vec{g}$.

The body reference system (subscript b) rotates with the rotor and is nominally aligned with the platform reference system at time zero. The origin of the body reference system is defined as the true mass center of the odd arm, even arm combination. Unit vectors $\hat{x}_b$, $\hat{y}_b$, $\hat{z}_b$ are defined by the principal axes of the two arm plus rotor instrument. The unit vectors defining the directions of the body axis system do not necessarily coincide with any of the instrument geometric axes, or the spin axis.

The sensor reference system (subscript s) has its origin at the ideal instrument mass center and at time zero the sensor system coincides exactly with the platform reference system. The sensor system rotates with the instrument rotor, and is nominally coincident with the body reference system.

The elastic reference system (subscript l) has its origin at the ideal instrument mass center and rotates with the rotor. Axis $\hat{z}_\ell$ coincides with the true elastic axis of the low compliance pivot of Fig. II-2 and is nominally coincident with $\hat{z}_s$.

D.3 Rotating Gravity Gradiometer Signal Equation, The Twice Frequency Torque

The rotating gravity gradiometer employs a piezoelectric crystal to measure differential rotations of the even arm with respect to the odd arm about the $\hat{z}_s$ axis. An ideal rotating gravity gradiometer is defined as one having as its output a signal which is due only to the gradient in the local gravity field. With ideal operation, a measurement of arm relative rotation may be directly transformed into an

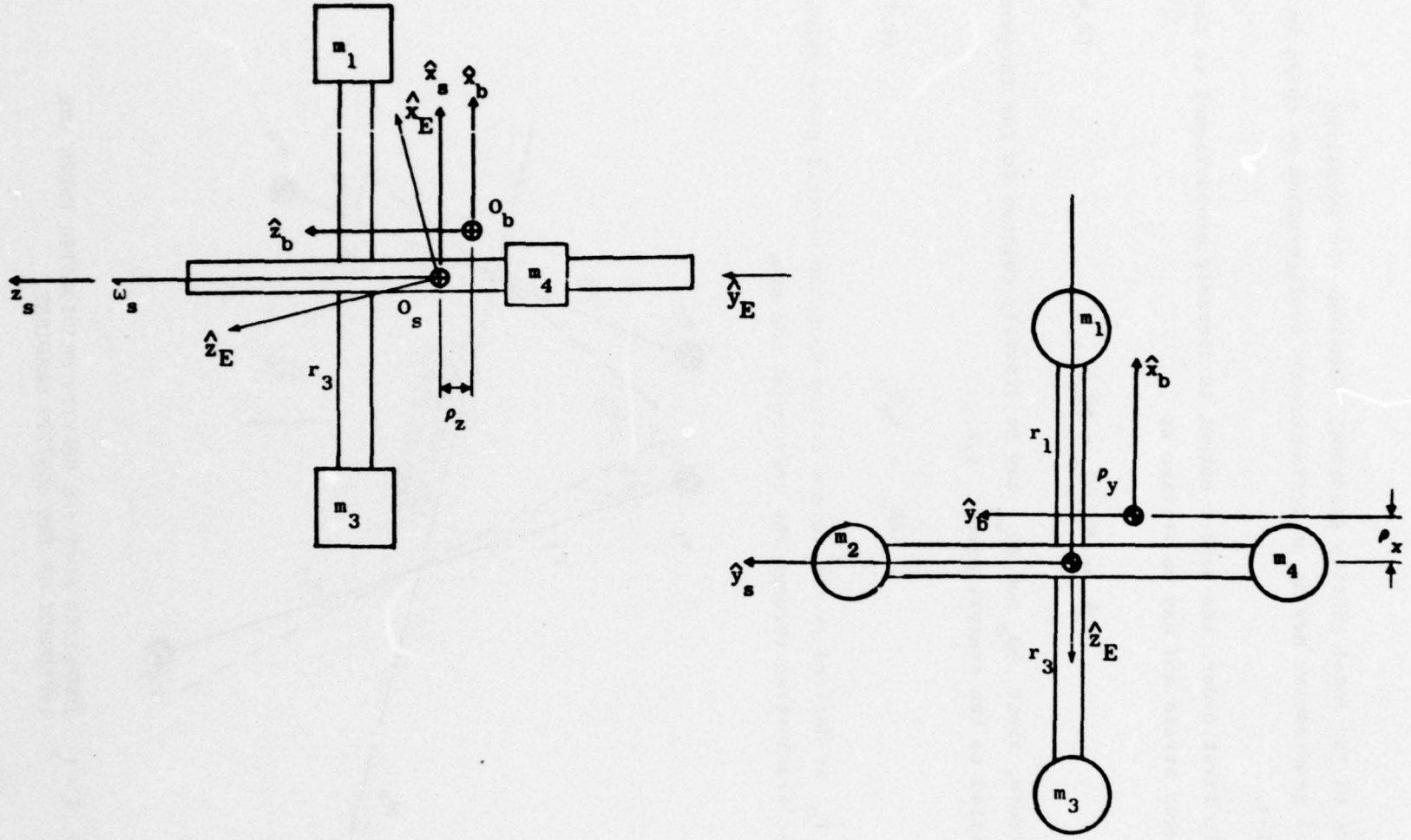


FIG. II-3 SIDE AND AXIAL VIEWS OF HUGHES RGG (rotating gravity gradiometer) FOR AXIS SYSTEM DEFINITION.

estimate of the local gravity gradient. Consider the idealized dumbbell gradiometer having an instantaneous configuration as shown in Fig. II-4.

To first order, the sensor output is linearly proportional to the transducer strain and may be written as

$$S = K_T(\delta\theta_o - \delta\theta_e) \ . \tag{2.8}$$

Furthermore, since $\delta\theta_o$ and $\delta\theta_e$ may be linearly related to the torques transmitted to the central pivot; i.e.,

$$\delta\theta_o = k_T T_o \tag{2.9}$$

where T_o is defined as the torque acting upon the central pivot which has been transmitted through the instrument odd arm.

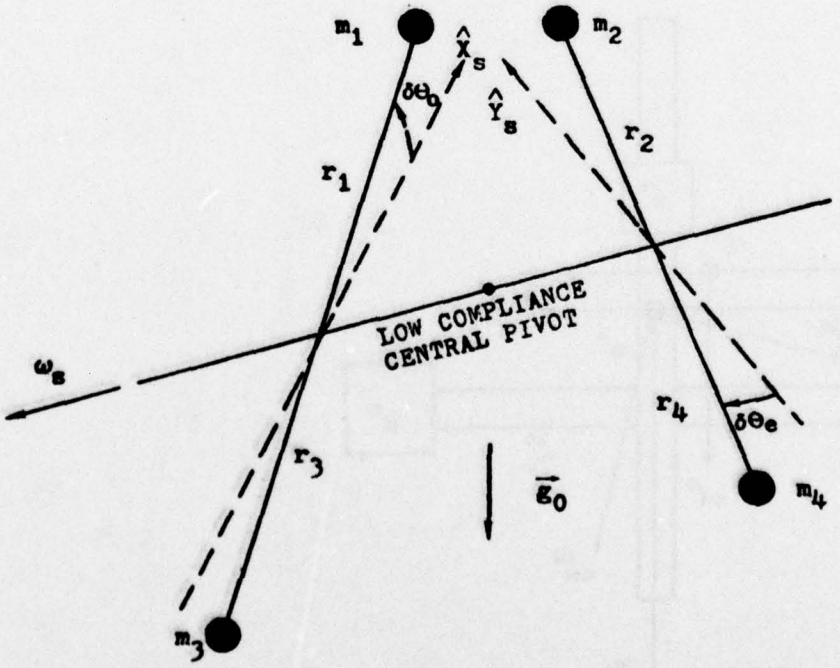


FIG. II-4 IDEALIZED ROTATING GRAVITY GRADIOMETER UNDER THE INFLUENCE OF THE GRAVITY GRADIENT.

A complete discussion of gradiometer output signal must account for the effects of arm dynamics upon that signal. The principle of operation can be illustrated with a simpler model so a consideration of the effects of arm dynamics has been deferred to Sect. D.4. Thus only the instrument steady state response is considered for which the sensor output may be written as

$$S = K_T k_T (T_o - T_e) . \tag{2.10}$$

With all instrument arm, relative motion restricted to that range over which transducer gains K_T and k_T remain constant, sensor output is directly proportional to the difference between the odd and even arm torques as shown in the simplified output signal diagram of Fig. II-5.

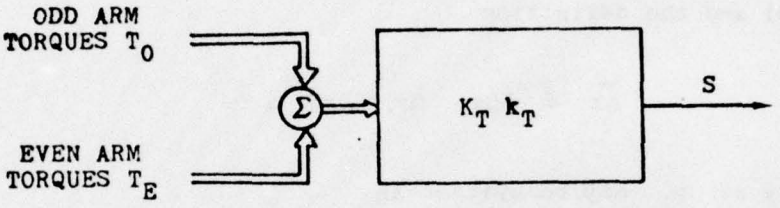


FIG. II-5 SIMPLIFIED SENSOR MODEL DISPLAYING SENSOR TORQUE TO SIGNAL CONVERSION

D.4 Simplified Gradiometer Signal Development. Steady State Operation Approximation.

Consider the ideal dumbbell gradiometer oriented with its spin axis $\hat{z}_s$ horizontal as shown in Fig. II-6. The vector $\vec{g}_0$ is the gravity vector at the origin of the sensor axis reference system and defines the local horizontal plane.

At any of the masses, m, for example, the gravity vector can be written in terms of $\vec{g}_0$ as in (2.11), (2.12), and (2.13).

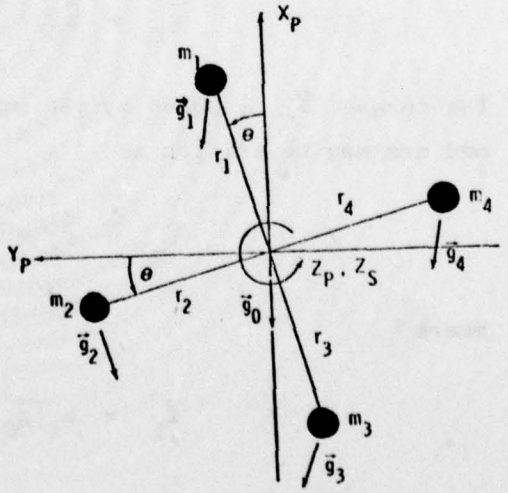


FIG. II-6 DUMBBELL GRADIOMETER

$$g_{1x} = g_{ox} + \frac{\partial g_x}{\partial x}\Delta x + \frac{\partial g_x}{\partial y}\Delta y + \frac{\partial g_x}{\partial z}\Delta z \qquad (2.11)$$

$$g_{1y} = g_{oy} + \frac{\partial g_y}{\partial x}\Delta x + \frac{\partial g_y}{\partial y}\Delta y + \frac{\partial g_y}{\partial z}\Delta z \qquad (2.12)$$

$$g_{1z} = g_{oz} + \frac{\partial g_z}{\partial x}\Delta x + \frac{\partial g_z}{\partial y}\Delta y + \frac{\partial g_z}{\partial z}\Delta z \ . \qquad (2.13)$$

Using (2.6) and the definition

$$\vec{\Delta r} \triangleq (\Delta x, \ \Delta y, \ \Delta z)^T \ , \qquad (2.14)$$

the gravity at m_1 may be written as

$$\vec{g}_1 = \vec{g}_0 + \bar{\bar{\Gamma}} \cdot \vec{\Delta r}_1 \ . \qquad (2.15)$$

Since Δr_1 refers to the displacement of m_1 from the origin of the sensor reference system,

$$\vec{\Delta r}_1 \equiv \vec{r}_1 \ , \qquad (2.16)$$

and (2.15) may be written as

$$\vec{g}_1 = \vec{g}_0 + \bar{\bar{\Gamma}} \cdot \vec{r}_1 \ . \qquad (2.17)$$

The torque $\vec{T}_0$ induced by the gravitational field influence upon the odd arm may be written as

$$\vec{T}_o = \vec{r}_1 \times \vec{f}_1 + \vec{r}_3 \times \vec{f}_3 \qquad (2.18)$$

where

$$\vec{f}_1 = m_1\{\vec{g}_0 + \bar{\bar{\Gamma}} \cdot \vec{r}_1\} \qquad (2.19)$$

and

$$\vec{f}_3 = m_3\{\vec{g}_0 + \bar{\bar{\Gamma}} \cdot \vec{r}_3\} \quad . \tag{2.20}$$

Since for an ideal instrument all four masses m_i are equal, and since

$$\vec{r}_3 = -\vec{r}_1 \, , \tag{2.21}$$

(2.18) can be rewritten as

$$\vec{T}_o = 2m\vec{r}_1 \times \{\bar{\bar{\Gamma}} \cdot \vec{r}_1\} \quad . \tag{2.22}$$

An equation similar to (2.22) can be written for even arm induced torques and therefore the differential output torque induced by the gravity gradient is

$$\vec{T}_o - \vec{T}_e = 2m\left\{[\vec{r}_1 \times \bar{\bar{\Gamma}} \cdot \vec{r}_1] - [\vec{r}_2 \times \bar{\bar{\Gamma}}\vec{r}_2]\right\} . \tag{2.23}$$

Along the sensitive axis, $\hat{z}_s$, the component of the differential torque vector of (2.23) is

$$(\vec{T}_o - \vec{T}_e) \cdot \hat{z}_s = 2mr^2\Big\{2(\Gamma_{yy} - \Gamma_{xx})\sin\theta\cos\theta + 2\Gamma_{xy}(\cos^2\theta - \sin^2\theta)\Big\} \tag{2.24}$$

or

$$(\vec{T}_o - \vec{T}_e)\cdot \hat{z}_s = 2mr^2\Big\{(\Gamma_{yy}-\Gamma_{xx})\sin 2\theta + 2\,\Gamma_{xy}\cos 2\theta\Big\}. \tag{2.25}$$

Note that (2.25) is the signal equation (2.7) given by Bell [BEL-1]. A similar equation which accounts for the actual arm moments of inertia (rather than the dumbbell assumption) is developed in Ames [AM-2]. Using this development (2.25) becomes

$$(\vec{T}_o - \vec{T}_e) \cdot \hat{z}_s = (I_{yy} - I_{xx})\left\{(\Gamma_{yy} - \Gamma_{xx})\sin 2\theta + 2\Gamma_{xy}\cos 2\theta\right\} \quad (2.26)$$

Since the rotation angle θ may be written as

$$\theta = \omega_s t \quad (2.27)$$

(2.25) may be written as

$$(\vec{T}_o - T_e) \cdot \hat{z}_s = 2mr^2\left\{(\Gamma_{yy} - \Gamma_{xx})\sin 2\omega_s t + 2\Gamma_{xy}\cos 2\omega_s t\right\}. \quad (2.28)$$

Hence the gravity gradient signal frequency is twice the instrument spin frequency. Direct measurement of sensor in-phase output at $2\omega_s$ yields a direct measurement of $\Gamma_{yy} - \Gamma_{xx}$. Direct measurement of the quadrature output at $2\omega_s$ yields a direct measurement of Γ_{xy}.

D.5 Rotating Gravity Gradiometer (RGG) Output Equation

In addition to the effects of the local field gravity gradient, gradiometer output is also a function of various instrument and dynamics related error sources. In this section, instrument dynamics have been neglected. For simplicity the differential torque has been referred to as the RGG output. A complete equation for the differential torque is given in (2.29).

$$\Delta T = \hat{z} \cdot \left[\sum_{i=1}^{4} (m_i \rho_i)(-1)^{i-1} \times \frac{\Pi}{R}\right] + \frac{d^I}{dt}\left[(I_o - I_e) \cdot \omega\right] \cdot \hat{z} + \hat{z} \cdot \Sigma\, T_{error} + \hat{z} \cdot \Sigma\, T(\vec{\nabla g}) \quad . \quad (2.29)$$

The first three terms on the right side of (2.29) are sources of output error resulting from instrument irregularities. The fourth term is the desired gravity gradient signal. The first term expresses the effect of instrument mass center position error upon instrument output. The second term relates output to sensor inertia properties and sensor rotational dynamics. The third term of (2.29) includes all other errors including arm anisoelasticity, sum mode mismatch, and the misalignment

between pivot principal and elastic axes. These errors are analyzed in Ch. III. All are dynamics dependent and can be modeled. Output errors due to temperature gradients, random noise, and other non-dynamics related sources are not considered in this document. Errors of this type are of such a nature that their resultant input disturbance cannot be measured.

D.6 Hughes Gradiometer Signal and Error Torque Levels

The desired gradiometer measurement accuracy is 1 EU where

$$1 \text{ EU} \triangleq 1 \times 10^{-9} \text{ sec}^{-2} . \tag{2.30}$$

At its surface, the earth has a vertical gravity gradient approximately equal to 3000 EU. Using (2.28) with the coefficient $2mr^2$ taken to be 3.56×10^{-3} kg m^2 (from Table II-1), the Γ_{xx} gradient produces a peak signal torque as expressed by (2.31).

$$|\Delta T_g|_{max} = (3.56 \times 10^{-3})(3 \times 10^{3})(1 \times 10^{-9}) \tag{2.31}$$

$$|\Delta T_g|_{max} = 1.068 \times 10^{-8} \text{ N m} . \tag{2.32}$$

A 1 EU gradiometer output signal error corresponds to 3.56×10^{-12} N m.

$$|\Delta T_{1 \text{ EU}}| = 3.56 \times 10^{-12} \text{ N m.} \tag{2.33}$$

This 1 EU torque corresponds to an arm relative orientation change of 2.1×10^{-14} rad when tuned to $2\omega_s$ (35 Hz).

E. DRAPER LABS FLOATED PROOF MASS GRAVITY GRADIOMETER

E.1 Cylindrical Gradiometer

The Draper Labs instrument senses the gravity gradient signal at zero frequency, i.e., the instrument does not rotate. A conceptual drawing of the Draper Labs single axis instrument is shown in Fig. II-7.

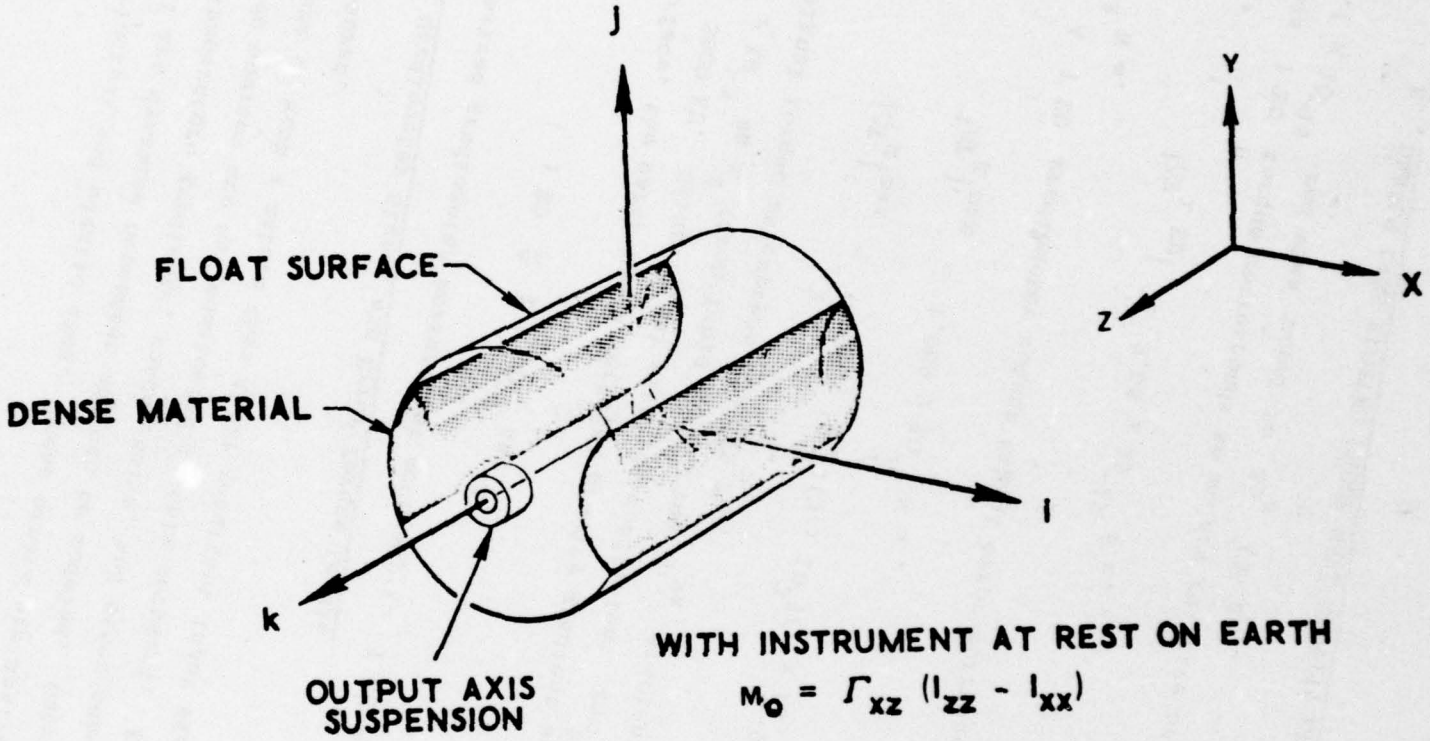


FIG. II-7 AXIALLY SYMMETRIC CYLINDRICAL FLOATED PROOF MASS GRAVITY GRADIOMETER

The x, y, z reference system of the figure is a geodetic earth fixed, earth centered system. The i, j, k system is fixed with respect to the instrument.

The heart of the Draper Labs gradiometer is a cylindrical float similar to that used in the construction of inertial quality gyros. The instrument is supported by bouyant fluid forces acting on the float and by electrical fields which act at the bearings. Symmetrically located within the float are two dense proof masses. The gravity gradient torque component along the output axis of the instrument shown in Fig. II-7 is

$$\bar{M} = \Gamma_{xy}(I_{yy} - I_{xx})\hat{k} \ . \qquad (2.34)$$

The torque $\bar{M}$ causes a rotation of the instrument with respect to its mounting structure. This rotation is sensed and nulled by a feedback electrostatic torque which is proportional to the component Γ_{xy} of the gradient tensor. By repositioning the nominal location of the dense material, and by developing combinations of the outputs from several differently oriented sensors, it is possible to extract measurements of all five independent terms of the gradient tensor.

The Draper Lab instrument extends state of the art floated inertia instrument technology, much of which was developed at the Draper Labs. Successful operation requires precise control of the instrument float as well as control of temperature and temperature gradients [WI-1].

E.2 Spherical Gradiometer

The single axis cylindrical instrument was used as a development model. The instrument now under development uses a spherical float with dense masses at two points giving it a dumbbell mass distribution as shown in Fig. II-8 [TR-2].

The torque about each of two axes perpendicular to the axis of symmetry provides two readouts per instrument. The flotation fluid is inviscid providing a degree of isolation from small amplitude (jitter) rotations of the case. The measurements of three instruments, when

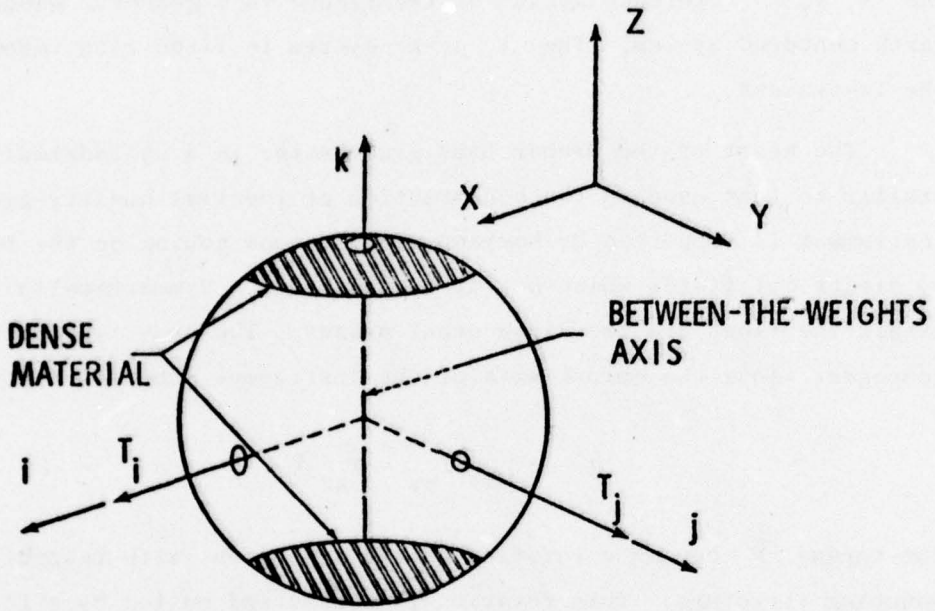


FIG. II-8 DRAPER LABS FLOATED SPHERICAL GRAVITY GRADIOMETER [from TR-2]

combined, provide the gravity gradient and information for jitter compensation.

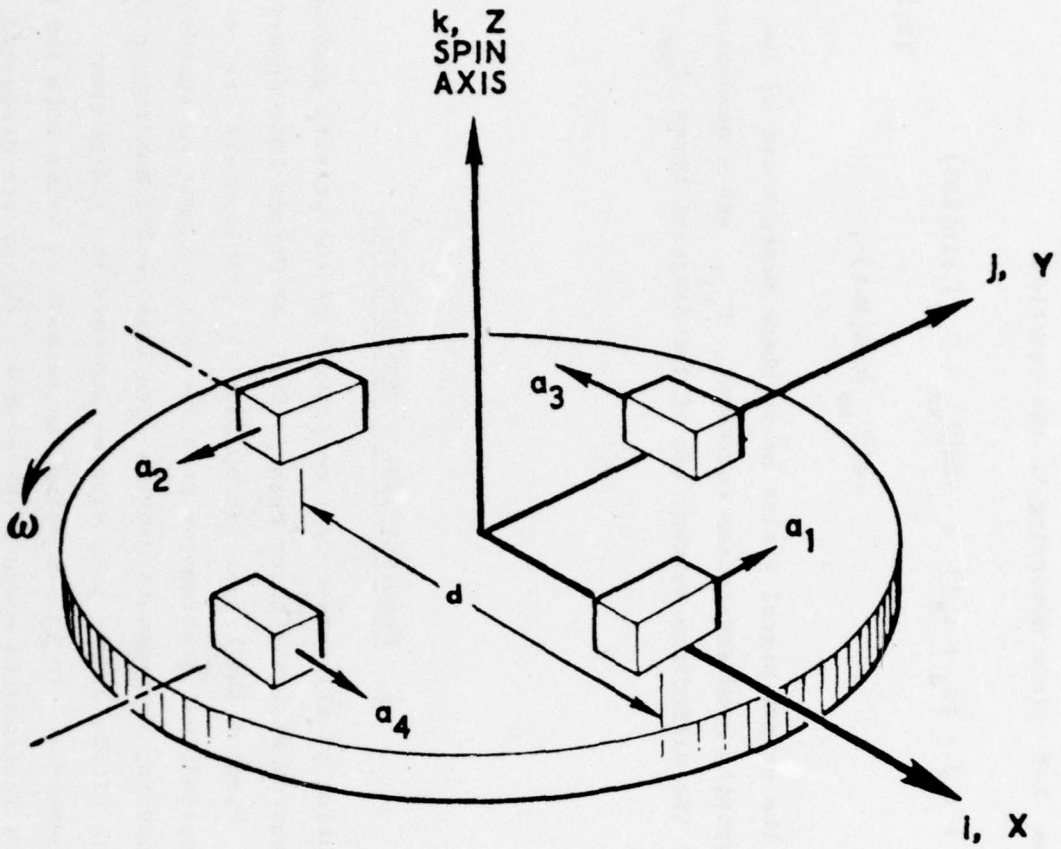
F. BELL AEROSPACE CORP. GRADIOMETER

The sensitive elements of the Bell Aerospace Corp. gravity gradiometer are four modified Bell Model VII pendulous accelerometers. The accelerometers are mounted symmetrically on a spin table with their sensitive axes in the tangential direction defined by $\hat{s}$, where

$$\hat{s} = \hat{\omega} \times \hat{r} . \qquad (2.35)$$

The nominal spin table rate is 0.5 Hz [ME-1]. A conceptual diagram of the Bell instrument is shown in Fig. II-9.

An instrument configured as shown in Fig. II-8 senses gravity



$$[(a_1 + a_2) - (a_3 + a_4)]_V = -2d(\Gamma_{xx} - \Gamma_{yy})\sin 2\omega t + 4d(\Gamma_{xy})\cos 2\omega t$$

FIG. II-9 BELL AEROSPACE HEAVY PROOF MASS ACCELEROMETER GRADIOMETER

gradient in the X-Y plane according to the equation

$$[(a_1 + a_2) - (a_3 + a_4)] = -2d[\Gamma_{xx} - \Gamma_{yy}] \sin(2\omega t) + 4d[\Gamma_{xy}]\cos(2\omega t) \quad (2.36)$$

Modulation of the output signal yields an in-phase measurement of the off-diagonal gravity gradient tensor component, Γ_{xy}, and a quadrature measurement of the difference between two of the diagonal terms $\Gamma_{xx} - \Gamma_{yy}$.

G. GRADIENT TENSOR DETERMINATION

Determination of all independent components of the gravity gradient tensor $\bar{\bar{\Gamma}}$ requires at least three Hughes, Bell, or Draper Labs spherical gradiometers. Five of the Draper Lab cylindrical gradiometers are required. The cylindrical gradiometer provides only a single measurement, whereas the rotating instruments provide both inphase and quadrature measurements. Each of the Draper Labs spheres provides two independent gradient measurements. In this section the methods by which both the Hughes and Draper Labs instruments measure the gradient tensor are discussed. Since the Hughes and the Bell instruments provide the same type of output signal, the number of Bell sensors required and their orientations can be inferred from the Hughes sensor. Hence, the Bell sensor is not considered separately.

G.1 Measuring the Gravity Gradient With the Hughes RGG Orthogonal Instrument Triad

A system for gradient measurement using three Hughes RGG is shown in Fig. II-10. The nominally identical sensors are rigidly mounted to an inertially stabilized platform such that the spin axis of one sensor points along each of the platform principal directions. With θ_i representing the sensor spin orientation, the output signal equations for the three sensors are

$$\vec{\Delta T}_3 \quad \hat{z}_3 = 4mr^2\left\{\tfrac{1}{2}(\Gamma_{yy}-\Gamma_{xx})\sin 2\theta_3 + \Gamma_{xy}\cos 2\theta_3\right\} \tag{2.37}$$

$$\vec{\Delta T}_2 \quad \hat{z}_2 = 4mr^2\left\{\tfrac{1}{2}(\Gamma_{zz}-\Gamma_{xx})\sin 2\theta_2 - \Gamma_{xz}\cos 2\theta_2\right\} \tag{2.38}$$

$$\vec{\Delta T}_1 \quad \hat{z}_1 = 4mr^2\left\{\tfrac{1}{2}(\Gamma_{yy}-\Gamma_{zz})\sin 2\theta_1 - \Gamma_{yz}\cos 2\theta_1\right\}. \tag{2.39}$$

Examination of (2.37), (2.38), and (2.39) indicates that the signal quadrature outputs yield direct measurements of the off-diagonal components of the gradient tensor. The inphase signal equation terms yield measurements of differences among the gradient tensor diagonal components as expressed by (2.40) through (2.42).

$$A_3^1 = \frac{1}{2}(\Gamma_{yy} - \Gamma_{xx}) \tag{2.40}$$

$$A_2^1 = \frac{1}{2}(\Gamma_{zz} - \Gamma_{xx}) \tag{2.41}$$

$$A_1^1 \quad \frac{1}{2}(\Gamma_{yy} - \Gamma_{zz}) \tag{2.42}$$

The foregoing equations are not linearly independent, and using only these equations, it is not possible to solve for Γ_{xx}, Γ_{yy}, and Γ_{zz}. However, using Laplace's equation, (2.5), it is possible to determine all three diagonal terms. A simple approach to the determination of the three

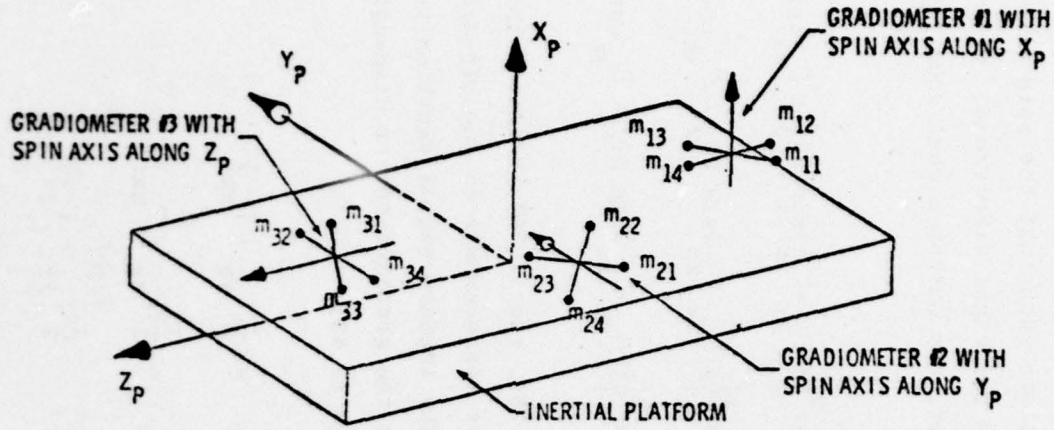


FIG. II-10 BASELINE HUGHES' GRADIOMETER GRADIENT MEASURING SYSTEM

terms from four equations is least squares estimation [LI-1]. The least squares estimate for the diagonal terms Γ_{jj} has the form

$$\vec{\Gamma} = (F^T F)^{-1} F^T \vec{A}' \tag{2.43}$$

where

$$\vec{\Gamma} \triangleq [\Gamma_{xx}, \ \Gamma_{yy}, \ \Gamma_{zz}]^T , \tag{2.44}$$

$$F \triangleq (\tfrac{1}{2}) \begin{bmatrix} -1 & 1 & 0 \\ -1 & 0 & 1 \\ 0 & -1 & 1 \\ 1 & 1 & 1 \end{bmatrix} \tag{2.45}$$

$$A' \triangleq [A'_3, \ A'_2, \ A'_1]^T \tag{2.46}$$

$$A'_j \triangleq \{\vec{\Delta T}_j \cdot \hat{z}_j\} \frac{1}{4mr^2} + v_j \tag{2.47}$$

where v_j is random measurement noise. Since

$$(F^T F) = \frac{3}{4}[I_{3\times 3}] \tag{2.48}$$

where $I_{3\times 3}$ is the identity matrix, $(F^T F)^{-1}$ always exists.

The error in the estimate of Γ, $\tilde{\Gamma}$, may be written as

$$\tilde{\Gamma} = (F^T F)^{-1} F^T \vec{v} \tag{2.49}$$

where

$$\vec{v} \triangleq [v_1, \ v_2, \ v_3, \ 0] \tag{2.50}$$

For an unbiased estimate,

$$\mathcal{E}[v_j] = 0 , \tag{2.51}$$

and an expected variance of the measurement noise

$$\mathcal{E}[v_j^2] = r_j , \tag{2.52}$$

$$\mathcal{E}[v_i v_j] = 0, \qquad i \neq j, \tag{2.53}$$

$$\mathcal{E}[\tilde{\tilde{\Gamma}}\tilde{\tilde{\Gamma}}^T] = (F^TF)^{-1}F^TRF(F^TF)^{-T} , \tag{2.54}$$

where

$$R = \begin{bmatrix} r_1 & & \bigcirc & \\ & r_2 & & \\ \bigcirc & & r_3 & \\ & & & 0 \end{bmatrix}_{4\times 4} \tag{2.55}$$

For similar measurement systems, the statistical properties of the measurements can reasonably be expected to have the same value, yielding

$$R = r\begin{bmatrix} 1 & & \bigcirc & \\ & 1 & & \\ \bigcirc & & 1 & \\ & & & 0 \end{bmatrix} = rJ_{4\times 4} \tag{2.56}$$

Substitution of (2.48) and (2.56) into (2.54) yields

$$\mathcal{E}[\tilde{\Gamma}\tilde{\Gamma}^T] = \frac{4r}{9} F^TJF , \tag{2.57}$$

or

$$\mathcal{E}[\tilde{\Gamma}\tilde{\Gamma}^T] = \frac{4r}{9}\begin{bmatrix} 2 & -1 & -1 \\ -1 & 2 & -1 \\ -1 & -1 & 2 \end{bmatrix} \tag{2.58}$$

Equation (2.58) represents the covariance of the error in the estimate of the gradient tensor diagonal terms which results from estimation based upon a signle set of valid measurement. The standard deviation, $1\sigma_{\tilde{\Gamma}_{jj}}$, of the error in any estimate Γ_{jj} is

$$1\sigma_{\tilde{\Gamma}_{jj}} = \frac{2\sqrt{2}}{3}\sqrt{r} \quad . \tag{2.59}$$

For signal measurements which have 1 EU rms error, i.e.,

$$r = 1(\mathrm{EU})^2 \ , \tag{2.60}$$

$$1\sigma_{\tilde{\Gamma}_{jj}} = 0.889 \text{ EU} \tag{2.61}$$

or

$$1\sigma_{\tilde{\Gamma}_{jj}} = 0.943 \text{ EU} \tag{2.62}$$

For quadrature measurement errors having the same statistical properties as given by (2.51), (2.52), (2.53), and (2.60), the error in the estimate of an off-diagonal term of the gradient tensor is 1 EU.

G.2 Measuring the Gravity Gradient with the Hughes RGG Non-Orthogonal Instrument Triad

Consider now the three-instrument, orthogonal RGG system shown in Fig. II-10. Associated with each instrument , define a platform fixed reference system which is referred to as the measurement reference system. These reference systems are shown in Fig. II-11.

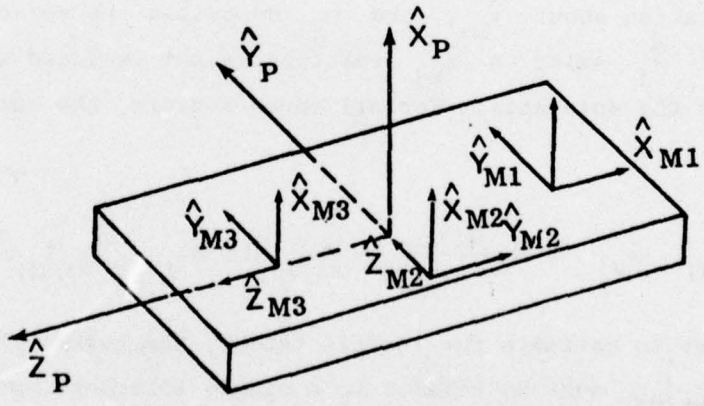


FIG. II-11 MEASUREMENT REFERENCE SYSTEM ORIENTATIONS FOR THREE ORTHOGONAL RGG (Rotating Gravity Gradiometers).

The measurement reference system associated with RGG No. 3, M3, is identical to the platform reference system. Measurement reference system M1 is related to M3, and the platform, by a +90 degree rotation is about $\hat{y}_{M3}$. Hence, the spin vector of sensor No. 1 points along $\hat{x}_p$, and

$$T_{M1/M3} = \begin{bmatrix} 0 & 0 & -1 \\ 0 & 1 & 0 \\ 1 & 0 & 0 \end{bmatrix} . \qquad (2.63)$$

Similarly,

$$T_{m2/M3} = \begin{bmatrix} 1 & 0 & 0 \\ 0 & 0 & -1 \\ 0 & 1 & 0 \end{bmatrix} . \qquad (2.64)$$

The spin axis of sensor No. 2 points in the $\hat{y}_p$ direction. Suppose now that the spin axes of two of these sensors (No. 1, S1; and No. 2, S2) are skewed with respect to the orthogonal alignment. It is desired to determine the effect of non-orthogonal spin axis orientation upon overall gravity gradient measurement accuracy. Let both sensors (S2 and S1) be rotated through a [2, 1] Euler rotation sequence where α_j describes the rotation about $\hat{y}_{Mj}$, and β_j describes the rotation about the subsequent $\hat{x}_j$ axis. A $\hat{z}_{Mj}$ rotation is not included since for al sensors $\hat{z}_{Mj}$ is the spin axis. For all three sensors, the output torque equation is

$$\vec{\Delta T}_{Mj} \cdot \hat{z}_{Mj} = 4mr^2\left\{\frac{1}{2}[\Gamma_{yy}-\Gamma_{xx}]_{Mj}\sin 2\theta_j + [\Gamma_{xy}]_{Mj}\cos 2\theta_j\right\} . \qquad (6.65)$$

In order to estimate the inertia tensor, the terms $[\Gamma_{xx}]_{Mj}$, $[\Gamma_{yy}]_{Mj}$, and $[\Gamma_{xy}]_{Mj}$ must be related to a single reference system. The platform, or M3 reference system is used in this analysis. It is easy to show that for two reference systems A and B,

$$\Gamma_B = T^T_{A/B}\, \Gamma_A T_{A/B} \tag{2.66}$$

Therefore, by expressing the gravity gradient tensor for arbitrary rotations α_j and β_j in terms of the gradient tensor in the platform reference system, the output signals of all three sensors can be combined to yield an estimate of the gradient tensor in the platform reference system. The errors in these measurements can then be compared with the measurement errors associated with the orthogonal gradiometer triad. Using (2.63) and (2.64), and the {2, 1} Euler rotation sequence, transformations (2.67) and (2.68) evolve.

$$T_{M2/P} = \begin{bmatrix} \cos\alpha_2 & -\sin\alpha_2 & 0 \\ \sin\beta_2 \sin\alpha_2 & \sin\beta_2 \cos\alpha_2 & -\cos\beta_2 \\ \cos\beta_2 \sin\alpha_2 & \cos\beta_2 \cos\alpha_2 & \sin\beta_2 \end{bmatrix} \tag{2.67}$$

$$T_{m1/P} = \begin{bmatrix} -\sin\alpha_1 & 0 & -\cos\alpha_1 \\ \sin\beta_1 \cos\alpha_1 & \cos\beta_1 & -\sin\beta_1 \sin\alpha_1 \\ \cos\beta_1 \cos\alpha_1 & -\sin\beta_1 & -\cos\beta_1 \sin\alpha_1 \end{bmatrix} \tag{2.68}$$

For α_2 and β_2—both equal to zero, equation (2.66) yields

$$[\Gamma]_{M2} = \begin{bmatrix} \Gamma_{xx} & -\Gamma_{xz} & \Gamma_{xy} \\ -\Gamma_{xz} & \Gamma_{zz} & -\Gamma_{yz} \\ \Gamma_{xy} & -\Gamma_{yz} & \Gamma_{yy} \end{bmatrix}_P \tag{2.69}$$

Substitution of the components of the gradient tensor of (2.69) into (2.65) yields

$$\vec{\Delta T}_{m2} \cdot \hat{z}_{M2} = 4mr^2\left\{\frac{1}{2}[\Gamma_{zz}-\Gamma_{xx}]_P \sin 2\theta_2 - [\Gamma_{xz}]_P \cos 2\theta_2\right\} \tag{2.70}$$

which agrees with (2.38). A similar test for sensor No. 1 is found to agree with (2.39). General expressions for symmetric matrices $[\Gamma]_{M2}$ and $[\Gamma]_{M1}$ are given in terms of $[\Gamma]_P$ in (2.71) through (2.82)

$$(\Gamma_{11})_{M2} = \Gamma_{xx}\cos^2\alpha_2 - 2\Gamma_{xy}\sin\alpha_2\cos\alpha_2 + \Gamma_{yy}\sin^2\alpha_2; \quad (2.71)$$

$$(\Gamma_{12})_{M2} = (\Gamma_{xx}-\Gamma_{yy})\sin\alpha_2\cos\alpha_2\sin\beta_2 + \Gamma_{xy}\sin\beta_2(\cos^2\alpha_2 - \sin^2\alpha_2) - \Gamma_{xz}\cos\alpha_2\cos\beta_2 + \Gamma_{yz}\sin\alpha_2\cos\beta_2; \quad (2.72)$$

$$(\Gamma_{13})_{M2} = (\Gamma_{xx}-\Gamma_{yy})\sin\alpha_2\cos\alpha_2\cos\beta_2 + \Gamma_{xy}\cos\beta_2(\cos^2\alpha_2 - \sin^2\alpha_2) + \Gamma_{xz}\cos\alpha_2\sin\alpha_2 - \Gamma_{yz}\sin\alpha_2\sin\beta_2; \quad (2.73)$$

$$(\Gamma_{22})_{M2} = \Gamma_{xx}\sin^2\alpha_2\sin^2\beta_2 + \Gamma_{yy}\cos^2\alpha_2\sin^2\beta_2 + \Gamma_{zz}\cos^2\beta_2 + 2\Gamma_{xy}\sin\alpha_2\cos\alpha_2\sin^2\beta_2 - 2\Gamma_{xz}\sin\alpha_2\sin\beta_2\cos\beta_2 - 2\Gamma_{yz}\cos\alpha_2\sin\beta_2\cos\beta_2; \quad (2.74)$$

$$(\Gamma_{23})_{M2} = \Gamma_{xx}\sin^2\alpha_2\sin\beta_2\cos\beta_2 + \Gamma_{yy}\cos^2\alpha_2\sin\beta_2\cos\beta_2 - \Gamma_{zz}\sin\beta_2\cos\beta_2 + 2\Gamma_{xy}\sin\alpha_2\cos\alpha_2\sin\alpha_2\cos\beta_2 + \Gamma_{xz}\sin\alpha_2(\sin^2\beta_2-\cos^2\beta_2) + \Gamma_{yz}\cos\alpha_2(\sin^2\beta_2-\cos^2\beta_2); \quad (2.75)$$

$$(\Gamma_{33})_{M2} = \Gamma_{xx}\sin^2\alpha_2\cos^2\beta_2 + \Gamma_{yy}\cos^2\alpha_2\cos^2\beta_2 + \Gamma_{zz}\sin^2\beta_2 + 2\Gamma_{xy}\sin\alpha_2\cos\alpha_2\cos^2\beta_2 + 2\Gamma_{xz}\sin\alpha_2\sin\beta_2\cos\beta_2 + 2\Gamma_{yz}\cos\alpha_2\sin\beta_2\cos\beta_2; \quad (2.76)$$

$$(\Gamma_{11})_{M_1} = \Gamma_{xx}\sin^2\alpha_1 + 2\Gamma_{xz}\sin\alpha_1\cos\alpha_1 + \Gamma_{zz}\cos^2\alpha_3; \quad (2.77)$$

$$(\Gamma_{12})_{M1} = (\Gamma_{zz}-\Gamma_{xx})\sin\alpha_1\cos\alpha_1\sin\beta_1 - \Gamma_{xy}\sin\alpha_1\cos\beta_1 + \Gamma_{xz}\sin\beta_1(\sin^2\alpha_1-\cos^2\alpha_1) - \Gamma_{yz}\cos\alpha_1\cos\beta_1; \quad (2.78)$$

$$(\Gamma_{13})_{M1} = (\Gamma_{zz}-\Gamma_{xx})\sin\alpha_1\cos\alpha_1\cos\beta_1 + \Gamma_{xy}\sin\alpha_1\sin\beta_1 + \Gamma_{xz}\cos\beta_1(\sin^2\alpha_1-\cos^2\alpha_1) + \Gamma_{yz}\cos\alpha_1\sin\beta_1; \quad (2.79)$$

$$(\Gamma_{22})_{M1} = \Gamma_{xx}\cos^2\alpha_1\sin^2\beta_1 + \Gamma_{yy}\cos^2\beta_1 + \Gamma_{zz}\sin^2\alpha_1\sin^2\beta_1 + \quad (2.80)$$
$$+2\Gamma_{xy}\cos\alpha_1\sin\beta_1\cos\beta_1 - 2\Gamma_{xz}\sin\alpha_1\cos\alpha_1\sin^2\beta_1 -$$
$$-2\Gamma_{yz}\sin\alpha_1\sin\beta_1\cos\beta_1;$$

$$(\Gamma_{23})_{M1} = \Gamma_{xx}\cos^2\alpha_1\sin\beta_1\cos\beta_1 - \Gamma_{yy}\sin\beta_1\cos\beta_1 + \quad (2.81)$$
$$+ \Gamma_{zz}\sin^2\alpha_1\sin\beta_1\cos\beta_1 + \Gamma_{xy}\cos\alpha_1(\cos^2\beta_1-\sin^2\beta_1) -$$
$$-2\Gamma_{xz}\sin\alpha_1\cos\alpha_1\sin\beta_1\cos\beta_1+\Gamma_{yz}\sin\alpha_1(\sin^2\beta_1-\cos^2\beta_1);$$

$$(\Gamma_{33})_{M1} = \Gamma_{xx}\cos^2\alpha_1\cos^2\beta_1 + \Gamma_{yy}\sin^2\beta_1 + \Gamma_{zz}\sin^2\alpha_1\cos^2\beta_1 - \quad (2.82)$$
$$-2\Gamma_{xy}\cos\alpha_1\sin\beta_1\cos\beta_1 - 2\Gamma_{xz}\sin\alpha_1\cos\alpha_1\cos^2\beta_1 +$$
$$+2\Gamma_{yz}\sin\alpha_1\sin\beta_1\cos\beta_1 .$$

All terms Γ_{ij} on the right sides of (2.71) through (2.82) are components of $[\Gamma]_p$. Using these equations, the inphase A_{IPj} and quadrature A_{Qj} outputs of the sensors may be written as (2.85) through (2.90). These equations are based upon (2.65) with

$$A_{IPj} \triangleq \frac{1}{4mr^2\sin 2\theta_j}\{\vec{\Delta T}_{Mj} \cdot \hat{z}_{Mj}\}_{j=1,2} + v_{ij} \quad (2.83)$$

$$A_{Qj} \triangleq \frac{1}{4mr^2\cos 2\theta_i}\{\vec{\Delta T}_{Mj} \cdot \hat{z}_{mj}\}_{j=1,2} + v_{2j} . \quad (2.84)$$

$$A_{IP3} = \frac{1}{2}[\Gamma_{yy} - \Gamma_{xx}] + v_{13} \quad (2.85)$$

$$A_{Q3} = \Gamma_{xy} + v_{23} \quad (2.86)$$

$$A_{IP2} = \Gamma_{xx}[\sin^2\beta_2\sin^2\alpha_2-\cos^2\alpha_2] + \Gamma_{yy}[\cos^2\alpha_2\sin^2\beta_2-\sin^2\alpha_2] + \Gamma_{zz}[\cos^2\beta_2] + \Gamma_{xy}[2\sin\alpha_2\cos\alpha_2(\sin^2\beta_2-1)] + \Gamma_{xz}[-2\sin\alpha_2\sin\beta_2\cos\beta_2] + \Gamma_{yz}[-2\cos\alpha_2\sin\beta_2\cos\beta_2] + v_{12} \quad (2.87)$$

$$A_{Q2} = \Gamma_{xx}[\sin\alpha_2\cos\alpha_2\sin\beta_2] + \Gamma_{yy}[-\sin\alpha_2\cos\alpha_2\sin\beta_2] + \Gamma_{xy}[\sin\beta_2(\cos^2\alpha_2-\sin^2\alpha_2)] + \Gamma_{xz}[-\cos\alpha_2\cos\beta_2] + \Gamma_{yz}[\sin\alpha_2\cos\beta_2] + v_{22} \quad (2.88)$$

$$A_{IP1} = \Gamma_{xx}[\cos^2\alpha_1\sin^2\beta_1-\sin^2\alpha_1] + \Gamma_{yy}[\cos^2\beta_1] + \Gamma_{zz}[\sin^2\alpha_1\sin^2\beta_1-\cos^2\alpha_1] + \Gamma_{xy}[2\cos\alpha_1\sin\beta_1\cos\beta_1] + \Gamma_{xz}[-2\sin\alpha_1\cos\alpha_1(\sin^2\beta_1+1)] + \Gamma_{yz}[-2\sin\alpha_1\sin\beta_1\cos\beta_1] + v_{11} \quad (2.89)$$

$$A_{Q1} = \Gamma_{xx}[-\sin\alpha_1\cos\alpha_1\sin\beta_1] + \Gamma_{zz}[\sin\alpha_1\cos\alpha_1\sin\beta_1] + \Gamma_{xy}[-\sin\alpha_1\sin\beta_1] + \Gamma_{xz}[\sin\beta_1(\sin^2\alpha_1-\cos^2\alpha_1)] + \Gamma_{yz}[-\cos\alpha_1\cos\beta_1] + v_{12} \quad . \quad (2.90)$$

Neglecting the noise terms v_{ij}, (2.85) through (2.90) can be written in matrix form as shown in (2.91).

$$
\begin{bmatrix} A_{IP3} \\ A_{Q3} \\ A_{IP2} \\ A_{Q2} \\ A_{IP1} \\ A_{Q1} \end{bmatrix} =
\left[\begin{array}{c|c|c}
-\frac{1}{2} & \frac{1}{2} & 0 \\
0 & 0 & 0 \\
\frac{1}{2}\begin{Bmatrix}\sin^2\beta_2\sin^2\alpha_2 \\ -\cos^2\alpha_2\end{Bmatrix} & \frac{1}{2}\begin{Bmatrix}\sin^2\beta_2\cos^2\alpha_2 \\ -\sin^2\alpha_2\end{Bmatrix} & \frac{1}{2}\cos^2\beta_2 \\
\sin\alpha_2\cos\alpha_2\sin\beta_2 & -\sin\alpha_2\cos\alpha_2\sin\beta_2 & 0 \\
\frac{1}{2}\begin{Bmatrix}\cos^2\alpha_1\sin^2\beta_1 \\ -\sin^2\alpha_1\end{Bmatrix} & \frac{1}{2}\cos^2\beta_1 & \frac{1}{2}\begin{Bmatrix}\sin^2\beta_1\sin^2\alpha_1 \\ -\cos^2\alpha_1\end{Bmatrix} \\
-\sin\alpha_1\cos\alpha_1\sin\beta_1 & 0 & \sin\alpha_1\cos\alpha_1\sin\beta_1
\end{array}\right. \qquad (2.91)
$$

$$
\left.\begin{array}{c|c|c}
0 & 0 & 0 \\
1 & 0 & 0 \\
-\sin\alpha_2\cos\alpha_2\cos^2\beta_2 & -\sin\alpha_2\sin\beta_2\cos\beta_2 & -\cos\alpha_2\sin\beta_2\cos\beta_2 \\
\sin\beta_2[\cos^2\alpha_2-\sin^2\alpha_2] & -\cos\alpha_2\cos\beta_2 & \sin\alpha_2\cos\beta_2 \\
\cos\alpha_1\sin\beta_1\cos\beta_1 & -\sin\alpha_1\cos\alpha_1[1+\sin^2\beta_1] & -\sin\alpha_1\sin\beta_1\cos\beta_1 \\
-\sin\alpha_1\sin\beta_1 & -\sin\beta_1[\sin^2\alpha_1-\cos^2\alpha_1] & -\cos\alpha_1\cos\beta_1
\end{array}\right]
$$

$$
\times \begin{bmatrix} \Gamma_{xx} \\ \Gamma_{yy} \\ \Gamma_{zz} \\ \Gamma_{xy} \\ \Gamma_{xz} \\ \Gamma_{yz} \end{bmatrix}
$$

In Sect. E.1, a system of three Hughes RGG was considered in which the spin axes of the instruments formed an orthogonal triad. It was shown that for such a system, direct inversion of the six available measurements was not possible due to the dependence of the inphase measurements. Equation (2.91) shows that this dependence of measurements holds for the general skewed gradiometer orientation considered in this section. With (2.91) rewritten as

$$[A]_{6\times1} = [L]_{6\times6}\,[\Gamma]_{6\times1}\,, \tag{2.92}$$

the first three columns of L can be used to show that $[L]^{-1}$ does not exist. With

$$L_j \triangleq j^{th} \text{ column of } L, \tag{2.93}$$

$$L_1 + L_2 + L_3 = [0]_{6\times1}\,. \tag{2.94}$$

Hence matrix L has rank less than 6 and cannot be inverted.

As for the case of orthogonal spin axes, all of the diagonal and off diagonal terms of $\bar{\bar{\Gamma}}$ are estimable upon inclusion of Laplace's equation added, (2.92) may be written

$$\begin{bmatrix} A_{IP3} \\ A_{Q3} \\ A_{IP2} \\ A_{q2} \\ A_{IP1} \\ A_{Q1} \\ 0 \end{bmatrix} = \left[\begin{array}{cccccc} & & & & & \\ & & L_{6\times6} & & & \\ & & & & & \\ \hline 1 & 1 & 1 & 0 & 0 & 0 \end{array}\right] \begin{bmatrix} \Gamma_{xx} \\ \Gamma_{yy} \\ \Gamma_{zz} \\ \Gamma_{xy} \\ \Gamma_{yz} \\ \\ \end{bmatrix}$$

Using (2.95) and standard equations for over-determined system parameter estimation (these equations are discussed in Ch. VII and by Likeness [LI-1]), the effect of sensor-to-sensor orientation upon gravity gradient tensor determination accuracy was investigated. The results of this study are shown graphically in Figs. II-12 through II-20. The orientation angles α_2, β_2, α_1, β_1 were incremented as specified in the figures. For each resulting set of sensor orientations the covariance matrix Σ of the errors in the estimates of the six† independent gradient tensor components was formed, and a cost function J defined as the sum of the diagonal terms Σ_{jj}, i.e.,

$$J = \Sigma_{jj} \qquad j = 1, 2, \ldots, 6 \tag{2.96}$$

was calculated.

All sensor measurements were assumed to contain 1 EU white Gaussian noise. Examination of Fig. II-12 through II-20 shows that as sensor spin axes become less orthogonal, the overall accuracy of the measurement of the gradient tensor generally decreases, as shown by the increase in J. The best measurement accuracy is reported in Fig. II-12 for the orthogonal sensor system, for which the cost function was found to be 5.667 EU^2. The covariance matrix, Σ, for the orthogonal system is given in (2.97)

$$\Sigma = \left[\begin{array}{ccc|c} 0.889 & -0.444 & -0.444 & \\ -0.444 & 0.889 & -0.444 & 0_{3\times3} \\ -0.444 & -0.444 & 0.889 & \\ \hline & 0_{3\times3} & & I_{3\times3} \end{array}\right] \tag{2.97}$$

† With Laplace's equation included as an equivalent measurement, the number of independent terms of the gradient tensor increases from 5 as specified in Sect. II-A to II-F.

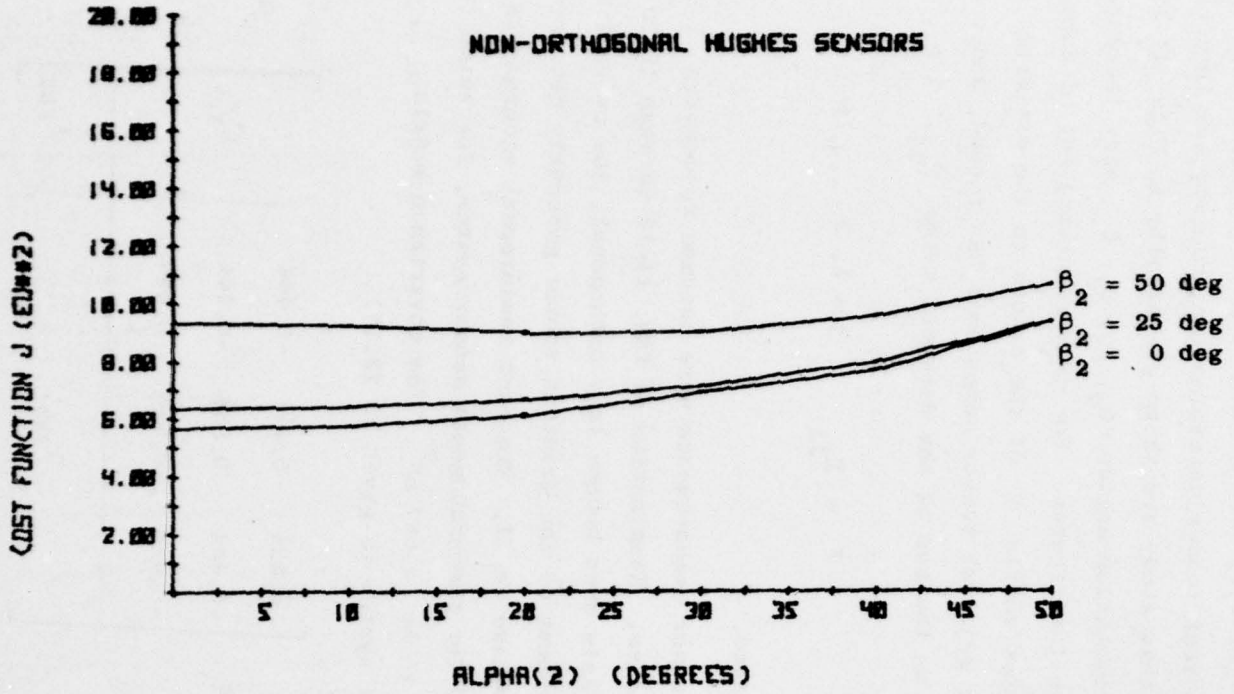


FIG. II-12 GRADIENT TENSOR ESTIMATE ERROR COST FUNCTION VS SENSOR $2\hat{y}$ AXIS ROTATION FROM NOMINAL. α_1 = zero deg. β_1 = zero deg.

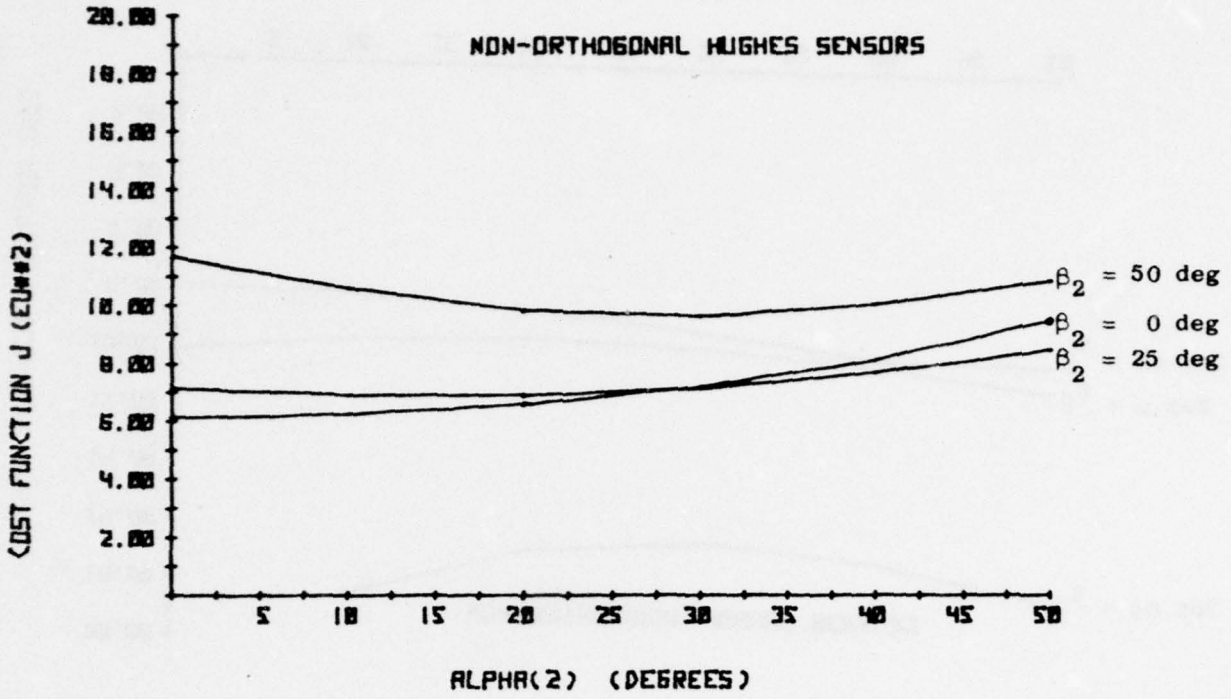


FIG. II-13 GRADIENT TENSOR ESTIMATE ERROR COST FUNCTION VS SENSOR $2\hat{y}$ AXIS ROTATION FROM NOMINAL. α_1 = 25 deg. β_1 = zero deg.

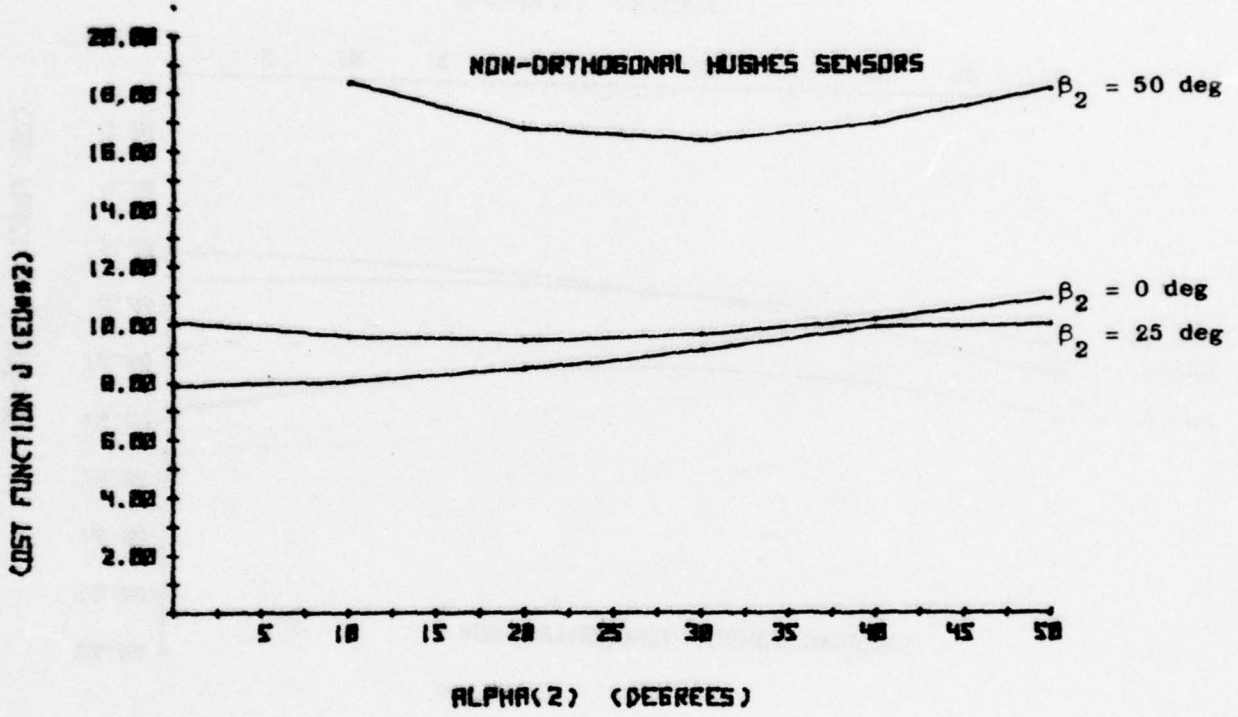


FIG. II-14 GRADIENT TENSOR ESTIMATE ERROR COST FUNCTION VS SENSOR $2\hat{y}$ AXIS ROTATION FROM NOMINAL. α_1 = 50 deg. β_1 = zero deg.

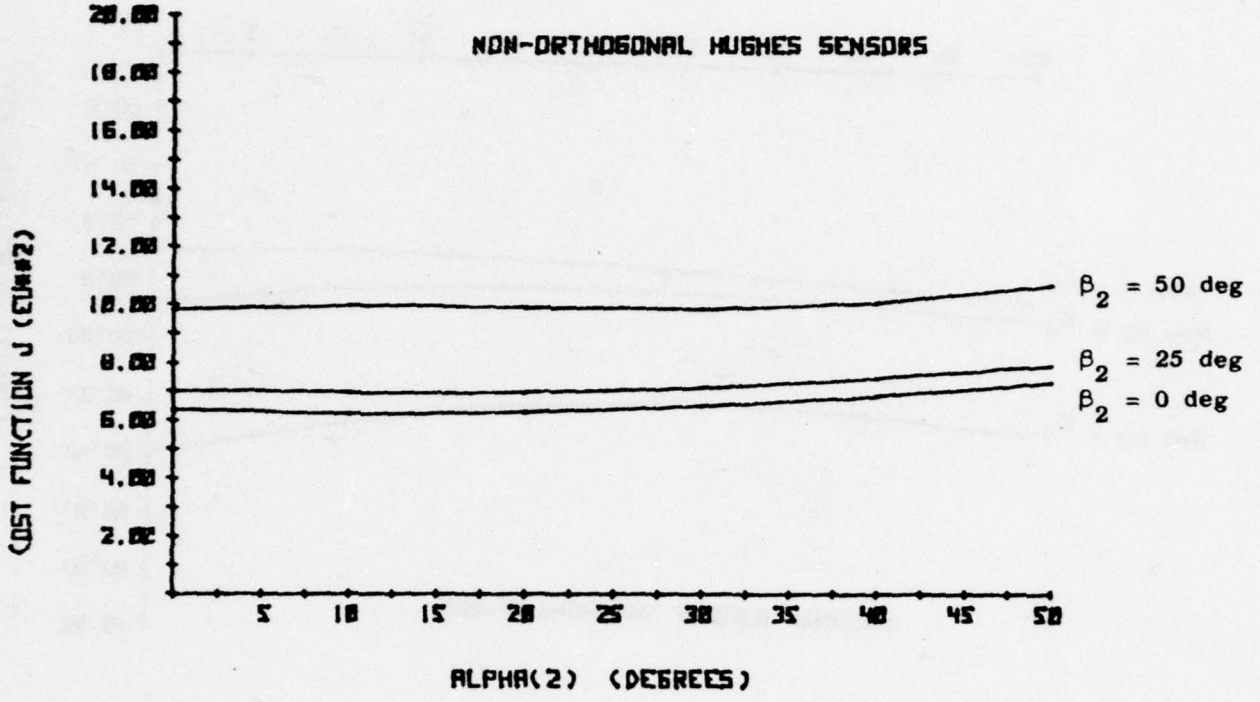


FIG. II-15 GRADIENT TENSOR ESTIMATE ERROR COST FUNCTION VS SENSOR $2\hat{y}$ AXIS ROTATION FROM NOMINAL. α_1 = 0 deg. β_1 = 25 deg.

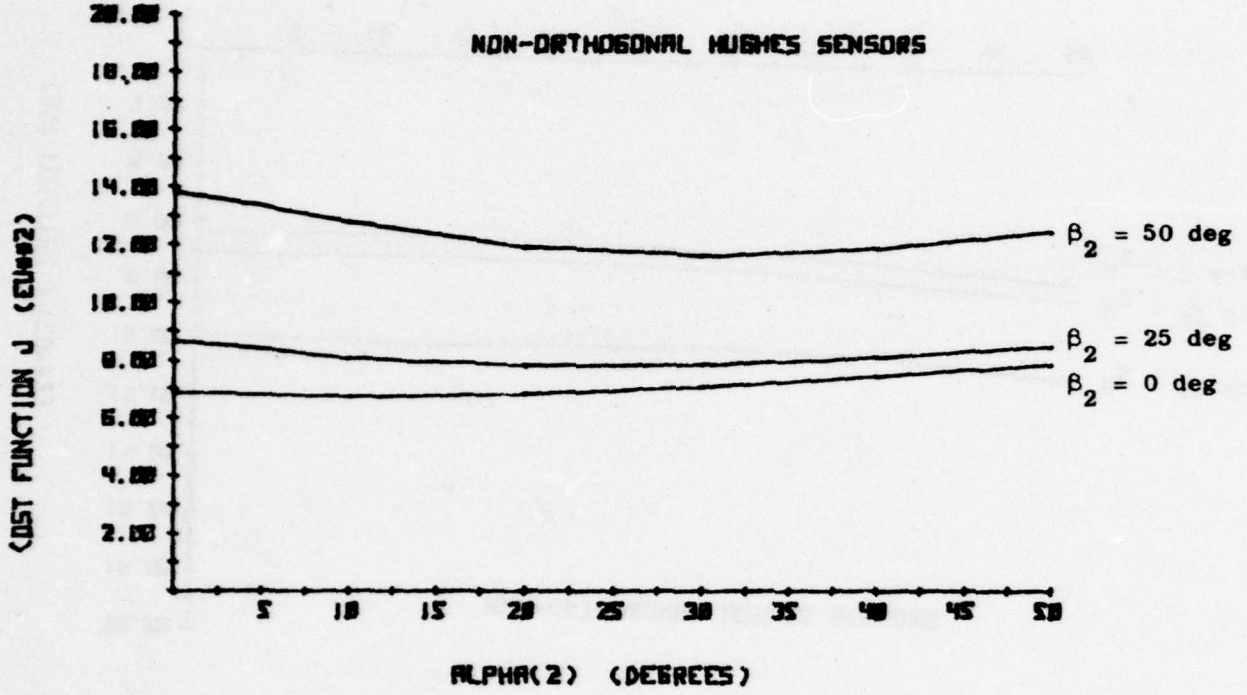


FIG. II-16 GRADIENT TENSOR ESTIMATE ERROR COST FUNCTION VS SENSOR $2\hat{y}$ AXIS ROTATION FROM NOMINAL. α_1 = 25 deg. β_1 = 25 deg.

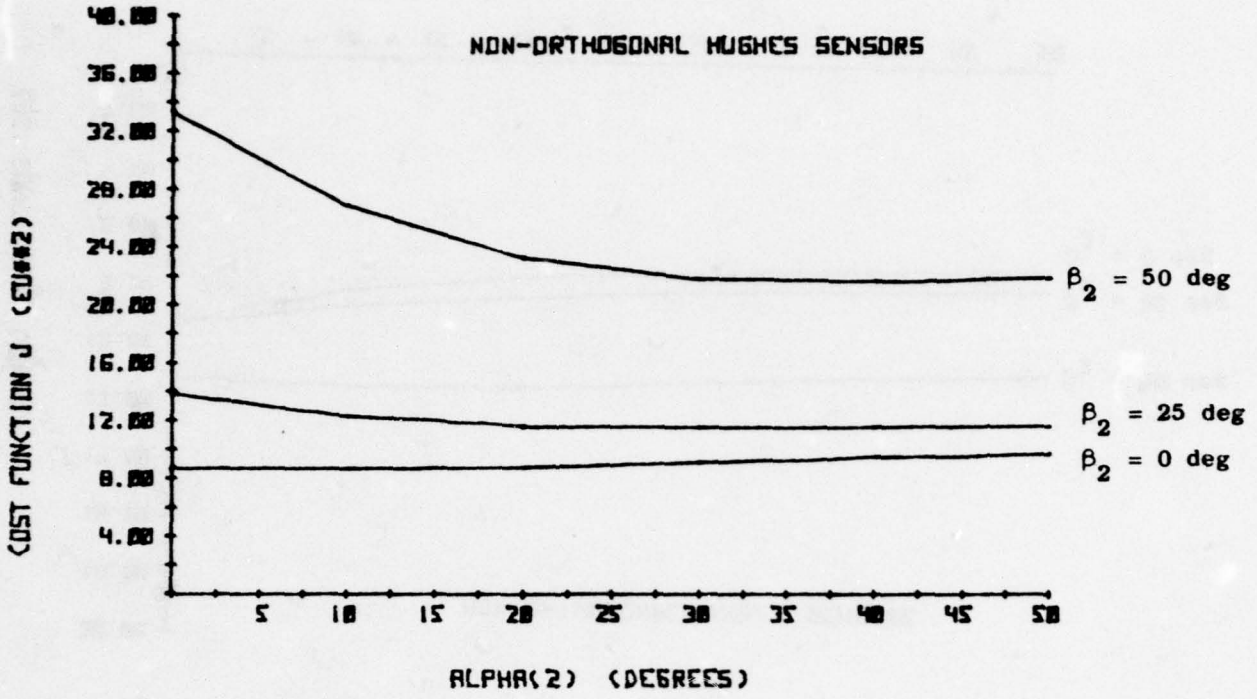


FIG. II-17 GRADIENT TENSOR ESTIMATE ERROR COST FUNCTION VS SENSOR 2ϑ AXIS ROTATION FROM NOMINAL. α_1 = 50 deg. β_1 = 25 deg.

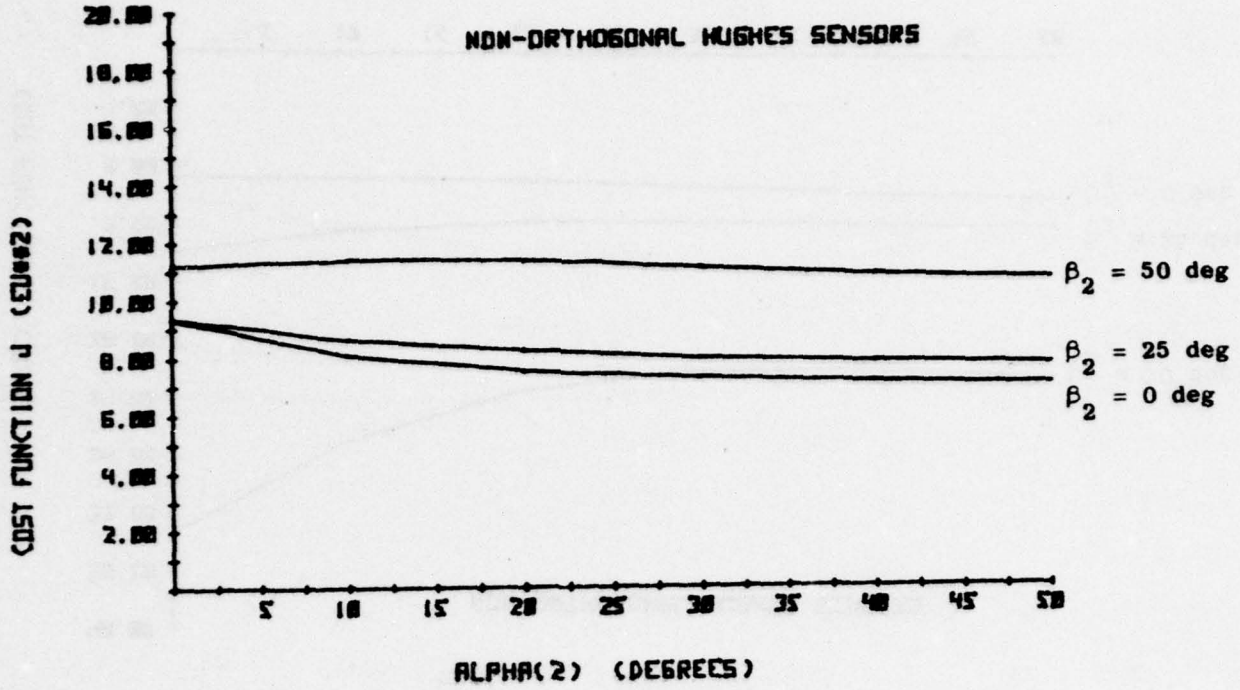


FIG. II-18 GRADIENT TENSOR ESTIMATE ERROR COST FUNCTION VS SENSOR $2\hat{y}$ AXIS ROTATION FROM NOMINAL. α_1 = zero deg. β_1 = 50 deg.

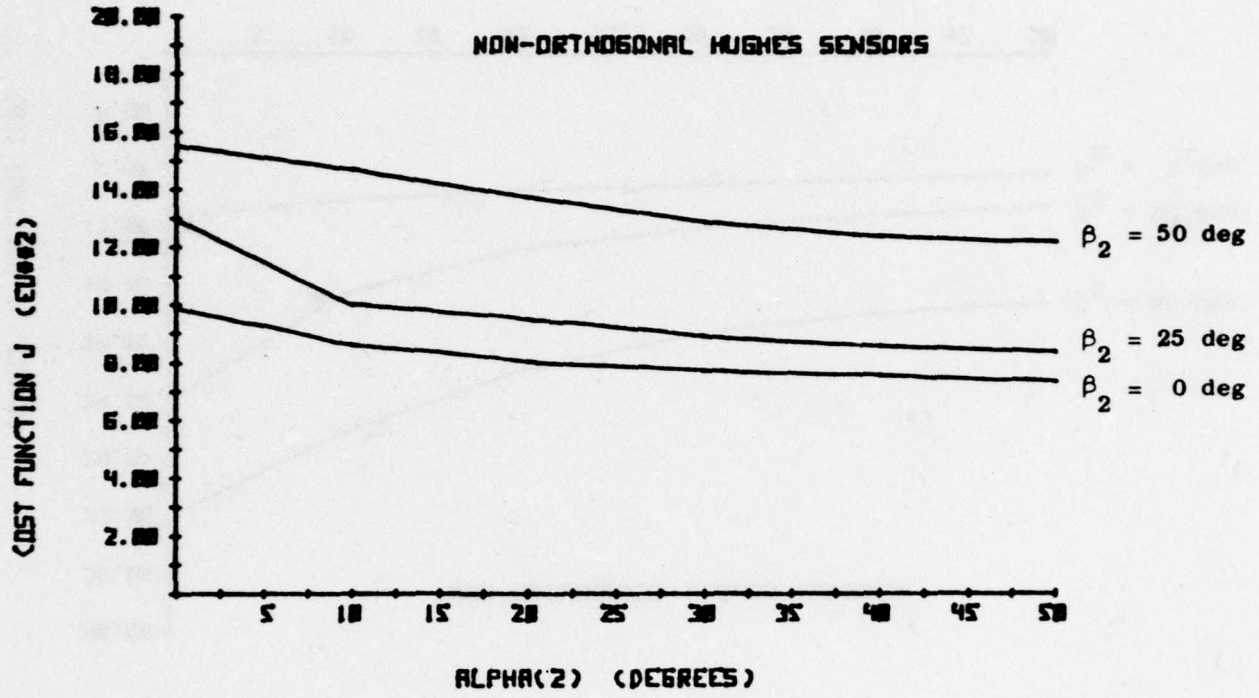


FIG. II-19 GRADIENT TENSOR ESTIMATE ERROR COST FUNCTION VS SENSOR $2\hat{y}$ AXIS ROTATION FROM NOMINAL. α_1 = 25 DEG. β_1 = 50 deg.

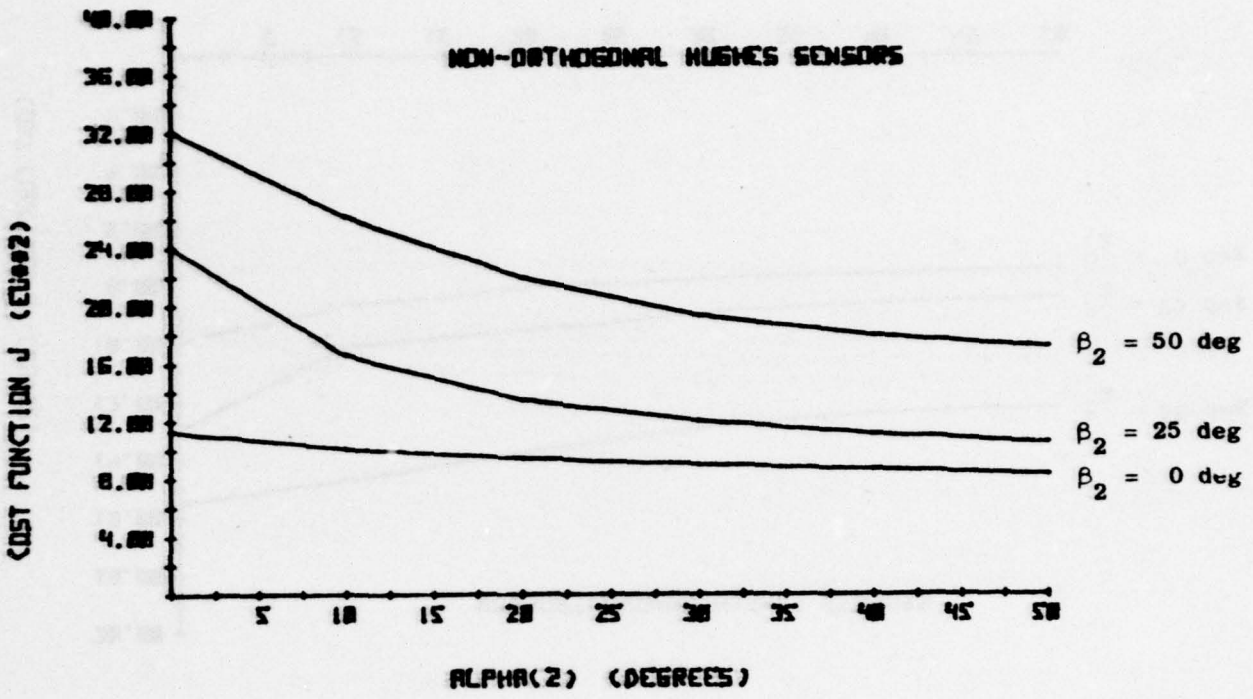


FIG. II-20 GRADIENT TENSOR ESTIMATE ERROR COST FUNCTION VS SENSOR $2\hat{y}$ AXIS ROTATION FROM NOMINAL. α_1 = 50 deg. β_1 = 50 deg.

G.8 Measuring the Gravity Gradient With the Draper Labs Cylindrical Gravity Gradiometer

A simplified representation of the Draper Labs cylindrical gravity gradiometer was shown in Fig. II-7. With the proof masses of that figure replaced by point masses each having mass m, Fig. II-7 is redrawn as Fig. II-21. The masses of the figure are situated such that, in the reference system shown,

$$\vec{r}_1 = [r_1, \quad 0, \quad 0]^T \tag{2.98}$$

and

$$\vec{r}_2 = [r_2, \quad 0, \quad 0]^T . \tag{2.99}$$

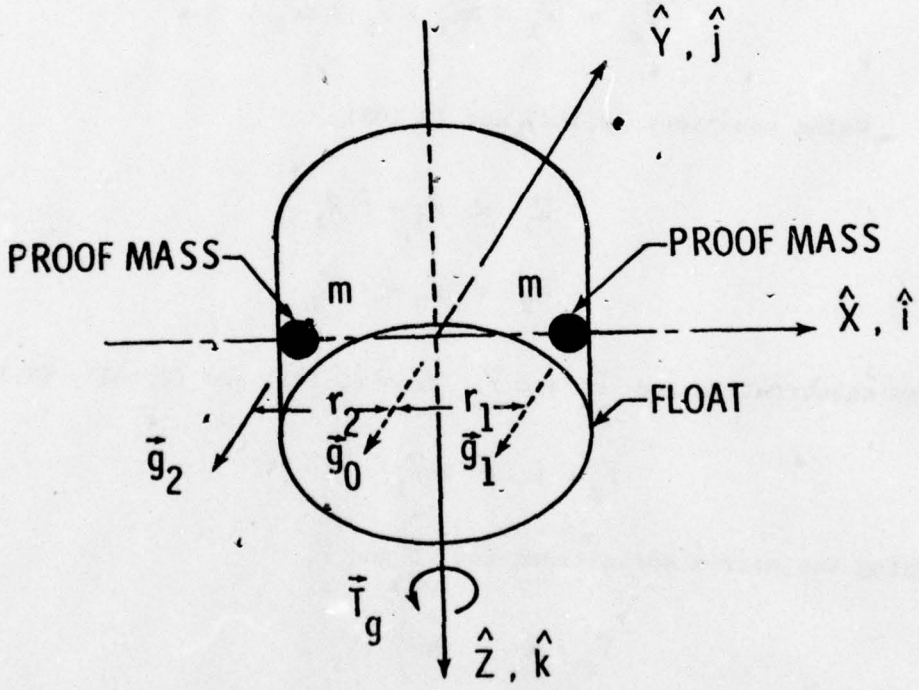


FIG. II-21 DRAPER LABS CYLINDRICAL GRADIOMETER WITH PROOF MASSES REPRESENTED AS POINT MASSES.

Under nominal conditions,

$$|\vec{r}_1| = |\vec{r}_2| \tag{2.100}$$

and the mass position radii of (2.98) and (2.99) may be rewritten as

$$\vec{r}_1 = r[1, \quad 0, \quad 0]^T, \tag{2.101}$$

$$\vec{r}_2 = r[-1, \quad 0, \quad 0]^T . \tag{2.102}$$

The cylindrical gradiometer is a single axis output instrument. The sensitive axis lies along z in the figure. The torque about the z axis for a stationary, ideal instrument may be written as

$$\vec{T}_g = \vec{r}_1 \times m\vec{g}_1 + \vec{r}_2 \times m\vec{g}_2 . \tag{2.103}$$

Using equations (2.104) and (2.105),

$$\vec{g}_1 = \vec{g}_0 + \bar{\bar{\Gamma}}\,\vec{r}_1 \tag{2.104}$$

$$\vec{g}_2 = \vec{g}_0 + \bar{\bar{\Gamma}}\,\vec{r}_2 \tag{2.105}$$

and substituting for $\vec{r}_1$ and $\vec{r}_2$ from (2.101) and (2.102), (2.103) becomes

$$\vec{T}_g \cdot \hat{k} = 2m\vec{r}_1 \times \bar{\bar{\Gamma}}\,\vec{r}_1 . \tag{2.106}$$

Using the matrix definitions for $\bar{\bar{\Gamma}}$ and $\vec{r}$,

$$\vec{T}_g \cdot \hat{k} = 2mr^2\,\Gamma_{xy} . \tag{2.107}$$

Hence, using the measured value of the output torque $(\vec{T}_g)_M$, Γ_{xy} can be estimated as

$$\hat{\Gamma}_{xy} = \frac{1}{2mr^2}[\vec{T}_g]_m . \tag{2.108}$$

By orienting the instrument sensitive axis along $\hat{x}$ and $\hat{y}$, the terms Γ_{yz} and Γ_{xz} can similarly be measured.

Suppose now that the gradiometer is oriented as shown in Fig. II-21 but that

$$\vec{r}_1 = r\left[\frac{\sqrt{2}}{2}, \quad \frac{\sqrt{2}}{2}, \quad 0\right]^T \tag{2.109}$$

and

$$\vec{r}_2 = -r\left[\frac{\sqrt{2}}{2}, \quad \frac{\sqrt{2}}{2}, \quad 0\right]^T \quad . \tag{2.110}$$

For these values of $\vec{r}_1$ and $\vec{r}_2$, (2.103) is still valid, and

$$[\vec{T}_g \cdot \hat{k}] = \left\{ 2mr \frac{\sqrt{2}}{2} \begin{bmatrix} 1 \\ 1 \\ 0 \end{bmatrix} \times [\bar{\Gamma}] \begin{bmatrix} 1 \\ 1 \\ 0 \end{bmatrix} \frac{\sqrt{2}}{2} \right\} \cdot \hat{k} \tag{2.111}$$

or

$$[\vec{T}_g \cdot \hat{k}] = mr^2[\Gamma_{yy} - \Gamma_{xx}] \quad . \tag{2.112}$$

By orienting the skewed mass cylindrical gradiometer such that the sensitive axis lies along $\hat{x}$ it is possible to measure $[\Gamma_{yy} - \Gamma_{zz}]$. If the sensitive axis lies along $\hat{y}$, one can measure $[\Gamma_{xx} - \Gamma_{zz}]$. As was the case with the Hughes instrument, when the Laplace equation is used, the separate diagonal components of the gradient tensor can be calculated. Hence, a minimum of five cylindrical gradiometers is required for complete gravity gradient determination. It is also noted that, as was the case with the Hughes RGG, the off-diagonal gradient tensor components are accompanied by a factor of 2 which is not present in the measurements of the diagonal term differences. Using 2 skewed mass cylindrical gradiometers, one having its sensitive axis along the $\hat{z}$ direction and one along the $\hat{x}$ direction, and using the Laplace equation as in Sect. G.1, the diagonal components of the gradient tensor may be estimated from equation (2.113)

$$\begin{bmatrix} \Gamma_{xx} \\ \Gamma_{yy} \\ \Gamma_{zz} \end{bmatrix} = \frac{1}{3} \begin{bmatrix} 2 & 1 & 1 \\ -1 & 1 & 1 \\ -1 & -2 & 1 \end{bmatrix} \begin{bmatrix} \vec{T}_{g1} \cdot \hat{z} \\ \vec{T}_{g2} \cdot \hat{x} \\ 0 \end{bmatrix} \frac{1}{mr^2} \tag{2.113}$$

$\vec{T}_{g1} \cdot \hat{z} \triangleq$ Torque measured by the gradiometer having its sensitive axis along $\hat{z}$ and its between the weights axis skewed with respect to the x and y axes. (2.114)

$\vec{T}_{g2} \cdot \hat{x} \triangleq$ Torque measured by the gradiometer having its sensitive axis along $\hat{x}$ and weights along the $\hat{y}$ and $\hat{z}$ bisector. (2.115)

The covariance matrix for the error in the estimate of the gradient diagonal terms is given by (2.116).

$$P = \frac{5r}{9} \begin{bmatrix} 5 & -1 & -4 \\ -1 & 2 & -1 \\ -4 & -1 & 5 \end{bmatrix} \tag{2.116}$$

Equation (2.116) can be compared directly with the similar equation, (2.58), which was developed for the Hughes instrument, bearing in mind the latter is for three measurements. If the value of r is taken to be $1\ EU^2$ as it was for the RGG covariance calculation, numerical values can be applied to the resulting gradient tensor component estimate errors for comparison. These values are listed in Table II-2.

By changing the two diagonal-term-sensitive axis directions of the Draper Labs sensors, different components can be selected to be minimum error components. If a third skewed mass sensor is added, the errors reduce exactly to the levels specified for the Hughes sensor.

Table II-2

COMPARISON OF THREE HUGHES AND TWO DRAPER LABS DIAGONAL GRADIENT COMPONENT ESTIMATE ERROR FOR THE TWO SKEWED MASS SENSOR CASE. GRADIENT ESTIMATION USING MINIMUM NUMBER OF SENSORS.

Component	Hughes Sensor Estimate rms Error (EU)	Draper Labs Sensor rms Error (EU)
Γ_{xx}	0.943	1.667
Γ_{yy}	0.943	1.054
Γ_{zz}	0.943	1.667

G.4 Measuring the Gravity Gradient With the Draper Labs Spherical Gravity Gradiometer

Consider the simplified drawing of the ideal spherical gradiometer shown in Fig. II-22. In this figure the distributed proof masses are again assumed to be point masses for purposes of simplicity. Output axes are assumed to be $\hat{i}$ and $\hat{k}$ in conformance with Trageser's notation [TR-2].

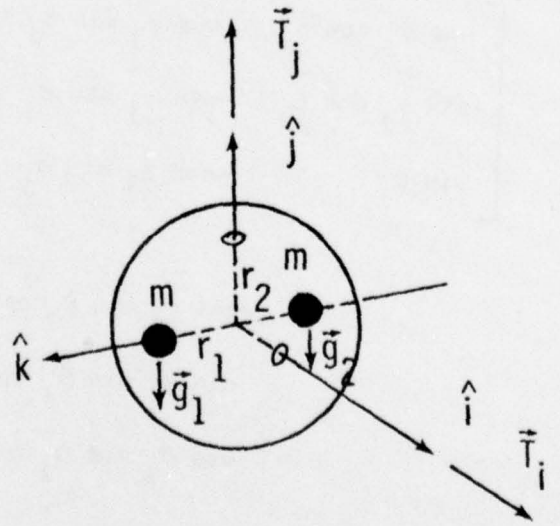


FIG. II-22 SIMPLIFIED REPRESENTATION OF DRAPER LABS SPHERICAL GRAVITY GRADIOMETER; OUTPUT AXES $\hat{i}$ and $\hat{j}$.

Vector equation (2.103) applied for spherical sensor output as it did for the output of the cylindrical instrument. For

$$\vec{r}_1 \triangleq r[0, \quad 0, \quad 1]^T \tag{2.117}$$

and

$$\vec{r}_2 = -\vec{r}_1 , \tag{2.118}$$

the output torque $\vec{T}_g$ is

$$[\vec{T}_g] = 2mr^2\{-\Gamma_{yz}, \quad \Gamma_{xz}, \quad 0\}^T . \tag{2.119}$$

The reference system $\{\hat{i}, \hat{j}, \hat{k}\}$ is referred to as the body reference system (subscript B).

Consider now the system of three spherical gravity gradiometers shown in Fig. II-23.

Using a $\{\hat{1}, \hat{2}, \hat{3}\}$ Euler rotation sequence, it is possible to specify the transformation to any of the body reference system, B_j, from the platform system P, given the values of the sequential rotations α, β, γ about the proper $\hat{1}$, $\hat{2}$, and $\hat{3}$ axes respectively.

$$T_{B_j/P} = \begin{bmatrix} \cos\gamma_j \cos\beta_j & \cos\gamma_j \sin\beta_j \sin\alpha_j + \sin\gamma_j \cos\alpha_j & -\cos\gamma_j \sin\beta_j \cos\alpha_j + \sin\gamma_j \sin\alpha_j \\ -\sin\gamma_j \cos\beta_j & -\sin\gamma_j \sin\beta_j \sin\alpha_j + \cos\gamma_j \cos\alpha_j & \sin\gamma_j \sin\beta_j \cos\alpha_j + \cos\gamma_j \sin\alpha_j \\ \sin\beta_j & -\cos\beta_j \sin\alpha_j & \cos\beta_j \cos\alpha_j \end{bmatrix} \tag{2.120}$$

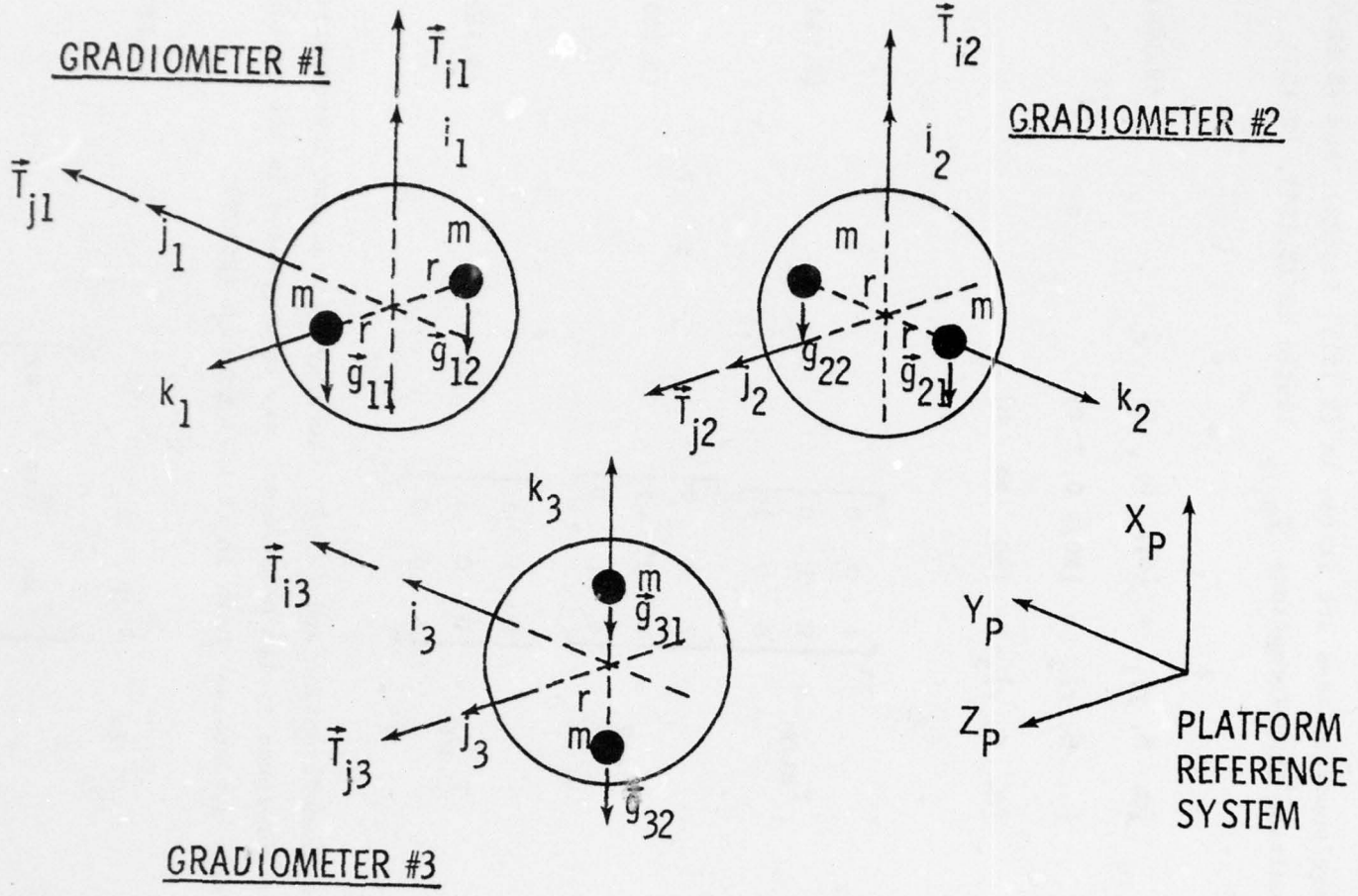


FIG. II-23 THREE SPHERICAL GRAVITY GRADIOMETERS

Figure II-17 represents special cases of the general rotation sequence. These special cases are listed in (2.121), (2.122), and (2.123), with the resulting transformations $T_{B_j/P}$ listed in (2.124), (2.125), and (2.126):

$$\{\alpha, \beta, \gamma\}_1 = \{0, 0, 0\} \tag{2.121}$$

$$\{\alpha, \beta, \gamma\}_2 = \{90, 0, 0\}$$

$$\{\alpha, \beta, \gamma\}_3 = \{90, 90, 0\}$$

$$T_{B1/P} = \begin{bmatrix} 1 & 0 & 0 \\ 0 & 1 & 0 \\ 0 & 0 & 1 \end{bmatrix} \tag{2.124}$$

$$T_{B2/P} = \begin{bmatrix} 1 & 0 & 0 \\ 0 & 0 & -1 \\ 0 & 1 & 0 \end{bmatrix} \tag{2.125}$$

$$T_{B3/P} = \begin{bmatrix} 0 & 1 & 0 \\ 0 & 0 & 1 \\ 1 & 0 & 0 \end{bmatrix} \tag{2.126}$$

Given these transformation and (2.67), the gravity gradient tensor written in platform reference system components, may be expressed in the various body reference systems as shown in (2.127) through (2.129).

$$[\bar{\bar{\Gamma}}]_{B1} = [\bar{\bar{\Gamma}}]_P \tag{2.127}$$

$$[\bar{\bar{\Gamma}}]_{B2} = \begin{bmatrix} \Gamma_{xx} & -\Gamma_{xz} & \Gamma_{xy} \\ -\Gamma_{xz} & \Gamma_{zz} & -\Gamma_{yz} \\ \Gamma_{xy} & -\Gamma_{yz} & \Gamma_{yy} \end{bmatrix} \tag{2.128}$$

$$[\bar{\bar{\Gamma}}]_{B3} = \begin{bmatrix} \Gamma_{yy} & \Gamma_{yz} & \Gamma_{xy} \\ \Gamma_{yz} & \Gamma_{zz} & \Gamma_{xz} \\ \Gamma_{xy} & \Gamma_{xz} & \Gamma_{xx} \end{bmatrix} \tag{2.129}$$

Using measurement equation (2.119), the six gradient measurements are specified by matrix equation

$$\begin{bmatrix} T_{1\hat{i}} \\ T_{1\hat{j}} \\ T_{2\hat{i}} \\ T_{2\hat{j}} \\ T_{3\hat{i}} \\ T_{3j} \end{bmatrix} = \begin{bmatrix} 0 & 0 & 0 & 0 & 0 & -1 \\ 0 & 0 & 0 & 0 & 1 & 0 \\ 0 & 0 & 0 & 0 & 0 & 1 \\ 0 & 0 & 0 & 1 & 0 & 0 \\ 0 & 0 & 0 & 0 & -1 & 0 \\ 0 & 0 & 0 & 0 & 0 & 0 \end{bmatrix} \begin{bmatrix} \Gamma_{xx} \\ \Gamma_{yy} \\ \Gamma_{zz} \\ \Gamma_{xy} \\ \Gamma_{xz} \\ \Gamma_{yz} \end{bmatrix} \tag{2.130}$$

None of the gradient diagonal terms is present in the six available measurements shown in (2.131). It is concluded from this example that it is necessary for the between-the-weight axes to be non-orthogonal in order to provide a complete measurement of the gradient tensor. For arbitrary rotations α, β, and γ of sensor j, gradient tensor components

$$\begin{aligned} [\Gamma_{xz}]_{Bj} = {} & [\cos\gamma\cos\beta\sin\beta]_j \Gamma_{xx} \\ & +[\cos\gamma\sin\alpha(\sin^2\beta-\cos^2\beta) + \sin\gamma\sin\beta\cos\alpha]_j\Gamma_{xy} \\ & +[-\cos\gamma\cos\alpha(\sin^2\beta-\cos^2\beta) + \sin\gamma\sin\beta\sin\alpha]_j\Gamma_{xz} \\ & +[-\cos\gamma\sin\beta\cos\beta\sin^2\alpha - \sin\gamma\cos\beta\sin\alpha\cos\alpha]_j\Gamma_{yy} \\ & +[2\cos\gamma\sin\beta\cos\beta\sin\alpha\cos\alpha+\sin\gamma\cos\beta(\cos^2\alpha-\sin^2\alpha)]_j\Gamma_{yz} \\ & +[\sin\gamma\cos\beta\sin\alpha\cos\alpha - \cos\gamma\sin\beta\cos\beta\cos^2\alpha]_j\Gamma_{zz}; \end{aligned} \tag{2.131}$$

$$
\begin{aligned}
[\Gamma_{yz}]_{Bj} = {} & [-\sin\gamma\cos\beta\sin\beta]_j\,\Gamma_{xx} \\
& +[-\sin\gamma\sin\alpha(\sin^2\beta-\cos^2\beta)+\cos\gamma\sin\beta\cos\alpha]_j\,\Gamma_{xy} \\
& +[\sin\gamma\cos\alpha(\sin^2\beta-\cos^2\beta)+\cos\gamma\sin\beta\sin\alpha]_j\,\Gamma_{xz} \\
& +[-\cos\gamma\cos\beta\sin\alpha\cos\alpha+\sin\gamma\sin\beta\cos\beta\sin^2\alpha]_j\,\Gamma_{yy} \\
& +[\cos\gamma\cos\beta(\cos^2\alpha-\sin^2\alpha)-2\sin\gamma\sin\beta\cos\beta\sin\alpha\cos\alpha]_j\Gamma_{yz} \\
& +[\sin\gamma\cos\beta\sin\beta\cos^2\alpha+\cos\gamma\cos\beta\sin\alpha\cos\alpha]_j\,\Gamma_{zz}\ .
\end{aligned}
\tag{2.132}
$$

Using (2.131) and (2.132) the matrix output equation for three arbitrarily oriented spherical gravity gradiometers is written in (2.133). Coefficient matrix M is specified by (2.134).

$$
\begin{bmatrix} T_{1\hat{i}} \\ T_{1\hat{j}} \\ T_{2\hat{i}} \\ T_{2\hat{j}} \\ T_{3\hat{i}} \\ T_{3\hat{j}} \end{bmatrix} = 2mr^2\ [M] \begin{bmatrix} \Gamma_{xx} \\ \Gamma_{yy} \\ \Gamma_{xy} \\ \Gamma_{xy} \\ \Gamma_{yz} \\ \Gamma_{yz} \end{bmatrix} \tag{2.133}
$$

Examination of the coefficient matrix M shows that the six measurements cannot be inverted directly to yield an estimate of $\bar{\bar{\Gamma}}$.

$$
M = \begin{bmatrix}
\sin\gamma_1 \cos\beta_1 \sin\beta_1 & \cos\gamma_1\cos\beta_1\sin\alpha_1\cos\alpha_1 & -\sin\gamma_1\cos\beta_1\sin\beta_1\cos^2\alpha_1 \\
 & -\sin\gamma_1\sin\beta_1\cos\beta_1\sin^2\alpha_1 & -\cos\gamma_1\cos\beta_1\sin\alpha_1\cos\alpha_1 \\
\cos\gamma_1 \cos\beta_1 \sin\beta_1 & -\cos\gamma_1\sin\beta_1\cos\beta_1\sin^2\alpha_1 & \sin\gamma_1\cos\beta_1\sin\alpha_1\cos\alpha_1 \\
 & -\sin\gamma_1\cos\beta_1\sin\alpha_1\cos\alpha_1 & -\cos\gamma_1\sin\beta_1\cos\beta_1\cos^2\alpha_1 \\
\sin\gamma_2 \cos\beta_2 \sin\beta_2 & \cos\gamma_2\cos\beta_2\sin\alpha_2\cos\alpha_2 & -\sin\gamma_2\cos\beta_2\sin\beta_2\cos^2\alpha_2 \\
 & -\sin\gamma_2\sin\beta_2\cos\beta_2\sin^2\alpha_2 & -\cos\gamma_2\cos\beta_2\sin\alpha_2\cos a_2 \\
\cos\gamma_2 \cos\beta_2 \sin\beta_2 & -\cos\gamma_2\sin\beta_2\cos\beta_2\sin^2\alpha_2 & \sin\gamma_2\cos\beta_2\sin\alpha_2\cos\alpha_2 \\
 & -\sin\gamma_2\cos\beta_2\sin\alpha_2\cos\alpha_2 & -\cos\gamma_2\sin\beta_2\cos\beta_2\cos^2\alpha_2 \\
\sin\gamma_3 \cos\beta_3 \sin\beta_3 & \cos\gamma_3\cos\beta_3\sin\alpha_3\cos\alpha_3 & -\sin\gamma_3\cos\beta_3\sin\beta_3\cos^2\alpha_3 \\
 & -\sin\gamma_3\sin\beta_3\cos\beta_3\sin^2\alpha_3 & -\cos\gamma_3\cos\beta_3\sin\alpha_3\cos\alpha_3 \\
\cos\gamma_3 \cos\beta_3 \sin\beta_3 & -\cos\gamma_3\sin\beta_3\cos\beta_3\sin^2\alpha_3 & \sin\gamma_3\cos\beta_3\sin\alpha_3\cos\alpha_3 \\
 & -\sin\gamma_3\cos\beta_3\sin\alpha_3\cos\alpha_3 & -\cos\gamma_3\sin\beta_3\cos\beta_3\cos^2\alpha_3
\end{bmatrix} \qquad (2.134)
$$

cont. ...

$$
\begin{bmatrix}
\begin{matrix}\sin\gamma_1\sin\alpha_1(\sin^2\beta_1-\cos^2\beta_1)\\ -\cos\gamma_1\sin\beta_1\cos\alpha_1\end{matrix} & \begin{matrix}-\sin\gamma_1\cos\alpha_1(\sin^2\beta_1-\cos^2\beta_1)\\ -\cos\gamma_1\sin\beta_1\sin\alpha_1\end{matrix} & \begin{matrix}-\cos\gamma_1\cos\beta_1(\cos^2\alpha_1-\sin^2\alpha_1)\\ +2\sin\gamma_1\sin\beta_1\cos\beta_1\sin\alpha_1\cos\alpha_1\end{matrix} \\
\begin{matrix}\cos\gamma_1\sin\alpha_1(\sin^2\beta_1-\cos^2\beta_1)\\ -\sin\gamma_1\sin\beta_1\cos\alpha_1\end{matrix} & \begin{matrix}-\cos\gamma_1\cos\alpha_1(\sin^2\beta_1-\cos^2\beta_1)\\ +\sin\gamma_1\sin\beta_1\sin\alpha_1\end{matrix} & \begin{matrix}2\cos\gamma_1\sin\beta_1\cos\beta_1\sin\alpha_1\cos\alpha_1\\ +\sin\gamma_1\cos\beta_1(\cos^2\alpha_1-\sin^2\alpha_1)\end{matrix} \\
\begin{matrix}\sin\gamma_2\sin\alpha_2(\sin^2\beta_2-\cos^2\beta_2)\\ -\cos\gamma_2\sin\beta_2\cos\alpha_2\end{matrix} & \begin{matrix}-\sin\gamma_2\cos\alpha_2(\sin^2\beta_2-\cos^2\beta_2)\\ -\cos\gamma_2\sin\beta_2\sin\alpha_2\end{matrix} & \begin{matrix}-\cos\gamma_2\cos\beta_2(\cos^2\alpha_2-\sin^2\alpha_2)\\ +2\sin\gamma_2\sin\beta_2\cos\beta_2\sin\alpha_2\cos\alpha_2\end{matrix} \\
\begin{matrix}\cos\gamma_2\sin\alpha_2(\sin^2\beta_2-\cos^2\beta_2)\\ +\sin\gamma_2\sin\beta_2\cos\alpha_2\end{matrix} & \begin{matrix}-\cos\gamma_2\cos\alpha_2(\sin^2\beta_2-\cos^2\beta_2)\\ +\sin\gamma_2\sin\beta_2\sin\alpha_2\end{matrix} & \begin{matrix}2\cos\gamma_2\sin\beta_2\cos\beta_2\sin\alpha_2\cos\alpha_2\\ +\sin\gamma_2\cos\beta_2(\cos^2\alpha_2-\sin^2\alpha_2)\end{matrix} \\
\begin{matrix}\sin\gamma_3\sin\alpha_3(\sin^2\beta_3-\cos^2\beta_3)\\ -\cos\gamma_3\sin\beta_3\cos\alpha_3\end{matrix} & \begin{matrix}-\sin\gamma_3\cos\alpha_3(\sin^2\beta_3-\cos^2\beta_3)\\ -\cos\gamma_3\sin\beta_3\sin\alpha_3\end{matrix} & \begin{matrix}-\cos\gamma_3\cos\beta_3(\cos^2\alpha_3-\sin^2\alpha_3)\\ +2\sin\gamma_3\sin\beta_3\cos\beta_3\sin\alpha_3\cos\alpha_3\end{matrix} \\
\begin{matrix}\cos\gamma_3\sin\alpha_3(\sin^2\beta_3-\cos^2\beta_3)\\ +\sin\gamma_3\sin\beta_3\cos\alpha_3\end{matrix} & \begin{matrix}-\cos\gamma_3\cos\alpha_3(\sin^2\beta_3-\cos^2\beta_3)\\ +\sin\gamma_3\sin\beta_3\sin\alpha_3\end{matrix} & \begin{matrix}2\cos\gamma_3\sin\beta_3\cos\beta_3\sin\alpha_3\cos\alpha_3\\ +\sin\gamma_3\cos\beta_3(\cos^2\alpha_3-\sin^2\alpha_3)\end{matrix}
\end{bmatrix} \qquad (2.134)
$$

$$M_j \triangleq j^{th} \text{ column of matrix, } M, \tag{2.135}$$

$$M_1 + M_2 + M_3 = 0 \tag{2.136}$$

for arbitrary α_j, β_j, and γ_j. Hence, as was found to be the case for the system of three Hughes gradiometers, estimation of the gravity gradient tensor $\bar{\bar{\Gamma}}$ using a system of three Draper Labs spherical gradiometers requires use of Laplace's equation. The six measurements alone do not contain information sufficient for estimation of all six independent gradient tensor terms.

Upon inclusion of Laplace's equation, matrix output equation (2.133) may be written

$$\begin{bmatrix} T_{1\hat{i}} \\ T_{1\hat{j}} \\ T_{2\hat{i}} \\ T_{2\hat{j}} \\ T_{3\hat{i}} \\ T_{3\hat{j}} \\ 0 \end{bmatrix} = 2mr^2 \left[\begin{array}{c} \\ M_{6\times 6} \\ \\ \hline 1\ 1\ 1\ 0\ 0\ 0 \end{array}\right] \begin{bmatrix} \Gamma_{xx} \\ \Gamma_{yy} \\ \Gamma_{zz} \\ \Gamma_{xy} \\ \Gamma_{xz} \\ \Gamma_{yz} \end{bmatrix} \tag{2.137}$$

Equation (2.137) has the same form as (2.96), the Hughes three sensor system matrix output equation. Using the overdetermined least squares estimation equations which were used for the Hughes system, a study to determine the optimal relative sensor orientations was performed. An optimal system was defined as one which minimized the covariance diagonal sum cost function given by (2.96). The covariance cost function was numerically evaluated for different sensor configurations. The results of this analysis are shown in Figs. II-24 through II-31. Figure II-24, II-25, and II-26 display plots of covariance cost function J versus instrument $\hat{y}_B$ rotation angle, β, for the cases where the three

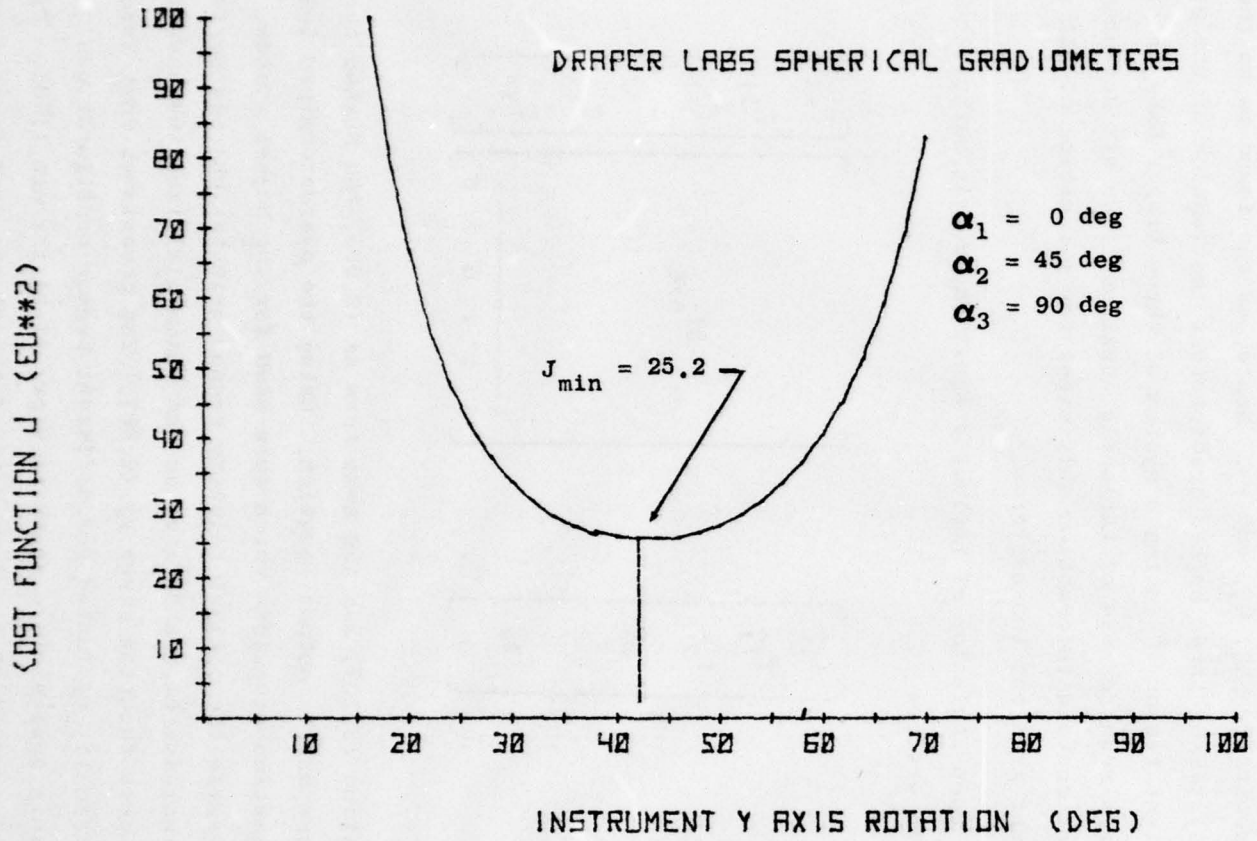


FIG. II-24 GRADIENT TENSOR ESTIMATE ERROR COST FUNCTION VS INSTRUMENT $\hat{y}_B$ ROTATION ANGLE. ALL SENSORS ROTATED THROUGH ANGLE β. α_1 = zero deg. α_2 = 45 deg. α_3 = 90 deg.

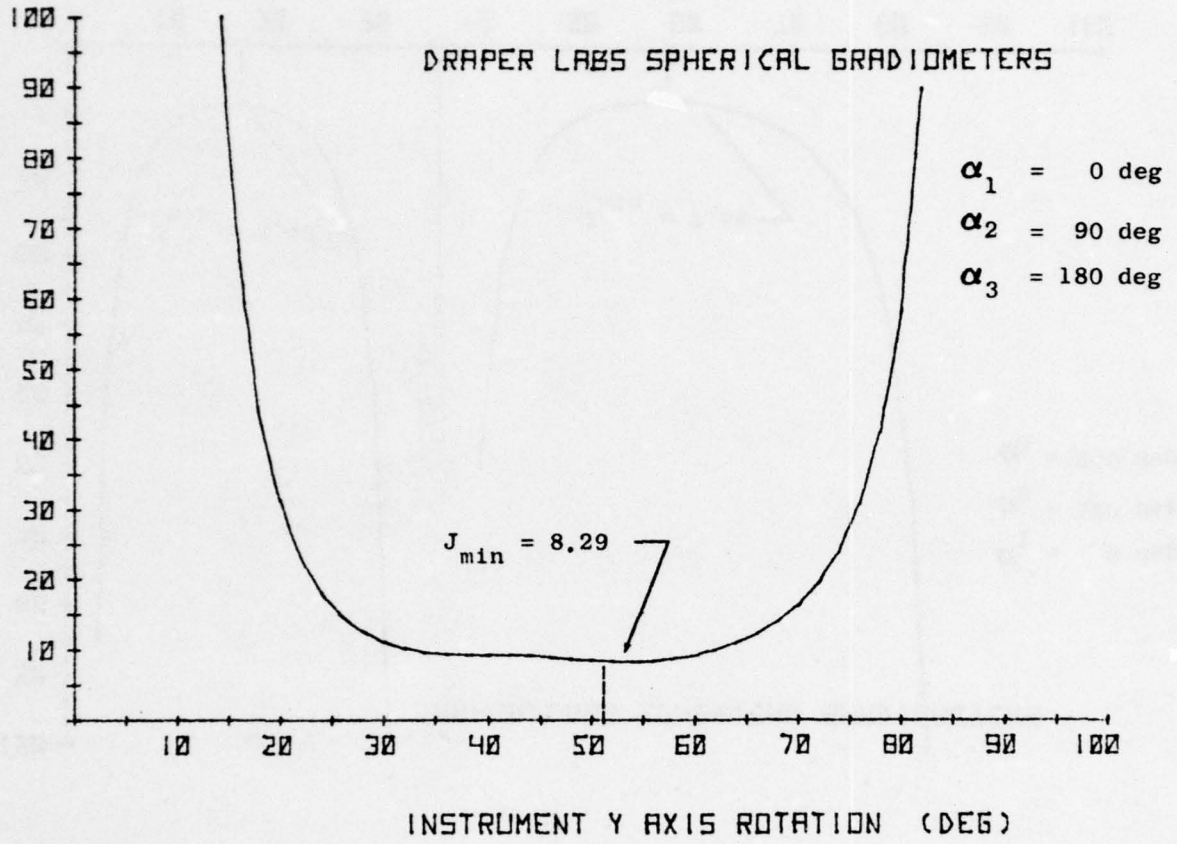


FIG. II-25 GRADIENT TENSOR ESTIMATE ERROR COST FUNCTION VS INSTRUMENT $\hat{y}_B$ ROTATION ANGLE. ALL SENSORS ROTATED THROUGH ANGLE β.
α_1 = zero deg. α_2 = 90 deg. α_3 = 180 deg.

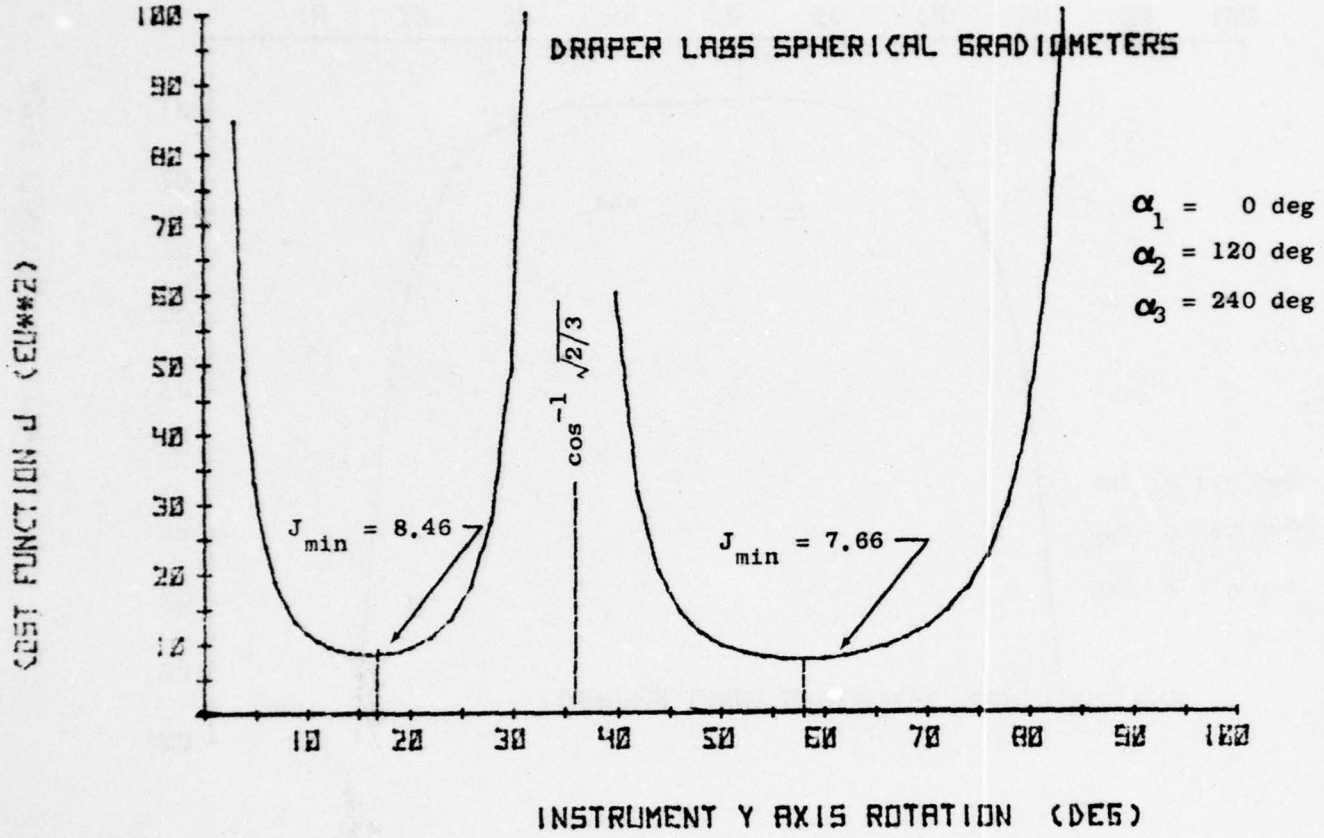


FIG. II-26 GRADIENT TENSOR ESTIMATE ERROR COST FUNCTION VS INSTRUMENT $\hat{y}_B$ ROTATION ANGLE. ALL SENSORS ROTATED THROUGH ANGLE β. α_1 = zero deg. α_2 = 120 deg. α_3 = 240 deg.

instruments have different $\hat{x}_B$ rotations as shown in the figures. A composite of the three curves is given in Fig. II-27 to allow performance comparisons. Examination of the curves indicates that the case of Fig. II-26 yields the minimum value of cost function J (7.66 EU^2).

For this case the α_j were selected to symmetrically locate the between-the-weights axes about the vertical with α_1, α_2, and α_3 having values equal to 0, 120, and 240 degrees respectively. Subsequent tests showed that it was the symmetry of sensor spacing, i.e., the constant 120 deg between the sensors which brought about the minimum cost function. The covariance matrix diagonal terms are a function of sensor spacing rather than sensor α-angle absolute value. As a demonstration of this sensitivity relationship, consider equations (2.137) through (2.140). The first two equations are coefficient matrices M for β_j equal to 16 deg. The values of the α_j are specified in the equations. Although the coefficient matrix for the system of (2.138) shows the effect of the 45 deg phase shift, the covariance matrix diagonal terms are identical for both cases.

$$M_1 = \begin{bmatrix} 0.000 & 0.000 & 0.000 & -0.276 & 0.000 & -0.961 \\ 0.265 & 0.000 & -0.265 & 0.000 & 0.848 & 0.000 \\ 0.000 & -0.416 & 0.416 & 0.138 & -0.239 & 0.481 \\ 0.265 & -0.199 & -0.066 & -0.734 & -0.424 & -0.229 \\ 0.000 & 0.416 & -0.416 & 0.138 & 0.239 & 0.481 \\ 0.265 & -0.199 & -0.066 & 0.734 & -0.424 & 0.229 \\ 1.000 & 1.000 & 1.000 & 0.000 & 0.000 & 0.000 \end{bmatrix} \quad (2.137)$$

α_1=0 deg
α_2=120 deg
α_3=240 deg

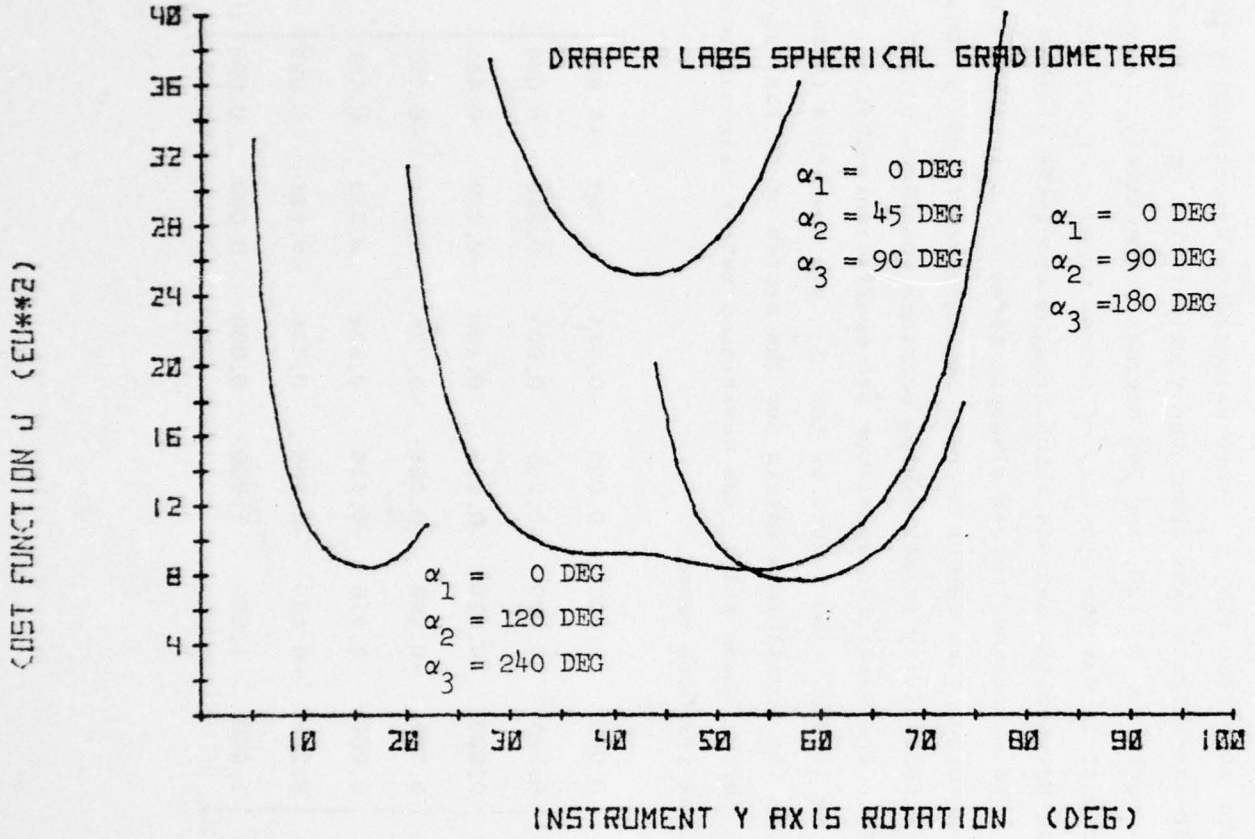


FIG. II-27 GRADIENT TENSOR ESTIMATE ERROR COST FUNCTION VS INSTRUMENT $\hat{y}_B$ ROTATION ANGLE. ALL SENSORS ROTATED THROUGH ANGLE β. SPHERICAL GRADIOMETER SYSTEM PERFORMANCE COMPARISON.

$$M_2 = \begin{bmatrix} 0.000 & 0.481 & -0.481 & -0.195 & -0.195 & 0.000 \\ 0.265 & -0.132 & -0.132 & -0.600 & 0.600 & 0.265 \\ 0.000 & -0.240 & 0.246 & 0.266 & -0.071 & -0.832 \\ 0.265 & -0.018 & -0.247 & -0.219 & -0.819 & -0.132 \\ 0.000 & -0.240 & 0.240 & -0.071 & 0.266 & 0.832 \\ 0.265 & -0.247 & -0.018 & 0.819 & 0.219 & -0.132 \\ 1.000 & 1.000 & 1.000 & 0.000 & 0.000 & 0.000 \end{bmatrix} \quad (2.138)$$

α_1=45 deg
α_2=165 deg
α_3=285 deg

$$\Sigma_1 = \begin{bmatrix} 2.110 & -1.055 & -1.055 & 0.000 & 0.000 & 0.000 \\ & 1.490 & -0.435 & 0.000 & -0.593 & 0.000 \\ & & 1.490 & 0.000 & 0.593 & 0.000 \\ & & & 1.203 & 0.000 & -0.593 \\ & & & & 1.203 & 0.000 \\ & & & & & 0.962 \end{bmatrix} \quad (2.139)$$

α_1=0 deg
α_2=120 deg
α_3=240 deg

$$\Sigma_2 = \begin{bmatrix} 2.110 & -1.055 & -1.055 & 0.000 & 0.000 & 0.000 \\ & 1.490 & -0.435 & 0.419 & 0.419 & 0.000 \\ & & 1.490 & -0.419 & -0.419 & 0.000 \\ & & & 1.203 & 0.000 & 0.419 \\ & & & & 1.203 & -0.419 \\ & & & & & 0.962 \end{bmatrix} \quad (2.140)$$

α_1=45 deg
α_2=165 deg
α_3=285 deg

The sensor orientations which yielded the minimum cost function J are defined in (2.141). This is approximately the cube face orientation

$$\begin{aligned} \{\gamma_1, \beta_1, \alpha_1\} &= \{0, 58, 60\} \\ \{\gamma_2, \beta_2, \alpha_2\} &\quad \{0, 58, 180\} \\ \{\gamma_3, \beta_3, \alpha_3\} &\quad \{0, 58, 300\} \end{aligned} \tag{2.141}$$

discussed by Trageser in [TR-2]. The covariance matrix corresponding to this case is given by (2.142).

$$\Sigma = \begin{bmatrix} 0.734 & -0.367 & -0.367 & 0.000 & 0.000 & 0.000 \\ & 1.798 & -1.431 & 0.000 & -0.447 & 0.000 \\ & & 1.798 & 0.000 & 0.447 & 0.000 \\ & & & 0.855 & 0.000 & -0.447 \\ & & & & 0.855 & 0.000 \\ & & & & & 1.615 \end{bmatrix} \tag{2.142}$$

The cost function curve of Fig. II 26 becomes unbounded for $\hat{y}_B$ axis rotations of $\cos^{-1}\sqrt{2/3}$ or $35 \cdot 2644$ degrees at which value the between-the-weights axes are orthogonal.

The optimum value of β differs by only about 3 degrees from the cube face orientation [TR-2] for which $\beta = 54.7$ deg. In the optimum case the between-the-weights axes are slightly more skewed at 54.7 deg than the 60 deg for the cube face case. As can be seen in Fig. II 26, the practical effect of the difference is negligible.

Figure II-28 shows the effect of $\hat{x}_B$ axis rotation symmetry upon the covariance matrix cost function. For this analysis all β_j were set to 58 deg. Angles α_1 and α_2 were set to zero deg and 120 deg respectively. Angle α_3 was then perturbed from 140 deg to 340 deg in 20 deg increments and the cost function J was plotted. The minimum value of J occurs for

AD-A048 252 STANFORD UNIV CALIF GUIDANCE AND CONTROL LAB F/G 8/5
STUDY TO DEVELOP GRADIOMETER TECHNIQUES.(U)
JUN 77 D B DEBRA, E J PELKA
UNCLASSIFIED F19628-74-C-0162
AFGL-TR-76-0297 NL

2 OF 4
AD
AD48252



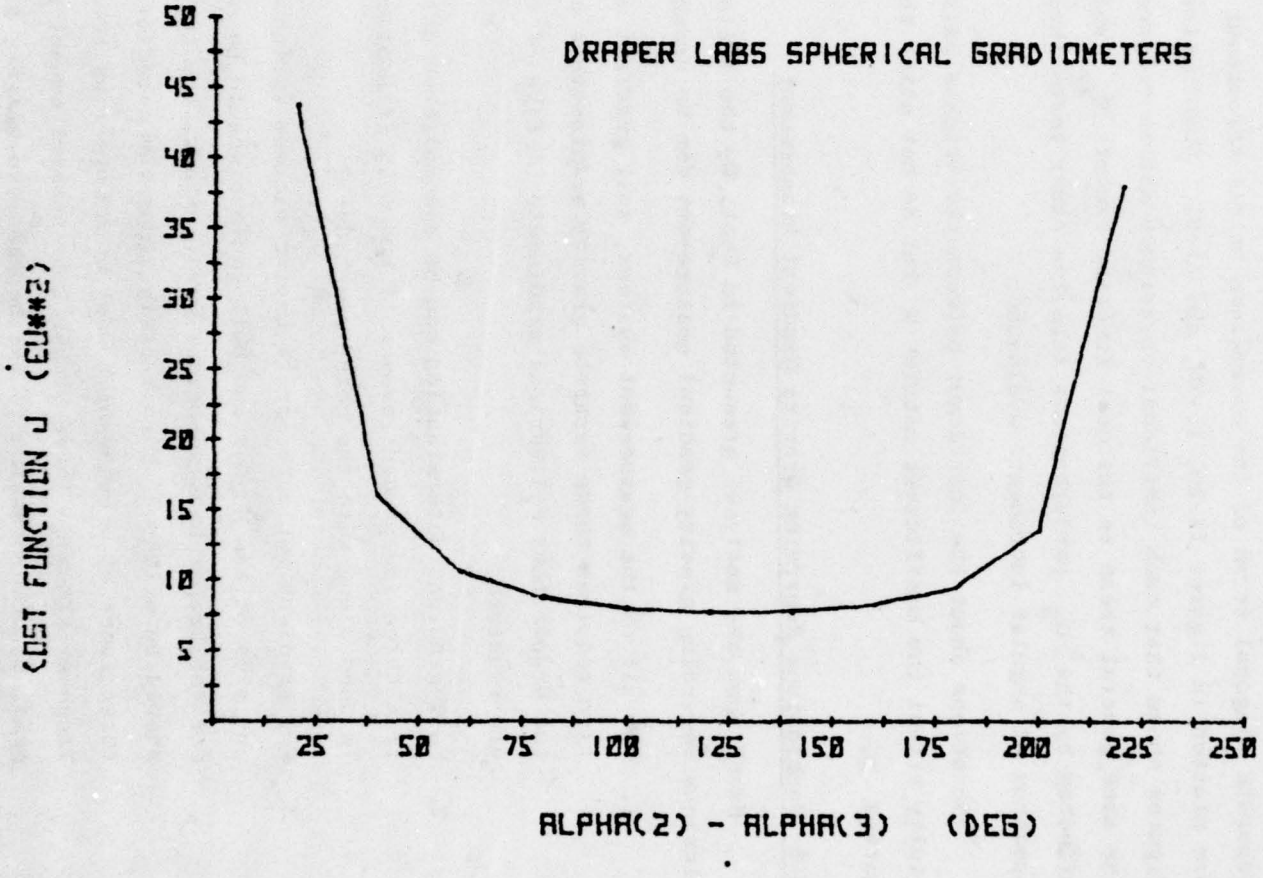


FIG. II-28 GRADIENT TENSOR ESTIMATE ERROR COST FUNCTION VS $\hat{x}_B$ ANGULAR ROTATION DIFFERENCE BETWEEN SENSORS 2 and 3. α_1 = zero deg. β_J = 58 deg.

$$|\alpha_2 - \alpha_3| = 120 \text{ deg} . \qquad (2.143)$$

and it is apparent that J does not increase substantially from that minimum within a ± 45 deg band about 120 deg. The variations in the separate diagonal terms of the covariance matrix throughout the test are plotted in figures II-29, II-30, and II-31. Examination of these figures shows that each individual covariance matrix component follows the same general trend as the cost function except Σ_{zz} which was less affected by the α_3 perturbations than the other terms throughout the spectrum of angular increments evaluated.

Rotations about the instrument between-the-weights axis substantially effect the coefficient matrix M but do not alter the covariance matrix Σ.

G-5 Conclusions Regarding Gravity Gradient Measurement

Based upon the analyses presented in Sect. G, the following conclusions regarding gravity gradient measurement can be drawn:

1. For all of the measurement systems, full gradient determination requires three separate gravity gradiometers except for the Draper Labs cylindrical gradiometer. Five of these sensors are required;

2. Full gradient determination can be accomplished using data from three independent sensor if and only if Laplace's equation is used along with the measurement data;

3. For gradient estimate errors having minimum variance, the output axes of the Hughes and Bell sensors should be orthogonal. For the Draper Labs spherical gradiometers, the three sensors should be oriented approximately along the bisector of the three faces of a cube which meet at a corner as recommended by Trageser [TR-2]. Three Draper Labs sensors cannot provide full gradient determination if the between-the-weights axes are orthogonal.

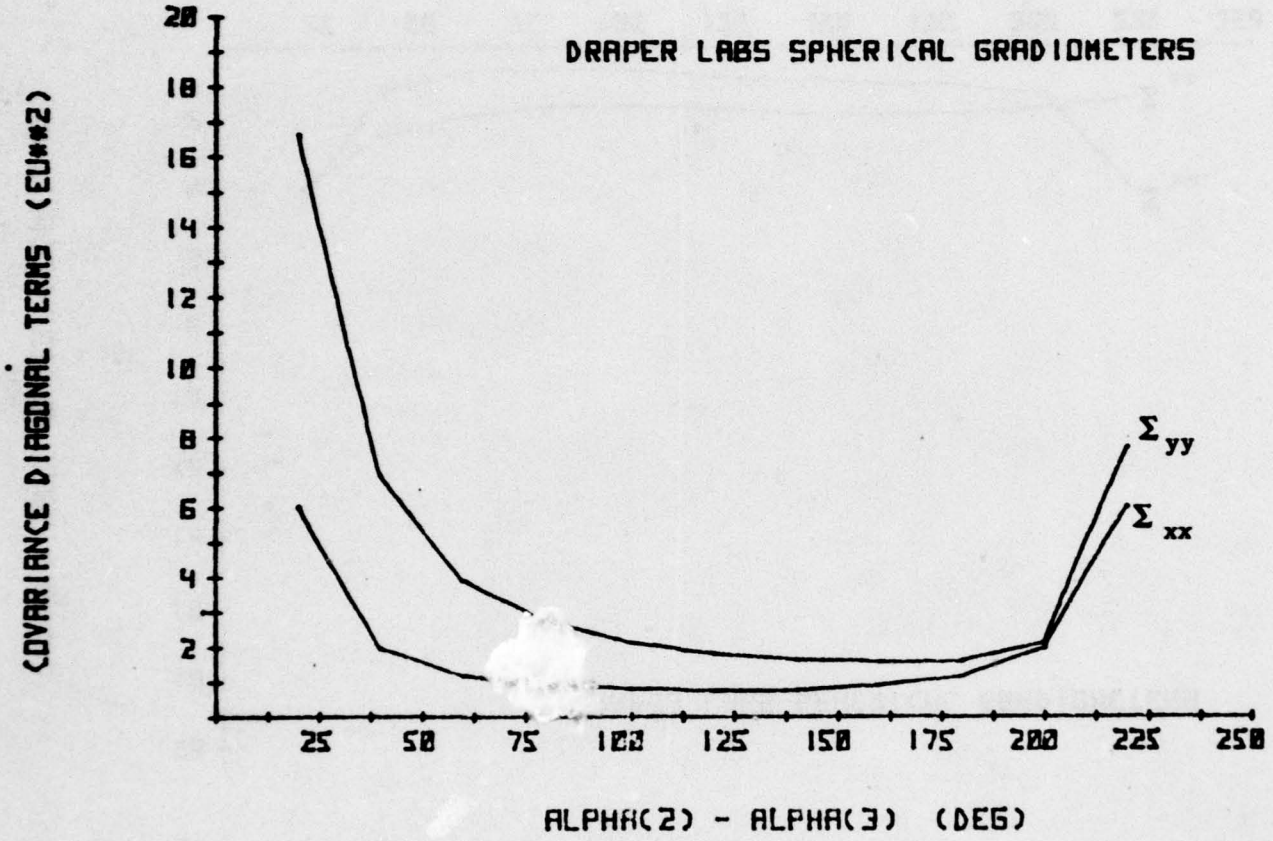


FIG. II-29 GRADIENT TENSOR ESTIMATE ERROR COVARIANCE MATRIX COMPONENTS VS $\hat{x}_B$ ANGULAR ROTATION DIFFERENCE BETWEEN SENSORS 2 and 3; Σ_{xx} and Σ_{yy}. α_1 = zero deg. β_j = 58 deg.

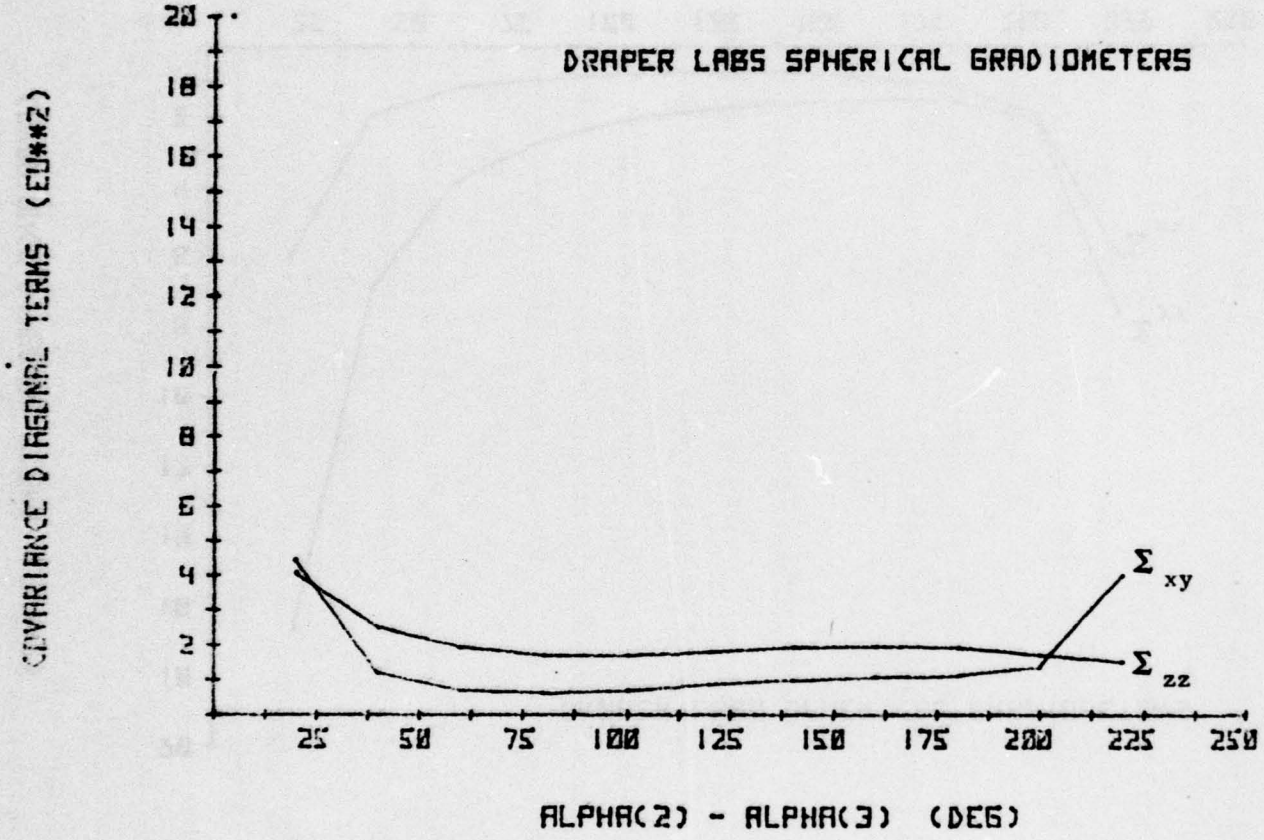


FIG. II-30 GRADIENT TENSOR ESTIMATE ERROR COVARIANCE MATRIX COMPONENTS VS $\hat{x}_B$ ANGULAR ROTATION DIFFERENCE BETWEEN SENSORS 2 and 3; Σ_{zz} and Σ_{xy}. α_1 = zero deg. β_j = 58 deg.

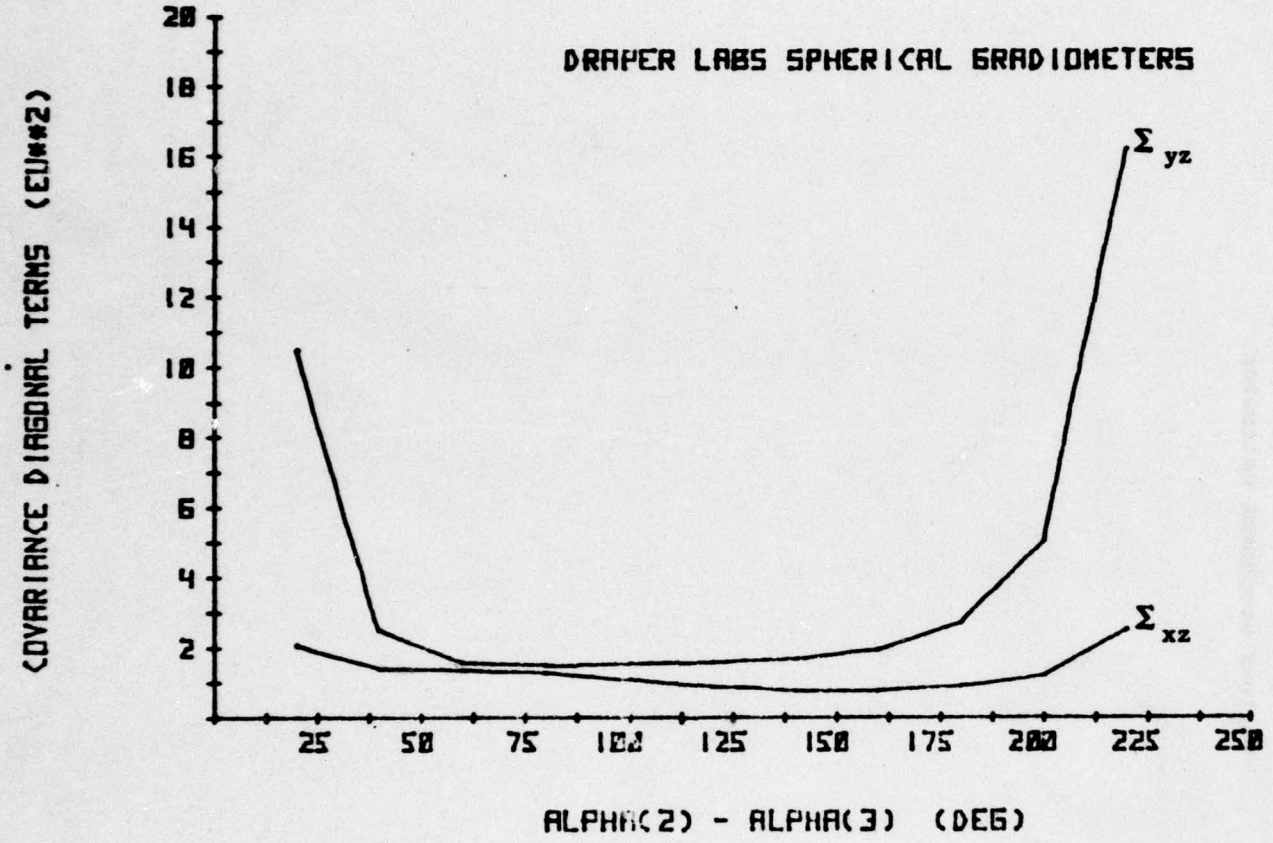


FIG. II-31 GRADIENT TENSOR ESTIMATE ERROR COVARIANCE MATRIX COMPONENTS vs $\hat{x}_B$ ANGULAR ROTATION DIFFERENCE BETWEEN SENSORS 2 and 3, Σ_{xz} and Σ_{yz}. α_1 = zero deg. β_j = 58 deg.

4. The addition of a fourth gradiometer into the system does not relax the requirement that Laplace's equation be included for full tensor identifiability. The use of additional sensors would, however, reduce the rms errors associated with the various component estimates.

Chapter III

HUGHES GRAVITY GRADIOMETER ERROR MODEL

A. INTRODUCTION

Three different gravity gradiometers were discussed in Chapter II. Each of these instruments has been designed to provide gravity gradient data to 1 EU rms accuracy, using a 10 sec data averaging period, at or near the earth's surface while operating from a mobile platform such as a truck, a ship, or an aircraft. To date, none has achieved this goal.

A major problem associated with reaching 1 EU performance is instrument response to its dynamic environment. All of the instruments are sensitive to angular velocity since there exists a gradient in the centripetal acceleration field just as one exists in the gravity field. Both gradients have an identical effect upon gradiometer output. Hence, the motion of the platform must be limited to either extremely small or to well known dynamics in order to eliminate the effect of jitter motion which exists and is tolerable on current inertial instrument platforms.

In addition to these systematic errors the output of each instrument contains errors due to imperfections in construction. The parameters associated with fabrication error transform angular velocity, angular acceleration, and linear acceleration into errors in gradiometer output. By writing the differential equations which represent the dynamic behavior of the instrument and its response to a general kinematic environment, it is possible to relate kinematic input to sensor output through the instrument parameters. Once these relationships are known, methods for reducing the effects of parameter irregularities upon sensor output can be sought if necessary. In the case of the moving base gravity gradiometer, such reductions are essential.

In this chapter a complete error model relating sensor parameters, dynamic environment, and sensor output is developed for the Hughes Rotating Gravity Gradiometer (RGG). The techniques for parameter identification

and correction and sensor output compensation appearing in subsequent chapters are specialized to the Hughes' (RGG) instrument. The general approach to parameter estimation and control can, however, be applied to any rotating instrument.

B. INSTRUMENT ERROR SOURCES

Instrument motion excites an instrument output signal. For an ideal gradiometer, the only output occurs at twice the spin frequency ($2\omega_s$) and is due to the gravity gradient. The instrument will, however, be constructed to finite nonzero tolerances. The gradiometer equations of motion provide a description of the output signal errors which result from kinematic excitation of an instrument possessing non-nominal physical characteristics. Parameters such as arm mass, moment-of-inertia, and mass center offset can be used to provide an indication of the level of manufacturing error associated with the instrument. The gradiometer error mechanisms which were modeled are discussed individually in this chapter. They are:

(a) Rigid Body Linear Dynamics. The kinematic input is linear acceleration. The associated instrument parameters are arm mass and mass center location. This error is treated in Sect. B-1.

(b) Axial Torsional Coupling. The kinematic input is linear acceleration. The associated instrument parameter is a cross-axis coupling coefficient. This error is treated in Sect. B-2.

(c) Rigid Body Rotational Dynamics. The kinematic inputs are angular velocity and angular acceleration. The associated instrument parameters are arm mass, arm mass center location, and arm moment-of-inertia. This error is treated in Sect. B-3.

(d) Sum Mode Mismatch. This error may be thought of as one which results from flexible body rotational dynamics. The kinematic inputs are angular velocity and angular acceleration. The

2/

associated instrument parameters are arm and instrument case moment-of-inertia, pivot compliance, and pivot damping ratio. This error is treated in Sect. B-6.

(e) Angular misalignment. The kinematic inputs are linear acceleration and angular velocity and acceleration. The associated instrument parameters are arm mass, mass center location, moment-of-inertia, and axial misalignment. This error is treated in Sects. B-4 and B-5.

(f) Arm Elasticity. This error results from flexible body linear dynamics. The kinematic input is linear acceleration. The associated instrument parameters are arm mass and compliance. This error is discussed in Sect. B-7.

In addition to the kinematic error mechanisms, numerous other sources of output error exist within the gradiometer. A list of primary, non-kinematic error sources includes:

(a) thermal or Brownian noise,

(b) temperature and temperature gradient,

(c) accoustic coupling,

(d) instrument and detector nonlinearities,

(e) signal processing errors.

The nonkinematically induced errors are not treated in this document.

Since only the Hughes gradiometer is discussed in the remainder of this document, it sill be subsequently referred to simply as the RGG (rotating gravity gradiometer). In the analysis which follows, the various output errors are denoted by the subscripted variable ϵ. For example, the variable ϵ_{LA} denotes the error in RGG output due to instrument mass center offset in the presence of linear acceleration.

B-1 Linear Acceleration Induced Torque, ϵ_{LA}

Arm mass center offset with respect to the $\hat{z}_s$ (or $\hat{z}_p$) axis responds to linear accelerations and gravity to cause an output error ϵ_{LA}.

3

In the sensor reference frame, with the sensor spin axis assumed to be horizontal,

$$\epsilon_{LA} = \begin{Bmatrix} [M_o\rho_{xo} - M_e\rho_{xe}][a_{yo}\cos\omega_s t - (a_x - g)\sin\omega_s t] \\ -[M_o\rho_{yo} - M_e\rho_{ye}][(a_{xp}-g)\cos\omega_s t - a_{yp}\sin\omega_s t] \end{Bmatrix} \quad (3.1)$$

Sensor response, ϵ_{LA}, is principally a reaction to gravity, which is relatively constant. Constant gravity causes an output error at the spin frequency ω_s. The effects of accelerations a_{xp} and a_{yp}, however, are dependent upon their frequency content. Inspection of (3.1) indicates that is a_{xp} or a_{yp} have frequency content at either ω_s or $3\omega_s$, an error at $2\omega_s$, the gravity gradient signal frequency is generated.

B-2 Axial-Torsional Coupling (Yankee Screwdriver Effect) ϵ_{YS}

The Yankee Screwdriver error, ϵ_{YS}, is so titled due to its similarity with the operating mechanism of the Yankee screwdriver. The torque ϵ_{YS} is defined as the sensor output torque about the $\hat{z}_s$ axis due to a sensor linear acceleration along that same axis, $\hat{z}_s$. The error torque is modeled as the difference of the two arm cross-axis compliance coefficients K_{YSO} and K_{YSE} and is written in (3.2) Based upon (3.2)

$$\epsilon_{YS} = [K_{YSo} - K_{YSe}]a_z \quad (3.2)$$

it is apparent that if the bracketed term is nonzero, and if a_z has components at twice the spin frequency, i.e., at $2\omega_s$, the Yankee screwdriver effect will produce an output error at the sensor signal frequency.

DeBra [DeB-2] has proposed two separate mechanical models as contributors to the axial-torsional coupling error. The first error model is shown schematically in Fig. III-1 and is referred to as the 'mower reel' effect. In Fig. III-1 the RGG has been simplified to consist only of the two arms and the central pivot. The arms are represented in the drawing as solid disks. The odd arm is assumed rigidly attached to a support. The central pivot is represented by the two twisted bars,

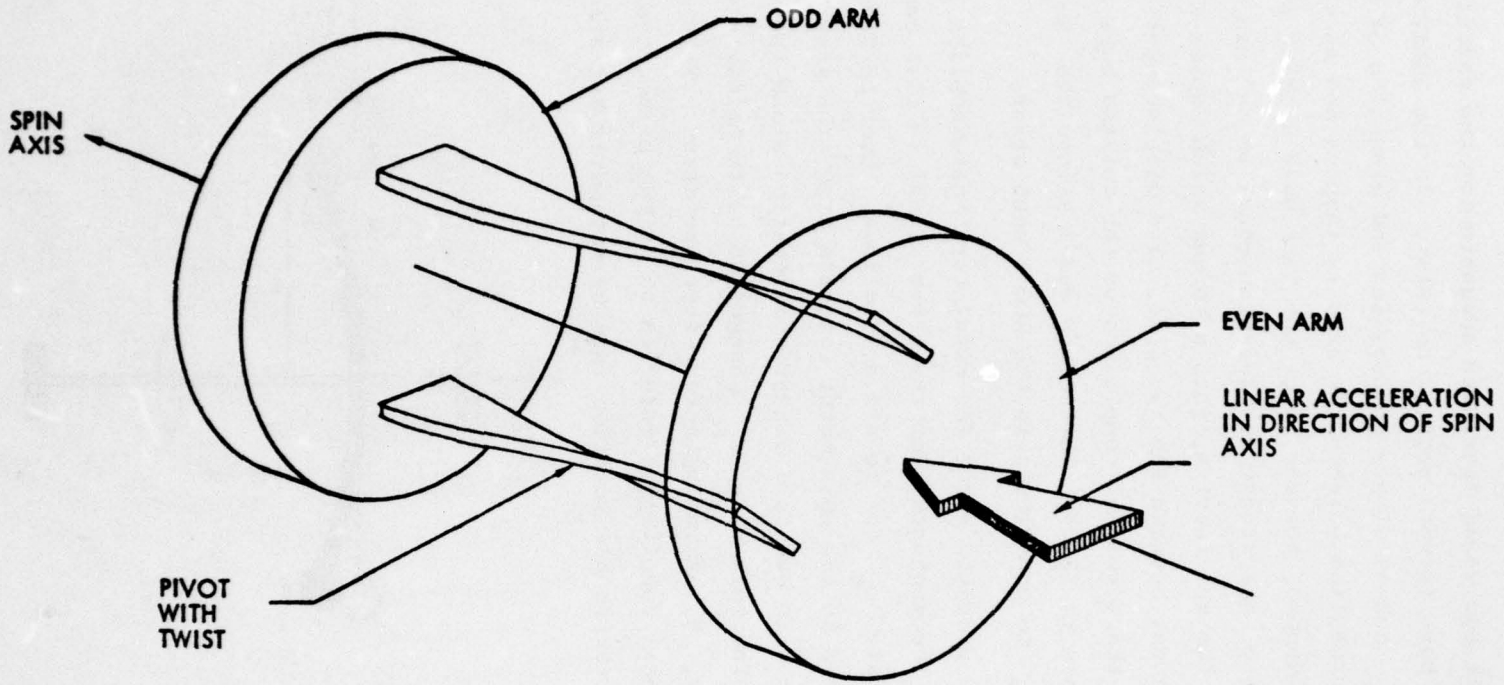


FIG. III-1 SIMPLIFIED ROTATING GRAVITY GRADIOMETER SCHEMATIC DEMONSTRATING THE MOWER REEL MODEL FOR THE AXIAL TORSIONAL COUPLING ERROR.

although a single bar would have been adequate for the model. Under ideal conditions, the bars (pivot) possess no twist. In the ideal case, linear acceleration a_z causes simple compression and expansion of the pivot. No differential rotation between the arms is induced and no error signal is generated. Suppose, however, that the bars have a twist angle φ_T. Than a component of the linear acceleration equal to $a_z \sin \varphi_T$ is converted, through the arm inertia, into a torque which causes a relative angular displacement between the two arms. The displacement has linear dependence upon the torsional compliance of the twisted bars and can be expressed as shown in (3.2). This error model allows the $2\omega_s$ frequency component of a_z to contribute to the RGG otupuc error.

The second proposed model for axial-torsional coupling is represented in Fig. III-2. The mechanism for the error signal in this case is the change in spin rate ω_s due to arm deflections. Over periods of time which are small compared to the spin motor response time, the arms can deflect through an angle $\Delta\theta$ due to a linear acceleration along the direction of the spin axis. The spin rate ω_s changes so as to maintain constant angular momentum, h, assuming torque-free operation. This mechanism for axial-torsional coupling is referred to as the piano stool effect, i.e., the instructor varies his rotation rate by extending his arms while spinning on a piano stool.

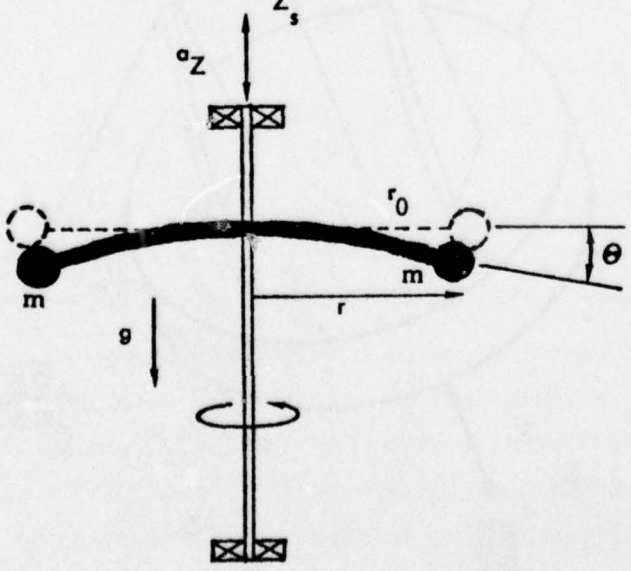


FIG. III-2 AXIAL-TORSIONAL COUPLING MODEL PIANO STOOL EFFECT.

3.6

For small angles,

$$\cos \psi \approx 1 - \frac{\psi^2}{2} \tag{3.2}$$

and

$$r \approx r_0(1 - \psi^2/2) \tag{3.3}$$

where

$$\psi = \psi_0 + mk(a + g) \tag{3.4}$$

The term ψ_0 in (3.4) represents a bias deflection due to manufacturing tolerance. The term mkg represents a bias deflection due to the vertical gravity field.

For these short periods, spin angular momentum h, where

$$h = 2mr^2\omega_s \tag{3.5}$$

may be considered constant. Hence,

$$\dot{h} = 0 \tag{3.6}$$

and

$$\dot{\omega}_s = -\frac{2\omega_s}{r}\dot{r} \ . \tag{3.7}$$

Using equations (3.3) and (3.4), and assuming g to be constant

$$\dot{\omega}_s = \frac{2\omega_s mk\dot{a}\{\psi_0 + mk(a + g)\}\{1 + \frac{\psi^2}{2}\}}{1 - (\psi_2/2)} \ . \tag{3.8}$$

and, from the binomial expansion

$$\dot{\omega}_s \approx 2\omega_s mk\dot{a}\{\psi_0 + mk(a + g)\}\ \{1 + \frac{\psi^2}{2}\} \tag{3.9}$$

Neglecting the ψ^2 term in (3.9),

$$\dot{\omega}_s = 2\omega_s mk\psi_0 \dot{a} + 2\omega_s (mk)^2 a\dot{a} + 2\omega_s (mk^2 g\dot{a} \quad . \tag{3.10}$$

Equations having the form of (3.10) can be written for the RGG odd and even arms. Taking the difference of these equations yields, when higher order terms are neglected,

$$\begin{aligned}(\dot{\omega}_s)_o - (\dot{\omega}_s)_e = {} & 2n\Delta[mk\psi_0]\dot{a} + 2na\dot{a}\Delta[(mk)^2] \\ & + 2ng\dot{a}\Delta[(mk)^2]\end{aligned} \tag{3.11}$$

where

$$n \triangleq \text{nominal RGG spin rate}$$

$$\Delta[(mk)^2] \triangleq (mk)_o^2 - (mk)_e^2 \tag{3.12}$$

$$\Delta[mk\psi_0] \triangleq (mk\psi_0)_o - (mk\psi_0)_e \quad . \tag{3.13}$$

Because ψ_{oe} and ψ_{oo} may have opposite signs in (3.13), there is no nominal cancellation as there is in (3.12). Double integration with respect to time of (3.11) yields a relative deflection $\Delta\theta$ of the odd and even arms as expressed by (3.14)

$$\begin{aligned}\Delta\theta = {} & \{2n\Delta(mk\psi_0) + 2ng\Delta[(mk)^2]\} \iint \dot{a}dt^2 \\ & + 2n\Delta[(mk)^2] \iint a\dot{a}dt^2 \quad .\end{aligned} \tag{3.14}$$

This angular deflection produces an output signal. If the arms are identical in terms of masses m and stiffness coefficients k, only the first term on the right side of (3.14) can be nonzero due to manufacturing angular offset mismatch. Hence, this axial-torsional coupling mechanism can provide an output error even for an RGG which is perfectly constructed in terms of arm mass and arm compliance. If

$$a = A \sin \omega_s t \,, \tag{3.15}$$

then $\dot{\omega}_s$ has $2\omega_s$ frequency content since aa is at $2\omega_s$. Similarly,

$$a = A \sin 2\omega_s t \tag{3.16}$$

$\dot{\omega}_s$ also has a $2\omega_s$ component since in this case ag and $\mathring{a}\theta_o$ have $2\omega_s$ frequency. In addition, it is shown in Sect. D that the mechanical gain through which an output signal is passed is a function of spin rate ω_s. If the spin rate varies with frequency $2\omega_s$, the signal gain will follow also at $2\omega_s$. The error induced by the change in the gain will be inseparable from the gravity gradient signal.

Both the mower reel and the piano stool effects are candidate mechanisms for describing RGG axial-torsional coupling error and they are distinguishable by their 90 deg phase difference due to the $\mathring{a}$ vs a dependence. The validity of each model and importance of each mechanism to RGG output error is currently being evaluated in the laboratory by Hughes. For the remainder of this document, consideration of axial-torsional coupling error will be limited to the mower reel model due to its simpler nature and the fact that the effects of the piano stool model have not yet been confirmed.

B-3 Non-principal Axis Spin and Mass Center Offset, ϵ_R

The moment imposed upon the RGG central pivot due to the angular motion of a single instrument arm about a set of axes skewed with respect to arm principal axes and possessing a mass center offset $\bar{c}$ may be written as

$$\bar{T} = \bar{r} \times \bar{F} \,. \tag{3.17}$$

Equation (3.17) is an alternate expression for the first two terms on the right side of the RGG output equation, (2.20), with only one arm considered. Assuming that the arm principal axes are not coincident with the sensor reference system basis vectors and furthermore, assuming

that the arm mass center is not coincident with the origin of the sensor reference system, (3.17), may be written in tensor notation as

$$\bar{T} = \bar{\bar{I}} \cdot \dot{\bar{\omega}} + \bar{\omega}^{s-I} \times \bar{\bar{I}} \cdot \omega^{s-I} . \qquad (3.18)$$

Expressing $\bar{\bar{I}}$ in a coordinate system aligned to the sensor system but having an origin displaced to coincide with the mass center of the arm, (3.18) may be written with respect to the sensor frame as shown in (3.19), where $\bar{\omega}$ is defined as the time rate of change of the sensor reference system with respect to the inertial reference system. The vector $\bar{\rho}$ defines the position of the arm mass center with respect to the sensor reference system. In (3.19) it is also written with respect to the sensor frame.

$$\begin{aligned}
\bar{T} = &\begin{bmatrix} I_{xx} + m(\rho_y^2 + \rho_z^2) & I_{xy} - m\rho_x\rho_y & I_{xz} - m\rho_x\rho_z \\ I_{xy} - m\rho_x\rho_y & I_{yy} + m(\rho_x^2 + \rho_z^2) & I_{yz} - m\rho_y\rho_z \\ I_{xz} - m\rho_x\rho_z & I_{yz} - m\rho_y\rho_z & I_{zz} + m(\rho_x^2 + \rho_y^2) \end{bmatrix} \begin{bmatrix} \dot{\omega}_x \\ \dot{\omega}_y \\ \dot{\omega}_z \end{bmatrix} \\
&+ \begin{bmatrix} (I_{xz} - m\rho_x\rho_z) & -(I_{xy} - m\rho_x\rho_y) & [I_{zz} - I_{yy} + m(\rho_y^2 - \rho_z^2)] \\ -(I_{yz} - m\rho_y\rho_z) & [I_{xx} - I_{zz} + m(\rho_z^2 - \rho_x^2)] & (I_{xy} - m\rho_x\rho_y) \\ [I_{yy} - I_{xx} + m(\rho_x^2 - \rho_y^2)] & (I_{yz} - m\rho_y\rho_z) & -(I_{xz} - m\rho_x\rho_z) \end{bmatrix} \begin{bmatrix} \omega_x\omega_y \\ \omega_x\omega_z \\ \omega_y\omega_z \end{bmatrix} \\
&+ \begin{bmatrix} 0 & (I_{yz} - m\rho_y\rho_z) & -(I_{yz} - m\rho_y\rho_z) \\ -(I_{xz} - m\rho_x\rho_z) & 0 & (I_{xz} - m\rho_x\rho_z) \\ (I_{xy} - m\rho_x\rho_y) & -(I_{xy} - m\rho_x\rho_y) & 0 \end{bmatrix} \begin{bmatrix} \omega_x^2 \\ \omega_y^2 \\ \omega_z^2 \end{bmatrix} .
\end{aligned} \qquad (3.19)$$

With (3.15) written for both the odd and even sensor arms, the RGG differential output torque vector may then be expressed as

$$\bar{\Delta T} = \bar{T}_o - \bar{T}_e \tag{3.20}$$

The resultant output error is

$$\epsilon_R = \bar{\Delta T} \cdot \hat{z}_s \ . \tag{3.21}$$

Two separate physical effects are displayed in (3.19). The first is the significance of arm principal axis system to sensor axis system misalignment and origin displacement. The effect of mass center offset is obvious in terms of its contribution to sensor output torque, and the origins of the product-of-inertia terms will be investigated in detail in the next section. The second effect to be considered is the nature of the angular velocities and accelerations. Due to the $\dot{\omega}$ terms of (3.19, any $2\omega_s$ frequency component associated with either transverse or axial rotation will be transmitted to the output signal. Furthermore, due to cross coupling and second order angular velocity terms, $1\omega_s$ and $3\omega_s$ angular velocity terms can combine to form a $2\omega_s$ output torque error.

B-4 Elastic/Spin/Principal Axis Misalignment, ϵ_{AM}

In order to establish the nature of the products of inertia of (3.19), the effects of axial misalignments upon one of the two instrument arms will now be considered. By developing a similar torque for the second arm and forming the difference, the output torque can be calculated.

Let the principal axes of one of the instrument arms be related to the sensor system spin reference axes according to the relation

$$C_{s/B} = \begin{bmatrix} 1 & 0 & -\xi_y \\ 0 & 1 & \xi_x \\ \xi_y & -\xi_x & 1 \end{bmatrix} \tag{3.22}$$

Furthermore, let the spin reference system be related to the pivot aligned elastic reference system according to the transformation

$$C_{E/s} = \begin{bmatrix} 1 & 0 & -\alpha_y \\ 0 & 1 & \alpha_x \\ \alpha_y & -\alpha_x & 1 \end{bmatrix} . \tag{3.23}$$

At any time t, the arm angular momentum may be written, in the elastic frame, as

$$H_E = \left\{ C_{E/s} [C^T_{B/s} I_{B/B} C_{B/s}] C_{E/s} \right\} C^T_{E/s} \omega_s \tag{3.24}$$

and hence

$$[T_{AM}]_E = \mathcal{J} C_{E/s} \dot{\omega}_s + [C_{E/s} \omega_s x]^{\sim} C_{E/s} \omega_s \tag{3.25}$$

where

$$\mathcal{J} \triangleq C_{E/s} \left\{ C^T_{B/s} I_{B/B} C_{B/s} \right\} C^T_{E/s} \tag{3.26}$$

and $I_{B/B} \triangleq$ arm inertia tensor with respect to arm principal axes. Inertia matrix $\mathcal{J}$ of (3.26) may be written as

$$\mathcal{J} \triangleq [I_{B/B}] + [\alpha \tilde{} I_{B/B}] . \tag{3.27}$$

Expansion of the second term on the right side of (3.27) yields

$$\mathcal{I} = [I_{B/B}] + \begin{bmatrix} (\alpha_y + \xi_y)\xi_y I_z & -(\alpha_y + \xi_y)\xi_x I_z & \xi_y I_x - (\alpha_y + \xi_y) I_z \\ -\xi_y(\alpha_x + \xi_x) I_z & \xi_x(\alpha_x + \xi_x) I_z & -\xi_x I_y + (\alpha_x + \xi_x) I_z \\ -\xi_y I_z + (\alpha_y + \xi_y) I_x & \xi_x I_z - (\alpha_x + \xi_x) I_y & \xi_y(\alpha_y + \xi_y) I_x + \xi_x(\alpha_x + \xi_x) I_y \end{bmatrix} \quad (3.28)$$

and

$$C_{E/s}[\omega]_s = \begin{bmatrix} \omega_x - \alpha_y \omega_z \\ \omega_y + \alpha_x \omega_z \\ \omega_z + \alpha_y \omega_x - \alpha_x \omega_y \end{bmatrix} \triangleq [\omega_s] + [\alpha\omega_s] \; . \quad (3.29)$$

Based upon the definitions of (3.28) and (3.29), (3.25) may be written as

$$\begin{aligned} [T_{AM}]_E = \; & I_{B/B}\dot{\omega}_s + (\omega_s x) I_{B/B}\omega_s \\ & + I_{B/B}(\alpha\dot{\omega}_s) + (\alpha\xi I_{B/B})\dot{\omega}_s + (\alpha\xi I_{B/B})(\alpha\dot{\omega}_s) \\ & + (\omega_s x) I_{B/B}(\alpha\omega_s) + (\alpha\omega_s x) I_{B/B}\omega_s + (\alpha\omega_s x) I_{B/B}(\alpha\omega_s) \\ & + (\omega_s x)(\alpha\xi I_{B/B})\omega_s + (\omega_s x)(\alpha\xi I_{B/B})(\alpha\omega_s) \\ & + (\alpha\omega_s x)(\alpha\xi I_{B/B})\omega_s + (\alpha\omega_s x)(\alpha\xi I_{B/B})(\alpha\omega_s) \; . \end{aligned} \quad (3.30)$$

The last ten terms on the right side of (3.30) represent the error in the output torque vector due to axial misalignments amond the elastic, spin, and arm principal reference systems. They are also the source of the product-of-inertia terms of (3.19), when (3.19) is referenced to the elastic rather than the spin reference system. With

$$[\omega_s]^T \triangleq [\omega_x, \; \omega_y, \; n + \omega_z] \quad (3.31)$$

where n is the nominal spin rate, and ω_z is the spin rate perturbation from nominal about the $\hat{z}_s$ axis, the single arm torque about the $\hat{z}_E$

axis (elastic system z axis), when higher order terms in ξ and α are neglected, may be written as in (3.32)

$$
\begin{aligned}
[T_{AM}]_E \cdot \hat{z}_E = & \begin{bmatrix} (\alpha_y I_z - \xi_y I_z + \alpha_y I_x + \xi_y I_x)\dot{\omega}_x \\ + (-\alpha_x I_z + \xi_x I_z - \alpha_x I_y - \xi_x I_y)\dot{\omega}_y \\ + (\xi_y I_x - \xi_x I_y)\dot{\omega}_z + (\alpha_x + \xi_x - \alpha_y - \xi_y) I_z \dot{\omega}_z \end{bmatrix} \\
& + \left[\alpha_y \omega_y (I_x - I_y) + \alpha_x \omega_x (I_y - I_x)\right](n + \omega_z) \\
& + \left[\xi_y (I_x - I_z) - \xi_x (I_y - I_z) + (\alpha_x - \alpha_y) I_z\right]\omega_x \omega_y
\end{aligned}
\qquad (3.32)
$$

The transition from single arm torque T_{AM} to the output signal error due to axial misalignments, ϵ_{AM}, is abvious. Inspection of the right side of (3.28) indicates that the second term in brackets $[\alpha_y \omega_y (I_x - I_y) + \alpha_x \omega_x (I_y - I_x)]$ is the dominant error term in the equation since it is the only term containing the nominal sensor spin rate, n. A misalignment of the spin and elastic axes propagates linearly into the output signal. Note that such a condition does not exist for a principal axis, spin axis misalignment. From Table II-1,

$$I_y - I_x = 3.061 \times 10^{-3} \text{ kg m}^2 . \qquad (3.33)$$

Furthermore, from Reference AM-1, the peak twice frequency component of ω_x or ω_y is

$$\left|\omega_x(2\omega_s)\right|_{max} = 4.55 \times 10^{-5} \text{ rad/sec} \qquad (3.34)$$

and

$$\left|\omega_x(2\omega_s\right|_{max} = 4.55 \quad 10^{-5} \text{ rad/sec} \qquad (3.35)$$

Rewriting (3.32) as

$$[T_{AM}]_E \cdot \hat{z}_E = [(\alpha_x \omega_x - \alpha_y \omega_y)(I_y - I_x)](n + \omega_z) \qquad (3.36)$$

a worst case single arm torque can be written as

$$[T'_{AM}]_E \cdot \hat{z}_E = 2\alpha_x \omega_x (I_y - I_x) n \qquad (3.37)$$

when α_x and α_y are assumed to have the same magnitude but opposite sign and when ω_x is taken to be equal to ω_y. Then, a worst case output error may be expressed as

$$[\epsilon'_{AM}]_E \cdot \hat{z}_E = 4\alpha_x \omega_x (I_y - I_x) n \; . \qquad (3.38)$$

With n equal to the spin rate (110 rad/sec), this error source will exceed 1 EU output error at $2\omega_s$

$$\alpha_x \geq 5.81 \times 10^{-8} \text{ rad} \qquad (3.39)$$

or

$$\alpha_x \geq 0.012 \text{ arcsec} \; . \qquad (3.40)$$

This is extremely precise alignment requirement. Close attention will be required by this alignment during instrument assembly. Furthermore, on-line identification and compensation or correction will be required.

B-5 Platform/Sensor Axis System Misalignment, ϵ_{PMA}

Misalignments between the platform and sensor reference systems become important in light of platform jitter and jitter compensation in the RGG output. Additionally, it will be suggested in subsequent chapters that in order to estimate a set of parameters which effect RGG output, a set of known inputs can be applied to the sensor through platform excitation. Since only platform motion can be measured by the platform instrumentation, sensor motion must be inferred by assumption of a rigid mounting structure linking the RGG to the platform. The platform angular velocity expressed in the platform reference system is

$$[\Omega]_p^T \triangleq [\Omega_{xp}, \; \Omega_{yp}, \; \Omega_{zp}] \; , \qquad (3.41)$$

and the small angle transformation

$$C_{so/po} = \begin{bmatrix} 1 & -\varphi_z & \varphi_y \\ \varphi_z & 1 & -\varphi_x \\ -\varphi_y & \varphi_x & 1 \end{bmatrix} \tag{3.42}$$

related the platform reference system to the sensor reference system at time zero. With the transformation from the initial position to current rotational position defined as

$$C_t = \begin{bmatrix} \cos \omega_s t & \sin \omega_s t & 0 \\ -\sin \omega_s t & \cos \omega_s t & 0 \\ 0 & 0 & 1 \end{bmatrix} \tag{3.43}$$

the platform angular velocity vector may be expressed in sensor axes according to (3.40).

$$[\Omega]_s = C_t C_{so/po} [\Omega]_p \, . \tag{3.44}$$

All platform angular rates, $(\Omega_i)p$, are much less than ω_s, the sensor spin rate. Hence, with a platform sensor misalignment and platform angular motion, the added contribution to output torque error is

$$\begin{aligned} \epsilon_{PMAR} = & \left[-\Delta M \rho_x \rho_z + \Delta I_{xz}\right] (\dot{\Omega}_{xs} - \Omega_{ys}\, \Omega_{zs}) \\ & + \left[-\Delta M \rho_y \rho_z + \Delta I_{yz}\right] (\dot{\Omega}_{ys} + \Omega_{xs} \Omega_{zs}) \\ & + \left[\Delta M(\rho_x^2 + \rho_y^2) + \Delta I_{zz}\right] (\dot{\Omega}_{zs}) \, . \\ & + \left[\Delta[M(\rho_x^2 - \rho_y^2)] + (\Delta I_{yy} - \Delta I_{xx})\right] (\Omega_{xs}\, \Omega_{ys}) \\ & + \left[\Delta M \rho_x \rho_y - \Delta I_{xy}\right] (\Omega_{ys}^2 - \Omega_{xs}^2) \end{aligned} \tag{3.45}$$

The linear acceleration perturbation due to platform/instrument misalignment may be written as

$$\epsilon_{PMAL} = \left[M_o\rho_{xo} - M_e\rho_{xe}\right]\left\{\begin{array}{l}\left[\varphi_z a_{xp} - \varphi_x a_{zp}\right]\cos\omega_s t \\ + \left[\varphi_z a_{yp} - \varphi_y a_{zp}\right]\sin\omega_s t\end{array}\right\} \qquad (3.46)$$

$$- \left[M_o\rho_{yo} - M_e\rho_{ye}\right]\left\{\begin{array}{l}\left[-\varphi_z a_{yp} + \varphi_y a_{zp}\right]\cos\omega_s t \\ \left[\varphi_z a_{xp} - \varphi_x a_{zp}\right]\sin\omega_s t\end{array}\right\}$$

B-6 Sum Mode Mismatch Error

The error sources developed thus far have, in general, been based upon assumptions of rigid body motion. It was pointed out in Ch. II that the sensor output signal comes from a piezoelectric crystal which measures central pivot strain (see Fig. II-2). It is therefore necessary to investigate the arm-to-arm dynamic behavior of the instrument in response to disturbance torques.

Relative to the case, the arms of the RGG (rotating gravity gradiometer) can rotate at either of two fundamental frequencies: (1) the sum mode, in which the arms move together with respect to the case; and (2) the difference mode, in which the arms rotate relative to each other.* It is the difference mode which is excited by the external gravity gradient to generate a gradient output signal. In an ideal sensor, spin axis disturbance torques excite only the sum mode motion which does not cause an error in the output signal. However, asymmetrics in arm inertias,

* This discussion taken from Ames [AM-2].

as well as pivot damping and compliance differences, cause spin axis angular acceleration disturbances to excite the difference mode.

The sensor model used for sum mode mismatch error analysis is shown in Fig. III-3.

$T_d \triangleq$ disturbance torque applied about the case.

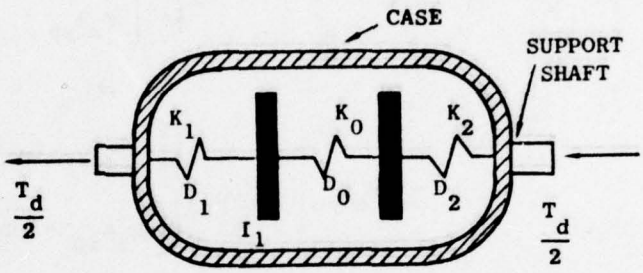


FIG. III-3 SYSTEM MODEL FOR SUM MODE MISMATCH ERROR DEVELOPMENT

With ideal alignment between the spin axis and sensor reference system assumed, and the gravity gradient signal neglected, the single axis equations of motion for the flexible RGG are written in (3.47) through (3.49).

$$I_{zzo}\ddot{\theta}_o + D_o(\dot{\theta}_o-\dot{\theta}_e) + K_0(\theta_o-\theta_e) + D_1(\dot{\theta}_o-\dot{\theta}_c) + K_1(\theta_o-\theta_c) = 0 \qquad (3.47)$$

$$I_{zze}\ddot{\theta}_e - D_o(\dot{\theta}_o-\dot{\theta}_e) - K_0(\theta_o-\theta_e) + D_2(\dot{\theta}_o-\dot{\theta}_c) + K_2(\theta_o-\theta_c) = 0 \qquad (3.48)$$

$$I_c\ddot{\theta}_c - D_1(\dot{\theta}_o-\dot{\theta}_c) - K_1(\theta_o-\theta_c) - D_2(\dot{\theta}_e-\theta_c) - K_2(\theta_e - \theta_c) = T_d. \qquad (3.49)$$

The term $I_{zzo}\ddot{\theta}_o$ in (3.40) is the same term which is written as $I_{zz}\dot{\omega}_z$ in (3.19). Note also that by calculating the difference between (3.47) and (3.48) the equation for the relative arm displacement, $(\theta_o - \theta_e)$ is derived. Assuming a linear piezoelectric effect for small values of $\theta_o - \theta_e$, this is the measured RGG output signal.

Examination of (3.47) through (3.49) indicates that extraction of a relative angular displacement difference, $(\theta_o - \theta_e)$, could be accomplished using only the first two of these equations if the variable θ_c rather than T_d, was treated as the disturbance function. The three-equation approach to this error was first used by Hughes [AM-2] in 1972. Since one of the instrument response frequencies, β_o, is a function of case inertia, I_c, and since the drive and drag uncertainties can be written directly as disturbance torques T_d, the three-equation approach to this error source was used.

Since the gravity gradient signal occurs at $2\omega_s$, and since the sensor has a mechanical resonance at that frequency, and furthermore, since the average spin rate is carefully controlled, only disturbance torques having $2\omega_s$ frequency content are significant if a sufficiently long data averaging time is used. The frequency content of the disturbance torques can be determined by harmonic analysis for any input.

The Laplace transformation of (3.47) through (3.49) yields the system of (3.50).

$$
\begin{aligned}
I_{zzo}s^2\theta_o + (D_o s + K_o)(\theta_o - \theta_e) + (D_1 s + K_1)(\theta_o - \theta_c) &= 0 \\
I_{zze}s^2\theta_e + (D_o s + K_0(\theta_e - \theta_o) + (D_2 s + K_2)(\theta_e - \theta_c) &= 0 \qquad (3.50 \\
I_c s^2\theta_c + (D_1 s + K_1)(\theta_c - \theta_o) + (D_2 s + K_2)(\theta_c - \theta_e) &= T_d(s) \ .
\end{aligned}
$$

The characteristic polynomial for this system is given by (3.51) as

$$
\Delta = s^2\left\{
\begin{aligned}
&I_{zzo}I_{zze}I_c\left(s^2 + \frac{B_o+B_2}{I_{zze}}\right)\left(s^2 + \frac{B_1+B_2}{I_c}\right) - I_{zzo}I_{zze}I_c\,\frac{B_2^2}{I_{zze}I_c} \\
&+ I_{zzo}I_{zze}I_c\left(\frac{B_o}{I_{zzo}}\right)\left(s^2 + \frac{B_1+B_2}{I_c}\right) + I_{zzo}I_{zze}I_c\,\frac{B_1B_2}{I_{zzo}I_c} \qquad (3.51) \\
&+ I_{zzo}I_{zze}I_c\,\frac{B_oB_2}{I_{zzo}I_{zze}} + I_{zzo}I_{zze}I_c\left(\frac{B_1}{I_{zzo}}\right)\left(s^2 + \frac{B_o+B_2}{I_{zze}}\right)
\end{aligned}
\right.
$$

19

or

$$\Delta = s^2\left(s^2 + \frac{\omega_o}{Q}\, s + \omega_o^2\right)\left(s^2 + \frac{\beta_o}{Q_\beta}\, s + \beta_o^2\right) \quad . \tag{3.52}$$

Equations (3.53) through (3.57) define the collected terms of (3.51) which formed the definitions used in (3.52).

$$B_0 = D_0 s + K_0 \tag{3.53}$$

$$B_1 = D_1 s + K_1 \tag{3.54}$$

$$B_2 = D_2 s + K_2 \tag{3.55}$$

$$\beta_o^2 = \frac{K_1}{I_{zzo}}\left[1 + \frac{2I_{zzo}}{I_c}\right] \tag{3.56}$$

$$\omega_o^2 = \frac{K_1}{I_{zzo}}\left[1 + \frac{2K_0}{K_1}\right] \tag{3.57}$$

$$\omega_o = \frac{K_1}{I_{zzo}}\; 1 + \frac{2K_0}{K_1} \tag{3.58}$$

The terms Q and Q_β of (3.52) are primarily functions of damping coefficients D_0, D_1, and D_2, and are listed in Table II-1.

The relative rotation between the arms, $\theta_o - \theta_e$ may be written as

$$(\theta_o - \theta_e) = \left\{\frac{1}{\Delta}\right\}\left(\frac{T_d}{I_c}\right)\left[\frac{1}{I_{zzo}}(D_1 s + K_1) - \frac{1}{I_{zze}}(D_2 s + K_2)\right] \tag{3.59}$$

or

$$(\theta_o - \theta_e) = \left\{\frac{1}{\Delta}\right\}\left(\frac{T_d}{I_c}\right)\left[\left(\frac{D_1}{I_{zzo}} - \frac{D_2}{I_{zze}}\right)s + \left(\frac{K_1}{I_{zzo}} - \frac{K_2}{I_{zze}}\right)\right] \tag{3.60}$$

Examination of (3.60) indicates that regardless of the magnitude and size

of the disturbance torque T_d, the RGG output due to the sum mode mismatch error is zero when the conditions of (3.61) and (3.62) are satisfied.

$$\frac{K_1}{I_{zzo}} - \frac{K_2}{I_{zze}} = 0 \tag{3.61}$$

$$\frac{D_1}{I_{zzo}} - \frac{D_2}{I_{zze}} = 0 \, . \tag{3.62}$$

The sum mode mismatch error mechanism is completely described in the Laplace domain by (3.51). The error is a function of the frequency of T_d. With

$$T_d \triangleq T \sin \Omega t \, . \tag{3.63}$$

the angular difference expressed by (3.60) may be written

$$(\theta_o - \theta_e) = \frac{T\Omega}{I_c} \frac{\frac{1}{I_{zzo}}[D_1 s + K_1] - \frac{1}{I_{zze}}[D_2 s + K_2]}{(s^2 + \Omega^2)\left(s^2 + \frac{\omega_o}{Q} s + \omega^2\right)\left(s^2 + \frac{\beta_o}{Q_\beta} s + \beta_o^2\right)} \tag{3.64}$$

Multiplication of both sides of (3.64) by K_0 and transformation back to the time domain yields

$$\epsilon_{sM} = \frac{K_0 T\Omega}{I_c} \left\{ \begin{array}{l} 2|A_1| \cos\left\{\Omega t + \sin^{-1}\left(\frac{I_m A_1}{|A_1|}\right)\right\} \\ +2|A_3| e^{-\omega_o t/2Q} \cos\left\{\omega_o t + \sin^{-1}\left(\frac{I_m A_3}{|A_3|}\right)\right\} \\ +2|A_5| e^{-\beta_o t/2Q\beta} \cos\left\{\beta_o t + \sin^{-1}\left(\frac{I_m A_5}{|A_5|}\right)\right\} \end{array} \right\} \tag{3.65}$$

where A_1, the undamped forced term is of primary interest.

$$A_1 \triangleq \left.\frac{\left(\frac{D_1}{I_{zzo}} - \frac{D_2}{I_{zze}}\right)s + \left(\frac{K_1}{I_{zzo}} - \frac{K_2}{I_{zze}}\right)}{(s+j\Omega)\left(s^2 + \frac{\omega_o}{Q}\, s+\omega^2\right)\left(s^2 + \frac{\beta_o}{Q_\beta}\, s + \beta_o^2\right)}\right|_{s=+j\Omega} . \tag{3.66}$$

The damped natural behavior is described by

$$A_3 \triangleq \left.\frac{\left(\frac{D_1}{I_{zzo}} - \frac{D_2}{I_{zze}}\right) s + \left(\frac{K_1}{I_{zzo}} - \frac{K_2}{I_{zze}}\right)}{(s^2+\Omega^2)\left(s + \frac{\omega_o}{2Q} + j\omega_o u_o\right)\left(s^2 + \frac{\beta_o}{Q_\beta}\, s + \beta_o^2\right)}\right|_{s=-\frac{\omega_o}{2Q}+j\omega_o u_o} \tag{3.67}$$

and

$$A_5 \triangleq \left.\frac{\left(\frac{D_1}{I_{zzo}} - \frac{D_2}{I_{zze}}\right) s + \left(\frac{K_1}{I_{zzo}} - \frac{K_2}{I_{zze}}\right)}{(s^2+\Omega^2)\left(s^2 + \frac{\omega_o}{Q}\, s+\omega_o^2\right)\left(s + \frac{\beta_o}{2Q_\beta} + j\beta_o u_\beta\right)}\right|_{s=-\frac{\beta_o}{2Q_\beta}+j\beta_o u_\beta} \tag{3.68}$$

and

$$u_o \triangleq \left[1 - \frac{1}{4Q^2}\right]^{\frac{1}{2}} \tag{3.69}$$

$$u_\beta \triangleq \left[1 - \frac{1}{4Q_\beta^2}\right]^{\frac{1}{2}} \tag{3.70}$$

Equations (3.61) through (3.68) indicate that differences in pivot damping, pivot compliance, and arm moment of inertia all contribute to an error in the RGG output through the sum mode error mechanism. At the lower frequencies, pivot compliance and moment of inertia relationships dominate the output error. As the forcing frequency increases, the difference in pivot damping coefficients contributes to the output error as a linear function of the forcing frequency. Near the instrument $2\omega_s$

signal frequency, the dominant contributor to the sum mode mismatch error continues to be pivot compliance related. The damping coefficient contribution to RGG output error is small compared to the contribution from the pivot compliance terms for frequencies below 1000 rad/sec. Nominal values for pivot compliance are specified in Table II-1. It is necessary that $[K_1/I_{zzo} - K_2/I_{zze}]$ be minimized in order to minimize RGG output error due to sum mode mismatch at the $2\omega_s$ signal frequency. Close manufacturing tolerances will be required regarding pivot as well as arm symmetry.

B-7 Arm Anisoelastic Error Torque, ϵ_A

The elastic nature of the proof mass arms produces a differential torque about $\hat{z}_s$ which, for a single arm, may be written as

$$\bar{T} = \bar{r} \times \bar{F} . \tag{3.77}$$

If $\vec{r}$ is due to the elastic strain in the arm induced by $\vec{F}$,

$$\bar{T} = [\bar{F} \cdot \bar{\bar{\psi}}] \times \bar{F} , \tag{3.72}$$

where $\bar{F}$ is an inertia force, and $\bar{\bar{\psi}}$ is the arm compliance tensor. In terms of odd and even arm mass, compliance, and acceleration

$$\bar{\Delta T} = M_o^2[a_i \psi_{ij}]_o \times \bar{a}_o - M_e^2[a_i \psi_{ij}]_e \times \bar{a}_e . \tag{3.73}$$

Then

$$\epsilon_A = \bar{\Delta T} \cdot \hat{z}_s \tag{3.74}$$

or, in terms of arm mass, compliance tensor, platform accelerations, and instrument rotation angle θ,

$$
\begin{aligned}
\mathbf{C}_A = & \left\{M_o^2(\psi_{11}-\psi_{22})_o - M_e^2(\psi_{11}-\psi_{22})_e\right\}\left\{\begin{array}{l}\frac{1}{2}[a_{yp} - (a_{xp}-g)^2\sin 2\theta \\ +(a_{xp}-g)a_y \cos 2\theta\end{array}\right\} \\
& + [M_o^2(\psi_{13})_o - M_e^2(\psi_{13})_e]\,[a_{yp}\cos\theta - (a_{xp}-g)\sin\theta]a_z \\
& - [M_o^2(\psi_{23})_o - M_e^2(\psi_{23})_e][(a_{xp}-g)\cos\theta + a_{yp}\sin\theta]a_z \\
& + [M_o^2(\psi_{12})_o - M_e^2(\psi_{12})_e]\left\{\begin{array}{l}(a_{yp}^2 - (a_{xp}-g)^2\cos 2\theta \\ -2(a_{xp}-g)a_{yp}\sin 2\theta\end{array}\right\} .
\end{aligned}
\tag{3.75}
$$

The instrument spin axis is assumed normal to the local gravity vector $\vec{g}$ in (3.75).

B-8 Spin/Elastic Axis Displacement

The effect of spin/elastic axis angular misalignment upon the RGG output error was considered in Sect. B-4. *A general representation of* spin/elastic axis *non*-coincidence requires that the elastic axis be displaced from the spin axis as well as rotated with respect to it. The case of general non-coincidence is shown in Fig. III-4. In the general case of non-coincidence, no point which lies along the pivot elastic axis also lies along the spin axis. The general case of non-coincidence can, to first order, be separated into two error forms:

(1) The case where the origin of the spin and elastic reference systems are coincident but where one system is rotated about a small angle vector χ with respect to the other. This case was treated in Sect. B-4;

(2) The case where the elastic axis is parallel to but displaced from the spin axis. This case is treated here.

Consider the end view of the RGG low compliance pivot shown in Fig. III-5.

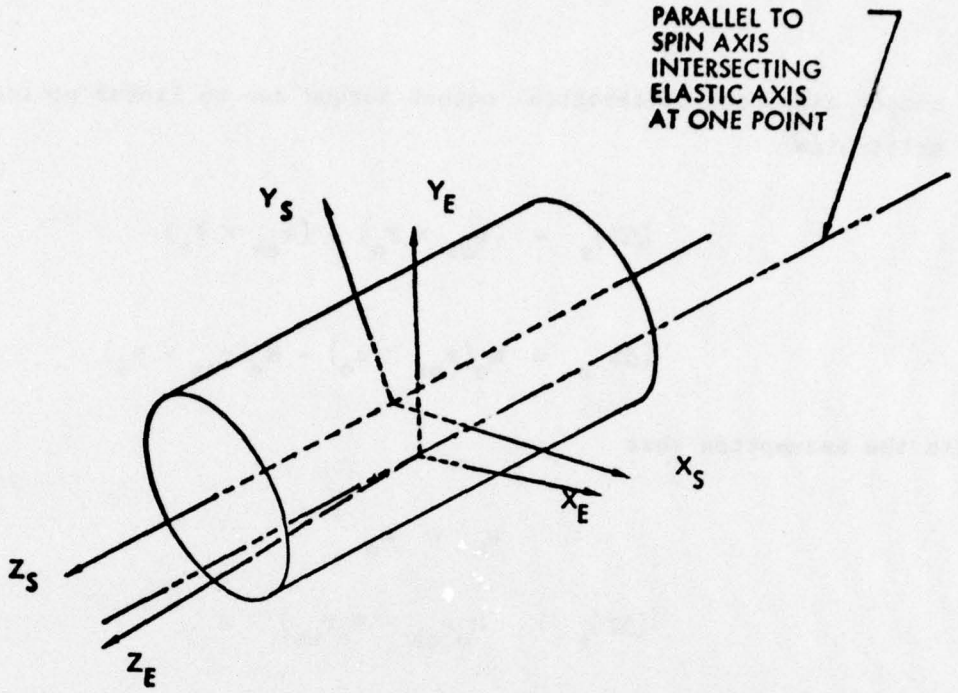


FIG. III-4 GENERAL CASE OF NON-COINCIDENCE BETWEEN THE SENSOR SPIN AND ELASTIC AXES.

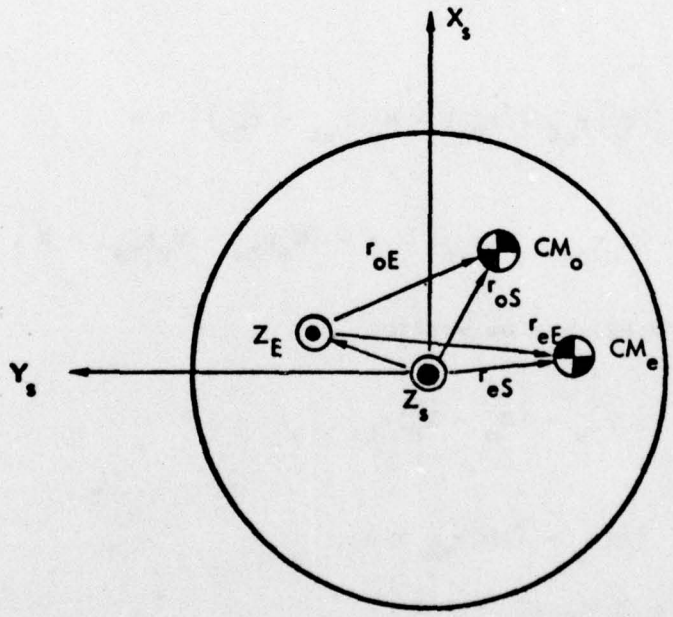


FIG. III-5 END VIEW OF RGG CENTRAL PIVOT SHOWING PARALLEL BUT DIS DISPLACED SPIN ($\hat{z}_S$) AND ELASTIC ($\hat{z}_E$) AXES.

In sensor axes, the differential output torque due to linear motion may be written as

$$[\Delta T]_s = (r_{os} \times F_o) - (r_{es} \times F_e) \tag{3.76}$$

or

$$[\Delta T]_s = M_o(r_{os} \times a_o) - M_e(r_{es} \times a_e) \tag{3.77}$$

With the assumption that

$$a_o = a_e \tag{3.78}$$

$$[\Delta T]_s = (M_o r_{os} - M_e r_{es}) \times a \ . \tag{3.79}$$

Similarly, in the elastic reference system,

$$[\Delta T]_E = (M_o r_{oE} - M_e r_{eE}) \times a \ . \tag{3.80}$$

Using Fig. III-5,

$$[\Delta T]_E = [M_o(r_{os} - r_{Es}) - M_e(r_{es} - r_{Es})] \times a \tag{3.81}$$

or

$$[\Delta T]_E = [M_o r_{os} - M_e r_{es}] \times a - [M_o r_{Es} - M_e r_{Es}] \times a \ . \tag{3.82}$$

In terms of ΔT_s, (3.82) may be written

$$[\Delta T]_E = [\Delta T]_s - (M_o' - M_e) r_{Es} \times a \tag{3.83}$$

or

$$[\Delta t]_E = [\Delta T]_s - (\Delta M) r_{Es} \times a \ . \tag{3.84}$$

In matrix form, (3.84) is

$$[\Delta T]_E = \begin{bmatrix} [\Delta(M\rho_y) - (\Delta M)r_{Esy}]a_z - [\Delta(M\rho_z) - (\Delta M)r_{Esz}]a_y \\ [\Delta(M\rho_z) - (\Delta M)r_{Esz}]a_x - [\Delta(M\rho_x) - (\Delta M)r_{Esx}]a_z \\ [\Delta(M\rho_x) - (\Delta M)r_{Esx}]a_y - [\Delta(M\rho_y) - (\Delta M)r_{Esy}]a_x \end{bmatrix} \quad (3.85)$$

The $(\Delta M)r_{ES}$ terms in the third component of (3.85) represent the effect of spin/elastic axis displacement on RGG output due to linear instrument excitation

The effect of non-principal axis spin and mass center offset is considered in Sect. B-3. Examination of (3.19) indicates that the form of that error equation will not be altered due to redefinition of the mass center terms (from sensor to the displaced elastic reference system). Linear displacement of the elastic and spin will have no effect on the form of (3.5). However, the numerical values of the $\Delta(M\rho_i\rho_j)$ terms will be altered.

C. DIFFERENTIAL TORQUE OUTPUT ERROR SUMMARY

The contribution of each of the error sources discussed in Sect. B to the $2\omega_s$ (signal frequency) output torque is presented in Table III-2. Physical and operational summptions required for the analysis are listed in Table III-1.

Table III-1

SENSOR ERROR ANALYSIS INPUT DATA

Parameter	Magnitude	Units
Arm-to-Arm Inertial Ratio Error	1.0×10^{-4}	%
Arm Mass Center Displacement	3.0×10^{-9}	m
Pivot Compliance Mismatch	2.0×10^{0}	%
Pivot Damping Ratio Mismatch	2.0×10^{-2}	%
Spin Motor Torque Error at $2\omega_s$	2.5×10^{-6}	N m
Sensor/Platform Misalignment	5.0×10^{1}	μrad/axis
Elastic/Spin/Principal Axis Misalignment	5.0×10^{1}	μ rad/axis
Maximum Linear Acceleration Error	1.0×10^{-4}	g
Maximum $\hat{x}_s$ or $\hat{y}_s$ Angular Accelerometer Error	1.0×10^{-2}	rad/sec^2
Maximum $\hat{x}_s$ or $\hat{y}_s$ Angular Rate Error	4.5×10^{-5}	rad/sec
Spin Rate Error	2.0×10^{-3}	rad/sec

Table III-2 is a listing of worst case effects of the various dynamics related error sources upon the $2\omega_s$ sensor output signal. Numerical values used as input for the analysis were taken, when available, from manufacturing tolerances [AM-1, AM-2]. The results of Table III-2 indicate that an instrument built to the currently specified tolerances will not achieve sub- 1 EU performance. These manufacturing errors

represent state of the art assembly techniques. It is apparent that error compensation will be required. Two forms of compensation are available: numerical output correction and active parameter control. Both techniques are considered in subsequent chapters.

Table III-2

DYNAMICALLY INDUCED ERRORS AT $2\omega_s$

Error Source	Output Torque Magnitude (N m)
1 EU Torque Level	3.56×10^{-12}
Spin Axis Angular Acceleration (rigid body)	1.57×10^{-9}
Transverse Angular Acceleration	3.65×10^{-11}
Transverse Angular Velocity	3.65×10^{-13}
Mass Center Error (rotation)	3.40×10^{-13}
Mass Center Error (linear acceleration)	3.13×10^{-11}
Sum Mode Mismatch	1.37×10^{-8}
Platform/Instrument Misalignment (linear acceleration)	7.80×10^{-18}
Platform/Instrument Misalignment	2.00×10^{-15}
Elastic/Principal/Spin Axis M/A:	
Spin Axis Angular Acceleration	8.90×10^{-14}
Transverse Angular Velocity	3.06×10^{-9}
Anisoelasticity	8.55×10^{-7}

Chapter IV

DEVELOPMENT OF PARAMETERS FOR ESTIMATION

A. INTRODUCTION

The errors discussed in Chapter III represent all known RGG dynamically induced error sources. They were introduced separately in that chapter to provide an intuitive justification for their inclusion in the error equation. In this chapter, a unified approach to the kinematically induced error equation is developed. A quasi-steady error model is derived for low frequency inputs which is used in Chapter VI for parameter identification.

The errors which arise in RGG output are the result of manufacturing and assembly imperfections. By developing a model of instrument output as a function of dynamic input, it is possible to estimate (or identify) the imperfect instrument parameters through input-output relationships. If it is subsequently possible to "trim" the parameters to some desired values, the quality of the output signal can be improved.

B. ERROR EQUATION DEVELOPMENT

A schematic drawing of the Hughes RGG is shown in Fig. IV-1. Under ideal conditions, the elastic axis $\hat{e}$ coincides with the spin axis $\hat{s}$ so that the vector $\vec{\mu}$ is zero. The angular velocity of the odd arm with respect to an inertial reference frame may be written as

$$\vec{\omega}^{o-i} = \vec{\omega}^{o-r} + \vec{\omega}^{r-c} + \vec{\omega}^{c-i} \quad . \tag{4.1}$$

The terms on the right side of (4.1) represent arm motion relative to the rotor (θ, $\dot{\theta}$, etc.), rotor motion relative to the case (spin), and case motion relative to inertial space (jitter or programmed input). The equation of motion for the odd arm may be written as

PRECEDING PAGE BLANK-NOT FILMED

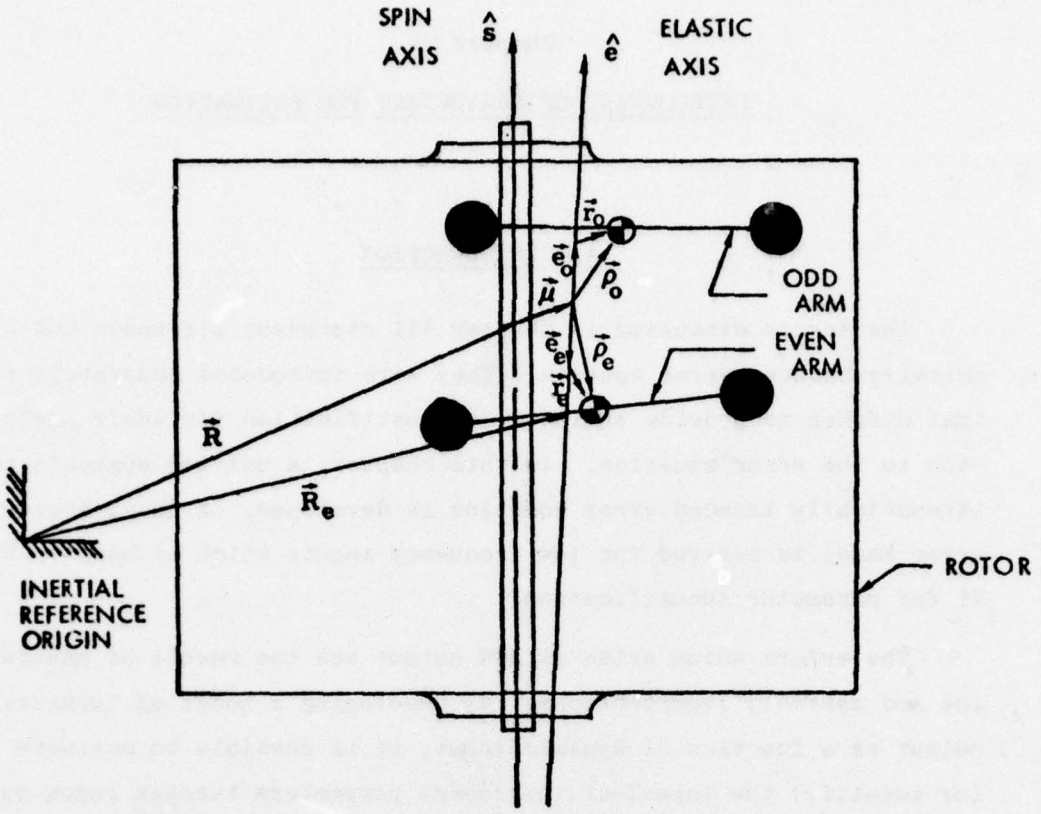


FIG. IV-1 SCHEMATIC DRAWING OF HUGHES ROTATING GRAVITY GRADIOMETER.

$$I_o \cdot \overset{oo}{\omega} + \omega_o \times I_o \cdot \omega_o = T_o - m_o r_o \times \overset{II}{R}_o - [m_o \overset{II}{R} \cdot \overline{\overline{\psi}}_o] \times [m_o \overset{II}{R}_o - \overline{\overline{K}}_{YSO}] - \overset{II}{R}_o \cdot \tag{4.2}$$

Equation 4.2 is the odd arm Euler equation. The left side of the equation represents the time rate of change of arm angular momentum with respect to inertial space. The first term on the right represents the applied torques, e.g., torques due to gravity and springs. The second term on the right side of (4.2) represents torques due to arm linear acceleration and mass center offset. The third represents torques due to arm compliance and linear acceleration. The fourth term on the right

side of (4.2) represents acceleration-torsional coupling compliance. The tensor $\bar{\bar{K}}_{yso}$ is assumed diagonal. T_o is expanded in (4.3).

$$T_o = -[K_1\theta^{o-r} + K_o\theta^{o-e}]\hat{e} + T_{go} + T_{do} \; . \tag{4.3}$$

The first term is the result of pivot elasticity; the second term the result of gravity acting on the arm; and the third term is due to disturbance torques. T_{go} represents the torques exerted on the odd arm by the gravity gradient.

Expanding (4.2),

$$\left.\begin{aligned} & I_o \cdot \overset{o}{\omega}{}^{o-r} + \omega^{o-r} \times I_o \cdot \omega^{o-r} \\ & + \omega^{o-r} \times I_o \cdot [\omega^{r-c} + \omega^{c-i}] \\ & + [\omega^{r-c} + \omega^{c-i}] \times I_o \cdot [\omega^{o-r}] \end{aligned}\right\} = \begin{aligned} & T^o - I_o \cdot [\overset{o}{\omega}{}^{r-c} + \overset{o}{\omega}{}^{c-i}] \\ & -[\omega^{r-c}+\omega^{c-i}] \times I_o \cdot [\omega^{r-c}+\omega^{c-i}] \\ & -m_o r_o \times [\ddot{R} + \ddot{\mu} + \ddot{e}_o + \ddot{r}_o] \\ & -[m_o \ddot{R}_o \cdot \psi_o] \times m_o \ddot{R}_o - \bar{\bar{K}}_{YSO} \cdot \ddot{R}_o \; . \end{aligned} \tag{4.4}$$

The vectors $\vec{\mu}$, $\vec{e}$, and $\vec{r}$ are fixed within the odd arm reference frame. Hence,

$$(\mu + e_o + r_o) = \left\{\begin{aligned} & \omega^{o-i} \times r_o + \omega^{o-i} \times [\omega^{o-i} \times r_o] \\ & +\overset{o}{\omega}{}^{r-i} \times (\mu + e_o) + \omega^{r-i} \times [\omega^{r-i} \times (\mu + e_o)] \end{aligned}\right\} \tag{4.5}$$

and (4.4) may be rewritten as

$$\begin{aligned} & I_o \cdot \overset{o}{\omega}{}^{o-r} + \omega^{o-r} \times I_o \cdot \omega^{o-r} + \omega^{o-r} \times I_o \cdot \omega^{r-i} + \omega^{r-i} \times I_o \cdot \omega^{o-r} \\ & + m_o r_o \times (\overset{o}{\omega}{}^{o-r} \times r) + m_o r_o \times [\omega^{o-r} \times (\omega^{o-r} \times r_o)] \\ & + m_o r_o \times [\omega^{o-r} \times (\omega^{r-i} \times r_o)] + m_o r_o \times [\omega^{r-i} \times (\omega^{o-r} \times r_o)] \end{aligned} \tag{4.6}$$

where

$$
\begin{aligned}
A'_{odd} = \quad & T_o - I_o \cdot {}^{o}\omega^{r-i} - [\omega^{r-c} + \omega^{c-i}] \times I_o \cdot [\omega^{r-c} + \omega^{c-i}] \\
& - m_o r_o \times \bar{a} - [m_o \bar{a} \cdot \bar{\bar{\psi}}_o] \times m_o \bar{a} - K_{YSO} \cdot \bar{a} \\
& - m_o r_o \times [{}^{o}\omega^{o-i} \times r_o + {}^{o}\omega^{r-i} \times (\mu_o + e_o)] \\
& - m_o r_o \times [\omega^{o-i} \times (\omega^{o-i} \times r_o)] - m_o r_o \times \{\omega^{r-i} \times (\omega^{r-i} \times (\mu + e_o))\}
\end{aligned}
\tag{4.7}
$$

and

$$
\bar{a} = \vec{\vec{R}}_o - \vec{g} \, . \tag{4.8}
$$

In the odd arm elastic reference frame

$$
\omega^{o-r} = [0, \; 0, \; \dot{\theta}_o]^T \quad \triangleq \quad [\dot{\theta}_o] \, , \tag{4.9}
$$

$$
\omega^{r-c} = [\delta_1, \; \delta_2, \; \delta_3 + \omega_s]^T \quad \triangleq \quad [\omega_s] \, , \tag{4.10}
$$

$$
\omega^{c-i} = [\omega_x, \; \omega_y, \; \omega_t]^T \quad \triangleq \quad [\omega] \, , \tag{4.11}
$$

where ω_s is the nominal spin rate. Equation 4.10 is an expression of the spin rate in odd arm elastic axes. The first and second components are the result of the misalignment between the spin and elastic axes. Using the definitions of (4.9) to (4.11), and with

$$
[\Lambda] \triangleq [\omega] + [\omega_s] \, , \tag{4.12}
$$

(4.6) may be written as

$$
\left\{ \begin{array}{l} I_o \cdot \ddot{\theta}_o + \dot{\theta}_o \times I_o \cdot \dot{\theta} \\ \quad + \dot{\theta} \times I_o \cdot \Lambda + \Lambda \times I_o \cdot \dot{\theta} \end{array} \right\} = A'_{odd} \, . \tag{4.13}
$$

Similarly, the right side of (4.6) may be written as

$$
\begin{aligned}
A'_{odd} = {} & T^{o} - \Lambda \times I_o \cdot \Lambda - I_o \cdot \dot{\Lambda} - m_o r_o \times a \\
& -[m_o a \cdot \bar{\bar{\Psi}}_o] \times m_o a - m_o r_o \times [(\ddot{\theta} + \dot{\Lambda}) \times r_o] \\
& -m_o r_o \times [\dot{\Lambda} \times (\mu + e_o)] - \bar{\bar{K}}_{YSo} \cdot a \\
& -m_o r_o \times [(\dot{\theta} + \Lambda) \times [(\dot{\theta} + \Lambda \times r_o)] \\
& -m_o r_o \times [\Lambda \times (\Lambda \times (\mu + e_o))] \, .
\end{aligned}
\tag{4.14}
$$

Rearranging terms and substituting the dot product identity for the vector triple product yields

$$
\begin{aligned}
A'_{odd} = {} & T_o - \Lambda \times I_o \cdot \Lambda - I_o \cdot \dot{\Lambda} - m_o r_o \times a \\
& -[m_o a \cdot \bar{\bar{\Psi}}_o] \times m_o a - \bar{K}_{YSo} \cdot a \\
& -m_o (r_o \cdot r_o)\ddot{\theta} - m_o [(r_o \cdot r_o)\dot{\Lambda} - (r_o \cdot \dot{\Lambda}) r_o] \\
& -m_o [(r_o \cdot (\mu + e_o)]\dot{\Lambda} - (r_o \cdot \dot{\Lambda})(\mu + e)] \\
& -m_o r_o \times (\Lambda \cdot r_o)\dot{\theta} - m_o r_o \times (\Lambda \cdot r_o)\Lambda \\
& -m_o r_o \times [(\Lambda \cdot (\mu + e_o)]\Lambda - (\Lambda \cdot \Lambda)(\mu + e_o)] \, .
\end{aligned}
\tag{4.15}
$$

Substituting (4.3) and (4.15) into (4.13), and moving the ϑ, $\dot{\theta}$, and $\ddot{\vartheta}$ dependent terms to the left side of the equation yields

$$
\left.
\begin{aligned}
& I_o \cdot \ddot{\theta}_o + \dot{\theta}_o \times I_o \dot{\theta}_o \\
& + \dot{\theta}_o \times I_o \cdot \Lambda + \Lambda \times I_o \cdot \dot{\theta} \\
& + m_o (r_o \cdot r_o)\ddot{\theta} - m_o r_o \\
& \times (\Lambda \cdot r_o)\dot{\theta} + K_1 \theta
\end{aligned}
\right\} =
\begin{aligned}
& -K_0 \theta^{o-e} + T_{go} + T_{do} - \Lambda \times I_o \cdot \Lambda - I_o \cdot \dot{\Lambda} \\
& -m_o r_o \times a - [m_o a \cdot \bar{\bar{\Psi}}_o] \times m_o a - \bar{\bar{K}}_{YSo} \cdot a \\
& -m_o (r_o \cdot r_o)\dot{\Lambda} + m_o (r_o \cdot \dot{\Lambda}) r_o \\
& -m_o [r_o \cdot (\mu + e_o)]\dot{\Lambda} + m_o (r_o \cdot \dot{\Lambda})(\mu + e_o) \\
& -m_o r_o \times (\Lambda \cdot r_o)\Lambda - m_o r_o \times [\Lambda \cdot (\mu + e_o)]\Lambda \\
& +m_o r_o \times (\Lambda \cdot \Lambda)(\mu + e_o) \, .
\end{aligned}
\tag{4.16}
$$

With

$$A_{odd} \triangleq A'_{odd} + m_o(r_o \cdot r_o)\ddot{\theta} + m_o r_o \times[(\Lambda \cdot r_o)\theta] + K_0\dot{\theta}^{o-e} \quad . \tag{4.17}$$

(4.16) may be written as

$$\left.\begin{aligned} &[I_o + m_o(r_o \cdot r_o)]\ddot{\theta} + \dot{\theta} \times I_o \cdot \dot{\theta} \\ &+ \dot{\theta} \times I_o \cdot \Lambda + \Lambda \times I_o \cdot \dot{\theta} \\ &-m_o r_o \times (\Lambda \cdot r_o)\dot{\theta} + K_1\theta \end{aligned}\right\} = -K_0\theta^{o-e} + A_{odd} \quad . \tag{4.18}$$

Neglecting the term in (4.18) which is nonlinear in θ (it will be 2nd order small), and taking the component of (4.18) along $\hat{e}$ yields the scalar output axis torque equation as given in (4.19).

$$\begin{aligned} &[I_o + m_o r_o^2]\ddot{\theta} + [\Lambda \times I_o - I_o \cdot \Lambda \times \hat{e}] \cdot \hat{e}\dot{\theta} + K_1\theta \\ &= -K_0\theta^{o-e} + A_{odd} \cdot \hat{e} \ ; \end{aligned} \tag{4.19}$$

$$I_o + m_o(r_o \cdot r_o) \triangleq \mathcal{I}_o \tag{4.20}$$

$$\hat{e} \cdot [\Lambda \times I_o - I_o \cdot \Lambda \times \hat{e} - m_o r_o(\Lambda \cdot r_o) \times \hat{e}] \triangleq B_o \tag{4.21}$$

$$\theta + \frac{B_o\theta}{\mathcal{I}_o} + \frac{K_1\theta}{\mathcal{I}_o} = -\frac{K_0\theta^{o-e}}{\mathcal{I}_o} + \frac{A_{odd}}{\mathcal{I}_o} \cdot \hat{e} \quad . \tag{4.22}$$

With definitions (4.20) and (4.21), (4.19) may be rewritten as (4.22). In the Laplace domain, (4.22) may be written as

$$\left[s^2 + \frac{B}{\mathcal{I}_o}s + \frac{K_1}{\mathcal{I}_o}\right]\theta^{o-r} = -\frac{K_0\theta^{o-e}}{\mathcal{I}_o} + \frac{\hat{e} \cdot A_{odd}(s)}{\mathcal{I}_o} \tag{4.23}$$

and hence

$$\theta^{o-r} = \frac{-\left(\frac{K_o}{\mathcal{I}_o}\right)\theta^{o-e} + \frac{\hat{e} \cdot A_{odd}(s)}{\mathcal{I}_o}}{\left[s^2 + \frac{B}{\mathcal{I}_o}\, s + \frac{K_1}{\mathcal{I}_o}\right]} \tag{4.24}$$

Following an identical development for θ^{e-r}, the change in orientation of the even arm with respect to the rotor θ^{e-r} may be expressed as

$$\theta^{e-r} = \frac{\left(\frac{K_o}{\mathcal{I}_o}\right)\theta^{o-e} + \frac{\hat{e} \cdot A_{even}(s)}{\mathcal{I}_o}}{\left[s^2 + \frac{B_e}{\mathcal{I}_e}\, s + \frac{K_2}{\mathcal{I}_e}\right]} \tag{4.25}$$

Since

$$\theta^{o-e} = \theta^{o-r} - \theta^{e-r}, \tag{4.26}$$

(4.24) and (4.25) can be combined to yield

$$\left[1 + \frac{K_o/\mathcal{I}_o}{s^2 + \frac{B_o s}{\mathcal{I}_o} + \frac{K_1}{\mathcal{I}_o}} + \frac{K_o/\mathcal{I}_e}{s^2 + \frac{B_e s}{\mathcal{I}_e} + \frac{K_2}{\mathcal{I}_o}}\right]\theta^{o-e}(s)$$

$$= \frac{\hat{e} \cdot A_{odd}(1/\mathcal{I}_o)}{s^2 + \frac{B_o s}{\mathcal{I}_o} + \frac{K_1}{\mathcal{I}_o}} - \frac{\hat{e} \cdot A_{even}(1/\mathcal{I}_e)}{s^2 + \frac{B_e s}{\mathcal{I}_e} + \frac{K_2}{\mathcal{I}_e}}. \tag{4.27}$$

Letting s approach zero to form a steady state expression for θ^{o-e},

$$\theta^{o-e} = \left\{\frac{1}{1 + \frac{K_o}{K_1} + \frac{K_o}{K_2}}\right\}\left\{\frac{\hat{e} \cdot A_{odd}}{K_1} - \frac{\hat{e} \cdot A_{even}}{K_2}\right\} \tag{4.28}$$

or

$$\theta^{o-e} = \left\{ \frac{1/K_1}{1 + \frac{K_o}{K_1} + \frac{K_o}{K_2}} \right\} \left\{ A_{odd} - \left[1 - \left(\frac{K_1}{K_2} - 1 \right) \right] A_{even} \right\} \cdot \hat{e} . \quad (4.29)$$

Equation 4.29 is the equation which relates the steady state rotation of one sensor arm with respect to the other. For small strains, it is linearly related to the piezoelectric crystal output signal and is, with minor modifications, the sensor signal equation used for this analysis. Note that for an instrument which is ideally tuned, the second term in braces on the right side of (4.29) reduces simply to $\{A_{odd} - A_{even}\}$. The steady state approximation is used in Ch. VI as the basis for parameter identification. The input frequencies for which this approximation is valid are discussed in Sect. IV-D.

B.1 Output Equation Simplification

In order to write (4.29) in a form which could be used to develop a method of parameter estimation, three simplifying assumptions were made. These assumptions did not significantly alter the form of (4.29), nor did they alter the approach to parameter estimation. The assumptions which were made are:

1. The coefficient $\{1/K_1[1 + (K_o/K_1) + (K_o/K_2)]^{-1}\}$ which appears on the right side of (4.29) was assumed constant. The remaining term is the effective torque which produces the output signal. With the additional assumption of a linear relationship between differential torque and transducer output, this torque is proportional to the output expressed in (4.29) and can be referred to as the sensor output without altering component relative magnitudes. Compliance tuning, i.e., matching K_1 and K_2 is discussed in Ch. VI;

2. The disturbance torque terms T_{do} and T_{de} were negligible. The arms of the RGG are case-enclosed. Random disturbance torques acting upon the individual arms can be expected to be constrained to relatively low magnitude by adjusting the test signal level. Systematic but non-dynamics related torques could occur at the $2\omega_s$ frequency. Due to high instrument Q

(gain near $2\omega_s$) it is necessary that test signals be constrained to relatively low frequency. Thermal and magnetic gradients, which were not included within this study could contribute to the instrument output at the signal frequency. Unexplained error sources encountered during hardware testing should be evaluated with acknowledgment given to these unmodeled sources;

3. The sensor spin and elastic axes are coincident. This assumption simplifies the definition of the OEP but does not reduce the number of them. The distinction between these two axes is included in Sect. B-2 where the significance of the assumption is discussed.

Given the above assumptions,

$$[\vec{\mu}_o] = [0, 0, 0]^T \tag{4.30}$$

$$[\vec{e}_o] = [0, 0, \rho_{zo}]^T \tag{4.31}$$

$$[\vec{r}_o] = [\rho_{xo}, \rho_{yo}, 0]^T \quad . \tag{4.32}$$

Substitution of these definitions in (4.15) yields

$$\begin{aligned} A_{odd}\,\hat{e} = {} & -[I_{xzo} - m_o\rho_{xo}\rho_{zo}]\omega_x - [I_{yzo} - m_o\rho_{yo}\rho_{zo}]\omega_y \\ & -[I_{zzo} + m_o(\rho_{xo}^2 + \rho_{yo}^2)]\omega_z - [I_{xyo} - m_o\rho_{xo}\rho_{yo}](\omega_x^2 - \omega_y^2) \\ & -[(I_{xxo} - I_{yyo}) + m_o(\rho_{xo}^2 - \rho_{yo}^2)]\omega_x\omega_y - [I_{yzo} - m_o\rho_{yo}\rho_{zo}]\omega_x\omega_z \\ & +[I_{xzo} - m_o\rho_{xo}\rho_{zo}]\omega_y\omega_z - m_o\rho_{xo}a_y + m_o\rho_{yo}a_x - K_{YSo}a_z \\ & -m_o^2(\psi_{110} - \psi_{220})a_x a_y - m_o^2\psi_{130}a_y a_z \\ & +m_o^2\psi_{230}a_x a_z - m_o^2\psi_{120}(a_y^2 - a_x^2) \quad . \end{aligned} \tag{4.33}$$

With

$$\Delta[I_{ij} - m\rho_n\rho_p] \triangleq I_{ijo} - \left(\frac{K_1}{K_2}\right) I_{ije} + m_o\rho_{no}\rho_{po} - \left(\frac{K_1}{K_2}\right) m_e\rho_{ne}\rho_{pe}, \tag{4.34}$$

$$\Delta(m\rho_i) \triangleq m_o\rho_{io} - \left(\frac{K_1}{K_2}\right) m_e\rho_{ie} \tag{4.35}$$

$$\Delta(m^2\psi_{ij}) \triangleq m_o^2\psi_{ijo} - \left(\frac{K_1}{K_2}\right) m_e^2\psi_{ije}, \tag{4.36}$$

Equation 4.29 can be written

$$\begin{aligned}\theta^{o-e} = {} & \left\{\frac{1/K_1}{1 + \frac{K_0}{K_1} + \frac{K_0}{K_2}}\right\}\left\{T_{do} - \frac{K_1}{K_2} T_{de}\right\} - \left\{\frac{1/K_1}{1+\frac{K_0}{K_1} + \frac{K_0}{K_2}}\right\}\Delta[I_{xz} - m\rho_x\rho_z]\omega_x \\ & + \Delta(I_{yz} - m\rho y\rho_z]\omega_y \\ & + \Delta(I_{zz} + m(\rho_x^2 + \rho_y^2)]\omega_z \\ & + \Delta[I_{xy} - m\rho_x\rho_y](\omega_x^2 - \omega_y^2) \\ & + \Delta[(I_{xx} - I_{yy}) + m(\rho_x^2 - \rho_y^2)]\omega_x\omega_y \\ & + \Delta[I_{yz} - m\rho_y\rho_x]\omega_x\omega_z \\ & - \Delta[I_{xz} - m\rho_x\rho_z]\omega_y\omega_z \\ & + \Delta[m\rho_x]a_y - \Delta[m\rho_y]a_x + \Delta[K_{YX}]a_z \\ & + \Delta[m^2(\psi_{11} - \psi_{22})]a_x a_y \\ & + \Delta[m^2\psi_{13}]a_y a_x - \Delta[m^2\psi_{23}]\, a_x a_z \\ & + \Delta[m^2\psi_{12}](a_y^2 - a_x^2)\end{aligned} \tag{4.37}$$

The disturbance torques T_{do} and T_{de} discussed in assumption 2 appear in (4.37). The torques effecting the odd arm will be equal to those acting on the even arm. Hence, for an ideally tuned instrument, this error does go to zero. This error is critical to definition of compliance matching requirements. Note also that the gravity gradient terms have been omitted from (4.37).

Upon elimination of the disturbance torque terms and multiplication of both sides of (4.37) by K_0, the low compliance pivot stiffness, differential output torque error equation (4.38) is formed. This was the equation used to define the parameters to be identified and controlled. In subsequent chapters, it is shown that estimation of these parameters can be mechanized as an online process. These estimates are used as a feedback command to control (correct) the parameters.

$$\epsilon = -\frac{\frac{K_0}{K_1}}{1+\frac{K_0}{K_1}+\frac{K_0}{K_2}} \left\{ \begin{array}{l} \Delta[I_{xz}-m\rho_x\rho_z]\dot{\omega}_x + \Delta[I_{yz}-m\rho_y\rho_z]\dot{\omega}_y \\ + \Delta[I_{zz}+m(\rho_x^2+\rho_y^2)]\dot{\omega}_z + \Delta[I_{xy}-m\rho_x\rho_y](\omega_x^2-\omega_y^2) \\ + \Delta[(I_{xx}-I_{yy}) + m(\rho_x^2-\rho_y^2)]\omega_x\omega_y + \Delta[I_{yz}-m\rho_y\rho_z]\omega_x\omega_z \\ - \Delta[I_{xz}-m\rho_x\rho_z]\omega_y\omega_z + \Delta[m\rho_x]a_y - \Delta[m\rho_y]a_x + \Delta[K_{YS}]a_z \\ + \Delta[m^2(\psi_{11}-\psi_{22})]a_xa_y + \Delta[m^2\psi_{13}]a_ya_z - \Delta[m^2\psi_{23}]a_xa_z \\ + \Delta[m^2\psi_{12}](a_y^2 - a_x^2) \end{array} \right. \tag{4.38}$$

The coefficients of the dynamic forcing terms in (4.38) are defined as the Output Effective Parameters (OEPs). These are the terms which bring about errors in the RGG output signal. In order to drive the error torque, ρ, to zero it is only necessary to force the OEPs to zero. It is not required that the individual physical parameters such as I_{xz}, ρ_z, etc. be driven to nominal values. Alternatively, if all the OEPs can be identified, if all the dynamic forcing terms are known exactly, and if the error

equation contains all significant error terms, the RGG output can be compensated numerically without active control. The output effective parameters which result from (4.38) are listed in Table IV-1.

Table IV-1

OUTPUT EFFECTIVE PARAMETERS FOR THE CASE WHERE SPIN/ELASTIC AXIS MISALIGNMENTS

Parameter	Definition	Typical Value
P_1	$\Delta(I_{xz} - m\rho_x\rho_z)$	10^{-8} kg m^2
P_2	$\Delta(I_{yz} - m\rho_y\rho_z)$	10^{-8} kg m^2
P_3	$\Delta[I_{zz} + m(\rho_x^2 + \rho_y^2)]$	10^{-7} kg m^2
P_4	$\Delta[I_{xy} - m\rho_x\rho_y]$	10^{-8} kg m^2
P_5	$\Delta[I_{yy} - I_{xx} + m(\rho_x^2 - \rho_y^2)]$	6.12×10^{-3} kg m^2
P_6	$\Delta[I_{yz} - m\rho_y\rho_z]$	10^{-8} kg m^2
P_7	$-\Delta[I_{xz} - m\rho_x\rho_z]$	-10^{-8} kg m^2
P_{11}	$\Delta(M\rho_x)$	10^{-8} kg m
P_{12}	$-\Delta(M\rho_y)$	10^{-8} kg m
P_{13}	$\Delta(K_{ys})$	10^{-9} kg m
P_{14}	$\Delta[M^2(\psi_{11} - \psi_{22})]$	5×10^{-10} kg^2 $\frac{m}{N}$
P_{15}	$\Delta(M^2\psi_{13})$	4×10^{-11} kg^2 $\frac{m}{N}$
P_{16}	$\Delta(M^2\psi_{23})$	4×10^{-11} kg^2 $\frac{m}{N}$
P_{17}	$\Delta(M^2\psi_{12})$	5×10^{-13} kg^2 $\frac{m}{N}$

Note from Table IV-1 that P_8, P_9, and P_{10} are undefined. In addition, note that P_6 and P_2, and P_7 and P_1 are the same parameters. P_6 and P_7 were defined so as to provide a completely consistent method for formulating the OSPs with respect to the separate dynamic terms of (4.38). Each separate dynamic forcing term was associated with a separate OEP. These

OEPs become distinct when the elastic and spin axes are non-coincident, as in Sect. B-2. *In the analyses of (4.38) which follow* P_6 *and* P_7 *were* replaced by P_2 and P_1 during the processess of parameter identification and control.

B-2 Inclusion of Spin/Elastic Axis Misalignment Angles

Output equation (4.38) was based upon the assumption of sensor spin axis and elastic axis coincidence. It is likely that these misalignments can be held, during manufacturing, to less than 25 μrad (5 arcsec). It is not likely, however, that the instrument can be assembled with these misalignments constrained to less than the 0.012 arcsec per axis required for 1 E.U. operation (Sect. III-B-4). Even if such manufacturing tolerances were achievable, they could not be expected to be stable within the RGG dynamic environment.

The effect of spin/elastic axis misalignment on RGG as a function of angular acceleration and angular velocity was considered in Sect. III-B-4. These were the major contributors to RGG output due to spin/elastic axis misalignment. Consider the linear acceleration induced output torque errors. For the case where no spin/elastic axis misalignment exists, using assumption 1 of Sect. IV-B-1, the contribution to RGG output due to platform linear acceleration $\vec{a}_p$ is

$$\vec{\Delta T} = \{M_o \vec{\rho}_o - M_e \vec{\rho}_e\} \times \vec{a}_p \tag{4.39}$$

and in the sensor reference system

$$[\vec{\Delta t}]_s = \begin{bmatrix} 0 & -\Delta m\rho_z & \Delta m\rho_y \\ \Delta m\rho_z & 0 & -\Delta m\rho_x \\ -\Delta m\rho_y & \Delta m\rho_x & 0 \end{bmatrix} \begin{bmatrix} a_{xp} \\ a_{yp} \\ a_{zp} \end{bmatrix}_s . \tag{4.40}$$

Given the angular misalignments χ *between the spin and elastic reference* systems as specified in Ch. III-B-4, and given the transformation from

13

spin to the elastic reference system, $C_{E/s}$, as defined by (3.9), (4.40) may be written, in the elastic reference system, as

$$[\vec{\Delta T}]_E = \begin{bmatrix} 1 & 0 & -\chi_y \\ 0 & 1 & \chi_x \\ \chi_y & -\chi_x & 1 \end{bmatrix} \begin{bmatrix} \Delta(m\rho_y)a_z - \Delta(m\rho_z)a_y \\ \Delta(m\rho_z)a_x - \Delta(m\rho_x)a_z \\ \Delta(m\rho_x)a_y - \Delta(m\rho_y)a_x \end{bmatrix}_s , \tag{4.41}$$

and the $\hat{z}_E$ RGG output term is

$$\begin{aligned} [\vec{\Delta T}]_E \cdot \hat{z}_E = {} & \Delta(m\rho_x)a_y - \Delta(m\rho_y)a_x \\ & + \chi_y[\Delta(m\rho_y)a_z - \Delta(m\rho_z)a_y] \\ & - \chi_x[\Delta(m\rho_z)a_x - \Delta(m\rho_x)a_z] \ . \end{aligned} \tag{4.42}$$

Hence, with higher order terms neglected, spin/elastic axis misalignment does not effect the linear acceleration, mass center RGG error terms. A similar development for the RGG compliance related terms yields the same conclusion. Therefore, the only first order effects of spin/elastic axis misalignment on RGG error output occur due to sensor angular acceleration and angular velocity. Equation 3.18 may be written in terms of an incremental output torque as

$$\begin{aligned} [\Delta T_{AM}]_E \cdot \hat{z}_E = {} & \{-\Delta(\xi_y I_{yy}) + \chi_y \Delta I_{xx}\}\dot{\omega}_x \\ & + \{\Delta(\xi_x I_{xx}) - \chi_x \Delta I_{yy}\}\dot{\omega}_y \\ & + \{\Delta(\xi_x I_{xx}) - \Delta(\xi_y I_{yy})\}\dot{\omega}_z + \chi_y \Delta(I_{xx} - I_{yy})\omega_y\omega_z \\ & - \chi_x \Delta(I_{xx} - I_{yy})\omega_x\omega_z + \{\Delta(\xi_x I_{xx}) - \Delta(\xi_y I_{yy})\}\omega_x\omega_y . \end{aligned} \tag{4.43}$$

With spin/elastic axis misalignments included, (4.44) replaced (4.38) as the RGG output signal error equation. Comparison of (4.38) and (4.44) indicates changes only in parameters 1, 2, 6, and 7. When the spin/elastic

misalignment is included, the equalities which existed among these parameters under conditions of spin/elastic axis coincidence are eliminated. Table IV-2 lists a comparison of parameters 1, 2, 6, and 7 under conditions of principal axis coincidence and non-coincidence with the misalignment angles χ both taken to be 25 μrad.

$$\epsilon = -\frac{\frac{K_0}{K_1}}{1 + \frac{K_0}{K_1} + \frac{K_0}{K_2}} \left\{ \begin{array}{l} \{\Delta[I_{xa} - m\rho_x\rho_z] \sigma \chi_y \Delta I_{xx}\}\dot{\omega}_x \\ + \{\Delta[I_{yz} - m\rho_y\rho_z] - \chi_x \Delta I_{yy}\}\dot{\omega}_y \\ + \{\Delta[I_{zz} - m(\rho_x^2 + \rho_y^2)]\dot{\omega}_z \\ + \{\Delta[I_{xy} - m\rho_x\rho_y](\omega_x^2 - \omega_y^2) \\ + \{\Delta[(I_{xx} - I_{yy}) + m(\rho_x^2 - \rho_y^2)\}\omega_x\omega_y \\ + \{\Delta[I_{yz} - m\rho_y\rho_z[- \chi_x\Delta(I_{xx} - I_{yy})\}\omega_x\omega_z \\ - \{\Delta[I_{xz} - m\rho_x\rho_z] - \chi_y\Delta(I_{xx} - I_{yy})\}\omega_y\omega_z \\ + \Delta(m\rho_x)a_y - \Delta(m\rho_y)a_x + \Delta(K_{YS})a_z \\ + \Delta[m^2(\psi_{11} - \psi_{22})]a_x a_y \\ + \Delta[m^2\psi_1]a_y a_z - \Delta[m^2\psi_2]a_x a_z \\ + \Delta[m^2\psi_{12}](a_y^2 - a_x^2) \end{array} \right\} \quad (4.44)$$

Equations 4.38 and 4.44 are identical except for the required change in definitions of P_1, P_2, P_6, and P_7. For purposes of simplification, the analyses which follow treat (4.38) as the RGG error equation. The approach to be used for OEP estimation is the same for (4.38) and (4.44), although an additional forcing term is needed. Use of (4.38) substantially reduces the complexity of the algebra appearing in subsequent discussions without altering either the approach taken to OEP estimation or estimator performance.

Table IV-2

COMPARISON OF OEP WHICH CHANGE WHEN SPIN/ELASTIC AXIS MISALIGNMENTS BECOME NON-ZERO. (χ = 25 μrad)

Parameter Number	Definition	Approximate Spin/Elastic Coincidence Value (kg m^2)	Approximate Spin/Elastic Noncoincidence Value (kg m^2)
P_1	$\Delta[I_{xz}-m\rho_x\rho_z] + \chi_x\Delta I_{xx}$	10^{-8}	10^{-7}
P_2	$\Delta[I_{yz}-m\rho_y\rho_z] - \chi_x\Delta I_{yy}$	10^{-8}	10^{-7}
P_6	$\Delta[I_{yz}-m\rho_y\rho_z] - \chi_x\Delta[I_{xx}-I_{yy}]$	10^{-8}	10^{-7}
P_7	$\Delta[I_{xz}-m\rho_x\rho_z] - \chi_y\Delta[I_{xx}-I_{yy}]$	10^{-8}	10^{-7}

C. INPUT FOR PARAMETER IDENTIFICATION

Equation 4.38 is a general expression for the RGG output error equation. If the right side of (4.38) is zero, and if pivot compliances K_1 and K_2, as well as arm inertias I_{zzo} and I_{zze} are identical, a perfect gravity gradient signal results. Inspection of (4.38) indicates two ways in which the error torque can be driven to zero.

(1) All parameter error terms, such as $\Delta(I_{xz} - m\rho_x\rho_z)$ can be driven to zero;

(2) All instrument dynamic terms which are nominally zero, such as ω_x and a_y, can be driven to zero.

If the RGG is instrumented in such a way so that all dynamic terms i.e., ω_x, a_y, etc., of (4.38) can be measured, it is conceivable that all the various parameters which appear in (4.38) can be estimated. A

well established approach to parameter estimation is to provide relatively large inputs to the system containing the unknown parameters. By measuring both the input and system output, it is often possible to establish the system transfer function and hence the system parameters. There are numerous advantages to the selection of sinusoidal forcing functions to serve as the inputs. Two of the primary advantages of the sinusoid are limited peak magnitude and known spectral content. Reid [RE-1] has shown that for certain systems, sinusoidal inputs are optimal in terms of minimizing the errors associated with system parameter identification. No attempt has been made during this research to optimize the inputs used for OEP identification.

C-1 Measurement of Sensor Dynamics

It is impractical to measure RGG arm angular velocities and accelerations. It is possible, however, to rigidly mount the RGG to an inertially instrumented platform as shown in Fig. IV-2. The platform is assumed to be vibration isolated from its support as well as gimballed so that it can respond to torquer input. Three axes of platform angular velocity, angular acceleration, and linear acceleration are sensed by gyros and accelerometers. Case angular velocity and angular orientation about the spin axis are measured. The only degree of sensor freedom with respect to the platform is about the spin axis. Since case angular orientation is known, all platform dynamics can be transformed to the sensor reference system.

C-2 Parameter Identification Input Selection

The nominal inputs selected for RGG parameter identification are listed in (4.45) through (4.48)

$$\omega_{xp} = \Omega_x \sin(\nu_x t) \tag{4.45}$$

$$a_{xp} = A_x \sin(\alpha_x t) \tag{4.46}$$

$$a_{zp} = A_z \sin(\alpha_z t) \tag{4.47}$$

$$T_d = T \sin(\Omega t) \ . \tag{4.48}$$

17

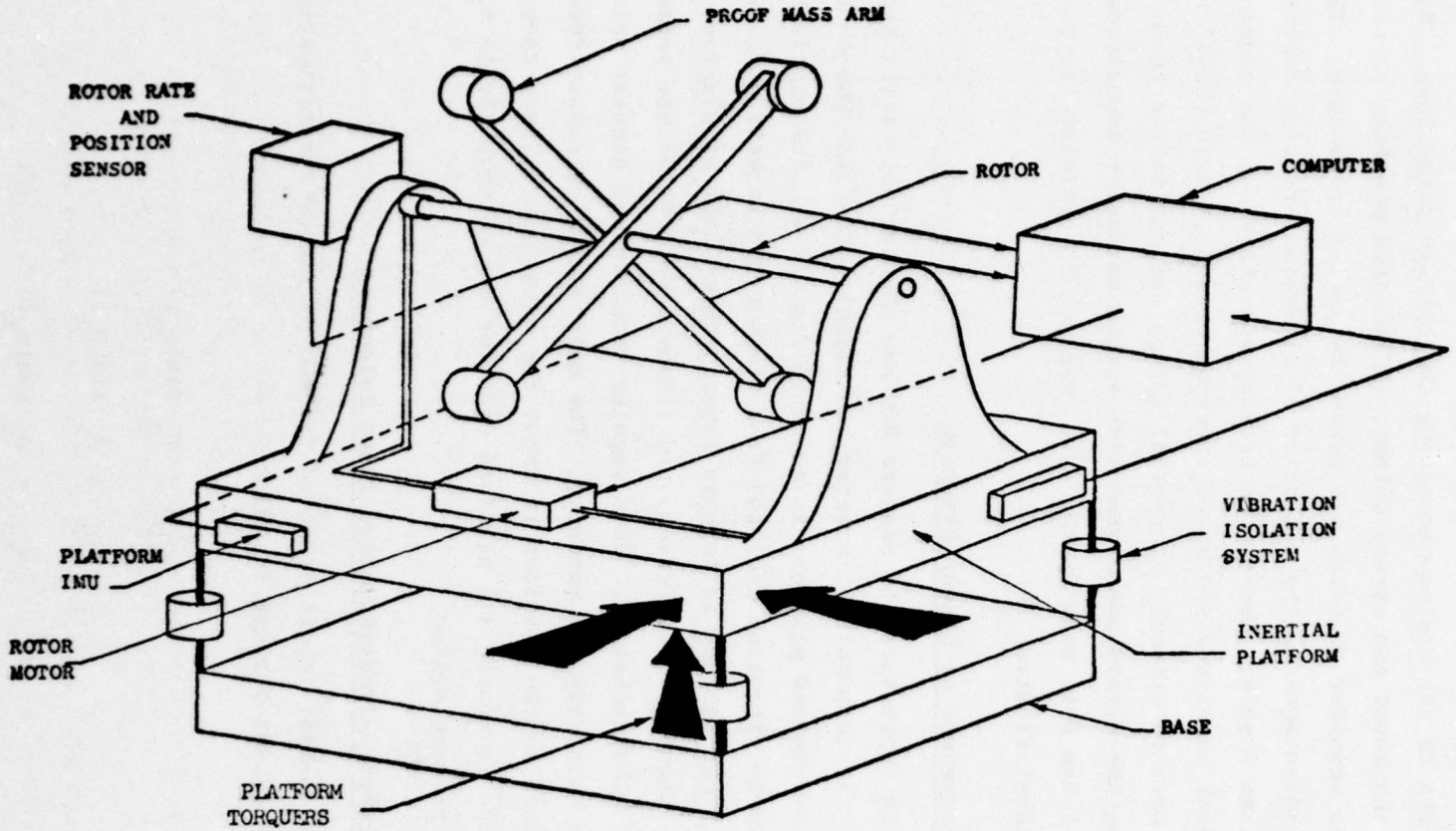


FIG. IV-2 SCHEMATIC DIAGRAM OF HUGHES' RGG (ROTATING GRAVITY GRADIOMETER TEST BED SYSTEM.

No other platform angular velocities or accelerations are intentionally excited and the platform is vibration isolated. Hence, all other platform dynamic conditions are nominally zero. Accelerometers and gyros, rigidly mounted to the inertial platform, measure the dynamics actually induced by the platform torquers.

The rotor torque T_d represents an input which alters the sensor spin rate by approximately 10^{-4} rad/sec. The actual value of $\dot{\omega}_z$ will be measured using either angular accelerometers or rate differentiation. The peak magnitude of the angular acceleration will be approximately $[T/(I_r + I_o + I_e)_z]$. The frequency is of greater significance with respect to parameter identification.

All input signals should be precisely calibrated prior to initiation of the estimation sequence.

Consideration of the actual values of ν_x, α_x, α_z, and Ω is deferred to Sect. F.

D. ERROR EQUATION WITH SPECIFIED INPUTS

Given the platform and sensor dynamics as specified by (4.45) through (4.48), and with the transformation $C_{s/P}$ (to sensor* from platform system) specified by

$$C_{s/P} = \begin{bmatrix} \cos\theta & \sin\theta & 0 \\ -\sin\theta & \cos\theta & 0 \\ 0 & 0 & 1 \end{bmatrix}_{\theta=\int\omega_s dt} \tag{4.49}$$

the error, ϵ, in sensor output may be written as shown in (4.50). This equation expresses the error in sensor output in the sensor reference frame.

---

* The reference systems are defined in Ch. II, D-2. The spin axis and elastic axis are assumed coincident as per Ch. IV, B-1.

The parameters P_j were defined in Table IV-1.

$$
\epsilon = -\frac{K/K_o}{1+\frac{K}{K_o}+\frac{K}{K_e}}
\left\{
\begin{aligned}
&\tfrac{1}{2} P_1 \bar{\Omega}_x \nu_x \cos[(\nu_x \pm \omega_s)t] + \tfrac{1}{2} P_2 \bar{\Omega}_x \nu_x \left\{-\sin[(\nu_x + \omega_s)t] + \sin[(\nu_x - \omega_s)t]\right\} \\
&+ P_3 \hat{\omega}_{zP} \\
&+ \tfrac{1}{4} P_4 \bar{\Omega}_x^2 \left\{2\cos 2\omega_s t - \cos[2(\nu_x \pm \omega_s)t]\right\} \\
&+ \tfrac{1}{8} P_5 \bar{\Omega}_x^2 \left\{-2\sin 2\omega_s t + \sin[2(\nu_x + \omega_s)t] - \sin[2(\nu_x - \omega_s)t]\right\} \\
&+ P_8 \times \cos \Omega t + P_9 e^{-(\omega_s/Q)t} \cos 2\omega_s t + P_{10} e^{-(\beta_o/2Q_\beta)t} \cos \beta_0 t \\
&+ P_{11}\left\{g \sin \omega_s t - \frac{A_x}{2}\cos(\omega_s - \alpha_x)t + \frac{A_x}{2}\cos(\alpha_x + \omega_s)t\right\} \\
&+ P_{12}\left\{g \cos \omega_s t - \frac{A_x}{2}\sin(\alpha_x + \omega_s)t + \frac{A_x}{2}\sin(\omega_s - \alpha_x)t\right\} \\
&+ P_{13} A_z \sin \alpha_z t \\
&+ P_{14}^* \left\{
\begin{aligned}
&\frac{A_x^2}{8}\sin[2(\omega_s \pm \alpha_x)t] + \tfrac{1}{2}\left[-\frac{A_x^2}{2} + g^2\right]\sin 2\omega_s t \\
&-\frac{gA_x}{2}\left(\cos[2\omega_s + \alpha_x]t - \cos[(2\omega_s - \alpha_x)t]\right)
\end{aligned}
\right\} \\
&+ P_{15}^* \left\{
\begin{aligned}
&\frac{A_x A_z}{4}\Big(\sin[(\alpha_x + \alpha_z + \omega_s)t] + \sin[(\omega_s - \alpha_x - \alpha_z)t] \\
&\qquad - \sin[(\alpha_x - \alpha_z + \omega_s)t] - \sin[(\omega_s + \alpha_z - \alpha_x)t]\Big) \\
&-\frac{gA_z}{2}\left(\cos[(\alpha_z + \omega_s)t] - \cos[(\omega_s - \alpha_z)t]\right)
\end{aligned}
\right\} \\
&- P_{16}^* \left\{
\begin{aligned}
&\frac{A_x A_z}{4}\Big(\cos[(\alpha_x + \alpha_z + \omega_s)t] - \cos[(\alpha_x - \alpha_z + \omega_s)t] \\
&\qquad - \cos[(\alpha_x + \alpha_z - \omega_s)t] + \cos[(\omega_s + \alpha_z - \alpha_x)t]\Big) \\
&+\frac{gA_z}{2}\left(\sin[(\alpha_z + \omega_s)t] - \sin[(\omega_s - \alpha_z)t]\right)
\end{aligned}
\right\} \\
&+ P_{17}^* \left\{
\begin{aligned}
&\frac{A_x^2}{4}\left(\cos[2(\alpha_x + \omega_s)t] + \cos[2(\alpha_x - \omega_s)t]\right) \\
&+gA_x\left(\sin[(2\omega_s - \alpha_x)t] - \sin[(2\omega_s - \alpha_x)t]\right) \\
&-\left(g^2 + \frac{A_x^2}{2}\right)\cos 2\omega_s t
\end{aligned}
\right\}
\end{aligned}
\right. \tag{4.50}
$$

Table IV-3 lists the various frequencies associated with the different OEPs.

Table IV-3

OUTPUT FREQUENCIES ASSOCIATED WITH THE OUTPUT EFFECTIVE PARAMETERS

Parameter	Associated Frequency
P_1	$\nu_x \pm \omega_s$
P_2	$\nu_x \pm \omega_s$
P_3	Ω
P_4	$2\omega_s$; $2(\omega_s \pm \nu_x)$
P_5	$2\omega_s$; $2(\omega_s \pm \nu_x)$
P_6	$\nu_x \pm \omega_s$
P_7	$\nu_x \pm \omega_s$
P_{11}	ω_s; $(\omega_s \pm \alpha_x)$
P_{12}	ω_s; $(\omega_s \pm \alpha_x)$
P_{13}	α_z
P_{14}	$2\omega_s$; $2(\omega_s \pm \alpha_x)$; $2\omega_s \pm \alpha_x$
P_{15}	$\omega_s \pm \alpha_x \pm \alpha_z$
P_{16}	$\omega_s \pm \alpha_x \pm \alpha_z$
P_{17}	$2\omega_s$; $2(\omega_s \pm \alpha_x)$; $2\omega_s \pm \alpha_x$

Examination of the frequencies associated with P_1, P_2, P_6, and P_7 indicates that only two frequencies, $\nu_x \pm \omega_s$, are associated with the four parameters. Given the parameter definitions of (4.44), these frequencies would not be adequate for estimation of all four parameters. If (4.44) were used as the error equation it would be sufficient to provide an ω_{yp} input as well as ω_{xp}. This additional input would allow separability and identifiability of all four (P_1, P_2, P_6, P_7) parameters. The additional input would also substantially complicate (4.50) in terms of trigonometric functions but would not change the overall nature of the equation.

E. PARAMETER INDEPENDENCE

Not all 17 OEPs must be individually estimated. Of the seven parameters associated with angular velocity and acceleration in (4.38), only P_1 through P_5 are independent.

$$P_6 \equiv P_2 \tag{4.51}$$

and

$$P_7 \equiv -P_1 \ .$$

While 9 independent parameters would intuitively be associated with moment of inertia components and mass center offsets, two of the inertia tensor components, I_{yy} and I_{xx}, appear only in P_5, while cross products appear only with corresponding mass center offsets. Therefore, of the 9 parameters only 5 are independent in terms of the OEP; whereas for (4.44), 7 OEPs are independent.

A similar situation exists with regard to the elasticity tensor. Of the six independent components of this tensor, five would be expected to contribute to differential torques about the sensor $\hat{z}$ axis (ψ_{33} would not). However, ψ_{11} and ψ_{22} appear only as a difference in P_{14} reducing the number of independent OEP associated with arm elasticity to four.

With respect to (4.38), of the 14 listed OEPs, only 12 are independent.

F. SENSOR INPUT-TO-OUTPUT TRANSFER FUNCTION

A simplified model for the sensor input-to-output transfer function, consisting only of a constant gain, was presented in Fig. II-5. The arm relative displacement equation, (4.29), was based upon the assumption that high frequency arm dynamics could be neglected, yielding a steady state relative deflection between the two arms. In order to establish the input frequencies at which (4.29) is a valid approximation to RGG output, it is necessary to consider in mor detail the RGG input-to-output relationship. A block diagram which traces the flow of an input through the sensor is given in Fig. IV-3.

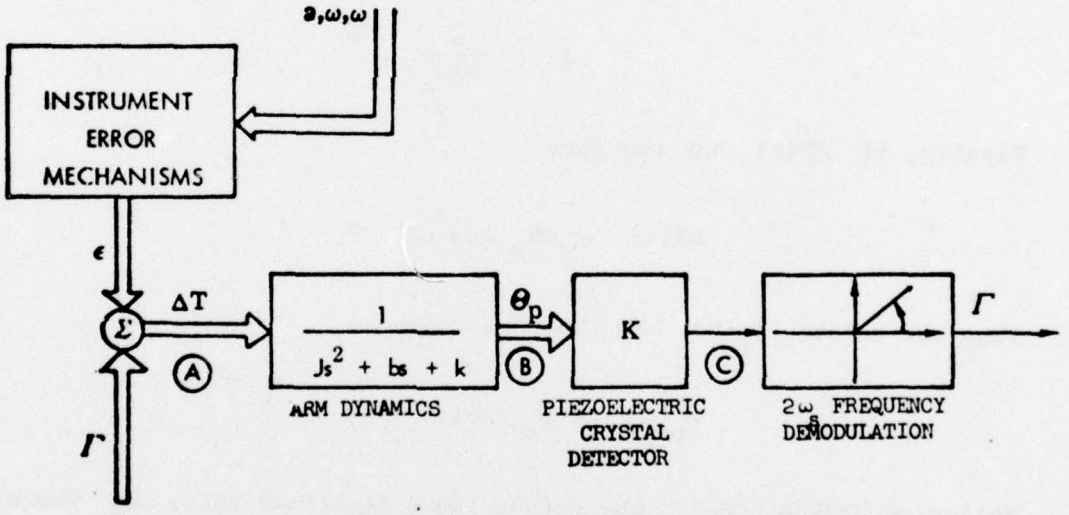


FIG. IV-3 INPUT-TO-OUTPUT DIFFERENTIAL TORQUE FLOW

The ideal position for differential torque pickoff is at (A) (Fig. IV-3). It is not possible to make the measurement at (A), however, since it is the mechanism of the arm relative motion which brings about a signal from the sensor. The differential torque signal is first available at (C),

23

after it has been mechanically filtered by the central pivot structure. It is therefore necessary to consider the effect of the arm dynamics transfer function upon the input-output relationship. With θ_p defined as the central pivot twist, the input-output relationship across the arm dynamics transfer function may be expressed, as shown in IV-B, by

$$\theta_p(s) = \frac{1}{Js^2 + bs + k} \Delta T(s) \tag{4.53}$$

or

$$\theta_p(s) = \frac{1}{\left(\frac{s}{\omega_n}\right)^2 + 2\xi\left(\frac{s}{\omega_n}\right) + 1} \left\{\frac{1}{k} \Delta T(s)\right\} \tag{4.54}$$

where

$$\omega_n \triangleq (k/J)^{\frac{1}{2}} \tag{4.55}$$

$$\xi \triangleq \frac{b}{2J\omega_n} \, . \tag{4.56}$$

Finally, if $\Delta T(t)$ has the form

$$\Delta T(t) = \Delta T_m \cos \omega t \tag{4.57}$$

then the output $\theta_p(t)$ has the form

$$\theta_p(t) = \theta_m \cos(\omega t + \psi) \, . \tag{4.58}$$

Following Cannon [CA-1], the output-input magnitude ratio α, where

$$\alpha \triangleq \frac{\theta_m}{\Delta T_m / k} \tag{4.59}$$

may be written as

$$\alpha = \left\{(1 - \beta^2)^2 + (2\xi\beta)^2\right\}^{-\frac{1}{2}} \tag{4.60}$$

where

$$\beta \triangleq \frac{\omega}{\omega_n} \quad . \tag{4.61}$$

Furthermore, the phase angle ψ_f is

$$\psi = -\tan^{-1}\left[\frac{2\xi\beta}{1-\beta^2}\right] . \tag{4.62}$$

Hughes has specified the differential mode quality factor Q to be 300. The actual mechanical Q us greater thatn 300 but is reduced to this value by loading the piezoelectric crystal. This very careful trim of the mechanical gain is carried out to assure accurate knowledge of Q. Since

$$\xi = \frac{1}{2Q} \quad , \tag{4.63}$$

the differential mode damping ratio is 0.00167. Plots of α (4.60), and ψ (4.61) for this second order system appear in Figs. IV-4 and IV-5 respectively. Examination of those figures indicates that only at very low forcing frequencies is the output/input ratio near 1. Instrument operation to an accuracy better than 1 E.U. in the presence of a 3000 E.U. signal requires that

$$\alpha - 1 \leq 0.0001 \tag{4.64}$$

for which

$$\omega < 2.2 \text{ rad/sec} . \tag{4.65}$$

In order that the phase angle ψ be less than 10^{-4} rad,

$$\omega \leq 6.5 \text{ rad/sec.} \tag{4.66}$$

Consider an ideal instrument mounted such that its spin axis is horizontal, and its reference direction aligned with the principal gradient direction. If the instrument is perfect, the gravity gradient

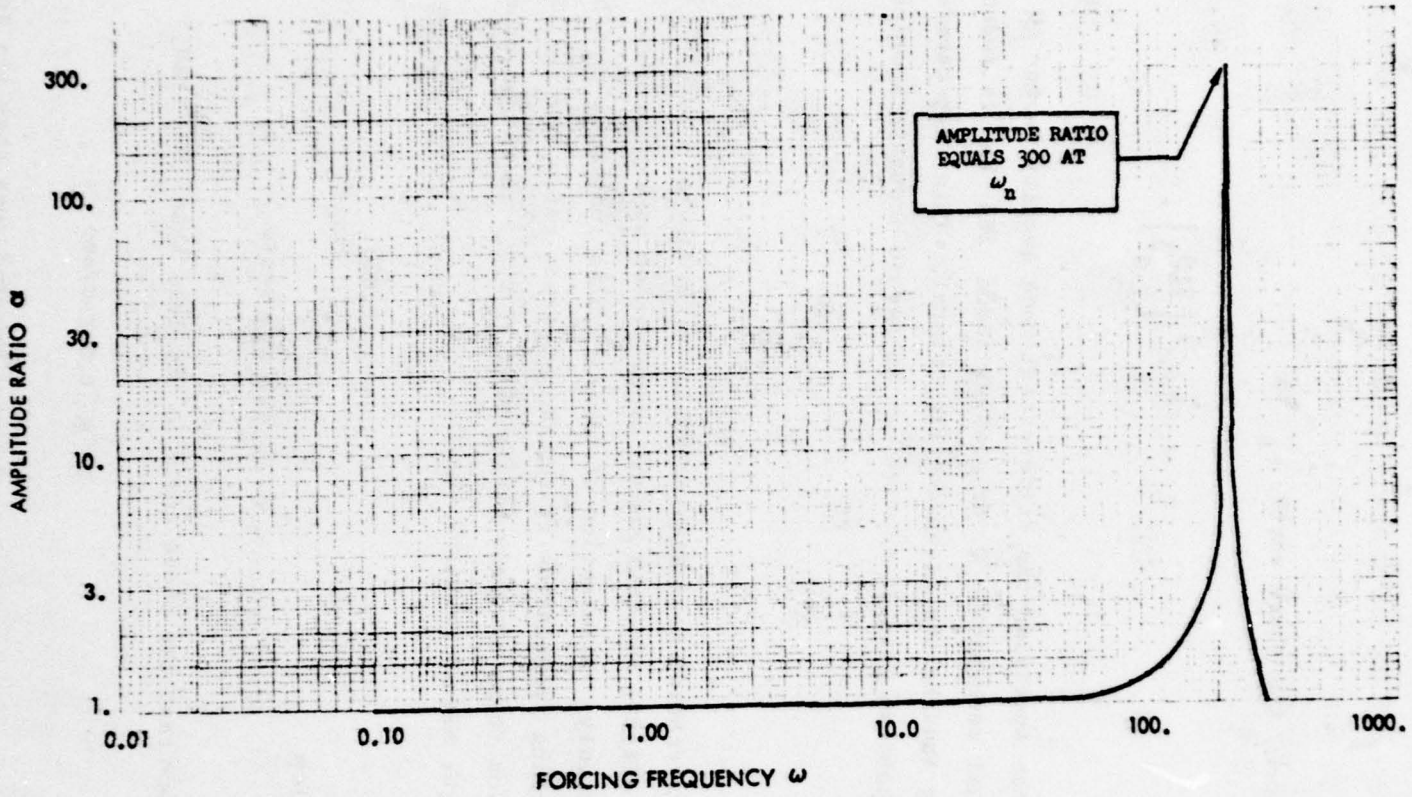


FIG. IV-4 PEAK OUTPUT-TO-INPUT AMPLITUDE RATIO FOR DIFFERENTIAL MODE.

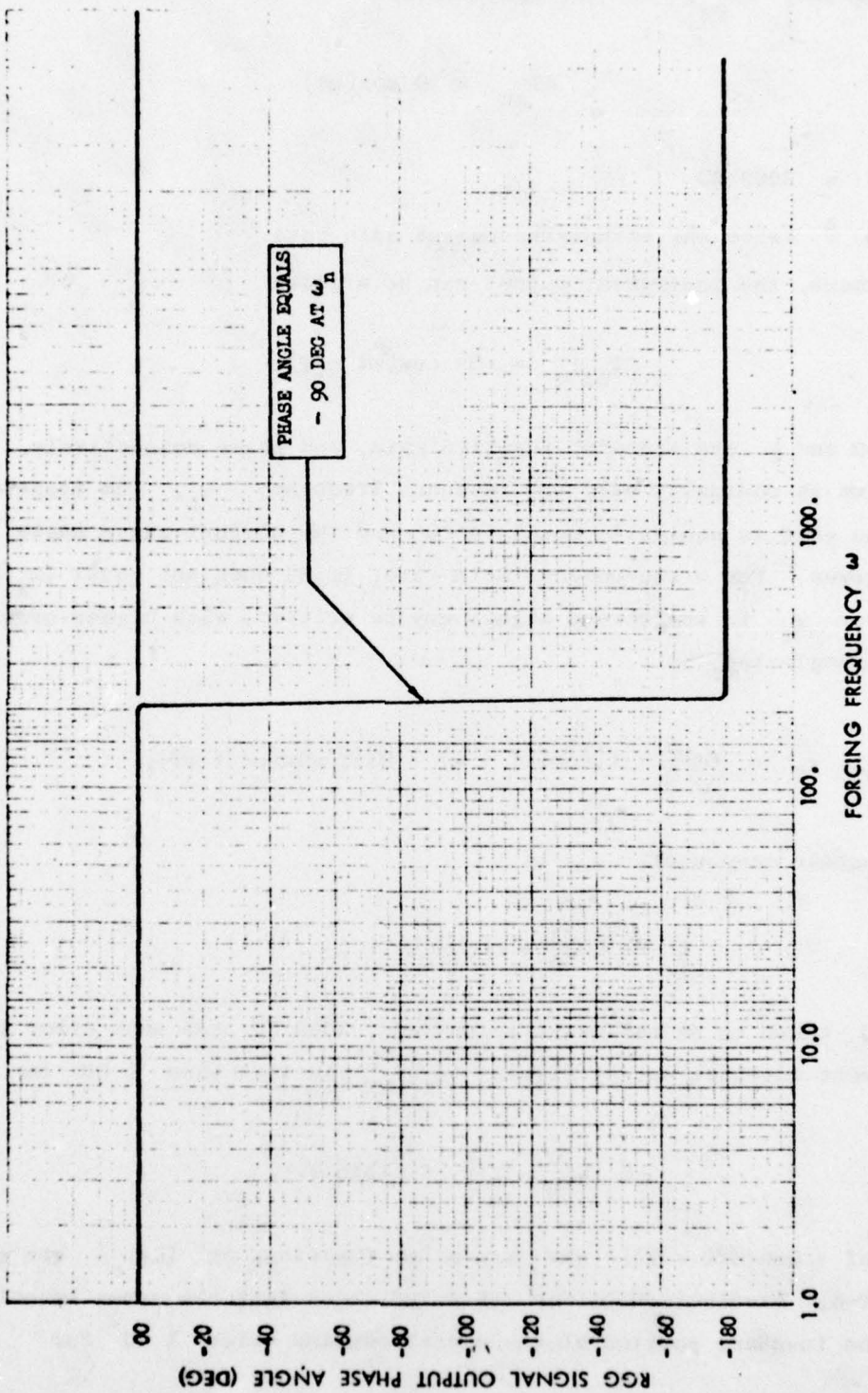


FIG. IV-5 DIFFERENTIAL MODE PHASE ANGLE RELATING INPUT-TO-OUTPUT.

27

input torque, ΔT_{gg}, can be expressed as

$$\Delta T_{gg} = G \cos(\omega t) \tag{4.67}$$

where

$$G = 3000 \text{ EU} \tag{4.68}$$

$$\omega \triangleq \text{twice the actual instrument spin rate.} \tag{4.69}$$

Furthermore, the instrument output can be written

$$\Delta T_{gg}\Big|_o = G\alpha \cos(\omega t + \psi) \tag{4.70}$$

where α and ψ are transfer function gain, and phase respectively. The spin rate is nominally half the resonant frequency, ω_n. The transfer function gain is nominally equal to Q and the nominal phase angle ψ_n is -90 degrees. For a non-nominal spin rate, $(\omega/2)$ does not equal $(\omega_n/2)$. The error ϵ_T in the torque signal may be written, with higher order terms in $\Delta\psi$ neglected, as

$$\epsilon_T = GQ\{\frac{\alpha}{Q} - 1\}\cos(\omega t + \psi) - G\alpha\Delta\psi \sin(\omega t + \psi) , \tag{4.71}$$

The in-phase component, ϵ, is

$$\epsilon = GQ\{\frac{\alpha}{Q} - 1\}\cos(\omega t + \psi) . \tag{4.72}$$

With G taken to be the gravity gradient, 3000 EU, the peak error in instrument in-phase output signal $(\epsilon_i)_{max}$ is less than 1 EU for

$$Q\left|G(\frac{\alpha}{Q} - 1)\right| < \left|\sin\psi\right| . \tag{4.73}$$

Plots of $Q\{G(\alpha/Q - 1)\}$ and $\sin\psi$ as functions of (ω/ω_n) are given in Fig. IV-5. Examination of Fig. IV-6 indicates that the error associated with the in-phase portion of the signal remains below 1 EU for

$$\left|1 - \frac{\omega}{\omega_n}\right| < 4 \times 10^{-5} . \tag{4.74}$$

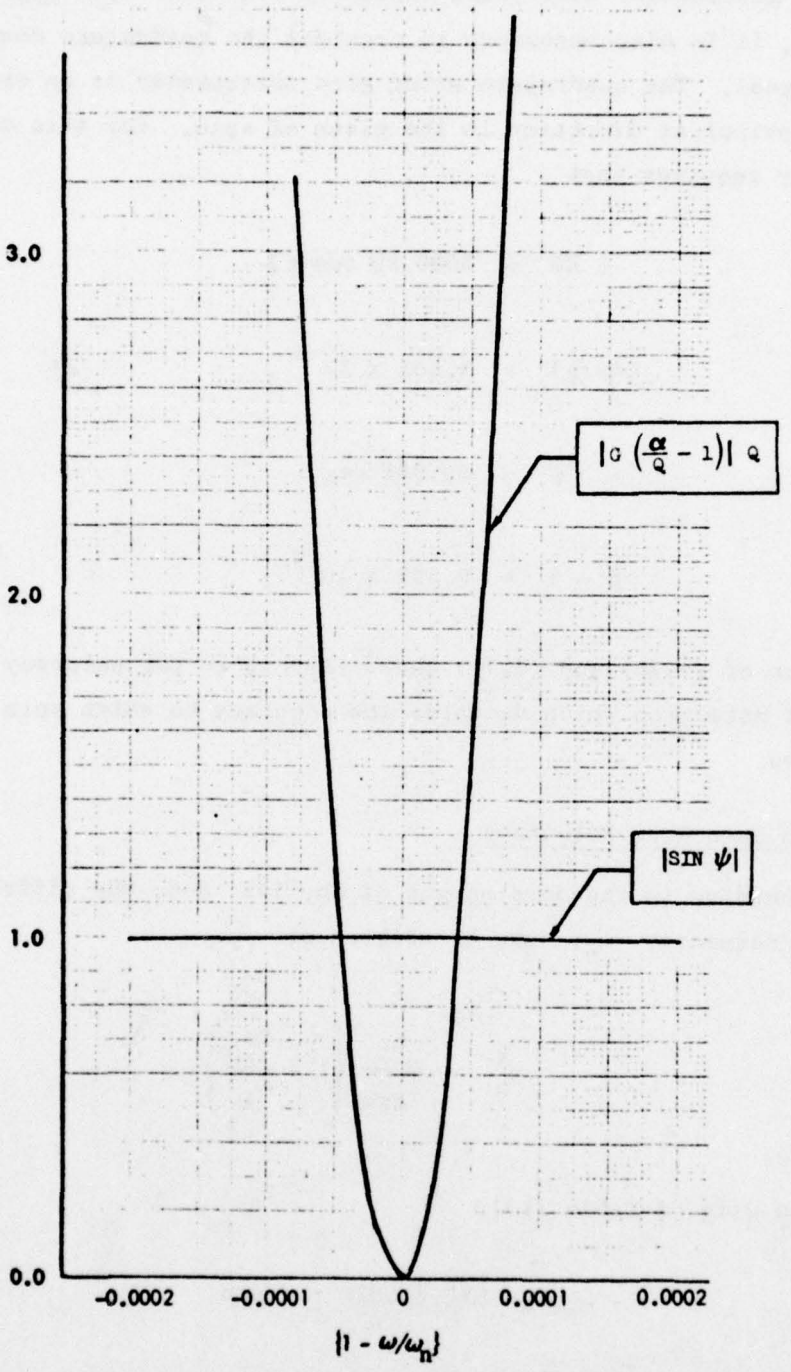


FIG. IV-6 PEAK IN-PHASE ERROR AND PHASE ANGLE AS A FUNCTION OF $(1 - \omega/\omega_n)$.

Since the gradiometer uses phase sensitive demodulation for gradient signal detection, it is also necessary to consider the quadrature component of the output signal. The quadrature error gets interpreted as an error in the gradient principal direction in the plane of spin. For this component, a 1 EU error requires that

$$1 \text{ EU} = 3000 \text{ EU} \cos(\psi) \tag{4.75}$$

or

$$\cos(\psi) = 3.333 \times 10^{-4} . \tag{4.76}$$

Hence,

$$\psi = 89.981 \text{ deg}, \tag{4.77}$$

and

$$\beta - 1 = 5.555 \times 10^{-7} . \tag{4.78}$$

Comparison of (4.75) and (4.78) shows that it is the accuracy of quadrature component detection which dictates the accuracy to which spin rate must be controlled.

F-1 RGG Spin Rate Selection

According to the development of Ch. III, B-6, the difference mode natural frequency, ω_n, may be written as

$$\omega_n^2 = \frac{K_1}{I_{zzo}} \left\{ 1 + \frac{2K_0}{K_1} \right\} . \tag{4.79}$$

Using the data of Table II-1,

$$\omega_n = 220.412929 \text{ rad/sec} \tag{4.80}$$

or

$$\omega_n = 35.079807 \text{ Hz}. \tag{4.81}$$

Sensor spin rate is not set at $\frac{1}{2}\omega_n$, but rather to the value of ω such

$$\frac{d\alpha}{d\beta} = 0 . \tag{4.82}$$

Selection of ω_s such that (4.80) is satisfied minimizes the effect which small perturbations in sensor spin rate have upon sensor gain. From (4.60)

$$\frac{d\alpha}{d\beta} = -\frac{1}{2}\{(1-\beta^2)^2 + (2\xi\beta)^2\}^{-\frac{3}{2}}\{(-4\beta)(1-\beta^2)+8\xi^2\beta\} \tag{4.83}$$

and from (4.80),

$$\beta = (1 - 2\xi^2)^{\frac{1}{2}} \tag{4.84}$$

or

$$\beta = 9.9999\ 444 \times 10^{-1} \tag{4.85}$$

and

$$2\omega_s = \beta\omega_n$$

from which the nominal spin rate is found to be

$$\omega_s = 110.20585 \text{ rad/sec} \tag{4.86}$$

or

$$\omega_s = 17.539806 \text{ Hz} \tag{4.87}$$

$$2\omega_s = 35.079612 \text{ Hz} . \tag{4.88}$$

Note that this spin rate results in a phase angle ψ equal to

$$\psi = -89.809 \text{ deg} \tag{4.89}$$

instead of the -90 deg phase angle associated with spin at the instrument natural frequency. This difference in-phase angle must be taken into account during signal detection. The allowable spin rate for 1 EU performance is, using (4.78) and (4.86)

$$110.20578 \leq \omega_s \leq 110.20591 \text{ rad/sec.} \qquad (4.90)$$

G. EFFECT OF FREQUENCY CONSIDERATIONS ON PARAMETER IDENTIFICATION INPUT

The ability to provide a known, calibrated input to a system can aid significantly towards identification of parameters associated with that system. Error equation (4.38) which was developed for the RGG was based upon a quasi-steady state relationship between the instrument arms. In order for the effect of arm-to-arm dynamics to be negligible to within 0.01% it will be necessary to constrain the forcing frequencies associated with parameter identification such that the output frequency of interest is less than 2.2 rad/sec. An alternate approach to satisfaction of this constraint is to account for the phase angle and magnitude gain by deterministically scaling the demodulated sensor output and by accounting for the phase lag within the estimation software. The magnitude gain and phase angle curves are both deterministic quantities which can be calculated during preassembly test. This approach to the arm dynamics problem eliminates the frequency restriction mentioned above. In this document it was assumed that the software approach was taken to account for arm dynamics although specific reference to phase angle and scaling has not been included.

H. A COMMENT ON PARAMETER IDENTIFIABILITY

Independent of the method ultimately selected for parameter identification, it is necessary that the RGG output torque at (C) of Fig. IV-2 contain information at enough different frequencies such that each independent OEP can be tagged to a specific, separate frequency and phase. Parameter identifiability or observability has been thoroughly investigated and is discussed in Chapter VI.

Chapter V

OUTPUT EFFECTIVE PARAMETER (OEP) ESTIMATION USING PARALLEL KALMAN FILTERS AND PHASE SENSITIVE SIGNAL DEMODULATION (PSSD)

A. INTRODUCTION

Output compensation for the rotating gravity gradiometer (RGG) can theoretically be achieved either with active parameter control or with numerical compensation of the instrument's output signal. Signal compensation minimizes the amount of hardware required within a system for parameter control. In addition, the study of signal compensation techniques provides insight to methods of active parameter control if such methods are required.

The estimation of parameters associated with a physical system is a problem which has, over the last decade, received considerable attention, although the linear problem was first posed and solved by Gauss in the nineteenth century. The Gauss least square error solution [G-1], [LI-1], [BR-1], is currently widely applied as a method of parameter estimation for systems which are linear in the estimated parameters.

The Kalman filter, using state augmentation [BR-1], [BR-2], has also been used to estimate parameters. A direct approach to Kalman filter state augmentation for OEP (output effective parameters) estimation was considered but was found to be unacceptable. System nonlinearity and the subsequent necessity for model linearization about some set of predetermined nominal values requires calculation of both the nominal and perturbed states for the linearized Kalman filter. The size of the system (26 states for the filter), the frequencies associated with the dynamics (up to 35 Hz), and the need for real time or near real time filter operation prohibited simple state augmentation.

Another commonly used approach to parameter estimation when the parameter is associated with a signal of known frequency is that of phase sensitive signal demodulation (PSSD). When the signal of interest occurs at a known frequency, synchronous demoduclation attenuates all signal frequencies except the frequency of interest. PSSD improves the signal-to-noise ratio in proportion to the amount of time allowed for signal averaging. One can speculate, however, as to whether Kalman filtering could provide better estimates of the OEP than could be obtained from PSSD. The goal of this chapter is to establish the capabilities of the Kalman filter as an OEP estimator and to compare this performance with that of a PSSD.

B. PARALLEL FILTER FORMULATION--P_1, P_2 ESTIMATION

A Kalman filter solution was ultimately developed which circumvented the system nonlinearity problem. This formulation consists of two independent recursive filters which operate in parallel. The first estimates platform related states and parameters (the rate or acceleration filter), while the second (the torque filter) estimates sensor differential output torques occurring at a specified frequency. The estimates generated by the two independent filters are then mathematically combined to yield an estimate of a particular OEP. Parallel filters were defined and evaluated for estimation of P_1, P_2, P_{14}, and P_{17}. This sampling spanned the various classes of output torque error sources. An example of this parameter identification method is given in Sect. B. The OPTSYS digital computer program was used to evaluate filter performance [BR-3].

As written in Eq. (4.38), the total RGG spin axis differential output torque is

$$\Delta T_z = \omega_x P_1 + \omega_y P_2 + \omega_x \omega_z P_2 - \omega_y \omega_z P_1 + \cdots . \qquad (5.1)$$

Comparison of (5.1) with (4.38) shows that P_7 and P_6 have been replaced by $-P_1$ and P_2 as discussed in Sect. IV-E.

The selection of sinusoidal platform inputs for OEP estimation was briefly discussed in Sect. IV:C-2. Since the parameters are multiplicatively associated with the dynamic states [as shown in (5.1)], it is possible to enhance the relative contribution of any particular parameter to the total differential torque output, ΔT_z, by providing the proper excitations to the platform. If, by contrast, a dynamic state remains zero for all time, the associated parameter remains unidentifiable. Sine wave platform inputs were selected because of the advantageous properties discussed by Reid [RE-1]. In addition, sinusoids are easily handled analytically, and allow a direct comparison between the Kalman filter approach to parameter estimation and parameter estimation using phase sensitive demoduclation.

The sinusoidal platform input command was taken to be the zero phase reference. Subsequent shifts in phase between the reference and the actual platform input were combined into the single phase angle φ_x. With a known sinusoidal input about the platform $\hat{x}_p$ axis having magnitude $\bar{\Omega}_x$, and frequency ν_x, such that

$$\omega_{xp} = \bar{\Omega}_x \sin[\nu_x t + \varphi_x] , \tag{5.2}$$

where φ_x is a constant phase angle, the RGG differential torque output ΔT_z may be written in functional form as

$$\Delta T_z = \Delta T_z(t, \nu_x, \omega_s, P_1, P_2, P_3, P_4, P_5) . \tag{5.3}$$

No platform inputs other than ω_{xp} are provided. The phase angle φ_x is, by definition, zero, if the input about $\hat{x}_p$ is initiated at the instant of $\hat{x}_p$ and $\hat{x}_s$ coincidence.

If sufficient filtering is applied to the torque signal output such that all frequencies other than $\nu_x \pm \omega_s$ are negligible, output equation (4.44) becomes

3

$$\Delta T_z = + \left\{ \frac{-K_0/K_1}{1 + \frac{K_0}{K_1} + \frac{K_0}{K_2}} \right\} \left\{ \frac{1}{2} P_1 \bar{\Omega}_x \nu_x \cos[\tfrac{1}{2}\nu_x \pm \omega_s t)] \right.$$

$$\left. - \frac{1}{2} P_2 \bar{\Omega}_x \nu_x \left(\sin[(\nu_x + \omega_s)t - \sin[(\nu_x - \omega_x)t] \right) \right\} \tag{5.4}$$

The coefficient

$$\left\{ \frac{-K_0/K_1}{1 + \frac{K_0}{K_1} + \frac{K_0}{K_2}} \right\}$$

is taken to be known exactly. It is a constant and is discussed in Ch. VI. Under this restriction, (5.4) becomes, with the coefficient taken to be 1,

$$\Delta T_z = \frac{1}{2} P_1 \bar{\Omega}_x \nu_x \{\cos[(\nu_x + \omega_s)t] + \cos[\nu_x - \omega_s)t]\} \tag{5.5}$$

$$- \frac{1}{2} P_2 \bar{\Omega}_x \nu_x \{\sin[(\nu_x + \omega_s)t] - \sin[(\nu_x - \omega_s)t]\} + \mathbf{v}$$

where v is taken to be the noise in the measured signal ΔT_z. Time zero is defined to be the time at which the sensor $\hat{x}_s$ axis lies in the platform $x - z$ plane. The measurement vectors $[z]_r$ and $[z]_t$ used in filter development are defined according to (5.6) through (5.10).

$$[z_1]_r \triangleq \bar{\Omega}_x \sin(\nu_x t + \varphi_x) + v_{1r} \quad \text{platform rate about the } \hat{x}_p \text{ axis} \tag{5.6}$$

$$[z_2]_r \triangleq \nu_x t + \varphi_x + v_{2r} \quad \text{platform phase angle} \tag{5.7}$$

$$[z_3]_r \triangleq \omega_s + v_{3r} \quad \text{sensor spin rate} \tag{5.8}$$

$$[z_1]_t \triangleq P_1 \frac{\bar{\Omega}_x}{2} \nu_x \cos[(\nu_x+\omega_s)t + \varphi_x] - P_2 \frac{\bar{\Omega}_x}{2} \nu_x \sin[(\nu_x+\omega_s)t + \varphi_x] + v_{1t} \; ; \quad (5.9)$$

Differential output torque at $(\nu_x+\omega_s)$ rad/sec

$$[z_2]_t \triangleq P_1 \frac{\bar{\Omega}_x}{2} \nu_x \cos[(\nu_x-\omega_s)t + \varphi_x] + P_2 \frac{\bar{\Omega}_x}{2} \nu_x \sin[(\nu_x-\omega_s)t + \varphi_x] + v_{2t} \; . \quad (5.10)$$

Differential output torque at $(\nu_x + \omega_s)$ rad/sec

The platform rate measurement, z_{1r}, is obtained from a gyro which is mounted upon the platform. The platform phase angle measurement, z_{2r}, is available from either the controller which is forcing the platform or the gyro. The sensor spin rate measurement, z_{3r}, is obtained by differentiation of the eight discrete rotor position pickoff signals. The torque measurements, z_{1t} and z_{2t}, are obtained by passing the torque ΔT_z of (5.5) through two separate notch filters, one passing frequency $(\nu_x + \omega_s)$, the other passing frequency $(\nu_x - \omega_s)$. The phase lag associated with the notches is assumed to be small, known, and constant. The notches are assumed to exist within digital software and act as prefilters on the measured RGG data.

The filters which were formulated were designed to require minimum computation time, having the form of simple oscillators. No hardware dynamics such as arm-to-arm relative motion were modeled. The filters act primarily to the effects of random noise upon RGG output.

B-1 Rate Filter Formulation

The rate filter state vector $[x]$ is defined as

$$[x]^T \triangleq [\bar{\Omega}_x \sin(\nu_x t+\varphi_x), \; \bar{\Omega}_x \cos(\nu_x t+\varphi_x), \; \varphi_x, \; \omega_s] \; . \quad (5.11)$$

The objective of the rate filter is to provide an estimate of the platform rate which is more accurate than the estimate of rate which is

5

contained in the gyro measurement. The information provided by this filter will subsequently be combined with the output of the torque filter to provide estimates of P_1 and P_2.

The equation of motion for the state vector of (5.11) may be written as

$$\begin{bmatrix} \dot{x}_1 \\ \dot{x}_2 \\ \dot{x}_3 \\ \dot{x}_4 \end{bmatrix} = \left[\begin{array}{cc:cc} 0 & \nu_x & & \\ -\nu_x & 0 & \multicolumn{2}{c}{0} \\ \hdashline & & & \\ \multicolumn{2}{c:}{0} & \multicolumn{2}{c}{0} \end{array}\right] \begin{bmatrix} x_1 \\ x_2 \\ x_3 \\ x_4 \end{bmatrix} + \begin{bmatrix} 1 & 0 & 0 \\ 1 & 0 & 0 \\ 0 & 1 & 0 \\ 0 & 0 & 1 \end{bmatrix} \begin{bmatrix} w_{1r} \\ w_{2r} \\ w_{3r} \end{bmatrix} \tag{5.12}$$

where the vector [w] represents system process noise with

$$\delta[w_r] = 0 \tag{5.13}$$

and

$$\delta[w_r w_r^T] = Q_r \delta(t) = \begin{bmatrix} q_{1r} & 0 & 0 \\ 0 & q_{2r} & 0 \\ 0 & 0 & q_{3r} \end{bmatrix} \tag{5.14}$$

The observation vector is defined as

$$\begin{bmatrix} z_1 \\ z_2 \\ z_3 \end{bmatrix} = \begin{bmatrix} z_{1r} \\ z_{2r} - \nu_x t \\ z_{3r} \end{bmatrix} = \left[\begin{array}{cccc} 1 & 0 & 0 & 0 \\ 0 & 0 & 1 & 0 \\ 0 & 0 & 0 & 1 \end{array}\right] \left|\begin{array}{c} x_1 \\ x_2 \\ x_3 \\ x_4 \end{array}\right. + [v_r] \tag{5.15}$$

where

$$\mathcal{E}[v_r] = 0 \tag{5.16}$$

and

$$\mathcal{E}[v_r v_r^T] \triangleq R_r \delta(t) = \begin{bmatrix} r_{1r} & 0 & 0 \\ 0 & r_{2r} & 0 \\ 0 & 0 & r_{3r} \end{bmatrix} \tag{5.17}$$

Using this model for platform motion, a filter was formulated and the steady state filter covariance levels evaluated. The evaluation was based upon the numerical data appearing in Table V-1.

Table V-1

STATISTICAL VALUES USED FOR RATE FILTER PERFORMANCE EVALUATION

Noise Source	Typical Value For Relevant State	Random Noise 1σ Level
w_{1r}	10^{-5} rad/sec	10^{-12} rad/sec^2
w_{2r}	10^{-2} rad	10^{-7} rad/sec
w_{3r}	10^{2} rad/sec	10^{-5} rad/sec^2
v_{1r}	10^{-5} rad/sec	10^{-10} rad/sec
v_{2r}	10^{-2} rad	10^{-7} rad
v_{3r}	10^{2} rad/sec	10^{-3} rad/sec

Nominal operational values are listed in equations (5.18) through (5.20).

$$\omega_s = 110 \text{ rad/sec} \tag{5.18}$$

$$\nu_x = 10 \text{ rad/sec} \tag{5.19}$$

$$\bar{\Omega}_x = 10^{-5} \text{ rad/sec} . \tag{5.20}$$

The only observation noise considered for this analysis was based upon 16 bit A/D conversion. Input command 1σ disturbance noise level was based upon 16 bit torque command quantization and a platform inertia of 100 kg m^2. Phase angle 1σ level assumed a 1 nano sec random variation in command issuance. Spin rate random variation was taken from the spin rate control requirements developed in Ch. IV:D. The steady state estimate error variance levels associated with this rate filter were calculated using the OPTSYS computer program. These variances are listed in Table V-2.

Table V-2

STEADY STATE RATE FILTER PERFORMANCE

State	Estimate Error Variance
$\Omega_x \sin[\nu_x t + \varphi_x]$	1.41×10^{-22} deg^2/sec^2
$\Omega_x \cos[\nu_x t + \varphi_x]$	1.41×10^{-22} deg^2/sec^2
φ_x	1.00×10^{-14} deg^2
ω_s	1.00×10^{-8} deg^2/sec^2

Using the data of Table V-2 it is straightforward to show that

$$\mathcal{E}[\tilde{\Omega}_x] = 0 \tag{5.21}$$

and that, with $\nu_x t$ known exactly,

$$\mathcal{E}[\tilde{\Omega}_x^2] = \mathcal{E}[\tilde{x}_1^2] + \mathcal{E}[\tilde{x}_2^2] + \Omega_x^2 \mathcal{E}[\tilde{x}_3^2] \tag{5.22}$$

or

$$\mathcal{E}[\tilde{\Omega}_x^2] = 2.84 \times 10^{-22} \text{ rad}^2/\text{sec}^2 . \tag{5.23}$$

§

B-2 Torque Filter Formulation

The torque filter is used to smooth the measurements of differential output torque after the torque signal has been passed through two parallel notch filters. These filters provide two separate torque measurements, one having frequency $(\omega_s + \nu_x)$ and the other having frequency $(\omega_s - \nu_x)$. A diagram of this method of this method of signal determination is given in Fig. V-1. Recall from (5.5) that the frequencies $\omega_s \pm \nu_x)$ are those associated with the P_1 and P_2 contribution to the output torque error when the platform is excited with a sinusoidal rate input.about the $\hat{x}_p$ axis, and has known frequency ν_x. The torque filter is a four state filter having as its states:

$$x_1 = \frac{1}{2}\bar{\Omega}_x\nu_x P_1\left\{\cos[(\nu_x+\omega_s)t+\varphi_x] - P_2 \sin[(\nu_x+\omega_s)t+\varphi_x]\right\} \quad (5.24)$$

$$x_2 = \frac{1}{2}\bar{\Omega}_x\nu_x P_1\left\{\sin[(\nu_x+\omega_s)t+\varphi_x] + P_2 \cos[(\nu_x+\omega_s)t+\varphi_x]\right\} \quad (5.25)$$

$$x_3 = \frac{1}{2}\bar{\Omega}_x\nu_x P_1\left\{\cos[(\nu_x-\omega_s)t+\varphi_x] + P_2 \sin[(\nu_x-\omega_s)t+\varphi_x]\right\} \quad (5.26)$$

$$x_4 = \frac{1}{2}\bar{\Omega}_x\nu_x P_1\left\{\sin[(\nu_x-\omega_s)t+\varphi_x] - P_2 \cos[(\nu_x-\omega_s)t+\varphi_x]\right\} \quad (5.27)$$

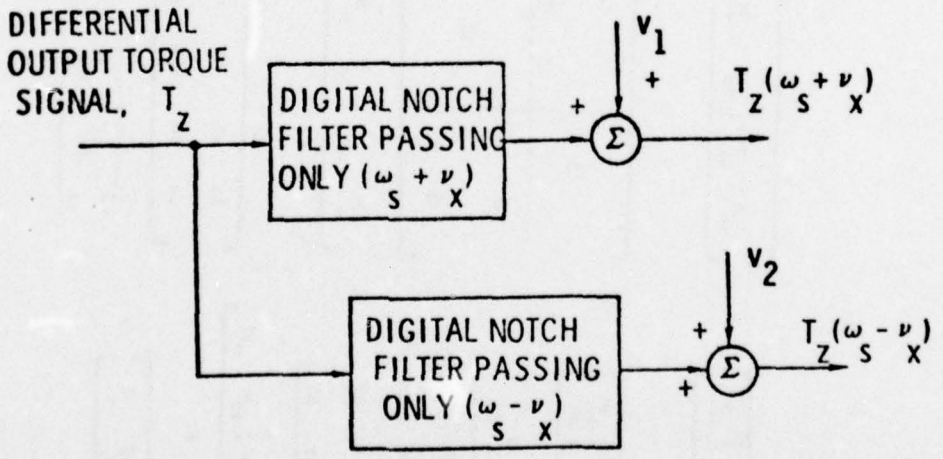


FIG. V-1 SCHEMATIC MODEL OF TORQUE FILTER MEASUREMENT GENERATION

The state x_1 corresponds to the high frequency output torque described in measurement equation (5.9), while x_3 corresponds to the low frequency output torque described by measurement equation (5.10). Using the definitions of (5.28)

$$\begin{aligned} \alpha &\triangleq \tfrac{1}{2}\,\bar{\Omega}_x\,\nu_x \\ \beta &\triangleq \nu_x + \omega_s \\ \gamma &\triangleq \nu_x - \omega_s \end{aligned} \tag{5.28}$$

the torque filter state vector may be written as

$$\left.\begin{aligned} x_1 &= \alpha P_1 \cos[\beta t + \varphi_x] - \alpha P_2 \sin[\beta t + \varphi_x] \\ x_2 &= \alpha P_1 \sin[\beta t + \varphi_x] + \alpha P_2 \cos[\beta t + \varphi_x] \\ x_3 &= \alpha P_1 \cos[\gamma t + \varphi_x] + \alpha P_2 \sin[\gamma t + \varphi_x] \\ x_4 &= \alpha P_1 \sin[\gamma t + \varphi_x] - \alpha P_2 \cos[\gamma t + \varphi_x] \end{aligned}\right\}$$

The dynamic model for the measured torques z_{1t} and z_{2t} is then

$$\begin{bmatrix} \dot{x}_1 \\ \dot{x}_2 \\ \hline \dot{x}_3 \\ \dot{x}_4 \end{bmatrix} = \left[\begin{array}{cc|cc} 0 & -\beta & \multicolumn{2}{c}{\multirow{2}{*}{0}} \\ \beta & 0 & & \\ \hline \multicolumn{2}{c|}{\multirow{2}{*}{0}} & 0 & -\gamma \\ & & \gamma & 0 \end{array}\right] \begin{bmatrix} x_1 \\ x_2 \\ \hline x_3 \\ x_4 \end{bmatrix} + \begin{bmatrix} 1 & 0 \\ 1 & 0 \\ 0 & 1 \\ 0 & 1 \end{bmatrix} \begin{bmatrix} w_1 \\ w_2 \end{bmatrix}$$

$$\begin{bmatrix} z_1 \\ \hline z_2 \end{bmatrix} = \begin{bmatrix} z_{1t} \\ \hline z_{2t} \end{bmatrix} = \begin{bmatrix} 1 & 0 & 0 & 0 \\ 0 & 0 & 1 & 0 \end{bmatrix} \begin{bmatrix} x_1 \\ x_2 \\ \hline x_3 \\ x_4 \end{bmatrix} + \begin{bmatrix} v_1 \\ v_2 \end{bmatrix}$$

10

From (5.29) and (5.30) it is clear that states 1 and 2 are completely decoupled from states 3 and 4, and these pairs could be treated separately The resultant torque filter is a pair of uncoupled, constant coefficient oscillators, one of which is related to the high frequency torque, the other to the low frequency torque. Torque filter performance was evaluated using the OPTSYS program. Process and measurement noise of 1σ levels which were input to the program are listed in Table V-3.

Table V-3

STATISTICAL VALUES APPLIED FOR TORQUE FILTER EVALUATION

Variable	Typical Value For Relevant State	Noise 1σ Level
w_{1t}, w_{2t}	10^{-11} (N m)	10^{-15} N m/sec
v_{1t}, v_{2t}	10^{-11} (N m)	10^{-16} N m

Process noise was specified by assuming 0.01% input randomness about the input signal. Measurement noise was specified by assuming 16 bit A/D conversion of the differential output torque. Torque filter state estimate error variances are listed in Table V-4.

Table V-4

STEADY STATE TORQUE FILTER PERFORMANCE

State	Estimate Error Variance $(N\ m)^2$
x_1	1.41×10^{-31}
x_2	1.50×10^{-31}
x_3	1.41×10^{-31}
x_4	1.32×10^{-31}

11

B-3 Parameter Estimation

For any given time t, the state estimates produced by the rate and torque filters can be combined to provide an estimate of the parameters P_1 and P_2. To extract these estimates, let $\hat{z}$ be the torque filter state vector for some specific time t. Then at time t,

$$\begin{bmatrix} \hat{z}_1 \\ \hat{z}_2 \\ \hat{z}_3 \\ \hat{z}_4 \end{bmatrix} = \begin{bmatrix} \alpha \cos(\hat{\beta}t+\hat{\varphi}_x) & -\alpha \sin(\hat{\beta}t+\hat{\varphi}_x) \\ \alpha \sin(\hat{\beta}t+\hat{\varphi}_x) & \alpha \cos(\hat{\beta}t+\hat{\varphi}_x) \\ \alpha \cos(\hat{\gamma}t+\hat{\varphi}_x) & \alpha \sin(\hat{\gamma}t+\hat{\varphi}_x) \\ \alpha \sin(\hat{\gamma}t+\hat{\varphi}_x) & -\alpha \cos(\hat{\gamma}t+\hat{\varphi}_x) \end{bmatrix} \begin{bmatrix} \hat{P}_1 \\ \hat{P}_2 \end{bmatrix} . \tag{5.33}$$

Equation (5.33) is decomposed to provide two estimates of $[P_1, P_2]$. The first of these decompositions may be written

$$\begin{bmatrix} \hat{z}_1 \\ \hat{z}_2 \end{bmatrix} = \begin{bmatrix} \frac{1}{2} \nu_x \hat{\Omega}_x \cos(\hat{\xi}) & -\frac{1}{2} \nu_x \hat{\Omega}_x \sin(\hat{\xi}) \\ \frac{1}{2} \nu_x \hat{\Omega}_x \sin(\hat{\xi}) & \frac{1}{2} \nu_x \hat{\Omega}_x \cos(\hat{\xi}) \end{bmatrix} \begin{bmatrix} \hat{P}_1 \\ \hat{P}_2 \end{bmatrix} \tag{5.34}$$

where α has been replaced according to (5.28), and

$$\hat{\xi} \triangleq (\nu_x + \hat{\omega}_s)\hat{t} + \hat{\varphi}_x . \tag{5.35}$$

Equation (5.34) may be simplified to

$$\begin{bmatrix} \hat{z}_1 \\ \hat{z}_2 \end{bmatrix} = \frac{1}{2} \nu_x \hat{\Omega} \begin{bmatrix} \cos \hat{\xi} & -\sin \hat{\xi} \\ \sin \hat{\xi} & \cos \hat{\xi} \end{bmatrix} \begin{bmatrix} \hat{P}_1 \\ \hat{P}_2 \end{bmatrix} \tag{5.36}$$

$$\triangleq \frac{1}{2} \nu_x \hat{\Omega} [\hat{A}] \begin{bmatrix} \hat{P}_1 \\ \hat{P}_2 \end{bmatrix} . \tag{5.37}$$

It is clear that

$$[\hat{A}]^{-1} = [\hat{A}]^T \tag{5.38}$$

and hence

$$\begin{bmatrix} \hat{P}_1 \\ \hat{P}_2 \end{bmatrix} = \frac{2}{\nu_x \hat{\Omega}} [\hat{A}]^T \begin{bmatrix} \hat{z}_1 \\ \hat{z}_2 \end{bmatrix} . \tag{5.39}$$

Furthermore,

$$\frac{2}{\nu_x \hat{\Omega}} = \frac{2}{\nu_x \Omega} \left[1 - \frac{\tilde{\Omega}}{\Omega} \right]^{-1} \tag{5.40}$$

From (5.39) and (5.40), when higher order terms are neglected, and

$$\tilde{P} \triangleq \hat{P} - P \tag{5.41}$$

$$\tilde{P} = \frac{2}{\nu_x \hat{\Omega}} \left\{ \tilde{A}^T \begin{bmatrix} z_1 \\ z_2 \end{bmatrix} + A^T \begin{bmatrix} \tilde{z}_1 \\ \tilde{z}_2 \end{bmatrix} \right\} \tag{5.42}$$

where

$$\tilde{A} \triangleq \hat{A} - A \tag{5.43}$$

and

$$\tilde{z} \triangleq \hat{z} - z . \tag{5.44}$$

Hence,

$$\mathcal{E}[\tilde{P}] = [0]_{2\times 1} \tag{5.45}$$

and

$$\mathcal{E}[\tilde{P}\tilde{P}^T] \triangleq \Sigma_p = \left(\frac{2}{\nu_x \Omega}\right)^2 \mathcal{E}\left[A^T[\tilde{z}\tilde{z}^T]A + \tilde{A}^T(zz^T)\tilde{A}\right] \quad . \tag{5.46}$$

Equation (5.46) can be expanded to

$$\mathcal{E}[\tilde{P}\tilde{P}^T] = \left(\frac{2}{\nu_x \Omega_x}\right) A^T \mathcal{E}[\tilde{z}\tilde{z}^T]A$$

$$+ \left(\frac{2}{\nu_x \Omega_x}\right) \mathcal{E}\begin{bmatrix} \tilde{a}_{11}^2 z_1^2 - 2\tilde{a}_{11}\tilde{a}_{12} z_1 z_2 + \tilde{a}_{12}^2 z_2^2 & \tilde{a}_{11}\tilde{a}_{22} z_1^2 + (\tilde{a}_{11}\tilde{a}_{22} - \tilde{a}_{12}^2) z_1 z_2 - \tilde{a}_{12}\tilde{a}_{22} z_2^2 \\ \tilde{a}_{11}\tilde{a}_{12} z_1^2 + (\tilde{a}_{11}\tilde{a}_{22} - \tilde{a}_{12}^2) z_1 z_2 - a_{12} a_{22} z_2^2 & \tilde{a}_{11}^2 z_1^2 + 2\tilde{a}_{12}\tilde{a}_{22} z_1 z_2 + \tilde{a}_{22}^2 z_{22}^2 \end{bmatrix}$$

and it can be shown through straightforward but lengthy calculations that

$$\mathcal{E}[\tilde{a}_{11}^2] = \frac{1}{4}\left\{\left[\Omega_x^2 \sigma_{\nu_x}^2 + \nu_x^2 \sigma_{\Omega_x}^2 + 2\nu_x \Omega_x \sigma^2_{\nu_x \Omega_x}\right] \cos^2[\xi + \omega_s t]\right\} \tag{5.47}$$

$$+ \nu_x^2 \Omega_x^2 \left[t^2 \sigma^2_{\omega_s} + \omega_s^2 \sigma_t^2 + \sigma_\xi^2\right] \sin^2(\xi + \omega_s t)$$

$$- \frac{1}{8} \nu_x \Omega_x \left[\Omega_x \sigma^2_{\nu_x \xi} + \nu_x \sigma^2_{\Omega_x \xi}\right] \sin[2(\xi + \omega_s t)] \; ;$$

$$\mathcal{E}[\tilde{a}_{12}^2] = \frac{1}{8} \left(\Omega_x^2 \sigma_{\nu_x}^2 + \nu_x^2 \sigma_{\Omega_x}^2\right) \sin^2(\xi + \omega_s t) \tag{5.48}$$

$$+ \Omega_x^2 \nu_x^2 (t^2 \sigma^2_{\omega_s} + \omega_s^2 \sigma_t^2 + \sigma_\xi^2) \cos^2(\xi + \omega_s t)$$

$$+ \frac{1}{8} \left[\nu_x \Omega_x \; \Omega_x \sigma^2_{\nu_x \xi} + \nu_x \sigma^2_{\Omega_x \xi}\right] \sin[2(\; + \omega_s t)] \; ;$$

$$\mathcal{E}[\tilde{a}_{11}\tilde{a}_{12}] = \frac{1}{8} \; \Omega_x^2 \sigma^2_{\nu_x} + 2\nu_x \Omega_x \sigma^2_{\Omega_x \nu_x} + \nu_x^2 \sigma^2_{\Omega_x} \; \sin[2(\xi + \omega_s t)] \tag{5.49}$$

$$- \frac{1}{8} [\nu_x \Omega_x]^2 [t^2 \sigma^2_{\omega_s} + \omega_s^2 \sigma_t^2 + \sigma^2] \sin[2(\xi + \omega_s t)]$$

$$+ \frac{1}{8} [\nu_x \Omega_x] \left\{\left[\Omega_x \sigma^2_{\nu_x \xi} + \nu_x \sigma^2_{\Omega_x \xi} \; \cos[2(\xi + \omega_s t)]\right]\right\} \; ;$$

$$\delta[\tilde{a}_{22}] = \delta[\tilde{a}_{11}^2] \ . \tag{5.50}$$

Equations (5.47) through (5.50) require that $\tilde{\omega}_s t$ remain small so that the approximation of $\sin(\tilde{\omega}_s t)$ by $\tilde{\omega}_s t$ remains valid. It is therefore assumed that t remains below 1000 sec.

Average values for the variance in the estimate of the separate components a_{ij} of the A matrix can be determined by eliminating the nonconstant terms of (5.47) through (5.50). Hence

$$\delta[\tilde{a}_{11}^2]_{av} = \frac{1}{8}\left\{\Omega_x^2\sigma_{\nu_x}^2 + \nu_x^2\sigma_{\Omega_x}^2 + 2\nu_x\Omega_x\sigma_{\nu_x\Omega_x}^2\right\} + \frac{1}{8}\left\{\nu^2\Omega^2\left[t^2\sigma_{\omega_s}^2 + \omega_s^2\sigma_t^2 + \sigma_\xi^2\right]\right\} \ ; \tag{5.51}$$

$$\delta[\tilde{a}_{12}^2]_{av} = \frac{1}{8}\left\{(\Omega_x^2\sigma_{\nu_x}^2 + \nu_x^2\sigma_{\Omega_x}^2) + \Omega_x^2\nu_x^2(t^2\sigma_{\omega_s}^2 + \omega_s^2\sigma_t^2 + \sigma_\xi^2)\right\} \ ; \tag{5.52}$$

$$\delta[\tilde{a}_{11}\tilde{a}_{12}]_{av} = 0 \ ; \tag{5.53}$$

$$\delta[\tilde{a}_{22}^2]_{av} = \delta[\tilde{a}_{11}^2]_{av} \ . \tag{5.54}$$

Data for evaluation of (5.46) through (5.50) were taken from rate and torque filter performance levels and are listed in Table V-5. Note that σ_t^2 has been set to 10^{-18} sec^2.

Table V-5

PARAMETER ESTIMATE ERROR EQUATION INPUT

Variable	Typical Value	σ^2
Ω_x^2	10^{-10} rad^2/sec^2	2.8×10^{-22} rad^2/sec^2
ν_x^2	100 rad^2/sec^2	0
ω_s^2	12100 rad^2/sec^2	1.0×10^{-8} rad^2/sec^2
$\nu_x^2 t^2$	10^6 rad^2	1.0×10^{-16} rad^2
$\nu_x\Omega_x$	10^{-4} rad^2/sec^2	0
t	1 sec	1.0×10^{-18} sec^2
ξ	0.001 rad	1.0×10^{-16} rad^2

Examination of (5.51) through (5.54) indicates that the $\sigma^2_{\omega s}$ term dominates by six orders of magnitude even for t as small as 1 sec. Hence,

$$\begin{bmatrix} \text{mag } \mathcal{E}(\tilde{a}^2_{11}) \\ \text{mag } \mathcal{E}(\tilde{a}^2_{12}) \\ \text{mag } \mathcal{E}(\tilde{a}_{11}\tilde{a}_{12}) \\ \text{mag } \mathcal{E}(\tilde{a}^2_{22}) \end{bmatrix}_{av} = \begin{bmatrix} 1.25 \times 10^{-17} \\ 1.25 \times 10^{-17} \\ 0 \\ 1.25 \times 10^{-17} \end{bmatrix} \frac{\text{rad}^2}{\text{sec}^2} . \tag{5.55}$$

With nominal values for the torques z_1 and z_2 taken to be 10^{-12} N m (using parameter values taken from Table IV-1),

$$\mathcal{E}[\tilde{P}\tilde{P}^T] = (4\times10^8) \begin{bmatrix} 1.4\times10^{-31} & -4.1\times10^{-33} \\ -4.1\times10^{-33} & 1.5\times10^{-31} \end{bmatrix} \tag{5.56}$$

$$+ (4\times10^8) \begin{bmatrix} (10^{-24})(1.25\times10^{-17} & -(10^{-24})(1.25\times10^{-17}) \\ -(10^{-24})(1.25\times10^{-17} & (10^{-24})(1.25\times10^{-17}) \end{bmatrix} .$$

Examination of (5.56) indicates that the errors associated with the torque filter output estimates dominate the parameter estimation covariance by approximately 10 orders of magnitude. Hence

$$\mathcal{E}[\tilde{P}\tilde{P}^T] \approx \begin{bmatrix} 5.6\times10^{-23} & -1.64\times10^{-24} \\ -1.64\times10^{-24} & 6.00\times10^{-23} \end{bmatrix} \tag{5.57}$$

and

$$\sigma_{\tilde{P}_1} = 7.5 \times 10^{-12} \text{ (kg m}^2\text{)}, \tag{5.58}$$

$$\tilde{P}_2 = 7.5 \times 10^{-12} \text{ (kg m}^2\text{)} . \tag{5.59}$$

Using these values for the standard deviation of P_1 and P_2, it is then possible to calculate the average uncompensatable portion of the twice frequency output signal error containing contributions from P_1 and P_2. Using

$$\delta\left[\left|\dot{\omega}_{xs}\right|_{2\omega_s}\right] = \delta\left[\left|\dot{\omega}_{ys}\right|_{2\omega_s}\right] = 0.01 \text{ rad/sec}^2 \tag{5.60}$$

the results of Table V-6 are derived.

Table V-6

MAXIMUM UNCOMPENSATED OUTPUT TORQUE AT $2\omega_s$ DUE TO $\tilde{P}_1$ and $\tilde{P}_2$ †

Dynamic Component	Output Equation Component	$2\omega_s$ Output Torque Error (N m)
$\dot{\omega}_{xs}$	$\dot{\omega}_{xs}\tilde{P}_1$	7.5×10^{-14}
$\dot{\omega}_{ys}$	$\dot{\omega}_{ys}\tilde{P}_2$	7.5×10^{-14}
$\omega_x\omega_z$	$\omega_x\omega_z\tilde{P}_2$	3.71×10^{-14}
$\omega_y\omega_z$	$\omega_y\omega_z\tilde{P}_1$	3.71×10^{-14}

† True parameter values taken from Table IV-1.

The torque outputs specified in Table V-6 correspond to 0.02 and 0.01 EU based on the 1 EU torque calculation of (2.24).

17

C. PARALLEL FILTER EVALUATION OF P_{14} AND P_{17}

A set of parallel filters, in this case acceleration and torque filters, was also developed to estimate parameters P_{14} and P_{17} which are associated with instrument anisoelasticity. The OEP 1σ error estimates corresponded, in this case, to torque output errors of 0.40 EU for both P_{14} and P_{17}.

D. PHASE SENSITIVE DEMODULATION

The Kalman filter approach to parameter estimation discussed in Sects. B and C was one method of successfully identifying the OEP. Due to the complexity of the output torque signal and the high signal frequencies contained within that output, it was necessary to construct the filters with dynamics which were simplified as much as possible. This simplification resulted in oscillators which were able to smooth measurement data. One of the principal advantages of a Kalman filter, that of using a detailed mathematical model of the dynamic system which it estimates, was not included within the filters due to real time operating requirements. As a result, the filters functioned as signal demodulators. Signal demodulators which are accurate to approximately the same level as were the filters (0.1% to 0.01%) relative to parameter estimation are commercially available. A conceptual drawing of how a phase sensitive signal demodulator (PSSD) operates to provide an estimate of a parameter P which is associated with a sinusoidal carrier signal of known frequency ν is shown in Fig. V-2.

The same signal which drives the instrument output also drives the demodulator. This single forcing function avoids the problem of tuning error which accompanies the notch filters which are used with the parallel Kalman filters discussed in Sects. A and B. The single forcing function of Fig. V-2 keeps the instrument and demodulator precisely tuned. Instrument output for the case of Fig. V-2 is shown in Fig. V-3. In Fig. V-4, the PSSD inphase output is shown, along with the inphase square wave signal. The corresponding PSSD out-of-phase output signal and square

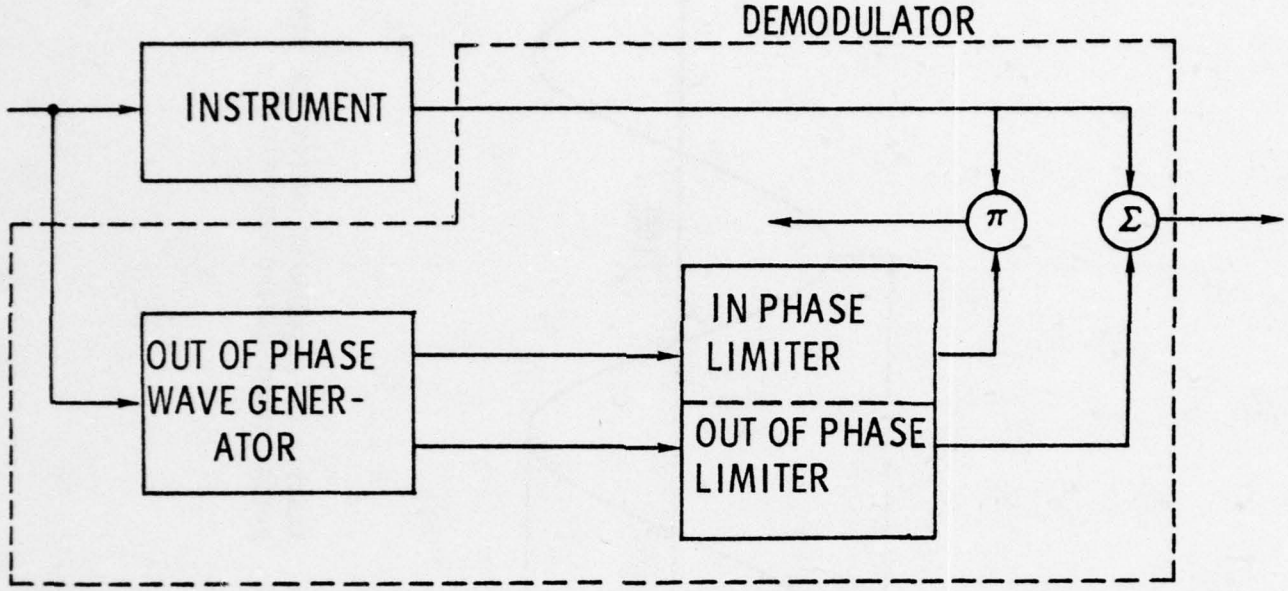


FIG. V-2 SCHEMATIC DRAWING OF A PHASE SENSITIVE SIGNAL DEMODULATOR

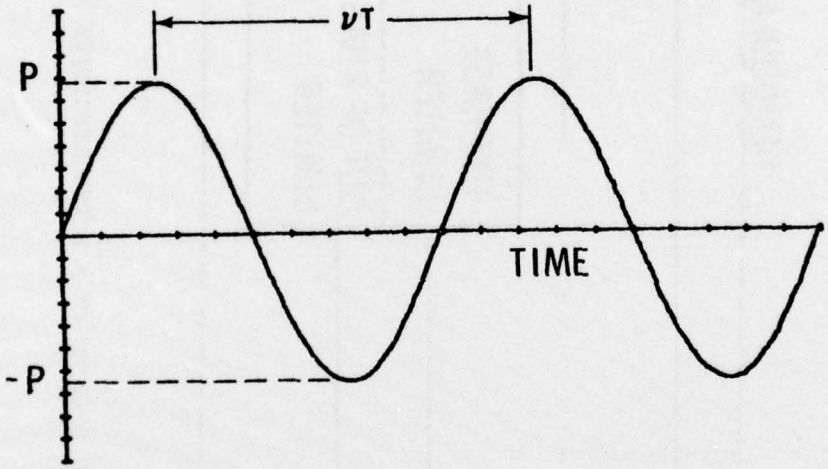


FIG. V-3 EXAMPLE OF INSTRUMENT OUTPUT FOR SINUSOIDAL INPUT HAVING FREQUENCY ν.

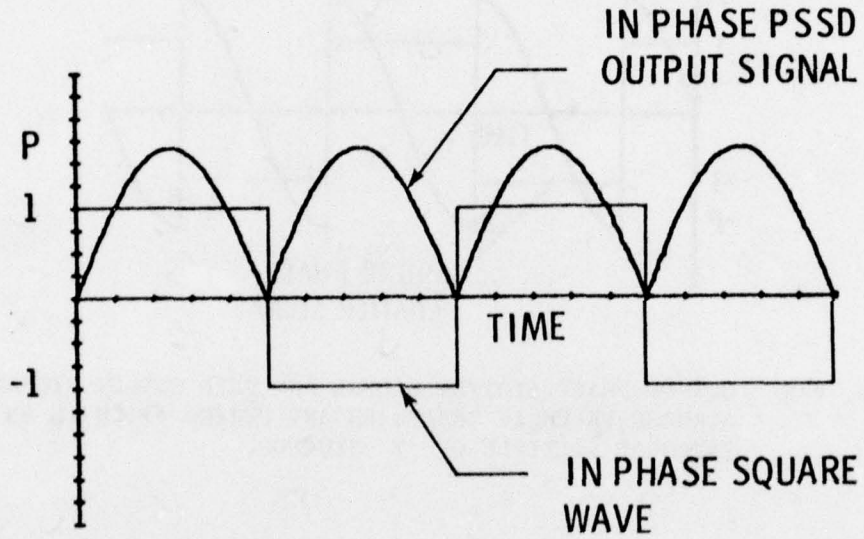


FIG. V-4 IN-PHASE LIMITER SIGNAL AND PSSD OUTPUT SIGNAL. Average value over any full period is $2/\pi$.

21

wave curves are shown in Fig. V-5. The mean value of the out-of-phase portion of the signal, when taken over a period which corresponds to an integer multiple of 2π radians remains zero so long as the phase angle change between forcing function input and instrument output is zero. So, for the zero phase shift case, multiplication of the inphase PSSD output by $(\pi/2)$ yields an estimate of P, the unknown parameter.

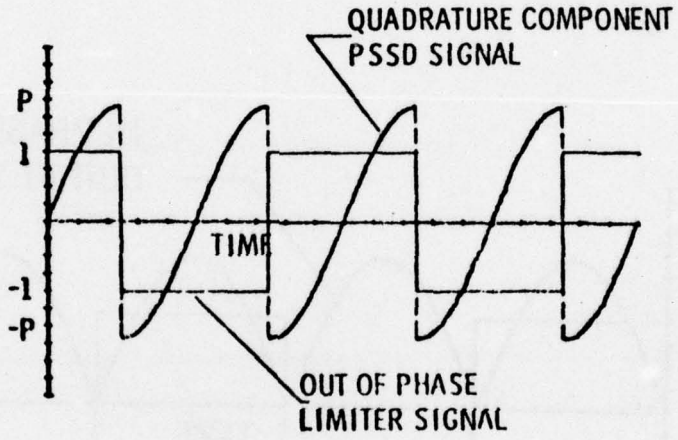


FIG. V-5 OUT-OF-PHASE LIMITER SIGNAL AND PSSD OUTPUT SIGNAL. AVERAGE VALUE IS ZERO OVER ANY PERIOD WHICH IS AN INTEGRAL MULTIPLE OF T SECONDS.

The PSSD approach to parameter estimation outlined above can be conveniently applied to estimation of RGG output effective parameters (OEPs). A schematic diagram showing a PSSD approach to P_1 and P_2 estimation is shown in Fig. V-6. The square wave limiters used in Fig. V-2 are replaced in Fig. V-6 by sinusoidal waves. Either type of wave--sinusoidal or square--can be mechanized. The sinusoidal wave provides for easier analysis of system performance. Examination of Fig. V-6 indicates that for the RGG, the out-of-phase component of PSSD output is nominally nonzero. This nonzero term is due to the fact that P_1 and P_2 have the same output frequency content but are separated in phase by 90 degrees, as shown by (4.50).

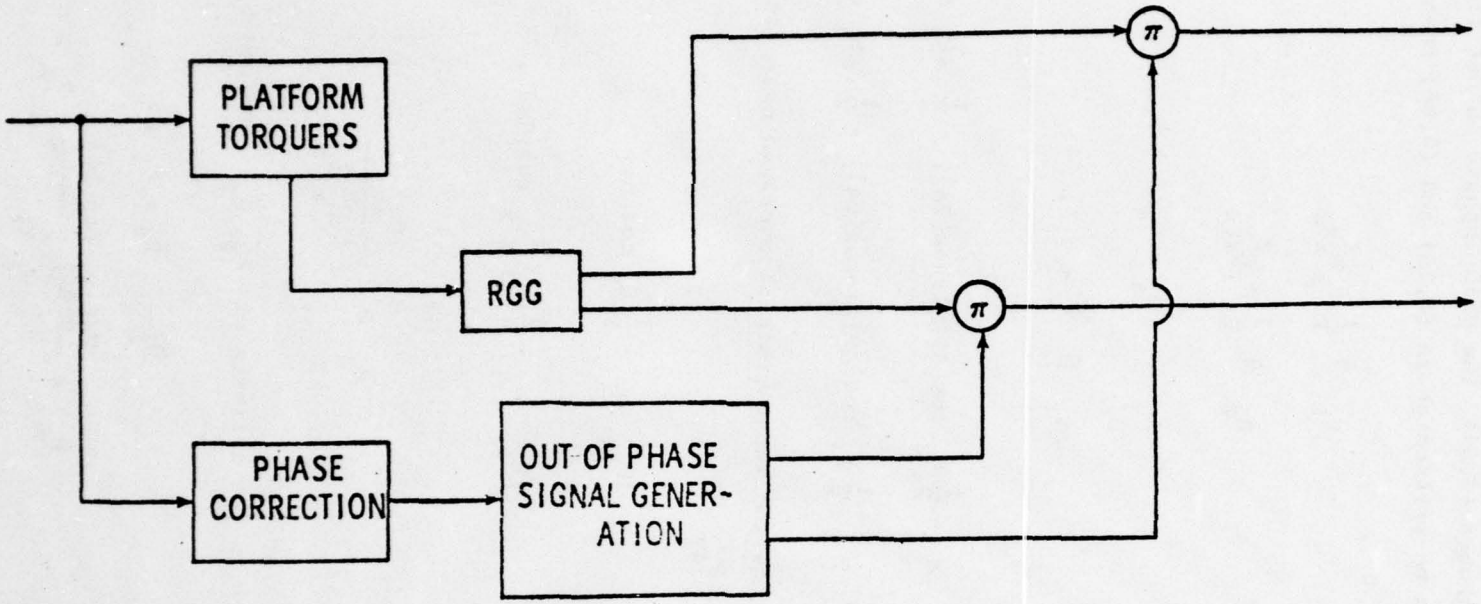


FIG. V-6 USE OF PSSD (phase sensitive signal demodulation) FOR RGG P_1 and P_2 ESTIMATION.

Using (5.61) through (5.64), the PSSD inphase output (IP) and out-of-phase output (OP) can be written as in (5.56) and (5.66) respectively.

$$B_1 \triangleq \frac{1}{2} P_1 \Omega_x^2 \nu_x \tag{5.61}$$

$$B_2 \triangleq \frac{1}{2} P_2 \Omega_x^2 \nu_x \tag{5.62}$$

$$A_+ \triangleq (\nu_x + \omega_s)t + \psi_+ \tag{5.63}$$

$$\Delta\psi_+ \triangleq \hat{\psi}_+ - \psi_+ \ . \tag{5.64}$$

$$IP = -\frac{1}{2} B_2 \cos(\Delta\psi)\{1-\cos(2A)\} - \frac{1}{2} \Delta\psi B_2 \sin(2A) \tag{5.65}$$

$$OP = \frac{1}{2} B_1 \cos(\Delta\psi)\{1+\cos(2A)\} - \frac{1}{2} \Delta\psi B_1 \sin(2A) \ . \tag{5.66}$$

Considering now the inphase signal averaged over $[4\pi/(\nu_x + \omega_s)]$ sec, the mean signal, IP_{av} is

$$IP_{av} = -\frac{1}{2} B_2 \cos(\Delta\psi) \tag{5.67}$$

or

$$IP_{av} = -\frac{1}{4} P_2 \Omega_x^2 \nu_x \cos(\Delta\psi) \ . \tag{5.68}$$

Hence,

$$\hat{P}_2 = \frac{IP_{av}}{-\frac{1}{2} \hat{\Omega}_x^2 \hat{\nu}_x} \ . \tag{5.69}$$

With the error in the estimate of P_2, $\tilde{P}_2$, defined by (5.20),

$$\tilde{P}_2 \triangleq \hat{P}_2 - P_2 \ , \tag{5.70}$$

$$\tilde{P}_2 = \frac{P_2 \Omega_x \nu_x \cos(\Delta\psi)}{\hat{\Omega}_x^2 \hat{\nu}_x} - P_2 \ . \tag{5.71}$$

Using the binomial theorem for expansion of the denominator of (5.71) and expressing $\cos(\Delta\psi)$ as a truncated Taylor series yields

$$\tilde{P}_2 = P_2\left[1 - \left(\frac{\tilde{\Omega}_x}{\Omega_x}\right)^2\right]\left[1 - \frac{\tilde{\nu}_x}{\nu_x}\right]\left[1 - \frac{\Delta\psi^2}{2}\right] - P_2 , \tag{5.72}$$

or, with higher order terms neglected,

$$\tilde{P}_2 = - P_2 \frac{\tilde{\nu}_x}{\nu_x} . \tag{5.73}$$

and

$$\sigma^2_{\tilde{P}_2} = P_2^2 \frac{\sigma^2_{\tilde{\nu}_x}}{\nu_x^2} . \tag{5.74}$$

Therefore, if the platform forcing frequency can be controlled to 0.01% accuracy, the parameter P_2 can be estimated to 0.01% accuracy using phase sensitive signal demodulation.

Using the out-of-phase component from the demodulator, a result corresponding to that of (5.74) can be developed for P_1. Demodulators can be used for estimation of all of the OEPs. The mechanizations are essentially the same as for P_1 and P_2 estimation. The parameters generally exist in frequency doubles, as did P_1 and P_2, one parameter being associated with inphase output, the second with the out-of-phase output. The estimation accuracy is 0.01% for all cases for sufficient averaging times. Several system 0.01% accuracy error outputs are listed in Table V-7. These results can be compared to the parallel filter results of Table V-6 and Sect. V-C.

Comparison of parallel filter and PSSD estimator performances show reasonable agreement for all cases listed except for P_{17}. This deviation is due to the fact that the filter estimation of P_{17} depends upon P_{14} estimation. With the PSSD, P_{17} is estimated independently of P_{14}.

Table V-7

MAXIMUM UNCOMPENSATED OUTPUT TORQUE DUE TO SIGNAL DEMODULATOR 0.01% PARAMETER ESTIMATE ERROR. (Parameter values taken from Table IV-1).

Dynamic Component	Output Equation Component	$2\omega_s$ Output Torque Error (N m)	$2\omega_s$ Output Torque Error (EU)
$\dot{\omega}_{xs}$	$\dot{\omega}_{xs}\tilde{P}_1$	1.0×10^{-14}	0.002
$\dot{\omega}_{ys}$	$\dot{\omega}_{yx}\tilde{P}_2$	1.0×10^{-14}	0.002
$\omega_x\omega_z$	$\omega_x\omega_z\tilde{P}_2$	5.0×10^{-15}	0.001
$\omega_y\omega_z$	$\omega_y\omega_z\tilde{P}_1$	5.0×10^{-15}	0.001
g^2	$\frac{1}{2} g^2\tilde{P}_{14}$	2.5×10^{-12}	0.700
g^2	$g^2\tilde{P}_{17}$	5.0×10^{-15}	0.001

E. COMMENTS ON THE PARALLEL FILTER AND PSSD APPROACHES TO OUTPUT EFFECTIVE PARAMETER ESTIMATION

The Kalman filter analysis presented in this chapter detailed an analytical approach to "steady state" variance estimation for systems which, using the standard approach to state variable definition, would have nonconstant coefficient matrices. For certain types of systems, variance levels can thereby be determined without digital covariance propagation. In addition, it was shown by using this procedure that a Kalman filter approach to OEP estimation would not provide better knowledge of the parameters than could be obtained using standard phase sensitive signal demodulation (PSSD) techniques.

Finally, although both approaches to parameter estimation indicated 1 EU performance capability, the error margin in both cases, due to P_{14},

was small. State of the art numbers were used, where available, for evaluation of estimator performance. Yet, in the single case of P_{14}, a 0.40 EU to 0.70 EU output error at the gravity gradient signal frequency ($2\omega_s$) remained. Based upon such marginal performance, it is apparent that simple numerical compensation of gravity gradiometer output, using either of these methods, is not an advisable method of instrument compensation. Two approaches to the solution of this problem are available.

1. Extensions of the basic PSSD approach to OEP estimation, including correlation techniques, should be considered. This analysis is provided in Chapter VI.

2. An approach to active parameter control should be developed. Active control of the OEP will allow instrument trim using an iterative procedure. Such an approach prevents a single, inordinately large parameter from corrupting the output signal to the extent where parameter estimation is ineffective. Active parameter control is developed in Chapters VII through IX.

Chapter VI

OUTPUT CORRELATION

A. INTRODUCTION

In Ch. V, Kalman filters and phase sensitive signal demodulators were evaluated for use as RGG (rotating gravity gradiometer) parameter estimators. Both were found to perform near the allowable 1 EU accuracy level required for the RGG. At this level both must be considered unadvisable approaches to single step estimation of system parameters and single step compensation of signal output. The margin between the accuracy required and the peak estimator accuracy capability is too small when the possibilities of unmodeled errors or excessive manufacturing errors are considered.

The broad band of frequencies contained within the RGG output prior to $2\omega_s$ filtering, and in particular, the fact that by proper selection of platform input it is possible to specify those frequencies, suggests a third approach to output effective parameter (OEP) identification. This third alternative is the method of output correlation. The correlation approach is similar to that of phase sensitive signal demodulation. Correlator mechanization is simpler than that of the parallel Kalman filters, but more complex than for PSSD. Various physical realizations are available for this approach, and the inputs to the correlator can be either random motion or known forced motion. The various options using correlation are discussed in this chapter.

B. OUTPUT CORRELATION CONCEPT

Consider the block diagram of Fig. VI-1 where, for convenience, the sensor output has been linearly modeled according to (4.38). The coefficient $\{K_0/K_1)/(1 + K_0/K_1 + K_0/K_2)\}$ is assumed known and compensated. The platform dynamics, as defined by the coefficients of the OEP of (4.38)

PRECEDING PAGE BLANK-NOT FILMED

are shown in Fig. VI-1, in the sensor reference system, as the variables x_1 through x_n.

Neglecting the gravity gradient torque, the differential torque output, ΔT, may be written as

$$\Delta T = \sum_{k=1}^{14} x_k P_k \quad . \tag{6.1}$$

To estimate the j^{th} parameter, P_j, the switch of Fig. VI-1 is closed to the j^{th} sensor dynamic component and the products x_j^2 and $\mathcal{J}_j$ are formed. It is assumed that data are collected over a long enough period such that any correlations among the dynamics, i.e., $\dot{\omega}_x$, $\dot{\omega}_y$, a_x are negligible. Under these conditions, the expression

$$\mathcal{J}'_j = \int_o^{t_f} x_j \sum_{k \neq j} P_k x_k \, dt \tag{6.2}$$

approaches zero. After a certain time τ,

$$\mathcal{J}_j = \int_o^{t_f} (\Delta T) x_j \, dt \tag{6.3}$$

and from (6.2)

$$\mathcal{J}_j \approx P_j \int_o^{t_f} x_j^2 \, dt \quad . \tag{6.4}$$

Hence, $\hat{P}_j$, the estimate of P_j, is

$$\hat{P}_j = \frac{\mathcal{J}_j}{\int_o^{t_f} x_j^2 dt} \quad . \tag{6.5}$$

AD-A048 252 STANFORD UNIV CALIF GUIDANCE AND CONTROL LAB F/G 8/5
STUDY TO DEVELOP GRADIOMETER TECHNIQUES.(U)
JUN 77 D B DEBRA, E J PELKA F19628-74-C-0162
UNCLASSIFIED AFGL-TR-76-0297 NL

3 OF 4
AD
AD48252



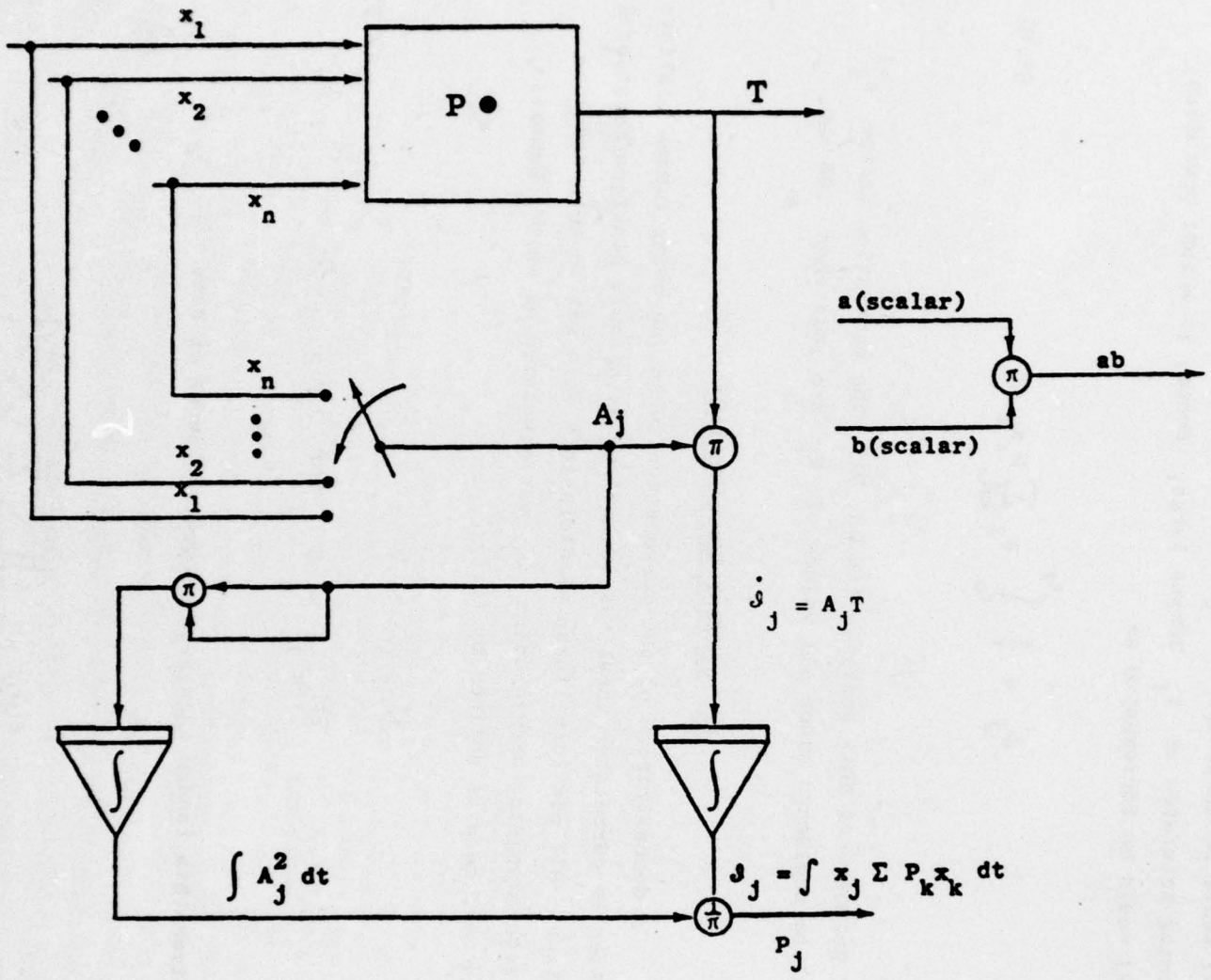


FIG. VI-1 IDENTIFICATION OF P_j VIA OUTPUT CORRELATION

Under conditions of actual operation, all of the integrals in (6.2) to (6.5) would be modulated by t_f^{-1} so as to prevent the integrator from becoming saturated as t_f became large. Hence, in actual operation, (6.2) would be implemented as

$$\mathcal{J}_j' = \frac{1}{t} \int_o^{t_f} x_j \sum_{k \neq j} P_k x_k \, dt \tag{6.6}$$

For purposes of this analysis (in Ch. VI), the modulation factor t_f^{-1} will be neglected since all values of t_f are less than 100 sec.

C. CONCEPT DEMONSTRATION

A demonstration of the correlation technique using random platform jitter as correlator input was mechanized using only platform rotational motion. All platform linear accelerations were set to zero and each platform angular acceleration $\dot{\omega}_j$ was simulated as white, Gaussian, and zero mean as defined by (6.7).

$$\begin{aligned} \mathcal{E}[\omega_j \omega_j] &= 0 \\ \mathcal{E}[\omega_k \omega_j] &= 0 \quad \text{for } j \neq k \,. \end{aligned} \tag{6.7}$$

Given this random angular acceleration input at some time t,

$$\mathcal{E}(\mathcal{J}_j) = \mathcal{E}\left\{ \int_o^t x_j \sum_{k=1}^{14} P_k x_k \, dt \right\} . \tag{6.8}$$

Assuming the interchangeability of the integral, expected value, and summation operators, (6.8) becomes

$$\delta(\vartheta_j) = \int_o^t \Sigma\delta(x_j P_k x_k)dt \ . \qquad (6.9)$$

Finally, due to the independence assumed for the $\dot{\omega}_k$, (6.9) reduces to

$$\delta(\vartheta_j) = \int_0^t P_j q_j \, dt \qquad (6.10)$$

and

$$\hat{P}_j = \delta(\vartheta_j) \,/\, \delta\left(\int x_j^2 \, dt\right). \qquad (6.11)$$

C-1 Simulation

A trial estimation of P_1 was performed, where

$$P_1 \triangleq \Delta I_{xz} - (m_o \rho_{xo} \rho_{zo} - m_e \rho_{xe} \rho_{ze}) \ . \qquad (6.12)$$

Implementation of this identification process req[illegible]s formulation of instrument dynamics ($\dot{\omega}_x$, $\dot{\omega}_y$, etc.) as functions of measured platform dynamics where

$$\dot{\omega}_x = \dot{\omega}_{xP} \cos\theta + \dot{\omega}_{yP} \sin\theta \ , \qquad (6.13)$$

$$\dot{\omega}_y = -\dot{\omega}_{xP} \sin\theta + \dot{\omega}_{yP} \cos\theta \ , \qquad (6.14)$$

$$\dot{\omega}_z = \dot{\omega}_{zP} \ . \qquad (6.15)$$

The statistical assumptions upon platform angular accelerations were

$$\dot{\omega}_{kP} = G(0, q_k) \qquad (6.16)$$

the $\dot{\omega}_{kP}$ taken as pairwise independent.

With only platform rotational motion allowed, the integral of (6.2) reduces to (6.17).

$$\delta(\mathcal{J}) = \int \delta \left\{ \begin{array}{l} P_1[\omega_{xP} - \omega_{yP}\omega_z]\cos\theta + P_1[\omega_{yP} + \omega_{xP}\omega_z]\sin\theta \\ -P_2[\omega_{xP} - \omega_{yP}\omega_z]\sin\theta + P_2[\omega_{yP} + \omega_{xP}\omega_z]\cos\theta \\ +P_3\,\dot{\omega}_{zP} \\ +P_4[(\omega_{xP}^2 - \omega_{yP}^2)\cos 2\theta + 2\omega_{xP}\omega_{yP}\sin 2\theta] \\ +P_5[\tfrac{1}{2}(\omega_{yP}^2 - \omega_{xP}^2)\sin 2\theta + \omega_{xP}\omega_{yP}\cos 2\theta] \end{array} \right\} \left\{ \begin{array}{l} \omega_{xP}\cos\theta \\ +\omega_{yP}\omega_t\cos\theta \end{array} \right\} dt \,. \qquad (6.17)$$

Specialization of the diagram of Fig. VI-1 to the randomly forced P_1 estimation case is shown in Fig. VI-2. Theoretically,

$$\lim_{t_f \to \infty} \mathcal{J} = \lim_{t_f \to \infty} \int_o^{t_f} P_1[\dot{\omega}_{xP} + \omega_{yP}\omega_z]^2 \cos^2\theta \, dt \,. \qquad (6.18)$$

The degeneration of $\mathcal{J}$ from (6.2) to (6.3) depends upon the statistical independence of the ω_{kP} as well as the functional orthogonality of the sine and cosine functions. The results of the test simulation are shown graphically in Fig. VI-3. The test case was scaled such that all P_k were equal to 1. From the simulation,

$$\hat{P}_1 = 0.943 \text{ (units)} \qquad (6.19)$$

after 5 sec, and the error $\tilde{P}_1$ in the estimate of P_1 is

$$\tilde{P}_1 = 0.057 \text{ (units)} = 5.5\% \,. \qquad (6.20)$$

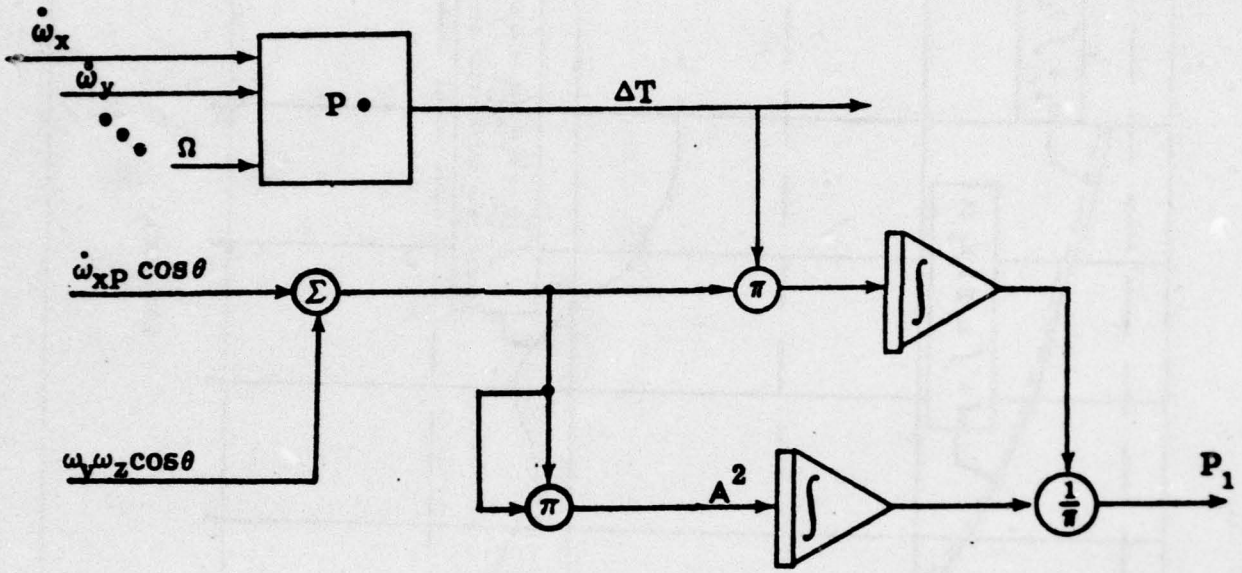


FIG. VI-2 IDENTIFICATION OF P_1 VIA OUTPUT CORRELATION.

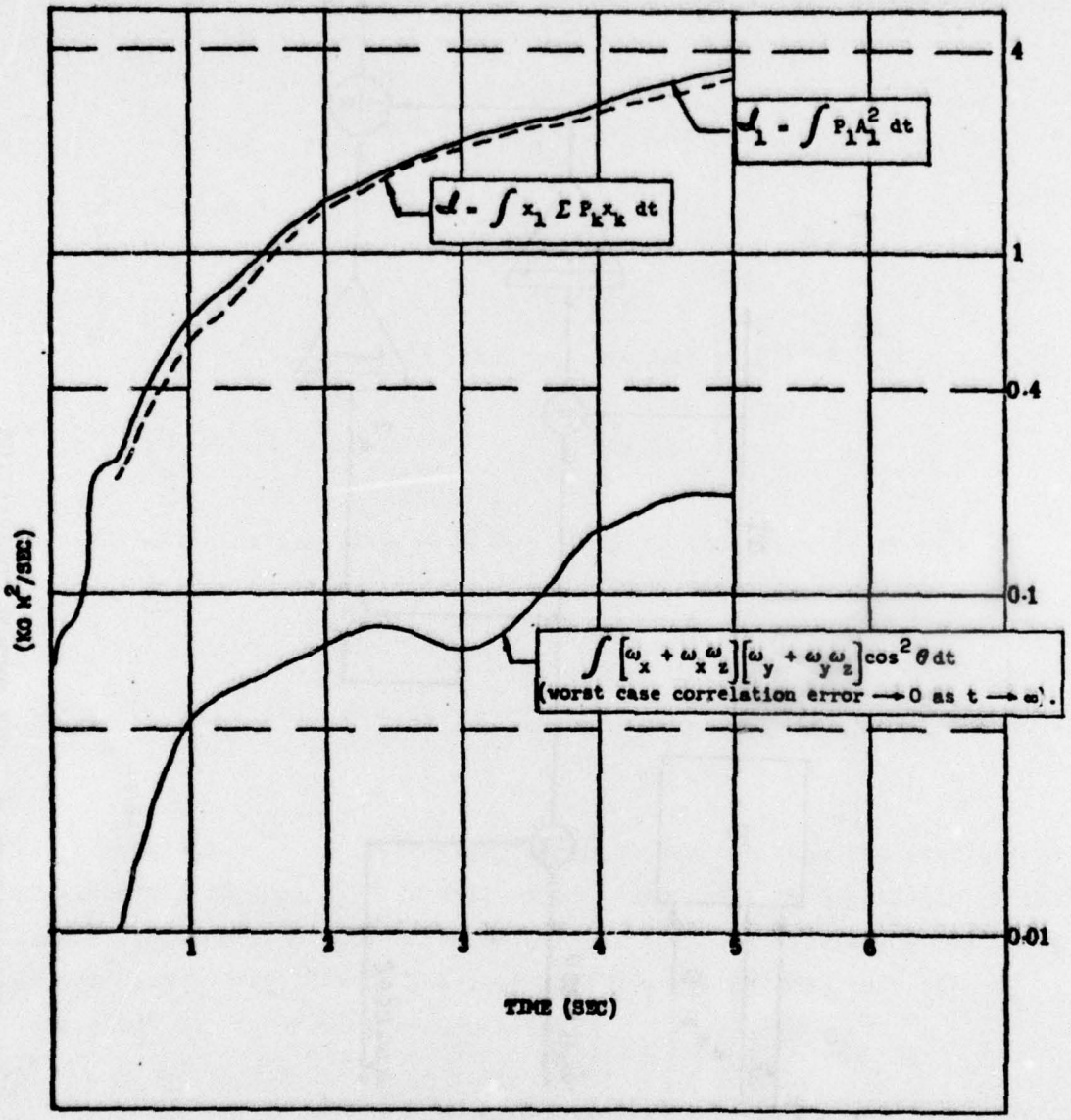


FIG. VI-3 TIME HISTORY OF INTEGRATOR OUTPUT FOR ESTIMATION OF P_1

8

D. THE EFFECTS OF CORRELATED RANDOM INPUT ON ESTIMATOR PERFORMANCE

Given that the RGG is equipped with an active parameter control system, the random input correlator described in Sect. VI-C provides relatively accurate parameter estimates in short periods of time, with the parameter estimates serving as error signals for the controller. Correlator performance levels, however, are based upon the assumption of independence among the random inputs. Numerous mechanisms, such as sinusoidal aircraft vibrations and vibration isolator axis-to-axis dynamic coupling, can be postulated for which the random vibrations sensed by the platform gyros and accelerometers are not independent. To demonstrate the effects of input coupling, consider again the test case of Sect. C, but with the added assumption that

$$\dot{\omega}_{yP} = \dot{\omega}_{yPR} + u\dot{\omega}_{xP} \tag{6.21}$$

where

$\dot{\omega}_{yPR}$ $\triangleq$ a random angular acceleration input about the $\hat{Y}_P$ axis which is uncorrelated with both $\dot{\omega}_{xP}$ and $\dot{\omega}_{zP}$,

u $\triangleq$ a nonzero coupling coefficient which represents the correlation between $\dot{\omega}_{xP}$ and $\dot{\omega}_{yP}$.

Under this condition of random input dependence, (6.17) becomes

$$\lim_{t\to\infty} \delta(\vartheta) = \lim_{t\to\infty} \int_0^{t_f} P_1[\omega_{xP} + \omega_{yP}\omega_{zP}]^2 \cos^2\theta \, dt + \lim_{t\to\infty} \int_0^{t_f} P_2 u \omega_{xP}^2 \cos^2\theta \, dt . \tag{6.22}$$

The second term of (6.22) is the error in the correlator output signal which arises due to the correlated input. Based upon the angular rate and acceleration errors specified in Table III-1, the term $\omega_{yP}\omega_z$

can be of approximately the same magnitude as $\dot{\omega}_{xp}$. With this approximation, the error due to correlation, $\tilde{P}_{1c}$, may be written as

$$\tilde{P}_{1c} \approx P_2 u \,. \tag{6.23}$$

Based upon this result, it is concluded that the random input correlator is a feasible approach to OEP estimation only if relatively low correlation levels exist among the platform jitter signals. Implementation of this approach would require a validation program which would guarantee the independent nature of the random input.

E. THE FORCED INPUT CORRELATOR. DEFINITION OF THE CORRELATION FUNCTION

An alternative approach to the random input correlator which would provide acceptable parameter estimates without overly complicating either the mathematical model or the actual correlator hardware was developed based upon the idea of forced platform motion. Using measured platform jitter levels as a design constraint, known platform inputs at least one order of magnitude greater than the jitter levels would dominate the RGG output and reduce the significance of the random motion upon RGG output to a tolerable level (approximately 5% error in parameter estimate for 50% random signal correlation).

The forced input correlation technique was designed specifically to take advantage of the known frequency content of the RGG output, and the calculable effect of known platform motion upon this output. To this end, the random platform vibrations were replaced by known platform rate and acceleration inputs. This change resulted in a set of predetermined correlation functions, all of which appear in the instrument output torque, (4,50). In addition, the simple integrators of Fig. VI-2 were replaced by multiple lag networks so as to speed estimate convergence and minimize the effect of integrator biases. Several modifications to this basic system were also considered and are discussed in detail in this section.

E.1 The L^2 (Second Order Lag) System: The Basic Forced Input Correlator

Consider again the instrument output error torque as written in (4.38), and consider the case of P_{14} estimation as an example. For a given known platform, linear acceleration input in the direction of $\hat{x}_p$ and having a sinusoidal form with frequency α_x, there are five distinct output frequencies associated with P_{14}, one of the elasticity related parameters. These frequencies are specified in Table IV-3. Each of these frequencies is a candidate correlation frequency except $2\omega_s$, the gravity gradient signal frequency. Selection of a particular correlation frequency, f_c given that α_x and ω_s are fixed, is based upon the type of correlator to be implemented and the resultant correlation function. For digital correlator implementation, the lower frequencies offer the advantage of minimizing digital processor execution time. For an analog implementation, the higher frequencies speed real time estimate convergence. For estimation of P_{14}, $(2\omega_s - \alpha_x)$ has been selected as the correlation frequency. Selection of f_c as $(2\omega_s \pm \alpha_x)$ provides a correlation function having maxima which are large compared to A_x^2. The L^2 system for P_{14} estimation is shown in Fig. VI-4, and the correlation function A is

$$A = \cos[(2\omega_s - \alpha_x)t + \varphi] . \tag{6.24}$$

The correlation frequency $(2\omega_s - \alpha_x)$ is one of two frequencies associated with the P_{14} $(gA_x/2)$ coefficient of (4.50). The phase angle φ is included as compensation for a signal lag between the platform and sensor and in practice, must be estimated. For purposes of analysis, however, the angle φ may be associated with the error signal component at $(2\omega_s - \alpha_x)$ rather than with A. The effect of an error in φ, the estimate of $\hat{\varphi}$, at the correlation frequency is to reduce the magnitude of the estimate of $\hat{P}_{14}$ by a factor of $(1 - \cos \tilde{\varphi})$ where

$$\tilde{\varphi} \triangleq \hat{\varphi} - \varphi . \tag{6.25}$$

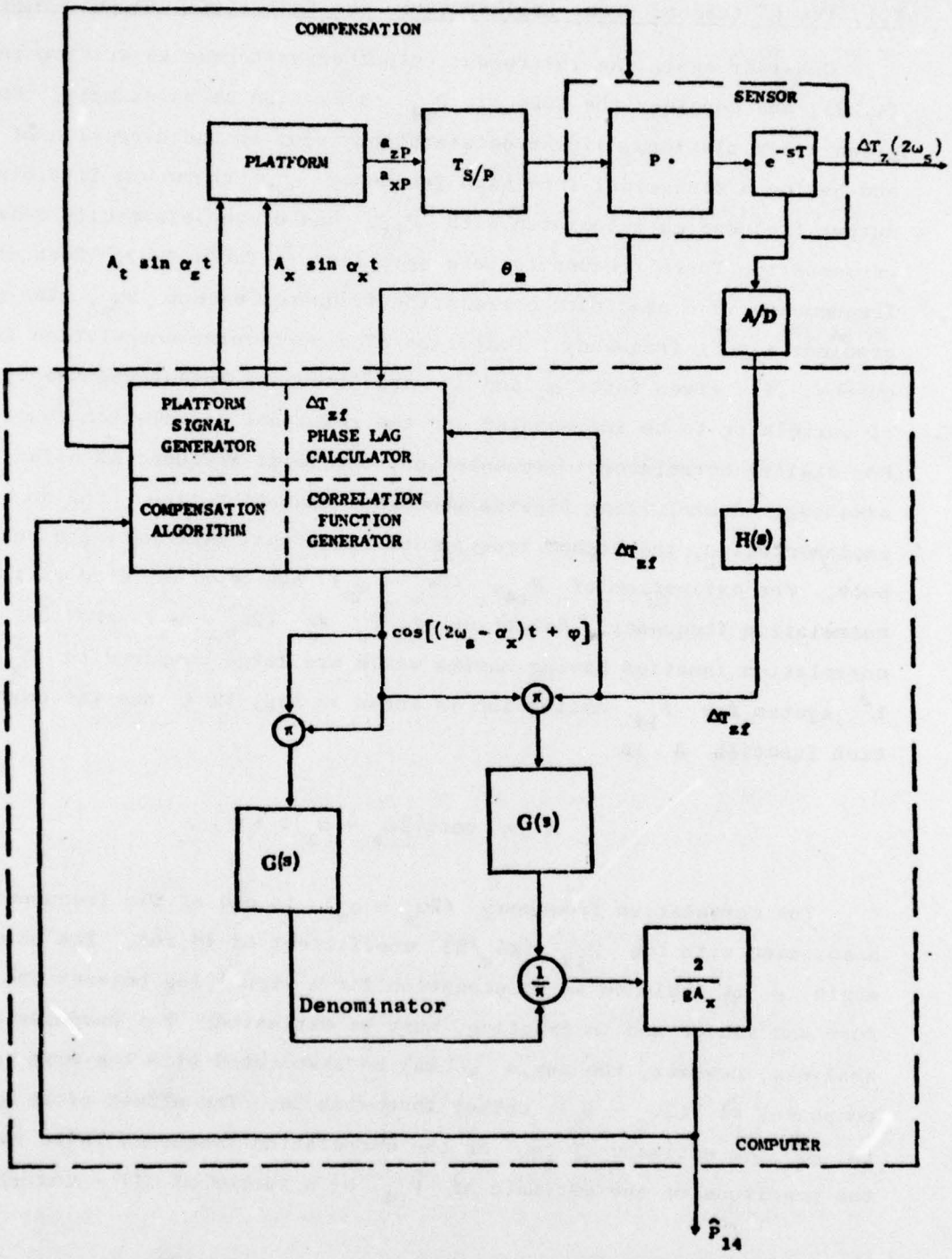


FIG. VI-4 P_{14} IDENTIFICATION VIA THE L^2 SYSTEM

For all other frequencies, $\tilde{\varphi}$ simply shifts the output phase of the oscillatory terms. Making this assumption for φ, the correlated output torque may be written as

$$T(s) = \mathcal{L}\left\{\Delta T_z \cos[f_c t]\right\}\frac{a}{(s+a)^2} . \tag{6.26}$$

For purposes of numerical analysis, the break frequency has been set to 1 rad/sec. The output filter H for the L^2 system is equal to 1, while G(s) has the form

$$G(s) = \frac{a}{(s+a)^2} . \tag{6.27}$$

In addition to the second order lag (L^2) system, several other forced input correlators, using different forms of G and H were developed and evaluated. These various mechanizations are listed in Table VI-1 and discussed in subsequent sections of this chapter.

The product of the RGG output, ΔT_{zf} (Fig. VI-4), and the correlation function A produces a constant term and, with forcing functions as specified in Ch. IV, many sinusoids. The constant term is used to determine the OEP of interest. The sinusoids are noise in the correlator output and corrupt the quality of the parameter estimate.

The RGG error equation, (6.50) has the form

$$\Delta T = P_k \sin \mu t + P_j \cos \mu t + P_m \sin \rho t + \cdots . \tag{6.28}$$

With correlation function A defined as

$$A = \sin(\mu t) \tag{6.29}$$

the product of (6.28) and (6.29) is

13

Table VI-1

FORCED INPUT CORRELATOR MECHANIZATIONS

Type	G(s)	H(s)	Remarks
Basic Integrator	$\frac{1}{s}$	1	Concept only
Second Order Lag	$\frac{a^2}{(s+a)^2}$	1	Section VI:E-1
Frequency Discrimination	$\frac{a^2}{(s+a)^2}$	$\frac{s^2 + 2\xi_N \omega s + \omega^2}{s^2 + 2\xi_D \omega s + \omega^2}$	Section VI:E-2
Integrated Second Order Lag	$\frac{a^2}{s(s+a)^2}$	1	Concept only Section VI:E-3
Sixth Order Lag	$\frac{a^6}{(s+a)^6}$	1	Section VI:E-

$$A \times \Delta T = P_k \sin^2 \mu t + P_j \sin \mu t \cos \mu t + P_m \sin \mu t \sin \rho t + \cdots . \quad (6.30)$$

Of the three terms on the right side of (6.30), only the first has a zero frequency or d-c component for the case where μ and ρ are unequal. After the correlator product $(A \times \Delta T)$ is formed, it is passed through the second order lag which filters the high frequency noise. In Table VI-2 the various components of the L^2 system correlator output are written in both the Laplace and time domain. The frequency ω_b is used as a dummy variable to represent the different frequencies which result from correlation. The purpose of the Table is to demonstrate the effect of the correlator on the RGG output, showing the constant term which can be associated with a particular OEP. The purpose of transfer function $G(s)$ is to increase the signal-to-noise ratio at the output of the correlator. Row 1 of Table VI-2 represents that portion of the correlated output function ϑ associated with the estimated parameter P_{14} at zero frequency. Not all the terms of Rows 2 and 3 possess exponential decay, implying that the correlated output, ϑ, will maintain oscillatory residuals which persis within a magnitude ratio envelope which is nondiminishing with respect to the zero frequency term. Based upon instrument design specifications and typical parameter values as listed in Ch. IV, analysis of the L^2 system indicates less than a 1 order of magnitude improvement in the quality of parameter estimates as compared to the PSSD. Using the L^2 system as a baseline, five alternatives exist for improvement of correlation technique performance:

1. Manufacturing specifications can be set to a standard such that the parameters accompanying the oscillatory residuals allow adequate estimation of the desired parameter;
2. A frequency discrimination (notch) filter may be added to the loop prior to correlation which possesses a center frequency at f_c;
3. Additional integrators can be inserted into the estimation loop to augment the low pass filter;

Table VI-2 SECOND ORDER LAG CORRELATOR FUNCTIONS

Row	Form of Term in Correlator Product	Laplace Transform of Correlator Product Term	Laplace Transform of Filtered Correlator Output	Time Domain Representation of Filtered Correlator Output	Remarks
1	$1(t)$	$\frac{1}{s}$	$\frac{1}{s(s+\sigma_a)^2}$	$\frac{1}{\sigma_a^2}\{1 - e^{-\sigma_a t}\} - \frac{1}{\sigma_a} te^{-\sigma_a t}$	d-c term is useful correlator output
2	$\sin(\omega_b t)$	$\frac{\omega_b}{s^2 + \omega_b^2}$	$\frac{\omega_b}{(s^2+\omega_b^2)(s+\sigma_a)^2}$	$\frac{2\omega_b\sigma_a}{b^4} e^{-\sigma_a t} + \frac{\omega_b}{b^2} te^{-\sigma_a t}$ $+ \frac{\sigma_a^2 - \omega_b^2}{b^4} \sin(\omega_b t)$ $- \frac{2\sigma_a\omega_b}{b^4} \cos(\omega_b t)$;	All terms are noise. Not all terms possess exponential decay.
3	$\cos(\omega_b t)$	$\frac{s}{s^2 + \omega_b^2}$	$\frac{s}{(s+\sigma_a)^2(s^2+\omega_b^2)}$	$-\frac{2\sigma_a^2}{b^4} e^{-\sigma_a t} + \{\frac{1}{2}\}\{1-\sigma_a t\} e^{-\sigma_a t}$ $+ \frac{\sigma_a^2 - \omega_b^2}{b^4} \cos(\omega_b t)$ $+ \frac{2\sigma_a\omega_b}{b^4} \sin(\omega_b t)$.	All terms are noise. Not all terms possess exponential decay.

$$b^2 = \sigma_a^2 + \omega_b^2$$

4. The order of the low pass filter can be increased (this is only a slight variation from method 3);

5. An active parameter compensation control system can be designed and implemented which would relax requirements on parameter estimation.

Since state of the art manufacturing techniques have already been assumed for instrument manufacturing specifications, only the last four items of the alternatives list could be implemented.

E-2 The Frequency Discrimination Filter Correlator

The form of the discrimination filter correlator is specified in Table VI-1. The notch at the correlation frequency is intended to minimize RGG output signals at frequencies other than the correlation frequency, f_c. Analysis of this system indicates that errors associated with frequency tuning and sensor orientation offset the advantages gained with the notch filter. The frequency discrimination filter was therefore not pursued beyond the initial analysis.

E-3 The IL^2 System (Integrated Second Order Lag)

The IL^2 system is defined in Table VI-1. This mechanization simply integrates the output of the L^2 system. The significant contribution of the additional integrator is related to the integrator's effect upon the zero frequency portion of the low pass filter output, changing this zero frequency term from a constant into a ramp function. The ramp continually reduces the significance of the extraneous oscillatory terms associated with the residual sinusoidal functions. The components and transformations associated with the IL^2 system are given in Table VI-3.

Transformation of Row 1 of Table VI-3 displays the expected effect upon the output of the correlation loop due to the addition of a pure integration. It is also noted that this integration produces zero frequency terms in transformation of Row 2. Additional pure integrations extend the biases of Table VI-3 into ramps, parabolas, etc. The zero frequency term of transformation 2 is proportional to ω_b^{-1}, where, for the sample case being considered (P_{14} estimation), ω_b has the value of 132 rad/sec. Hence, with linear signal growth in transformation 2,

TABLE VI-3 INTEGRATED SECOND ORDER LAG CORRELATOR FUNCTIONS

Row	Form of Term in Correlator Product	Laplace Transform of Correlator Product Term	Laplace Transform of Filtered Output	Time Domain Representation of Filtered Correlator Output.	Remarks
1	$1(t)$	$\frac{1}{s}$	$\frac{1}{s^2(s+\sigma_a)^2}$	$-\frac{2}{\sigma_a^3}(1-e^{-\sigma_a t}) + \frac{1}{\sigma_a^2} t\{1+e^{-\sigma_a t}\}$	Ramp function is useful information
2	$\sin(\omega_b t)$ $b^2 = \sigma_a^2 + \omega_b^2$	$\frac{\omega_b}{(s^2+\omega_b^2)}$	$\frac{\omega_b}{s(s^2+\omega_b^2)(s+\sigma_a)^2}$	$\frac{\omega_b}{\sigma_a^2\omega_b^2} - \omega_b\left\{\frac{t}{\sigma_a(\sigma_a^2+\omega_b^2)} + \frac{2\sigma_a^2+(\sigma_a^2+\omega_b^2)}{\sigma_a^2(\sigma_a^2+\omega_b^2)^2}\right\}e^{-\sigma_a t}$ $-\frac{(\sigma_a^2-\omega_b^2)\omega_b}{\omega_b^2(\sigma_a^2+\omega_b^2)^2}\cos\omega_b t$ $-\frac{2\sigma_a\omega_b^2}{\omega_b^2(\sigma_a^2+\omega_b^2)^2}\sin\omega_b t$	All terms are noise.
3	$\cos(\omega_b t)$	$\frac{s}{s^2+\omega_b^2}$	$\frac{1}{(s^2+\omega_b^2)(s+\sigma_a)^2}$	Refer to Transformation 2 of Table VI-2.	All terms are noise.

a six order-of-magnitude separation between the parameter estimate signal and the zero frequency error terms implies a convergence time of approximately 7.5×10^3 sec ($\approx$ 2 hours). Implementation of additional pure integrations could reduce the time required at the expense of numerical accuracy due to the introduction of additional integrator biases and computational dynamic range problems.

E-4 Higher Order Filters: The L^6 (Sixth Order Lag) System

The higher order filter is a logical extension of IL^2 system. The second order lags, $(s + a)^{-2}$ are replaced by $(s + a)^{-n}$ as shown in Table VI-1. In the Laplace domain, the functions of interest with respect to correlator output error are

$$\frac{Ks + m}{(s^2+\omega^2)(s+\alpha)^n} = \frac{A_1}{s + j\omega} + \frac{A_2}{s - j\omega} + \sum_{i=1}^{n} \frac{B_i}{(s + \alpha)^i} \qquad (6.31)$$

and

$$\frac{1}{s(s + \alpha)^n} = \frac{C_1}{s} + \sum_{i=1}^{n} \frac{D_i}{(s + \alpha)^i} \quad . \qquad (6.32)$$

With $\eta_1(s)$ and $\eta_2(s)$ defined by

$$\eta_1(s) \triangleq \frac{Ks + m}{(s^2 + \omega^2)(s + \alpha)^n} \qquad (6.33)$$

$$\eta_2(s) \triangleq \frac{1}{s(s + \alpha)^n} \qquad (6.34)$$

the functions exist within the time domain as given by (6.35) and (6.36).

$$\eta_1(t) = 2|A_1| \cos(\omega t + \angle A_1 + e^{-\alpha t} \sum_{i=1}^{n} B_i \frac{t^{i-1}}{(i-1)!} \qquad (6.35)$$

$$\eta_2(t) = c_1 + e^{-\alpha t} \sum_{i=1}^{n} D_i \frac{t^{i-1}}{(i-1)!} \quad . \qquad (6.36)$$

The significant error associated with the correlated torque output is proportional to $|A_1|$. Furthermore, $|A_1|$ is inversely proportional to $(s + a)^n|_{s=j\omega}$.

It is possible that for certain special case relationships of the OEP, a second order lag system, the L^2 system, would be adequate for parameter estimation. However, evaluation of estimator performance with parameter errors set to approximately 2 orders of magnitude greater than design specifications indicate the advisability of a higher order filter since some of the associated output frequencies are separated from each other by as little as $0.1\ \omega_s$. A 6th order system has been found adequate for parameter estimation under these conditions. Coefficients A, B, C, and D of equations (6.35) and (6.35) for a 6th order system are given in (6.37) through (6.46).

$$|A_1| = \left| \frac{m - jK\omega}{(-j^2\omega)(\alpha + j\omega)^6} \right| \qquad (6.37)$$

$$\angle A_1 = \tan^{-1}[\mathfrak{Im}(A_1)/R_e(A_1)] \qquad (6.38)$$

$$B_6 = (Ks + m)(s^2 + \omega^2)^{-1}\Big|_{s=-\alpha} \tag{6.39}$$

$$B_5 = (s^2+\omega^2)\ \{K - 2s(Ks+m)(s^2+\omega^2)^{-1}\}_{s=-\alpha} \tag{6.40}$$

$$= (s^2+\omega^2)^{-2}\{-2m - 6Ks + 4s^2(Ks+m)(s^2+\omega^2)^{-1}\}_{s=-\alpha} \tag{6.41}$$

$$B_3 = (s^2+\omega^2)^{-3}\{(6Ks+2m+K)4s^2 - (16s+8K)s^3(Ks+m)(s^2+\omega^2)^{-1}\}_{s=-\alpha} \tag{6.42}$$

$$+ (s^2+\omega^2)^{-2}\{-6K + 8s(Ks+m)(s^2 + \omega^2)^{-1}\}_{s=-\alpha}$$

$$B_2 = (s^2+\omega^2)^{-4}\left\{\begin{matrix} s^3[-176Ks-64m - 8K^2-24K] \\ -4s^4(16s+8K)(Ks+m)(s^2+\omega^2)^{-1} - 3s^3(16s+8K)(Ks+m)\end{matrix}\right\} \tag{6.43}$$

$$+(s^2+\omega^2)^{-3}\ \{72Ks^2 + 8s(2m + K)\}$$

$$B_1 = -8s(s^2 + \omega^2)^{-5}\left\{\begin{matrix} s^3[-176Ks-64m-8K^2-24K] \\ -4s^4(16s+8K)(Ks+m)(s^2+\omega^2)^{-1} \\ -3s^3(16s+8K)(Ks+m)\end{matrix}\right\} \tag{6.44}$$

$$+ (s^2 + \omega^2)^{-4}\left\{\begin{matrix} 3s^2[-176Ks-64m - 8K^2-24K] - 176Ks^3 \\ -16s^3(16s+8K)(Ks+m)(s^2+\omega^2)^{-1} \\ -64s^3(Ks+m)(s^2+\omega^2)^{-1} - 4Ks^4(16s+8K)(s^2+\omega^2)^{-1} \\ +8s^5(16s+8K)(Ks+m)(s^2+\omega^2)^{-2} \\ -9s^2(16s+8K)(Ks+m) - 48s^4(Ks+m) - 3Ks^3(16s+8K)\end{matrix}\right\}$$

$$- 3(s^2 + \omega^2)^{-4}\ [72Ks^2 + 8s(2m + K)]$$

$$+ (s^2 + \omega^2)^{-3}\ [144Ks + 8(2m + K)]\Big|_{s=-\alpha} .$$

21

$$c = \alpha^{-6} \tag{6.45}$$

$$D_i = -\alpha^{-(7-i)} \, . \tag{6.46}$$

The 6th order lag system has been used to demonstrate correlation technique parameter estimation in Sect. G. However, prior to exercising this procedure it was necessary to determine a set of platform inputs which would permit identification of all output *effective parameters*.

F. PLATFORM INPUT FREQUENCY SELECTION

Proper platform input frequency selection is critical to the success of the correlation technique. Care must be taken to insure the integrity of each selected output channel such that correlation results in a zero frequency term associated with only the desired OEP in each separate case. The problem is accentuated by the requirement that these outputs be generated simultaneously over separate channels so as to minimize the time per iteration required to establish a set of parameter estimates.

F-1 The Correlation Functions

In order to demonstrate the existence of at least one set of platform inputs satisfying (4.45) through (4.48) while permitting estimation of all OEPs, the correlation functions which appear in (4.50) have been rewritten and identified by number in Table VI-4. Those correlation functions marked with a dagger (†) have been selected for use in parameter identification although such selection is not restricted to these functions. The 40 functions of Table VI-4 were coded on to a computer routine and various sets of platform frequencies for ω_x, α_x, and α_z were tested. Ranges for these frequencies were $0.1\ \omega_s$ to $0.8\ \omega_s$ and incrementation was set at $0.1\ \omega_s$. A large group of acceptable candidate frequency sets was found. Each acceptable group yielded a nimimum frequency term other than the desired zero frequency term of $0.1\ \omega_s$. Six such sets are given in Table VI-5. The first set of platform frequencies listed in Table VI-5 is used throughout the remainder of this analysis. The capability of

Table VI-4

OEP CORRELATION FUNCTIONS

Asso. OEP	No.	½ sin/cos	Frequency
P_1	1	2†	$\nu_x + \omega_s$
	2	2	$\nu_x - \omega_s$
P_2	3	1†	$\nu_x + \vartheta_s$
	4	1	$\nu_x - \omega_s$
P_4	6	2	$2\omega_s$
	7	2†	$2(\nu_x + \omega_s)$
	8	2	$2(\nu_x - \omega_s)$
P_5	9	1	$2\vartheta_s$
	10	1†	$2(\nu_x + \omega_s)$
	11	1	$2(\nu_x - \omega_s)$
P_3	12	2†	Ω
P_{11}	15	1	ω_s
	16	2†	$\omega_s - \alpha_x$
	17	2	$\omega_s - \alpha_x$
P_{12}	18	2	ω_s
	19	1	$\omega_s + \alpha_x$
	20	1†	$\omega_s - \alpha_x$
P_{13}	21	1†	α_z
P_{14}	22	1	$2(\vartheta_s + \alpha_x)$
	23	1	$2(\omega_s - \alpha_x)$
	24	1	$2\vartheta_s$
	25	2	$2\vartheta_s + \alpha_x$
	26	2†	$2\omega_s - \alpha_x$
P_{15}	27	1	$\alpha_x+\alpha_z+\vartheta_s$
	28	1	$\vartheta_s-\alpha_x-\alpha_z$
	29	1	$\alpha_x-\alpha_z+\omega_s$
	30	1†	$\omega_s+\alpha_z+\omega_s$
	31	2	$\omega_s+\alpha_z$
	32	2	$\vartheta_s-\alpha_z$
P_{16}	33	2	$\alpha_x+\alpha_z+\omega_s$
	34	2	$\alpha_x-\alpha_z+\omega_s$
	35	2	$\alpha_x+\alpha_z-\alpha_s$
	36	2†	$\omega_s+\alpha_z-\alpha_x$
	37	1	$\omega_s+\alpha_z$
	38	1	$\omega_s-\alpha_z$
P_{17}	39	2	$2(\omega_s+\alpha_x)$
	40	2	$2(\omega_s-\alpha_x)$
	41	1	$2\omega_s+\alpha_x$
	42	1	$2\vartheta_s-\alpha_x$
	43	2	$2\omega_s$

Table VI-5

SAMPLE CORRELATION FREQUENCIES

(units of ω_s)

Channel	Set 1	Set 2	Set 3	Set 4	Set 5	Set 6
ω_x	0.5	0.6	0.2	0.3	0.3	0.4
α_x	0.7	0.3	0.7	0.4	0.6	0.5
α_z	0.1	0.8	0.1	0.6	0.5	0.7

this set of frequencies to provide the correlation performance required is demonstrated by Table VI-6. In Table VI-6, each of the correlation functions of Table VI-4 marked by the dagger is in turn operated upon by all of the functions present in the instrument output. Each zero frequency output having magnitude greater than zero is underlined. From the Table it is clear that each correlation function produces a nonzero magnitude, zero frequency term only under conditions of operating upon itself. Hence, this set of platform input frequencies provides adequate spectral separation within the RGG output signal ΔT for OEP identification.

Table VI-6

CORRELATED FREQUENCY OUTPUT AS A FUNCTION OF CORRELATION FREQUENCY

CORRELATION FUNCTION NO. 1

1	COS(3.0)T+COS(0.0)T	330.00	0.00
2	COS(1.0)T+COS(-2.0)T	110.00	-220.00
3	SIN(3.0)T+SIN(0.0)T	330.00	0.00
4	SIN(1.0)T+SIN(-2.0)T	110.00	-220.00
5	SIN(1.5)T+SIN(-1.5)T	165.00	-165.00
6	COS(3.5)T+COS(.5)T	385.00	55.00
7	COS(4.5)T+COS(1.5)T	495.00	165.00
8	COS(.5)T+COS(-2.5)T	55.00	-275.00
9	SIN(3.5)T+SIN(.5)T	385.00	55.00
10	SIN(4.5)T+SIN(1.5)T	495.00	165.00
11	SIN(2.5)T+SIN(-.5)T	275.00	-55.00
12	COS(6.5)T+COS(3.5)T	715.00	385.00
13	COS(3.5)T+COS(.5)T	385.00	55.00
14	COS(2.5)T+COS(-.5)T	275.00	-55.00
15	SIN(2.5)T+SIN(-.5)T	275.00	-55.00
16	COS(1.8)T+COS(-1.2)T	198.00	-132.00
17	COS(3.2)T+COS(.2)T	352.00	22.00
18	COS(2.5)T+COS(-.5)T	275.00	-55.00
19	SIN(3.2)T+SIN(.2)T	352.00	22.00
20	SIN(1.8)T+SIN(-1.2)T	198.00	-132.00
21	SIN(1.6)T+SIN(-1.4)T	176.00	-154.00
22	SIN(4.9)T+SIN(1.9)T	539.00	209.00
23	SIN(2.1)T+SIN(-.9)T	231.00	-99.00
24	SIN(3.5)T+SIN(.5)T	385.00	55.00
25	COS(4.2)T+COS(1.2)T	462.00	132.00
26	COS(2.8)T+COS(-.2)T	308.00	-22.00
27	SIN(3.3)T+SIN(.3)T	363.00	33.00
28	SIN(1.7)T+SIN(-1.3)T	187.00	-143.00
29	SIN(3.1)T+SIN(.1)T	341.00	11.00
30	SIN(1.9)T+SIN(-1.1)T	209.00	-121.00
31	COS(2.6)T+COS(-.4)T	286.00	-44.00
32	COS(2.4)T+COS(-.6)T	264.00	-66.00
33	COS(3.3)T+COS(.3)T	363.00	33.00
34	COS(3.1)T+COS(.1)T	341.00	11.00
35	COS(1.3)T+COS(-1.7)T	143.00	-187.00
36	COS(1.9)T+COS(-1.1)T	209.00	-121.00
37	SIN(2.6)T+SIN(-.4)T	286.00	-44.00
38	SIN(2.4)T+SIN(-.6)T	264.00	-66.00
39	COS(4.9)T+COS(1.9)T	539.00	209.00
40	COS(2.1)T+COS(-.9)T	231.00	-99.00
41	SIN(4.2)T+SIN(1.2)T	462.00	132.00
42	SIN(2.8)T+SIN(-.2)T	308.00	-22.00
43	COS(3.5)T+COS(.5)T	385.00	55.00

CORRELATION FUNCTION NO. 3

1	SIN(3.0)T-SIN(0.0)T	330.00	0.00
2	SIN(1.0)T-SIN(-2.0)T	110.00	-220.00
3	COS(0.0)T-COS(3.0)T	0.00	330.00
4	COS(-2.0)T-COS(1.0)T	-220.00	110.00
5	COS(-1.5)T-COS(1.5)T	-165.00	165.00
6	SIN(3.5)T-SIN(.5)T	385.00	55.00
7	SIN(4.5)T-SIN(1.5)T	495.00	165.00
8	SIN(.5)T-SIN(-2.5)T	55.00	-275.00
9	COS(.5)T-COS(3.5)T	55.00	385.00
10	COS(1.5)T-COS(4.5)T	165.00	495.00
11	COS(-.5)T-COS(2.5)T	-55.00	275.00
12	SIN(6.5)T-SIN(3.5)T	715.00	385.00
13	SIN(3.5)T-SIN(.5)T	385.00	55.00
14	SIN(2.5)T-SIN(-.5)T	275.00	-55.00
15	COS(-.5)T-COS(2.5)T	-55.00	275.00
16	SIN(1.8)T-SIN(-1.2)T	198.00	-132.00
17	SIN(3.2)T-SIN(.2)T	352.00	22.00
18	SIN(2.5)T-SIN(-.5)T	275.00	-55.00
19	COS(.2)T-COS(3.2)T	22.00	352.00
20	COS(-1.2)T-COS(1.8)T	-132.00	198.00
21	COS(-1.4)T-COS(1.6)T	-154.00	176.00
22	COS(1.9)T-COS(4.9)T	209.00	539.00
23	COS(-.9)T-COS(2.1)T	-99.00	231.00
24	COS(.5)T-COS(3.5)T	55.00	385.00
25	SIN(4.2)T-SIN(1.2)T	462.00	132.00
26	SIN(2.8)T-SIN(-.2)T	308.00	-22.00
27	COS(.3)T-COS(3.3)T	33.00	363.00
28	COS(-1.3)T-COS(1.7)T	-143.00	187.00
29	COS(.1)T-COS(3.1)T	11.00	341.00
30	COS(-1.1)T-COS(1.9)T	-121.00	209.00
31	SIN(2.6)T-SIN(-.4)T	286.00	-44.00
32	SIN(2.4)T-SIN(-.6)T	264.00	-66.00
33	SIN(3.3)T-SIN(.3)T	363.00	33.00
34	SIN(3.1)T-SIN(.1)T	341.00	11.00
35	SIN(1.3)T-SIN(-1.7)T	143.00	-187.00
36	SIN(1.9)T-SIN(-1.1)T	209.00	-121.00
37	COS(-.4)T-COS(2.6)T	-44.00	286.00
38	COS(-.6)T-COS(2.4)T	-66.00	264.00
39	SIN(4.9)T-SIN(1.9)T	539.00	209.00
40	SIN(2.1)T-SIN(-.9)T	231.00	-99.00
41	COS(1.2)T-COS(4.2)T	132.00	462.00
42	COS(-.2)T-COS(2.8)T	-22.00	308.00
43	SIN(3.5)T-SIN(.5)T	385.00	55.00

BEST AVAILABLE COPY

Table VI-6 (Cont)

CORRELATION FUNCTION NO. 7

1	COS(4.5)T+COS(-1.5)T	495.00	-165.00
2	COS(2.5)T+COS(-3.5)T	275.00	-385.00
3	SIN(4.5)T+SIN(-1.5)T	495.00	-165.00
4	SIN(2.5)T+SIN(-3.5)T	275.00	-385.00
5	SIN(3.0)T+SIN(-3.0)T	330.00	-330.00
6	COS(5.0)T+COS(-1.0)T	550.00	-110.00
7	COS(6.0)T+COS(0.0)T	660.00	0.00
8	COS(2.0)T+COS(-4.0)T	220.00	-440.00
9	SIN(5.0)T+SIN(-1.0)T	550.00	-110.00
10	SIN(6.0)T+SIN(0.0)T	660.00	0.00
11	SIN(4.0)T+SIN(-2.0)T	440.00	-220.00
12	COS(8.0)T+COS(2.0)T	880.00	220.00
13	COS(5.0)T+COS(-1.0)T	550.00	-110.00
14	COS(4.0)T+COS(-2.0)T	440.00	-220.00
15	SIN(4.0)T+SIN(-2.0)T	440.00	220.00
16	COS(3.3)T+COS(-2.7)T	363.00	-297.00
17	COS(4.7)T+COS(-1.3)T	517.00	-143.00
18	COS(4.0)T+COS(-2.0)T	440.00	-220.00
19	SIN(4.7)T+SIN(-1.3)T	517.00	-143.00
20	SIN(3.3)T+SIN(-2.7)T	363.00	-297.00
21	SIN(3.1)T+SIN(-2.9)T	341.00	-319.00
22	SIN(6.4)T+SIN(.4)T	704.00	44.00
23	SIN(3.6)T+SIN(-2.4)T	396.00	-264.00
24	SIN(5.0)T+SIN(-1.0)T	550.00	-110.00
25	COS(5.7)T+COS(-.3)T	627.00	-33.00
26	COS(4.3)T+COS(-1.7)T	473.00	-187.00
27	SIN(4.8)T+SIN(-1.2)T	528.00	-132.00
28	SIN(3.2)T+SIN(-2.8)T	352.00	-308.00
29	SIN(4.6)T+SIN(-1.4)T	506.00	-154.00
30	SIN(3.4)T+SIN(-2.6)T	374.00	-286.00
31	COS(4.1)T+COS(-1.9)T	451.00	-209.00
32	COS(3.9)T+COS(-2.1)T	429.00	-231.00
33	COS(4.8)T+COS(-1.2)T	528.00	-132.00
34	COS(4.6)T+COS(-1.4)T	506.00	-154.00
35	COS(2.8)T+COS(-3.2)T	308.00	-352.00
36	COS(3.4)T+COS(-2.6)T	374.00	-286.00
37	SIN(4.1)T+SIN(-1.9)T	451.00	-209.00
38	SIN(3.9)T+SIN(-2.1)T	429.00	-231.00
39	COS(6.4)T+COS(.4)T	704.00	44.00
40	COS(3.6)T+COS(-2.4)T	396.00	-264.00
41	SIN(5.7)T+SIN(-.3)T	627.00	-33.00
42	SIN(4.3)T+SIN(-1.7)T	473.00	-187.00
43	COS(5.0)T+COS(-1.0)T	550.00	-110.00

CORRELATION FUNCTION NO. 10

1	SIN(4.5)T-SIN(-1.5)T	495.00	-165.00
2	SIN(2.5)T-SIN(-3.5)T	275.00	-385.00
3	COS(-1.5)T-COS(4.5)T	-165.00	495.00
4	COS(-3.5)T-COS(2.5)T	-385.00	275.00
5	COS(-3.0)T-COS(3.0)T	-330.00	330.00
6	SIN(5.0)T-SIN(-1.0)T	550.00	-110.00
7	SIN(6.0)T-SIN(0.0)T	660.00	0.00
8	SIN(2.0)T-SIN(-4.0)T	220.00	-440.00
9	COS(-1.0)T-COS(5.0)T	-110.00	550.00
10	COS(0.0)T-COS(6.0)T	0.00	660.00
11	COS(-2.0)T-COS(4.0)T	-220.00	440.00
12	SIN(6.0)T-SIN(2.0)T	880.00	220.00
13	SIN(5.0)T-SIN(-1.0)T	550.00	-110.00
14	SIN(4.0)T-SIN(-2.0)T	440.00	-220.00
15	COS(-2.0)T-COS(4.0)T	-220.00	440.00
16	SIN(3.3)T-SIN(-2.7)T	363.00	-297.00
17	SIN(4.7)T-SIN(-1.3)T	517.00	143.00
18	SIN(4.0)T-SIN(-2.0)T	440.00	-220.00
19	COS(-1.3)T-COS(4.7)T	-143.00	517.00
20	COS(-2.7)T-COS(3.3)T	-297.00	363.00
21	COS(-2.9)T-COS(3.1)T	-319.00	341.00
22	COS(.4)T-COS(6.4)T	44.00	704.00
23	COS(-2.4)T-COS(3.6)T	-264.00	396.00
24	COS(-1.0)T-COS(5.0)T	-110.00	550.00
25	SIN(5.7)T-SIN(-.3)T	627.00	-33.00
26	SIN(4.3)T-SIN(-1.7)T	473.00	-187.00
27	COS(-1.2)T-COS(4.8)T	-132.00	528.00
28	COS(-2.8)T-COS(3.2)T	-308.00	352.00
29	COS(-1.4)T-COS(4.6)T	-154.00	506.00
30	COS(-2.6)T-COS(3.4)T	-286.00	374.00
31	SIN(4.1)T-SIN(-1.9)T	451.00	-209.00
32	SIN(3.9)T-SIN(-2.1)T	429.00	-231.00
33	SIN(4.8)T-SIN(-1.2)T	528.00	-132.00
34	SIN(4.6)T-SIN(-1.4)T	506.00	-154.00
35	SIN(2.8)T-SIN(-3.2)T	308.00	-352.00
36	SIN(3.4)T-SIN(-2.6)T	374.00	-286.00
37	COS(-1.9)T-COS(4.1)T	-209.00	451.00
38	COS(-2.1)T-COS(3.9)T	-231.00	429.00
39	SIN(6.4)T-SIN(.4)T	704.00	44.00
40	SIN(3.6)T-SIN(-2.4)T	396.00	-264.00
41	COS(-.3)T-COS(5.7)T	-33.00	627.00
42	COS(-1.7)T-COS(4.3)T	-187.00	473.00
43	SIN(5.0)T-SIN(-1.0)T	550.00	-110.00

BEST AVAILABLE COPY

BEST AVAILABLE COPY

Table VI-6 (Cont)

CORRELATION FUNCTION NO. 12

1	COS(6.5)T+COS(-3.5)T	715.00	-385.00
2	COS(4.5)T+COS(-5.5)T	495.00	-605.00
3	SIN(6.5)T+SIN(-3.5)T	715.00	-385.00
4	SIN(4.5)T+SIN(-5.5)T	495.00	-605.00
5	SIN(5.0)T+SIN(-5.0)T	550.00	-550.00
6	COS(7.0)T+COS(-3.0)T	770.00	-330.00
7	COS(8.0)T+COS(-2.0)T	880.00	-220.00
8	COS(4.0)T+COS(-6.0)T	440.00	-660.00
9	SIN(7.0)T+SIN(-3.0)T	770.00	-330.00
10	SIN(8.0)T+SIN(-2.0)T	880.00	-220.00
11	SIN(6.0)T+SIN(-4.0)T	660.00	-440.00
12	COS(10.0)T+COS(0.0)T	1100.00	0.00
13	COS(7.0)T+COS(-3.0)T	770.00	-330.00
14	COS(6.0)T+COS(-4.0)T	660.00	-440.00
15	SIN(6.0)T+SIN(-4.0)T	660.00	-440.00
16	COS(5.3)T+COS(-4.7)T	583.00	-517.00
17	COS(6.7)T+COS(-3.3)T	737.00	-363.00
18	COS(6.0)T+COS(-4.0)T	660.00	-440.00
19	SIN(6.7)T+SIN(-3.3)T	737.00	-363.00
20	SIN(5.3)T+SIN(-4.7)T	583.00	-517.00
21	SIN(5.1)T+SIN(-4.9)T	561.00	-539.00
22	SIN(8.4)T+SIN(-1.6)T	924.00	-176.00
23	SIN(5.6)T+SIN(-4.4)T	616.00	-484.00
24	SIN(7.0)T+SIN(-3.0)T	770.00	-330.00
25	COS(7.7)T+COS(-2.3)T	847.00	-253.00
26	COS(6.3)T+COS(-3.7)T	693.00	-407.00
27	SIN(6.8)T+SIN(-3.2)T	748.00	-352.00
28	SIN(5.2)T+SIN(-4.8)T	572.00	-528.00
29	SIN(6.6)T+SIN(-3.4)T	726.00	-374.00
30	SIN(5.4)T+SIN(-4.6)T	594.00	-506.00
31	COS(6.1)T+COS(-3.9)T	671.00	-429.00
32	COS(5.9)T+COS(-4.1)T	649.00	-451.00
33	COS(6.8)T+COS(-3.2)T	748.00	-352.00
34	COS(6.6)T+COS(-3.4)T	726.00	-374.00
35	COS(4.8)T+COS(-5.2)T	528.00	-572.00
36	COS(5.4)T+COS(-4.6)T	594.00	-506.00
37	SIN(6.1)T+SIN(-3.9)T	671.00	-429.00
38	SIN(5.9)T+SIN(-4.1)T	649.00	-451.00
39	COS(8.4)T+COS(-1.6)T	924.00	-176.00
40	COS(5.6)T+COS(-4.4)T	616.00	-484.00
41	SIN(7.7)T+SIN(-2.3)T	847.00	-253.00
42	SIN(6.3)T+SIN(-3.7)T	693.00	-407.00
43	COS(7.0)T+COS(-3.0)T	770.00	-330.00

CORRELATION FUNCTION NO. 16

1	COS(1.8)T+COS(1.2)T	198.00	132.00
2	COS(-.2)T+COS(-.8)T	-22.00	-88.00
3	SIN(1.8)T+SIN(1.2)T	198.00	132.00
4	SIN(-.2)T+SIN(-.8)T	-22.00	-88.00
5	SIN(.3)T+SIN(-.3)T	33.00	-33.00
6	COS(2.3)T+COS(1.7)T	253.00	187.00
7	COS(3.3)T+COS(2.7)T	363.00	297.00
8	COS(-.7)T+COS(-1.3)T	-77.00	-143.00
9	SIN(2.3)T+SIN(1.7)T	253.00	187.00
10	SIN(3.3)T+SIN(2.7)T	363.00	297.00
11	SIN(1.3)T+SIN(.7)T	143.00	77.00
12	COS(5.3)T+COS(4.7)T	583.00	517.00
13	COS(2.3)T+COS(1.7)T	253.00	187.00
14	COS(1.3)T+COS(.7)T	143.00	77.00
15	SIN(1.3)T+SIN(.7)T	143.00	77.00
16	COS(.6)T+COS(0.0)T	66.00	0.00
17	COS(2.0)T+COS(1.4)T	220.00	154.00
18	COS(1.3)T+COS(.7)T	143.00	77.00
19	SIN(2.0)T+SIN(1.4)T	220.00	154.00
20	SIN(.6)T+SIN(0.0)T	66.00	0.00
21	SIN(.4)T+SIN(-.2)T	44.00	-22.00
22	SIN(3.7)T+SIN(3.1)T	407.00	341.00
23	SIN(.9)T+SIN(.3)T	99.00	33.00
24	SIN(2.3)T+SIN(1.7)T	253.00	187.00
25	COS(3.0)T+COS(2.4)T	330.00	264.00
26	COS(1.6)T+COS(1.0)T	176.00	110.00
27	SIN(2.1)T+SIN(1.5)T	231.00	165.00
28	SIN(.5)T+SIN(-.1)T	55.00	-11.00
29	SIN(1.9)T+SIN(1.3)T	209.00	143.00
30	SIN(.7)T+SIN(.1)T	77.00	11.00
31	COS(1.4)T+COS(.8)T	154.00	88.00
32	COS(1.2)T+COS(.6)T	132.00	66.00
33	COS(2.1)T+COS(1.5)T	231.00	165.00
34	COS(1.9)T+COS(1.3)T	209.00	143.00
35	COS(.1)T+COS(-.5)T	11.00	-55.00
36	COS(.7)T+COS(.1)T	77.00	11.00
37	SIN(1.4)T+SIN(.8)T	154.00	88.00
38	SIN(1.2)T+SIN(.6)T	132.00	66.00
39	COS(3.7)T+COS(3.1)T	407.00	341.00
40	COS(.9)T+COS(.3)T	99.00	33.00
41	SIN(3.0)T+SIN(2.4)T	330.00	264.00
42	SIN(1.6)T+SIN(1.0)T	176.00	110.00
43	COS(2.3)T+COS(1.7)T	253.00	187.00

Table VI-6 (Cont)

CORRELATION FUNCTION NO. 20

1	SIN(1.8)T-SIN(1.2)T	198.00	132.00
2	SIN(-.2)T-SIN(-.8)T	-22.00	-88.00
3	COS(1.2)T-COS(1.8)T	132.00	198.00
4	COS(-.8)T-COS(-.2)T	-88.00	-22.00
5	COS(-.3)T-COS(.3)T	-33.00	33.00
6	SIN(2.3)T-SIN(1.7)T	253.00	187.00
7	SIN(3.3)T-SIN(2.7)T	363.00	297.00
8	SIN(-.7)T-SIN(-1.3)T	-77.00	-143.00
9	COS(1.7)T-COS(2.3)T	187.00	253.00
10	COS(2.7)T-COS(3.3)T	297.00	363.00
11	COS(.7)T-COS(1.3)T	77.00	143.00
12	SIN(5.3)T-SIN(4.7)T	583.00	517.00
13	SIN(2.3)T-SIN(1.7)T	253.00	187.00
14	SIN(1.3)T-SIN(.7)T	143.00	77.00
15	COS(.7)T-COS(1.3)T	77.00	143.00
16	SIN(.6)T-SIN(0.0)T	66.00	0.00
17	SIN(2.0)T-SIN(1.4)T	220.00	154.00
18	SIN(1.3)T-SIN(.7)T	143.00	77.00
19	COS(1.4)T-COS(2.0)T	154.00	220.00
20	COS(0.0)T-COS(.6)T	0.00	66.00
**********			
21	COS(-.2)T-COS(.4)T	-22.00	44.00
22	COS(3.1)T-COS(3.7)T	341.00	407.00
23	COS(.3)T-COS(.9)T	33.00	99.00
24	COS(1.7)T-COS(2.3)T	187.00	253.00
25	SIN(3.0)T-SIN(2.4)T	330.00	264.00
26	SIN(1.6)T-SIN(1.0)T	176.00	110.00
27	COS(1.5)T-COS(2.1)T	165.00	231.00
28	COS(-.1)T-COS(.5)T	-11.00	55.00
29	COS(1.3)T-COS(1.9)T	143.00	209.00
30	COS(.1)T-COS(.7)T	11.00	77.00
31	SIN(1.4)T-SIN(.8)T	154.00	88.00
32	SIN(1.2)T-SIN(.6)T	132.00	66.00
33	SIN(2.1)T-SIN(1.5)T	231.00	165.00
34	SIN(1.9)T-SIN(1.3)T	209.00	143.00
35	SIN(.1)T-SIN(-.5)T	11.00	-55.00
36	SIN(.7)T-SIN(.1)T	77.00	11.00
37	COS(.8)T-COS(1.4)T	88.00	154.00
38	COS(.6)T-COS(1.2)T	66.00	132.00
39	SIN(3.7)T-SIN(3.1)T	407.00	341.00
40	SIN(.9)T-SIN(.3)T	99.00	33.00
41	COS(2.4)T-COS(3.0)T	264.00	330.00
42	COS(1.0)T-COS(1.6)T	110.00	176.00
43	SIN(2.3)T-SIN(1.7)T	253.00	187.00

CORRELATION FUNCTION NO. 21

1	SIN(1.6)T-SIN(1.4)T	176.00	154.00
2	SIN(-.4)T-SIN(-.6)T	-44.00	-66.00
3	COS(1.4)T-COS(1.6)T	154.00	176.00
4	COS(-.6)T-COS(-.4)T	-66.00	-44.00
5	COS(-.1)T-COS(.1)T	-11.00	11.00
6	SIN(2.1)T-SIN(1.9)T	231.00	209.00
7	SIN(3.1)T-SIN(2.9)T	341.00	319.00
8	SIN(-.9)T-SIN(-1.1)T	-99.00	-121.00
9	COS(1.9)T-COS(2.1)T	209.00	231.00
10	COS(2.9)T-COS(3.1)T	319.00	341.00
11	COS(.9)T-COS(1.1)T	99.00	121.00
12	SIN(5.1)T-SIN(4.9)T	561.00	539.00
13	SIN(2.1)T-SIN(1.9)T	231.00	209.00
14	SIN(1.1)T-SIN(.9)T	121.00	99.00
15	COS(.9)T-COS(1.1)T	99.00	121.00
16	SIN(.4)T-SIN(.2)T	44.00	22.00
17	SIN(1.8)T-SIN(1.6)T	198.00	176.00
18	SIN(1.1)T-SIN(.9)T	121.00	99.00
19	COS(1.6)T-COS(1.8)T	176.00	198.00
20	COS(.2)T-COS(.4)T	22.00	44.00
21	COS(0.0)T-COS(.2)T	0.00	22.00
**********			
22	COS(3.3)T-COS(3.5)T	363.00	385.00
23	COS(.5)T-COS(.7)T	55.00	77.00
24	COS(1.9)T-COS(2.1)T	209.00	231.00
25	SIN(2.8)T-SIN(2.6)T	308.00	286.00
26	SIN(1.4)T-SIN(1.2)T	154.00	132.00
27	COS(1.7)T-COS(1.9)T	187.00	209.00
28	COS(.1)T-COS(.3)T	11.00	33.00
29	COS(1.5)T-COS(1.7)T	165.00	187.00
30	COS(.3)T-COS(.5)T	33.00	55.00
31	SIN(1.2)T-SIN(1.0)T	132.00	110.00
32	SIN(1.0)T-SIN(.8)T	110.00	88.00
33	SIN(1.9)T-SIN(1.7)T	209.00	187.00
34	SIN(1.7)T-SIN(1.5)T	187.00	165.00
35	SIN(-.1)T-SIN(-.3)T	-11.00	-33.00
36	SIN(.5)T-SIN(.3)T	55.00	33.00
37	COS(1.0)T-COS(1.2)T	110.00	132.00
38	COS(.8)T-COS(1.0)T	88.00	110.00
39	SIN(3.5)T-SIN(3.3)T	385.00	363.00
40	SIN(.7)T-SIN(.5)T	77.00	55.00
41	COS(2.6)T-COS(2.8)T	286.00	308.00
42	COS(1.2)T-COS(1.4)T	132.00	154.00
43	SIN(2.1)T-SIN(1.9)T	231.00	209.00

BEST AVAILABLE COPY

BEST AVAILABLE COPY

Table VI-6 (Cont)

CORRELATION FUNCTION NO. 23

1	SIN(2.1)T-SIN(.9)T	231.00	99.00
2	SIN(.1)T-SIN(-1.1)T	11.00	-121.00
3	COS(.9)T-COS(2.1)T	99.00	231.00
4	COS(-1.1)T-COS(.1)T	-121.00	11.00
5	COS(-.6)T-COS(.6)T	-66.00	66.00
6	SIN(2.6)T-SIN(1.4)T	286.00	154.00
7	SIN(3.6)T-SIN(2.4)T	396.00	264.00
8	SIN(-.4)T-SIN(-1.6)T	-44.00	-176.00
9	COS(1.4)T-COS(2.6)T	154.00	286.00
10	COS(2.4)T-COS(3.6)T	264.00	396.00
11	COS(.4)T-COS(1.6)T	44.00	176.00
12	SIN(5.6)T-SIN(4.4)T	616.00	484.00
13	SIN(2.6)T-SIN(1.4)T	286.00	154.00
14	COS(1.6)T-SIN(.4)T	176.00	44.00
15	COS(.4)T-COS(1.6)T	44.00	176.00
16	SIN(.9)T-SIN(-.3)T	99.00	-33.00
17	SIN(2.3)T-SIN(1.1)T	253.00	121.00
18	SIN(1.6)T-SIN(.4)T	176.00	44.00
19	COS(1.1)T-COS(2.3)T	121.00	253.00
20	COS(-.3)T-COS(.9)T	-33.00	99.00
21	COS(-.5)T-COS(.7)T	-55.00	77.00
22	COS(2.8)T-COS(4.0)T	308.00	440.00
23	COS(0.0)T-COS(1.2)T	0.00	132.00
24	COS(1.4)T-COS(2.6)T	154.00	286.00
25	SIN(3.3)T-SIN(2.1)T	363.00	231.00
26	SIN(1.9)T-SIN(.7)T	209.00	77.00
27	COS(1.2)T-COS(2.4)T	132.00	264.00
28	COS(-.4)T-COS(.8)T	-44.00	88.00
29	COS(1.0)T-COS(2.2)T	110.00	242.00
30	COS(-.2)T-COS(1.0)T	-22.00	110.00
31	SIN(1.7)T-SIN(.5)T	187.00	55.00
32	SIN(1.5)T-SIN(.3)T	165.00	33.00
33	SIN(2.4)T-SIN(1.2)T	264.00	132.00
34	SIN(2.2)T-SIN(1.0)T	242.00	110.00
35	SIN(.4)T-SIN(-.8)T	44.00	-88.00
36	SIN(1.0)T-SIN(-.2)T	110.00	-22.00
37	COS(.5)T-COS(1.7)T	55.00	187.00
38	COS(.3)T-COS(1.5)T	33.00	165.00
39	SIN(4.0)T-SIN(2.8)T	440.00	308.00
40	SIN(1.2)T-SIN(0.0)T	132.00	0.00
41	COS(2.1)T-COS(3.3)T	231.00	363.00
42	COS(.7)T-COS(1.9)T	77.00	209.00
43	SIN(2.6)T-SIN(1.4)T	286.00	154.00

INPUT CORRELATION FUNCTION INDEX NUMBER
26

1	COS(2.8)T+COS(.2)T	308.00	22.00
2	COS(.8)T+COS(-1.8)T	88.00	-198.00
3	SIN(2.8)T+SIN(.2)T	308.00	22.00
4	SIN(.8)T+SIN(-1.8)T	88.00	-198.00
5	SIN(1.3)T+SIN(-1.3)T	143.00	-143.00
6	COS(3.3)T+COS(.7)T	363.00	77.00
7	COS(4.3)T+COS(1.7)T	473.00	187.00
8	COS(.3)T+COS(-2.3)T	33.00	-253.00
9	SIN(3.3)T+SIN(.7)T	363.00	77.00
10	SIN(4.3)T+SIN(1.7)T	473.00	187.00
11	SIN(2.3)T+SIN(-.3)T	253.00	-33.00
12	COS(6.3)T+COS(3.7)T	693.00	407.00
13	COS(3.3)T+COS(.7)T	363.00	77.00
14	COS(2.3)T+COS(-.3)T	253.00	-33.00
15	SIN(2.3)T+SIN(-.3)T	253.00	-33.00
16	COS(1.6)T+COS(-1.0)T	176.00	-110.00
17	COS(3.0)T+COS(.4)T	330.00	44.00
18	COS(2.3)T+COS(-.3)T	253.00	-33.00
19	SIN(3.0)T+SIN(.4)T	330.00	44.00
20	SIN(1.6)T+SIN(-1.0)T	176.00	-110.00
21	SIN(1.4)T+SIN(-1.2)T	154.00	-132.00
22	SIN(4.7)T+SIN(2.1)T	517.00	231.00
23	SIN(1.9)T+SIN(-.7)T	209.00	-77.00
24	SIN(3.3)T+SIN(.7)T	363.00	77.00
25	COS(4.0)T+COS(1.4)T	440.00	154.00
26	COS(2.6)T+COS(0.0)T	286.00	0.00
27	SIN(3.1)T+SIN(.5)T	341.00	55.00
28	SIN(1.5)T+SIN(-1.1)T	165.00	-121.00
29	SIN(2.9)T+SIN(.3)T	319.00	33.00
30	SIN(1.7)T+SIN(-.9)T	187.00	-99.00
31	COS(2.4)T+COS(-.2)T	264.00	-22.00
32	COS(2.2)T+COS(-.4)T	242.00	-44.00
33	COS(3.1)T+COS(.5)T	341.00	55.00
34	COS(2.9)T+COS(.3)T	319.00	33.00
35	COS(1.1)T+COS(-1.5)T	121.00	-165.00
36	COS(1.7)T+COS(-.9)T	187.00	-99.00
37	SIN(2.4)T+SIN(-.2)T	264.00	-22.00
38	SIN(2.2)T+SIN(-.4)T	242.00	-44.00
39	COS(4.7)T+COS(2.1)T	517.00	231.00
40	COS(1.9)T+COS(-.7)T	209.00	-77.00
41	SIN(4.0)T+SIN(1.4)T	440.00	154.00
42	SIN(2.6)T+SIN(0.0)T	286.00	0.00
43	COS(3.3)T+COS(.7)T	363.00	77.00

Table VI-6 (Cont)

CORRELATION FUNCTION NO. 30

1	SIN(1.9)T-SIN(1.1)T	209.00	121.00
2	SIN(-.1)T-SIN(-.9)T	-11.00	-99.00
3	COS(1.1)T-COS(1.9)T	121.00	209.00
4	COS(-.9)T-COS(-.1)T	-99.00	-11.00
5	COS(-.4)T-COS(.4)T	-44.00	44.00
6	SIN(2.4)T-SIN(1.6)T	264.00	176.00
7	SIN(3.4)T-SIN(2.6)T	374.00	286.00
8	SIN(-.6)T-SIN(-1.4)T	-66.00	-154.00
9	COS(1.6)T-COS(2.4)T	176.00	264.00
10	COS(2.6)T-COS(3.4)T	286.00	374.00
11	COS(.6)T-COS(1.4)T	66.00	154.00
12	SIN(5.4)T-SIN(4.6)T	594.00	506.00
13	SIN(2.4)T-SIN(1.6)T	264.00	176.00
14	SIN(1.4)T-SIN(.6)T	154.00	66.00
15	COS(.6)T-COS(1.4)T	66.00	154.00
16	SIN(.7)T-SIN(-.1)T	77.00	-11.00
17	SIN(2.1)T-SIN(1.3)T	231.00	143.00
18	SIN(1.4)T-SIN(.6)T	154.00	66.00
19	COS(1.3)T-COS(2.1)T	143.00	231.00
20	COS(-.1)T-COS(.7)T	-11.00	77.00
21	COS(-.3)T-COS(.5)T	-33.00	55.00
22	COS(3.0)T-COS(3.8)T	330.00	418.00
23	COS(.2)T-COS(1.0)T	22.00	110.00
24	COS(1.6)T-COS(2.4)T	176.00	264.00
25	SIN(3.1)T-SIN(2.3)T	341.00	253.00
26	SIN(1.7)T-SIN(.9)T	187.00	99.00
27	COS(1.4)T-COS(2.2)T	154.00	242.00
28	COS(-.2)T-COS(.6)T	-22.00	66.00
29	COS(1.2)T-COS(2.0)T	132.00	220.00
30	COS(0.0)T-COS(.8)T	0.00	88.00
31	SIN(1.5)T-SIN(.7)T	165.00	77.00
32	SIN(1.3)T-SIN(.5)T	143.00	55.00
33	SIN(2.2)T-SIN(1.4)T	242.00	154.00
34	SIN(2.0)T-SIN(1.2)T	220.00	132.00
35	SIN(.2)T-SIN(-.6)T	22.00	-66.00
36	SIN(.8)T-SIN(0.0)T	88.00	0.00
37	COS(.7)T-COS(1.5)T	77.00	165.00
38	COS(.5)T-COS(1.3)T	55.00	143.00
39	SIN(3.0)T-SIN(3.0)T	418.00	330.00
40	SIN(1.0)T-SIN(.2)T	110.00	22.00
41	COS(2.3)T-COS(3.1)T	253.00	341.00
42	COS(.9)T-COS(1.7)T	99.00	187.00
43	SIN(2.4)T-SIN(1.6)T	264.00	176.00

CORRELATION FUNCTION NO. 37

1	SIN(2.6)T-SIN(.4)T	286.00	44.00
2	SIN(.6)T-SIN(-1.6)T	66.00	-176.00
3	COS(.4)T-COS(2.6)T	44.00	286.00
4	COS(-1.6)T-COS(.6)T	-176.00	66.00
5	COS(-1.1)T-COS(1.1)T	-121.00	121.00
6	SIN(3.1)T-SIN(.9)T	341.00	99.00
7	SIN(4.1)T-SIN(1.9)T	451.00	209.00
8	SIN(.1)T-SIN(-2.1)T	11.00	-231.00
9	COS(.9)T-COS(3.1)T	99.00	341.00
10	COS(1.9)T-COS(4.1)T	209.00	451.00
11	COS(-.1)T-COS(2.1)T	-11.00	231.00
12	SIN(6.1)T-SIN(3.9)T	671.00	429.00
13	SIN(3.1)T-SIN(.9)T	341.00	99.00
14	SIN(2.1)T-SIN(-.1)T	231.00	-11.00
15	COS(-.1)T-COS(2.1)T	-11.00	231.00
16	SIN(1.4)T-SIN(-.8)T	154.00	-88.00
17	SIN(2.8)T-SIN(.6)T	308.00	66.00
18	SIN(2.1)T-SIN(-.1)T	231.00	-11.00
19	COS(.6)T-COS(2.8)T	66.00	308.00
20	COS(-.8)T-COS(1.4)T	-88.00	154.00
21	COS(-1.0)T-COS(1.2)T	-110.00	132.00
22	COS(2.3)T-COS(4.5)T	253.00	495.00
23	COS(-.5)T-COS(1.7)T	-55.00	187.00
24	COS(.9)T-COS(3.1)T	99.00	341.00
25	SIN(3.8)T-SIN(1.6)T	418.00	176.00
26	SIN(2.4)T-SIN(.2)T	264.00	22.00
27	COS(.7)T-COS(2.9)T	77.00	319.00
28	COS(-.9)T-COS(1.3)T	-99.00	143.00
29	COS(.5)T-COS(2.7)T	55.00	297.00
30	COS(-.7)T-COS(1.5)T	-77.00	165.00
31	SIN(2.2)T-SIN(0.0)T	242.00	0.00
32	SIN(2.0)T-SIN(-.2)T	220.00	-22.00
33	SIN(2.9)T-SIN(.7)T	319.00	77.00
34	SIN(2.7)T-SIN(.5)T	297.00	55.00
35	SIN(.9)T-SIN(-1.3)T	99.00	-143.00
36	SIN(1.5)T-SIN(-.7)T	165.00	-77.00
37	COS(0.0)T-COS(2.2)T	0.00	242.00
38	COS(-.2)T-COS(2.0)T	-22.00	220.00
39	SIN(4.5)T-SIN(2.3)T	495.00	253.00
40	SIN(1.7)T-SIN(-.5)T	187.00	-55.00
41	COS(1.6)T-COS(3.8)T	176.00	418.00
42	COS(.2)T-COS(2.4)T	22.00	264.00
43	SIN(3.1)T-SIN(.9)T	341.00	99.00

BEST AVAILABLE COPY

BEST AVAILABLE COPY

Table VI-6 (Cont)

CORRELATION FUNCTION NO. 41

1	SIN(4.2)T-SIN(-1.2)T	462.00	-132.00
2	SIN(2.2)T-SIN(-3.2)T	242.00	-352.00
3	COS(-1.2)T-COS(4.2)T	-132.00	462.00
4	COS(-3.2)T-COS(2.2)T	-352.00	242.00
5	COS(-2.7)T-COS(2.7)T	-297.00	297.00
6	SIN(4.7)T-SIN(-.7)T	517.00	-77.00
7	SIN(5.7)T-SIN(.3)T	627.00	33.00
8	SIN(1.7)T-SIN(-3.7)T	187.00	-407.00
9	COS(-.7)T-COS(4.7)T	-77.00	517.00
10	COS(.3)T-COS(5.7)T	33.00	627.00
11	COS(-1.7)T-COS(3.7)T	-187.00	407.00
12	SIN(7.7)T-SIN(2.3)T	847.00	253.00
13	SIN(4.7)T-SIN(-.7)T	517.00	-77.00
14	SIN(3.7)T-SIN(-1.7)T	407.00	-187.00
15	COS(-1.7)T-COS(3.7)T	-187.00	407.00
16	SIN(3.0)T-SIN(-2.4)T	330.00	-264.00
17	SIN(4.4)T-SIN(-1.0)T	484.00	-110.00
18	SIN(3.7)T-SIN(-1.7)T	407.00	-187.00
19	COS(-1.0)T-COS(4.4)T	-110.00	484.00
20	COS(-2.4)T-COS(3.0)T	-264.00	330.00
21	COS(-2.6)T-COS(2.8)T	-286.00	308.00
22	COS(.7)T-COS(6.1)T	77.00	671.00
23	COS(-2.1)T-COS(3.3)T	-231.00	363.00
24	COS(-.7)T-COS(4.7)T	-77.00	517.00
25	SIN(5.4)T-SIN(0.0)T	594.00	0.00
26	SIN(4.0)T-SIN(-1.4)T	440.00	-154.00
27	COS(-.9)T-COS(4.5)T	-99.00	495.00
28	COS(-2.5)T-COS(2.9)T	-275.00	319.00
29	COS(-1.1)T-COS(4.3)T	-121.00	473.00
30	COS(-2.3)T-COS(3.1)T	-253.00	341.00
31	SIN(3.8)T-SIN(-1.6)T	418.00	-176.00
32	SIN(3.6)T-SIN(-1.8)T	396.00	-198.00
33	SIN(4.5)T-SIN(-.9)T	495.00	-99.00
34	SIN(4.3)T-SIN(-1.1)T	473.00	-121.00
35	SIN(2.5)T-SIN(-2.9)T	275.00	-319.00
36	SIN(3.1)T-SIN(-2.3)T	341.00	-253.00
37	COS(-1.6)T-COS(3.8)T	-176.00	418.00
38	COS(-1.8)T-COS(3.6)T	-198.00	396.00
39	SIN(6.1)T-SIN(.7)T	671.00	77.00
40	SIN(3.3)T-SIN(-2.1)T	363.00	-231.00
41	COS(0.0)T-COS(5.4)T	0.00	594.00
**********	**********	**********	**********
42	COS(-1.4)T-COS(4.0)T	-154.00	440.00
43	SIN(4.7)T-SIN(-.7)T	517.00	-77.00

G. CORRELATION TECHNIQUE PERFORMANCE--6th ORDER SYSTEM

A closed form solution was developed for 6th order correlation of the RGG output error torque signal. The solution was evaluated for three specific OEPs--P_1, P_{11}, and P_{14}. These parameters are representative of the three different groups of OEP contained within the instrument model. P_1 is representative of the instrument rigid body characteristics, i.e., moment of inertia and mass center location. P_{11} is representative of the linear acceleration sensitive terms. P_{14} represents the anisoelasticity associated OEP.

Estimation results are based upon output associated with 12 of the 14 OEPs. The contribution of P_3 is not included since it is a function of platform angular acceleration about the platform $\hat{z}_p$ axis, and this state was set to zero. P_{13} was also set to zero since the proper analytical model for the Yankee Screwdriver effect had not yet been established. Rates, accelerations, and frequencies required for closed form evaluation of the parameter estimates are listed in Table VI-7.

Table VI-7

SYSTEM RATE AND ACCELERATION DATA

Variable	Magnitude	Units
ω_s	110	rad/sec
ν_x	55	rad/sec
α_x	77	rad/sec
α_z	11	rad/sec
Ω	100	rad/sec
$\bar{\Omega}_x$	10^{-4}	rad/sec
A_x	10^{-4}	m/sec^2
A_z	10^{-4}	m/sec^2

G-1 Closed Form Solution--P_{14} Estimation

Using the coefficient definitions of Table VI-8 and the frequency definitions of Table VI-9, the correlation equation for the P_{14} estimation may be written as shown in (6.47), where the preceding elasticity coefficient is again set equal to 1 for simplification.

Table VI-8

COEFFICIENT DEFINITIONS

Coefficient	Definition	Coefficient	Definition
k_1	$0.5\ P_1 \Omega_x \nu_x$	k_{15}	$P_{13}\ A_z$
k_2	$0.5\ P_2 \Omega_x \nu_x$	k_{16}	$0.125\ P_{14}\ A_x^2$
k_3	P_3	k_{17}	$P_{14}[0.5\ A_x^2 + g^2]$
k_4	$0.25\ P_4\ \bar{\Omega}_x^2$	k_{18}	$0.5\ P_{14} g\ A_x$
k_5	$0.125\ P_5 \bar{\Omega}_x^2$	k_{19}	$0.25\ P_{15} A_x A_x$
		k_{20}	$0.5\ P_{15} g\ A_z$
		k_{21}	$0.25\ P_{16}\ A_x A_z$
		k_{22}	$0.5\ P_{16} g\ A_z$
k_{11}	$P_{11}\ g$	k_{23}	$0.25\ P_{17}\ A_x^2$
k_{12}	$0.5\ P_{11} A_x$	k_{24}	$P_{17} g\ A_x$
k_{13}	$P_{12}\ g$	k_{25}	$P_{17}[0.5\ A_x^2 + g^2]$
k_{14}	$0.5\ P_{12} A_x$		

Note in (6.47) that a d-c term results with k_{18} as a coefficient.

Table VI-9

INPUT FREQUENCIES ASSOCIATED WITH P_{14} CORRELATED OUTPUT EQUATION

Variable	Definition	Variable	Definition
x1	$\nu_x + \omega_s$	x23	$2(\omega_s - \alpha_x)$
x2	$\nu_x - \omega_s$	x24	$2\omega_s$
x3	$\nu_x + \omega_s$	x25	$2\omega_s + \alpha_x$
x4	$\nu_x - \omega_s$	x26	$2\omega_s - \alpha_x$
x5	Ω	x27	$\alpha_x + \alpha_z + \omega_s$
x6	$2\omega_s$	x28	$\omega_s - \alpha_x - \alpha_t$
x7	$2(\omega_s + \nu_x)$	x29	$\alpha_x - \alpha_z + \omega_s$
x8	$2(\omega_s - \nu_x)$	x30	$\omega_s + \alpha_z - \alpha_x$
x9	$2\omega_s$	x31	$\omega_s + \alpha_z$
x10	$2(\omega_s + \nu_x)$	x32	$\omega_s - \alpha_z$
x11	$2(\nu_x - \omega_s)$	x33	$\alpha_x + \alpha_z + \omega_s$
		x34	$\alpha_x - \alpha_z + \omega_x$
		x35	$\alpha_x + \alpha_z - \omega_s$
		x36	$\omega_s + \alpha_z - \alpha_x$
		x37	$\alpha_z + \omega_s$
x16	$\omega_x - \alpha_x$	x38	$\omega_s - \alpha_z$
x17	$\omega_x + \alpha_x$	x39	$2(\alpha_x + \omega_s)$
x18	ω_s	x40	$2(\omega_x - \alpha_x)$
x19	$\omega_s + \alpha_x$	x41	$2\omega_s + \alpha_x$
x20	$\omega_s - \alpha_x$	x42	$2\omega_s - \alpha_x$
x21	α_x	x43	$2\omega_s$
x22	$2(\omega_s + \alpha_x)$		

$$\Delta T_z \cos(2\omega_s - \alpha_x)t = k_1\left[\cos(x_1 + x_{26}) + \cos(x_1 - x_{26})\right] + k_1\left[\cos(x_2 + x_{26}) + \cos(x_2 - x_{26})\right]$$

$$- k_2\left[\sin(x_3 + x_{26}) + \sin(x_3 - x_{26})\right] + k_2\left[\sin(x_4 + x_{26}) + \sin(x_4 - x_{26})\right]$$

$$+ k_3 Y_5 \cos x_{26}$$

$$+ \left[2k_5 + - k_{25}\right]\left[\cos(x_6 + x_{26}) + \cos(x_6 - x_{26})\right]$$

$$- k_4\left[\cos(x_7 + x_{26}) + \cos(x_7 - x_{26})\right] - k_4\left[\cos(x_8 + x_{26}) + \cos(x_8 - x_{26})\right]$$

$$+ \left[-2k_5 + \frac{1}{2} k_{17}\right]\left[\sin(x_9 + x_{26}) + \sin(x_9 - x_{26})\right]$$

$$+ k_5\left[\sin(x_{10} + x_{26}) + \sin(x_{10} - x_{26})\right] - k_5\left[\sin(x_{11} + x_{26}) + \sin(x_{11} - x_{26})\right]$$

$$+ k_{11}\left[\sin(x_{18} + x_{26}) + \sin(x_{18} - x_{26})\right]$$

$$- k_{12}\left[\cos(x_{16} + x_{26}) + \cos(x_{16} - x_{26})\right] + k_{12}\left[\cos(x_{17} + x_{26}) + \cos(x_{17} - x_{26})\right]$$

$$+ k_{13}\left[\cos(x_{18} + x_{26}) + \cos(x_{18} - x_{26})\right] + k_{15}\left[\sin(x_{21} + x_{26}) + \sin(x_{21} - x_{26})\right]$$

$$- k_{14}\left[\sin(x_{19} + x_{26}) + \sin(x_{19} - x_{26})\right] + k_{14}\left[\sin(x_{20} + x_{26}) + \sin(x_{20} - x_{26})\right]$$

(6.47)

(6.47)
Contd.

$$+ k_{16}\left[\sin (x_{22} + x_{26}) + \sin (x_{22} - x_{26})\right] + k_{16}\left[\sin (x_{23} + x_{26}) + \sin (x_{23} - x_{26})\right]$$

$$- k_{18}\left[\cos (x_{25} + x_{26}) + \cos (x_{25} - x_{26})\right]$$

$$+ k_{18} \cos \varphi\left[1 + \cos 2x_{26}\right] - k_{18} \sin \varphi\left[\sin 2x_{26}\right]$$

$$+ k_{19}\begin{Bmatrix} \sin (x_{27} + x_{26}) + \sin (x_{27} - x_{26}) + \sin (x_{28} + x_{26}) + \sin (x_{28} - x_{26}) \\ - \sin (x_{29} + x_{26}) - \sin (x_{29} - x_{26}) - \sin (x_{30} + x_{26}) - \sin (x_{30} - x_{26}) \end{Bmatrix}$$

$$- k_{20}\left[\cos (x_{31} + x_{26}) + \cos (x_{31} - x_{26}) - \cos (x_{32} + x_{26}) - \cos (x_{32} - x_{26})\right]$$

$$- k_{21}\begin{Bmatrix} \cos (x_{33} + x_{26}) + \cos (x_{33} - x_{26}) - \cos (x_{34} + x_{26}) - \cos (x_{34} - x_{26}) \\ - \cos (x_{35} + x_{26}) - \cos (x_{35} - x_{26}) + \cos (x_{36} + x_{26}) + \cos (x_{36} - x_{26}) \end{Bmatrix}$$

$$- k_{22}\left[\sin (x_{37} + x_{26}) + \sin (x_{37} - x_{26}) - \sin (x_{38} + x_{26}) - \sin (x_{38} - x_{26})\right]$$

$$+ k_{23}\left[\cos (x_{39} + x_{26}) + \cos (x_{39} - x_{26}) + \cos (x_{40} + x_{26}) + \cos (x_{40} - x_{26})\right]$$

$$+ k_{24}\left[\sin (x_{41} + x_{26}) + \sin (x_{41} - x_{26}) - \sin (x_{42} + x_{26}) - \sin (x_{42} - x_{26})\right]$$

A closed form solution was established by passing (6.47) through a 6th order lag having a break frequency at 1 rad/sec. A digital computer program for the solution was written and the performance of the 6th order lag system was examined.

P_{14} estimation results are shown for three separate cases in Figs. VI-5, VI-6, and VI-7. The various iterations referred to in the figure captions may be interpreted as indicators of different levels of parameter magnitudes. Lower iteration numbers imply larger parameter absolute values. Insets on the figures list actual parameter values. The horizontal dashed lines represent the true value of the parameter being estimated (P_{14}), while the solid line represents the 6th order correlation estimate of that parameter. The slanted dashed curve reflects correlation technique estimate error. The P_{14} estimate is seen to require approximately 25 sec for convergence. The peaks and overshoots shown in the figures are due to exponential decay terms in the solution for which time has not yet become large enough so that the terms are small compared to the constant parameter signal term. Estimate residuals at 50 sec for the iteration 1, 2, and 3 cases are 0.13%, 0.69%, and 0.001% respectively.

G-2 Correlation Technique Performance--P_1 Estimation

An example of correlator performance relative to P_1 estimation is given in Fig. VI-8. Using correlation function 1 as specified by Table VI-4 (26.26 Hz), P_1 estimate convergence for the iteration zero parameter set requires approximately 27 sec. The 50 sec estimate residual is 0.70% of the parameter's true value as specified by the inset.

G-3 Correlation Technique Performance--P_{11} Estimation

An example of estimator P_{11} estimation performance is given in Fig. VI-9. Correlation function 16 (5.25 Hz) was used and convergence required approximately 25 sec. The P_{11} 50 sec error residual was found to be less than 0.001%.

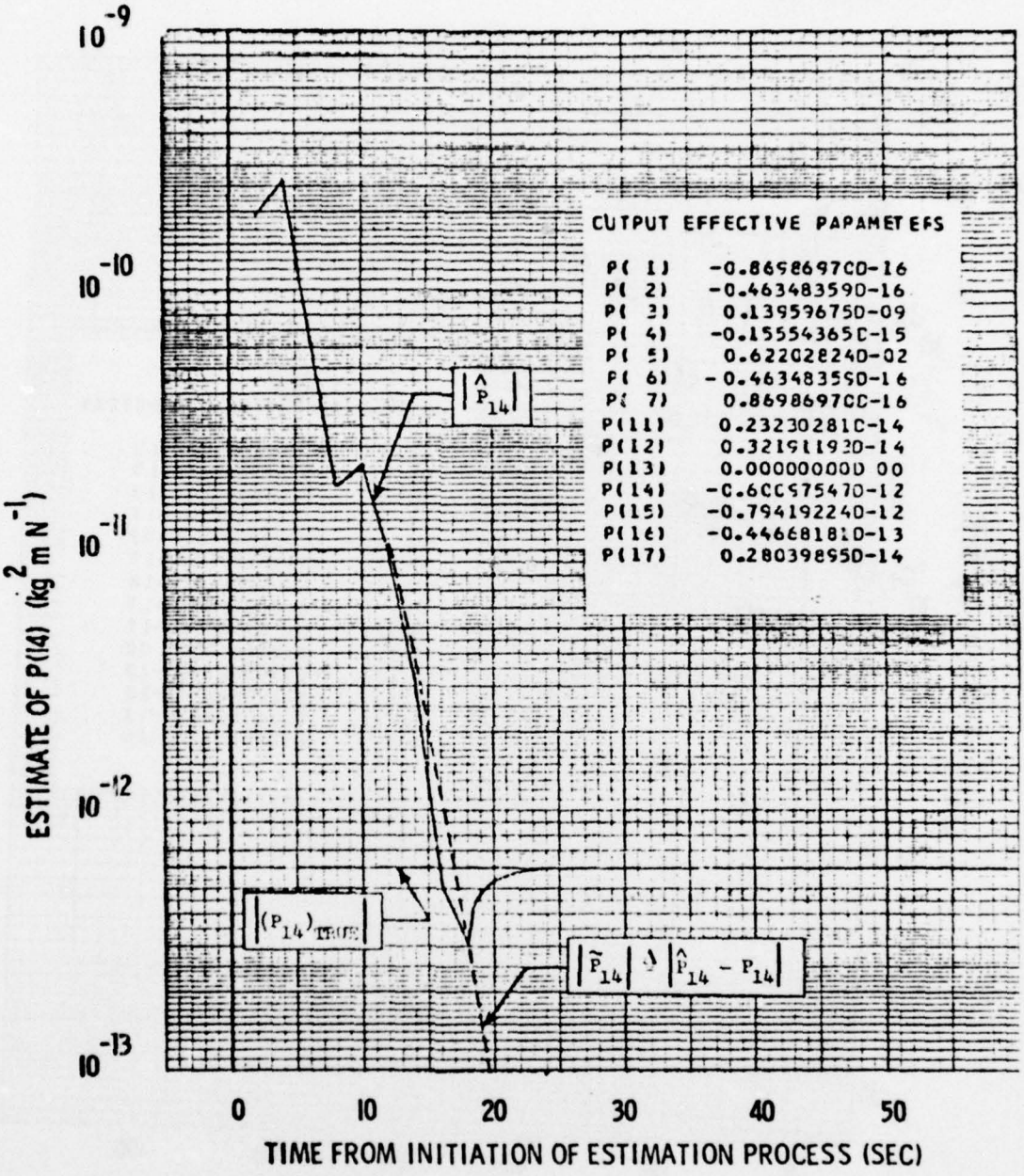


FIG. VI-5 P_{14} ESTIMATION -- ITERATION 1

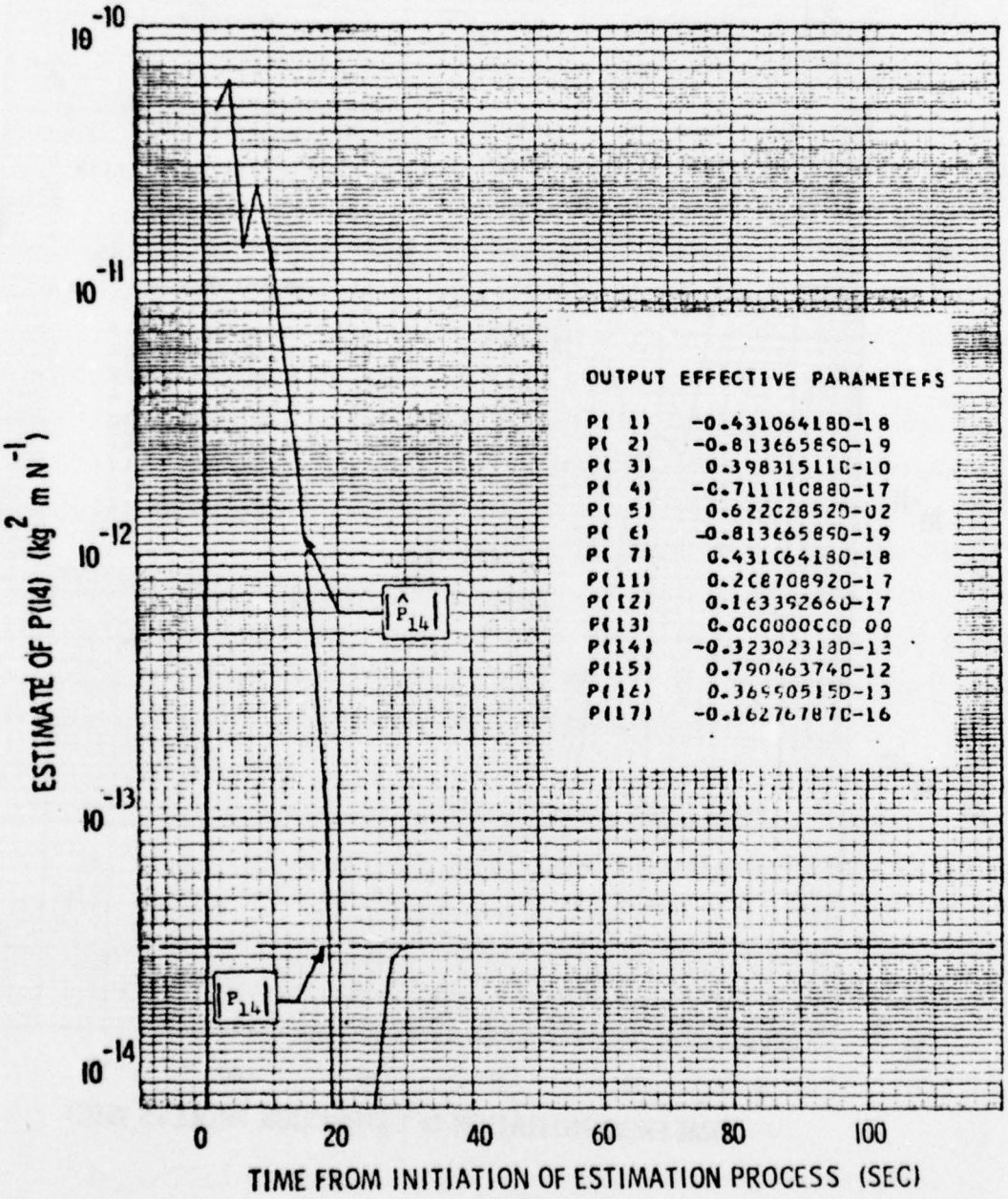


FIG. VI-6 P_{14} ESTIMATION -- ITERATION 2

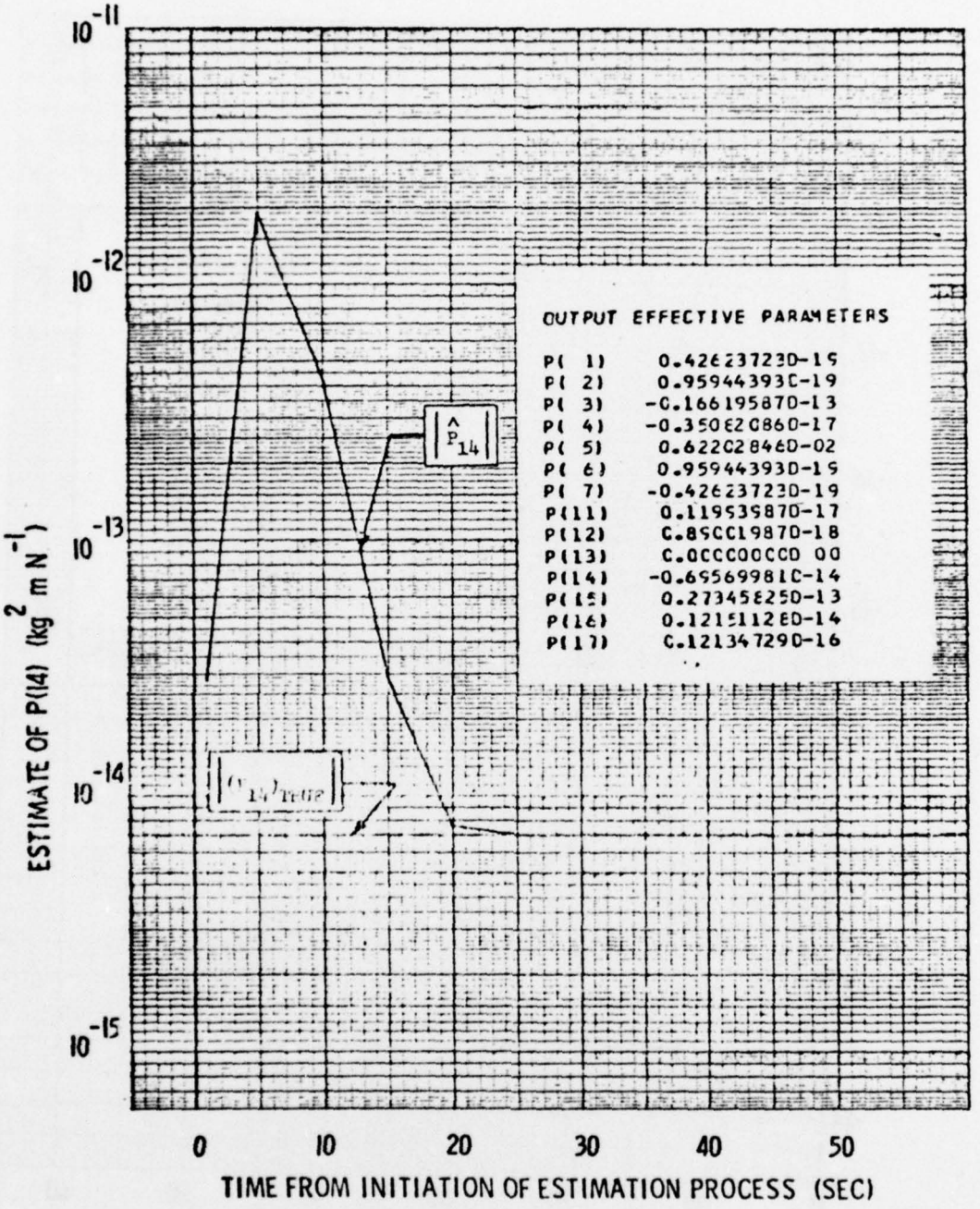


FIG. VI-7 P_{14} ESTIMATION -- ITERATION 3

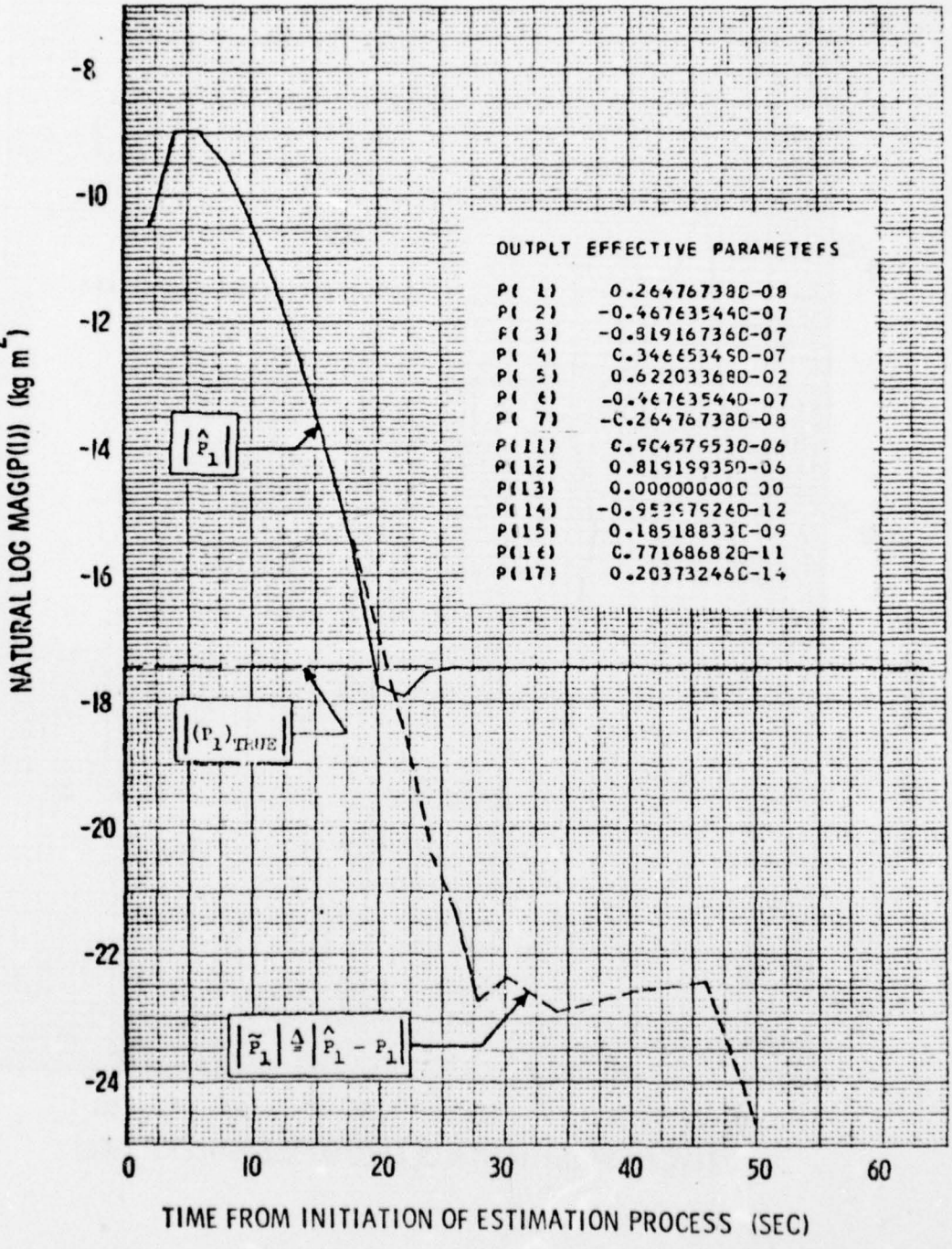


FIG. VI-8 P_1 ESTIMATION -- ITERATION ZERO

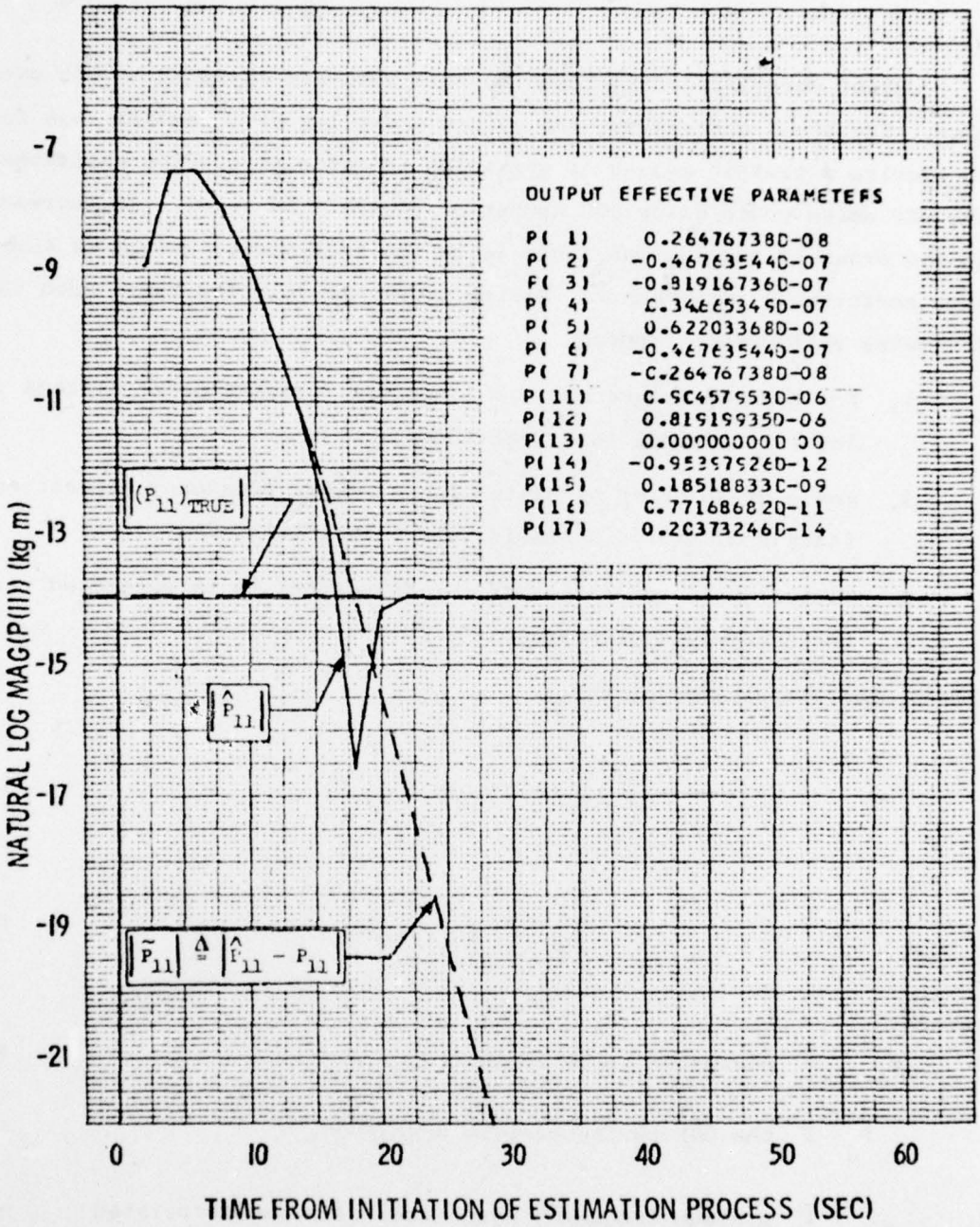


FIG. VI-9 P_{11} ESTIMATION — ITERATION ZERO

H. CONCLUSIONS REGARDING A CORRELATION APPROACH TO OUTPUT EFFECTIVE PARAMETER (OEP) IDENTIFICATION

Output correlation was found to be a workable approach to OEP estimation. The basic correlator, the second order lag or L^2 system, was found to require a certain amount of upgrading in order to provide estimates of the OEP which could allow RGG operation at the 1 EU level. An increase in the order of the lag was found to be the most direct method of correlator performance improvement. System order was selected based upon the following performance trades:

1. For a given frequency $\omega > 1$ rad/sec, higher order systems yield lower sinusoidal term magnitudes;
2. For a given order of system lag, a wider frequency separation (larger ω) yields a smaller sinusoidal term;
3. Variation of the ratios of the parameters to be estimated varies the required system order.

Based upon the assumption that

$$\frac{|P_j|}{|P_{est}|} = 10^4 \tag{6.48}$$

$$\omega_m = 10 \text{ rad/sec} \tag{6.49}$$

where

$P_{est} \triangleq$ parameter to be estimated, (6.50)

$P_j \triangleq$ the OEP having maximum magnitude, (6.51)

$\omega_{min} \triangleq$ minimum frequency associated with the correlated output torque, (6.52)

a 1% sinusoidal error criterion dictates the selection of a 6th order lag correlator using (6.53) where k is the parameter of system order definition.

$$0.01 = \frac{|P_j|}{|P_{est}|} \quad \frac{1}{(\omega_{min})^k} . \tag{6.53}$$

A single platform rate, ω_{xP_1}, two platform linear accelerations, A_x and A_z, and a spin motor torque of known frequency, T_d, form an adequate input set for estimation of all 12 independent OEPs. With input frequency quantized to $0.1\ \omega_s$, minimal output frequency separation was found to be $0.1\ \omega_s$. Numerous combinations of platform input frequencies can provide parameter identifiability.

Sixth order lag correlator performance results indicated the possibility of RGG operation within the specified 1 EU error bound using only the correlator and numerical output compensation. The quality of the correlator estimate of P_j is a function not only of $|P_j|$, but also of the magnitudes of all the other OEPs. A single OEP having a magnitude substantially larger than expected due, for example, to manufacturing error, could result in unacceptably large errors. Higher order lag systems could reduce the probability of such error at the expense of system complexity.

H-1 Pivot Stiffness Knowledge Requirements

The parameter estimation techniques of this chapter and Chapter V all assumed perfect knowledge of the pivot stiffnesses which combine to form the output error equation coefficient (from eq. 4.29)

$$c = \frac{1/K_1}{1 + \frac{K_0}{K_1} + \frac{K_0}{K_2}} . \tag{6.54}$$

Based upon the discussion which led to (4.29), the gravity gradient torque, T_{gg}, causes an arm to arm relative deflection θ^{o-e} which can be written as

(6.55)

From (2.24), a 1 EU torque corresponds to 3.56×10^{-12} N m. Hence, using the data of Table II-1, the 3000 EU gravity gradient torque produces an arm-to-arm relative angular deflection equal to

$$\theta_{gg}^{o-e} = 6.17 \times 10^{-11} \text{ rad.} \tag{6.56}$$

A 1 EU deflection corresponds to

$$\theta_{1EU}^{o-e} = 2.06 \times 10^{-14} \text{ rad.} \tag{6.57}$$

In order for the error in the knowledge of c to produce a negligible contribution to the overall output error, a 0.10 EU error level due to this source is defined as acceptable. This error contributes an extra 0.01 EU to the total RGG output when root sum^2 with the parameter error contribution. Since the stiffnesses K_0, K_1, and K_2 all have approximately the same value, the coefficient c, for purposes of this analysis, is written as

$$c + \Delta c = \frac{\dfrac{1}{K_1 + \Delta K_1}}{1 + 2\dfrac{K_0 + \Delta K_0}{K_1 + \Delta K_1}} \tag{6.58}$$

and using the binomial expansion

$$c + \Delta c = \frac{1}{K_1 + 2K_0}\left\{1 - \frac{\Delta K_1 + 2\Delta K_0}{K_1 + 2K_0}\right\} . \tag{6.59}$$

Using (6.55), (6.57), and assuming that

$$\Delta K_1 = \Delta K_0 \triangleq \Delta K , \tag{6.60}$$

a 0.10 EU output error requires that

$$2.06 \times 10^{-15}\,\text{rad} = -\frac{3\Delta K}{(K_1+2K_0)^2}\,(1.07 \times 10^{-8}\ \text{N m}) \qquad (6.61)$$

or

$$|\Delta K| = 1.92 \times 10^{-3}\ \text{N m/rad}\ . \qquad (6.62)$$

Hence, in order to assure the performance of the estimation techniques, it is necessary to determine, during preassembly test, each pivot stiffness to approximately 40 parts per million.

47

$$\Delta T_z \cos\left[(2\omega_s - \alpha_x)\, t\right] =$$

$$k_1\left[\cos(x_1 + x_{26}) + \cos(x_1 - x_{26})\right] + k_1\left[\cos(x_2 + x_{26}) + \cos(x_2 - x_{26})\right]$$

$$- k_2\left[\sin(x_3 + x_{26}) + \sin(x_3 - x_{26})\right] + k_2\left[\sin(x_4 + x_{26}) + \sin(x_4 - x_{26})\right]$$

$$+ K_3 x_5 \cos x_{26}$$

$$+ \left[2k_4 + - k_{25}\right]\left[\cos(x_6 + x_{26}) + \cos(x_6 - x_{26})\right] \qquad (1)$$

$$- k_4\left[\cos(x_7 + x_{26}) + \cos(x_7 - x_{26})\right] - k_4\left[\cos(x_8 + x_{26}) + \cos(x_8 - x_{26})\right]$$

$$+ \left[-2k_5 + \tfrac{1}{2} k_{17}\right]\left[\sin(x_9 + x_{26}) + \sin(x_9 - x_{26})\right]$$

$$+ k_5\left[\sin(x_{10} + x_{26}) + \sin(x_{10} - x_{26})\right] - k_5\left[\sin(x_{11} + x_{26}) + \sin(x_{11} - x_{26})\right]$$

Chapter VII

ACTIVE PARAMETER CONTROL

A. INTRODUCTION

In Chapters V and VI, two separate approaches to RGG parameter estimation were investigated. It was concluded that (Ch. III) for a RGG manufactured to the specified tolerances, simple numerical compensation of RGG output was a risky approach to achieving operation at an error level less than 1 EU, given current state of the art sensors and electronics. An active parameter control mechanism within the RGG system itself greatly enhances the likelihood that the RGG will achieve the 1 EU design goal. In this chapter such a control system is defined and elaborated upon through a simple example.

B. SELECTION OF A METHOD OF CONTROL

All output effective parameters (OEP) are direct functions of either arm mass, arm mass center position, or combinations of these physical parameters. This statement is obviously true with respect to parameters 1 to 7, and 11 and 12, and is here postulated without proof for OEP 13, the "Yankee screwdriver" torque parameter. That arm mass and mass position also effect the elasticity related parameters (A-17) will be demonstrated in Chapters VIII and IX. Given these dependences among RGG arm mass and the error producing OEP, two alternative methods for active parameter control are suggested:

(1) Mass reduction or addition, such as laser mass removal and mass sputtering;

(2) Arm mass redistribution.

1. Mass Removal Techniques

The concept of active, on-line mass removal or addition for instrument parameter control is not new. McKinley [MC-1] in 1968 demonstrated

both theoretically and experimentally the practicality of mass removal by laser as a method for orienting the principal axes of a spherical rotor gyro. In theory, this approach is a valid candidate for use with the RGG. Several practical considerations, however, make this approach unattractive. Firstly, temperature gradients within the RGG case must be less than 0.01 °C/m. Secondly, both the laser and sputtering processes create residues which are not controlled and could be unfavorably deposited on the instrument. Finally, the RGG must be kept compact. A laser would be a relatively bulky addition to the system as well as one which would require significant power for operation.

2. Mass Motion Compensation

Satellite dynamics compensation using mass motion within a system was demonstrated by Lorell [LO-1] in 1971. Mass redistribution is not subject to the detrimental side effects of mass removal. Finally, the design of the Hughes' instrument already includes mass balance tubes which can relocate mass. The question remains as to where the mass motion devices should be located to be most effective and what commands should be sent once an estimate of the OEP vector has been made.

C. CONTROL LAW DEVELOPMENT

In Chapter Iv it was pointed out that the instrument output error torque could be driven to zero if the vector of output effective parameters could likewise be driven to zero. This vector cannot be driven totally to zero sinc P_5 is, nominally, the parameter which provides the gravity gradient signal [PE-1]. All other OEPs, however, have nominal values equal to zero. Defining

$$P_{j0} \triangleq \text{nominal value of } P_j$$
$$\Delta P_j \triangleq P_j - P_{j0}\,, \tag{7-1}$$

the error ΔT_z in instrument output can be minimized if the vector ΔP

is driven to zero. Treating the mass movements as controls and the OEPs as states, various cost functions can be defined. A least squares control criterion is simple and adequate. The parameter control problem may be stated as follows:

- Given the vector of output effective parameters, P, or equivalently, the vector ΔP, and
- given a set of controls which may be expressed as the vector Δx,
- given a defining relationship between the vectors ΔP and Δx,
- $$\min \; J = \frac{1}{2} (\Delta x)^T B(\Delta x) \tag{7.2}$$

  subject to the constraint $$-\Delta P = F \, \Delta x. \tag{7.3}$$

The vector ΔP is taken to have dimension n. The vector Δx has dimension m, and

$$m > n. \tag{7.4}$$

This is the classical least squares minimization probelm for a system which is under-determined in Δx. The Hamiltonian, $\mathcal{H}$ (with B taken to be the identity matrix, is

$$\mathcal{H} = \frac{1}{2} (\Delta x)^T (\Delta x) + \lambda^T (\Delta P + F \Delta x) \; . \tag{7.5}$$

Then

$$\frac{\partial \mathcal{H}}{\partial \Delta x} = (\hat{\Delta x})^T + \lambda^T F \; , \tag{7.6}$$

and

$$(\hat{\Delta x}) = -F^T \lambda \; . \tag{7.7}$$

Substitution of (7.7) into (7.3) yields

$$+\Delta P = F F^T \lambda \tag{7.8}$$

when Δx is assumed equal to x. In order to guarantee that the

parameter vector ΔP can be driven to zero, it is necessary for the control system to have the capability to adjust any parameter of group of parameters while the others remain undisturbed. When this capacity for arbitrary parameter adjustment exists, the system is said to be controllable. Mathematically, the requirement for parameter controllability is that the sensitivity matrix F have rank n. It has been assumed in this discussion that controller specification and design are such that the $n \times m$ matrix F has rank n. It follows from this assumption that the matrix $(FF^T)^{-1}$ exists, yielding

$$\lambda = +(FF^T)^{-1}\Delta P \ . \tag{7.9}$$

Substitution of (7.9) into (7.7) then yields

$$\Delta\hat{x} = -F^T(FF^T)^{-1}\Delta P \ . \tag{7.10}$$

Equation (7.10) is the standard least squares solution for a system which is under-determined with respect to the parameter vector Δx. It is worthwhile at this time to point out an interesting duality between least squares parameter estimation and least squares parameter control. Consider again the stated problem, but this time define two distinct conditions: (1) $n > m$; (2) $n < m$.

The first of these conditions, which is referred to as over-determined in Δx, is widely used for estimation of the parameter vector Δx. The number m of parameters is fixed. For $n \geq m$ the solution for the estimate of Δx is unique. This uniqueness is intuitively acceptable since all observations are based upon the same set of parameters. As more independent observations P_j are added (n increased), the covariance matrix associated with the errors in the estimates of the parameters decreases [LI-1]. The extra observations $(n - m)$ reduce the effect of sensor noise upon the parameter estimates.

In contrast to the case of parameter estimation, a system which is under-determined in Δx $(n < m)$ is preferable for parameter control.

For this case, the observation vector P_n represents the vector of system parameters to be controlled. Hence, n has a fixed value. The vector Δx represents increments to the various control mechanisms. By adding additional controls, the size of m can be increased. For the case where $n < m$, the solution to (7.2) and (7.3) is not unique. As the number of controls m is increased, the number of possible solutions to (7.3) generally increases. This is a desirable result since more candidate solutions to the constraint equations yield more candidate solutions for cost function minimization. As more control mechanisms are added, the absolute value of the control output, $|\Delta x_j|$ which must be provided by any one control mechanism, can be expected to decrease. To summarize, for least squares parameter estimation of Δx, the system should be over-determined in Δx for best performance; i.e., the observation vector $(\Delta P)_{n\times 1}$ should have fewer components than the control vector $(\Delta x)_{m\times 1}$. For system controllability, it is necessary and sufficient that the coefficient matrix $F_{n\times m}$ have rank n. This discussion is given in tabular form in Table VII-1.

D. EXAMPLE OF UNDER-DETERMINED LEAST SQUARES PARAMETER CONTROL

As a numerical example of control by under-determined least squares, let the parameter vector ΔP be

$$\Delta P = \begin{bmatrix} 5 \\ 1 \\ -3 \end{bmatrix} \tag{7.11}$$

and let the sensitivity matrix

$$F = \begin{bmatrix} 1 & -2 & 1 & 3 \\ 2 & 1 & -1 & 1 \\ -1 & 3 & 3 & 1 \end{bmatrix}, \tag{7.12}$$

Table VII-1

LEAST SQUARES PARAMETER ESTIMATION AND CONTROL DUALITY

	Parameter Estimation	Parameter Control
Linear System	$\Delta P = F\,\Delta x$	$\Delta P = -F\Delta x$
$\Delta P_{n\times 1}$	Measurement Vector	Parameter Vector
$F_{n\times m}$	Coefficient Matrix	Coefficient Matrix
$\Delta x_{m\times 1}$	Parameter Vector	Control Vector
Classification	Overdetermined in Δx	Underdetermined in Δx
Rank (F)	m	n
Square matrix for inversion	$F^T F$	FF^T
Solution	$\Delta x = (F^T F)^{-1} F^T \Delta P$	$\Delta x = -F^T (FF^T)^{-1} \Delta P$

satisfy the constraint equation

$$\Delta P = -F[\Delta x] . \tag{7.13}$$

It is desired to find a control vector $\Delta x_{4\times 1}$ satisfying (7.13) while minimizing the quadratic cost function

$$J = \frac{1}{2} \Delta x^T \Delta x . \tag{7.14}$$

The control vector Δx, specified by (7.15) was calculated from (7.10).

$$[\Delta x]^T = -[0.51748, \ -1.005, \ -0.10939, \ 0.86064]. \tag{7.15}$$

The vector Δx of (7.15) satisfies (7.13) with

$$J = 1.015 . \tag{7.16}$$

The vector specified by (7.15) is not unique in its satisfaction of (7.13). The solution

$$[\Delta x]^T = -]1.57, \ -1.3, \ 0.84, \ 0] \tag{7.17}$$

also satisfies (7.13). Note, however, that the cost function J associated witn Δx as specified by (7.17) is 2.43, a more than twice the value which resulted from the least squares solution. The value of Δx as given by (7.17) is therefore extraneous.

Chapter VIII

EXTENSION OF THE INSTRUMENT MODEL TO A CONTROL COMPATIBLE FORM

A. INTRODUCTION

Under-determined least squares control is an attractive approach to the RGG parameter control problem. It is conceptually simple, and it is nondestructive. In this chapter, the output effective parameter (OEP) vector is rewritten in terms of basic instrument physical quantities so as to demonstrate OEP reachability using this control law. A parameter P is said to be reachable by a control C if $\partial P/\partial C$ has a nonzero value. Parameter reachability is a necessary condition for parameter controllability. The operating principle of the control system is simple repositioning of a set of amll control masses along a set of prescribed axes so as to change arm mass center and inertia characteristics. A significant result of the analysis presented in this chapter is that such mass repositioning can also be used for precision matching of arm lateral and axial elastic properties.

In order to investigate the applicability of repositioning as an approach to OEP control, it was necessary to express the OEP as functions of arm mass and arm mass position. Parameters described in this manner are referred to as being written in control compatible form. The dumbbell arm model used to describe the RGG arms in earlier sections of this analysis offered too few degrees of freedom among the various arm inertia and mass center properties to provide arbitrary values of the OEP. The four dumbbell masses were therefore replaced by 16 nominally identical masses which are referred to as 'model-masses.' In addition, odd and even arm terminology has been supplanted by reference to a four-arm sensor model when convenient. This revision from a two- to four-arm instrument model is particularly useful in our Chapter IX discussion of arm compliance control using mass redistribution. The instrument arm model revision permits each of the four model-masses

PRECEDING PAGE BLANK-NOT FILMED

located on each of the four instrument arms to be perturbed independently with respect to both mass and position. A conceptural drawing depicting model-mass placement is given in Fig. VIII-1.

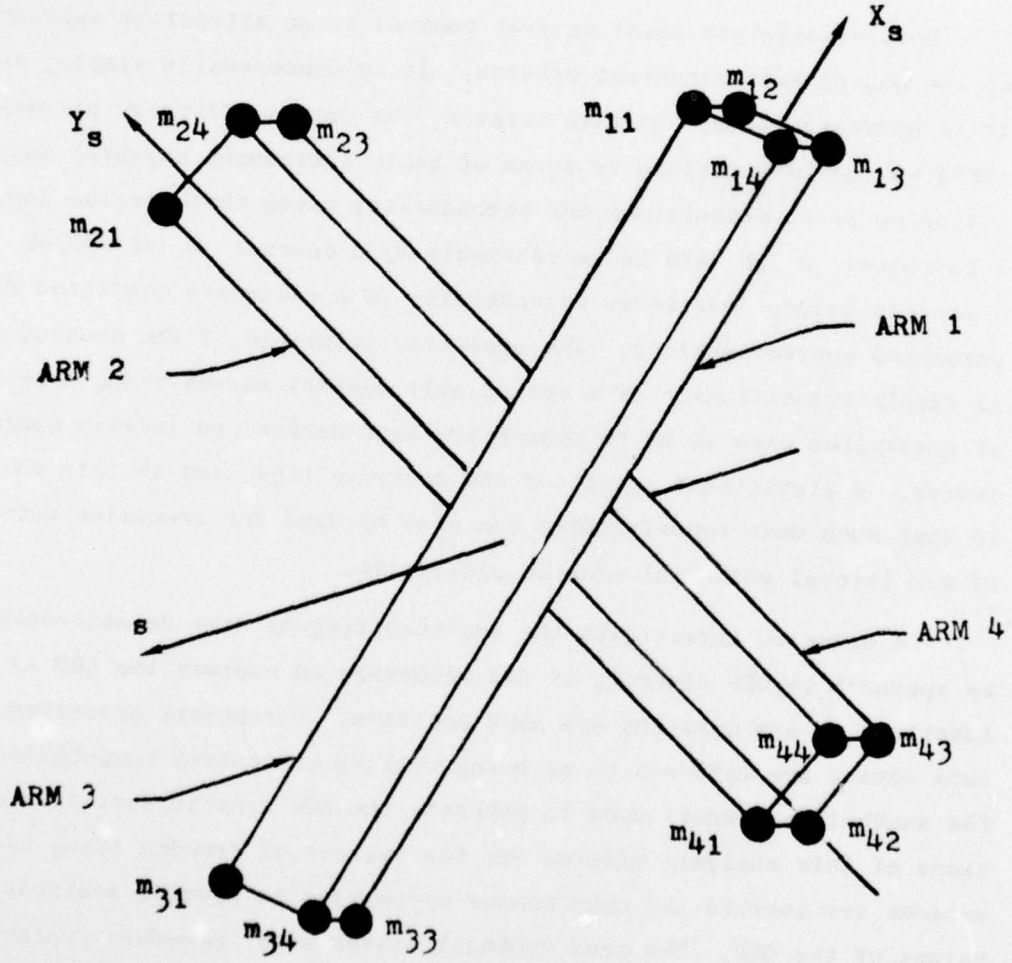


FIG. VIII-1 SIXTEEN MODEL-MASS CONFIGURATION FOR RGG PROOF MASS.

Each arm has 9 properties (3 mass center and 6 inertia) which can effect the OEP. The 16 model-mass arms therefore provide an analytical means for arbitrary mass, mass center, and inertia tensor specification.

Nominal numerical data for the 16-mass configuration are given in Table VIII-1. In the Table, the various model masses are listed in accordance with their respective subscripts. Hence, the mass of m_{11} appears in row 1, column 1 of the instrument sub-mass matrix. The mass of m_{34} appears in row 3, column 4 of that matrix.

B. EXPRESSION OF ARM MASS CENTERS AND INERTIAS IN CONTROL COMPATIBLE FORM

The output torque errors induced by the output effective parameters are sensed by the RGG in the elastic (or sensor) reference frame. In order to provide for simple calculation of the control, the direction of motion of each control mass is nominally along one of the sensor axis system reference directions. To write the mass center and inertia related parameters in control compatible form, it was necessary only to express the arm mass center locations and inertia tensor components relative to the origin of the sensor axis system and to perform the OEP in terms of these new expressions. Each model-mass and model-mass position is accompanied by two subscripts. These subscripts are defined by expressions (8.1) and (8.2),

$$m_{ij} = j^{th} \text{ model-mass of the } i^{th} \text{ arm} \tag{8.1}$$

$$x_{ij} = x \text{ component of the position of the } j^{th} \text{ model-mass of the } i^{th} \text{ arm relative to the sensor frame.} \tag{8.2}$$

1. Odd Arm Mass Center and Inertia Components

Using the definitions of expressions (8.1) and (8.2), the mass centers, ρ, and inertia tensor components, I, of the odd arm are

3

Table VIII-1

NOMINAL MASS AND POSITION DATA FOR 16 MODEL-MASS ROTATING GRAVITY GRADIOMETER CONFIGURATION (co-ordinates relative to sensor axis system) POSITIONS AS SHOWN WITHIN THE MATRICES CORRESPONDING TO MODEL-MASS SUBSCRIPTS.

INSTRUMENT SUB-MASS MATRIX

C.1953750 00	0.1953750 0C	C.1953750 CC	C.1953750 0C
C.1953750 CC	C.1953750 0C	C.1953750 00	0.1953750 0C
C.1953750 0C	0.1953750 0C	C.1953750 CC	C.1953750 0C
C.1953750 0C	0.1953750 00	0.1953750 00	0.1953750 0C

FOUR ARM CONFIG. SUB-MASS POSITION VECTORS X,Y,Z (M) SENSOR AXES

ARM 1

C.4602567CCD-01	0.1264710CCD-C1	C.1262180000-01
C.4602567000-01	0.1264710CCD-C1	-C.12621ECCCD-C1
C.4602567CCD-C1	-0.1264710CCC-01	-0.1262180000-01
C.4602567CCC-C1	-C.1264710CCD-C1	C.12621ECCOD-C1

ARM 3

-0.4602567CCD-01	0.1264710CCD-C1	C.1262180000-01
-0.4602567CCD-01	0.1264710000-01	-C.1262180000-01
-0.4602567CCD-01	-0.1264710000-01	-C.1262180000-01
-C.4602567COC-01	-0.1264710000-01	C.1262180000-01

ARM 2

-C.1263710000-01	0.4602567CCD-C1	C.12621ECCOD-C1
C.1265710000-01	0.4602567000-01	0.1262180000-01
C.1265710000-C1	C.46C2567CCD-C1	-C.1262180000-C1
-C.1263710000-01	0.4602567000-01	-0.12621800CD-C1

ARM 4

-0.1263710000-01	-0.4602567C0D-01	C.1262180000-01
0.1265710CCD-01	-C.4602567CCD-01	0.1262180000-01
0.1265710000-01	-0.4602567C00-01	-C.1262180000-C1
-0.1263710CC0-01	-C.46C2567C0D-01	-0.1262180000-01

are expressed relative to the sensor axis system by (8.3) through (8.11).

$$\rho_{xo} = \frac{\Sigma m_{1i} x_{1i} + \Sigma m_{3i} x_{3i}}{\Sigma m_{1i} + \Sigma m_{3i}} \tag{8.3}$$

$$\rho_{yo} = \frac{\Sigma m_{1i} y_{1i} + \Sigma m_{3i} y_{3i}}{M_o} \tag{8.4}$$

$$\rho_{zo} = \frac{\Sigma m_{1i} z_{1i} + \Sigma m_{3i} z_{3i}}{M_o} \tag{8.5}$$

$$I_{xxo} = \Sigma m_{1i}[(y_{1i}-\rho_{oy})^2+(z_{1i}-\rho_{oz})^2] + \Sigma m_{3i}[(y_{3i}-\rho_{yo})^2 + (z_{3i}-\rho_{zo})^2] \tag{8.6}$$

$$I_{yyo} = \Sigma m_{1i}[(x_{1i}-\rho_{xo})^2 + (z_{1i}-\rho_{zo})^2] + \Sigma m_{3i}[(x_{3i}-\rho_{xo})^2 + (z_{3i}-\rho_{zo})^2] \tag{8.7}$$

$$I_{zzo} = \Sigma m_{1i}[(x_{1i}-\rho_{xo})^2 + (y_{1i}-\rho_{yo})^2] + \Sigma m_{3i}[(x_{3i}-\rho_{xo})^2 + (z_{3i}-\rho_{zo})^2] \tag{8.8}$$

$$I_{xho} = \Sigma m_{1i}[(x_{1i}-\rho_{xo})(y_{1i}-\rho_{yo})] + \Sigma m_{3i}(x_{3i}-\rho_{xo})(y_{3i}-\rho_{yo}) \tag{8.9}$$

$$I_{xzo} = \Sigma m_{1i}(x_{1i}-\rho_{xo})(z_{1i}-\rho_{zo}) + \Sigma m_{3i}(x_{3i}-\rho_{xo})(z_{3i}-\rho_{zo}) \tag{8.10}$$

$$I_{yzo} = \Sigma m_{1i}(y_{1i}-\rho_{yo})(z_{1i}-\rho_{zo}) + \Sigma m_{3i}(y_{3i}-\rho_{yo})(z_{3i}-\rho_{zo}) \ . \qquad (8.11)$$

2. Even Arm Mass Center and Inertia Components

The expressions for the even arm mass center and inertia tensor components are similar to those developed for the odd arm. Examples of the even arm equations, for ρ_{xe}, I_{yye}, and I_{xae} are given in (8.12) to (8.14).

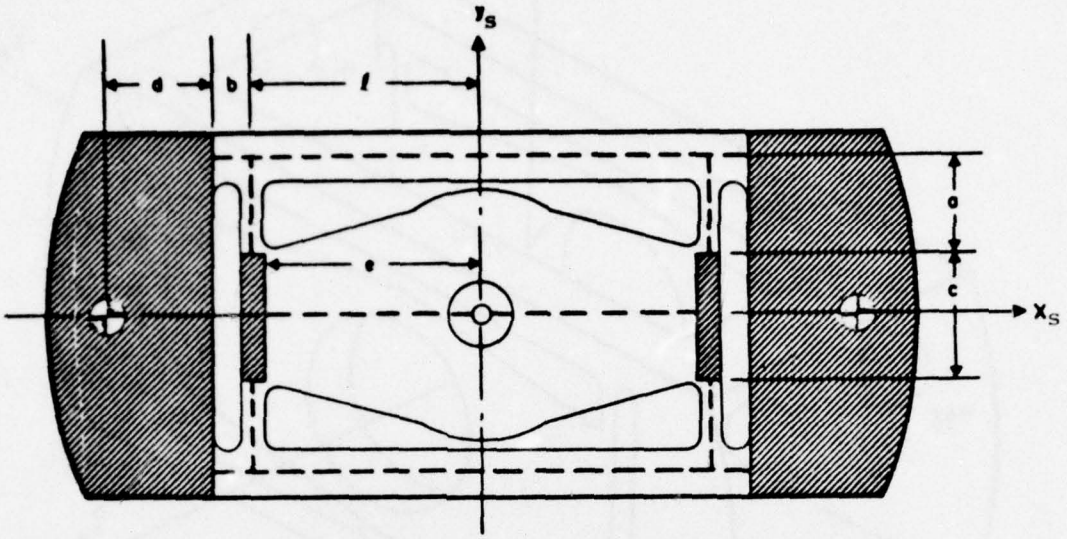
$$\rho_{xe} = \frac{\Sigma m_{2i} x_{2i} + \Sigma m_{4i} x_{4i}}{\Sigma m_{2i} + \Sigma m_{4i}} \qquad (8.12)$$

$$I_{yye} = \Sigma m_{2i}[(x_{2i} - \rho_{xe})^2 + (z_{2i} - \rho_{zi})^2] + \Sigma m_{4i}[(x_{4i} - \rho_{xe})^2 + (z_{4i} - \rho_{ze})^2] \qquad (8.13)$$

$$I_{xze} = \Sigma m_{2i}[(x_{2i} - \rho_{xe})(z_{2i} - \rho_{ze})] + \Sigma m_{4i}[(x_{4i} - \rho_{xe})(z_{4i} - \rho_{ze})] \ . \qquad (8.14)$$

C. ARM COMPLIANCE MODEL DEVELOPMENT

In order to express the compliance related OEP in control compatible form, it was necessary to extend the four arm instrument proof-mass model to one additional level of sophistication so as to account nominally for isoelastic arm design. The model used was suggested by Ames [AM-1], and is shown schematically in Fig. VIII-2. For purposes of compliance calculation, the mass is assumed to be concentrated at the position shown in Fig. VIII-2. Cross-hatched areas are assumed rigid and the support shaft is assumed isoelastic. The unmarked areas shown with centerlines



Section	Value
a	0.500 (in.)
b	0.200 (in.)
c	0.700 (in.)
d	0.600 (in.)(estimate)
e	1.181 (in.)
ℓ	1.243 (in.)
w_a	0.290

Section	Value
w_b	0.250 (in.)
w_c	0.290 (in.)
w_ℓ	0.250 (in.)
t	0.250 (in.)
E	3×10^7 ($lb_f/in.^2$) (est.)
G	1.25×10^7 ($lb_f/in.^2$) (est.)

FIG. VIII-2 ISOELASTIC ARM MODEL (ODD ARM)

are assumed compliant in axial compression, bending, and shear. A three-dimensional representation of the isoelastic odd arm is shown with model masses in Fig. VIII-3.

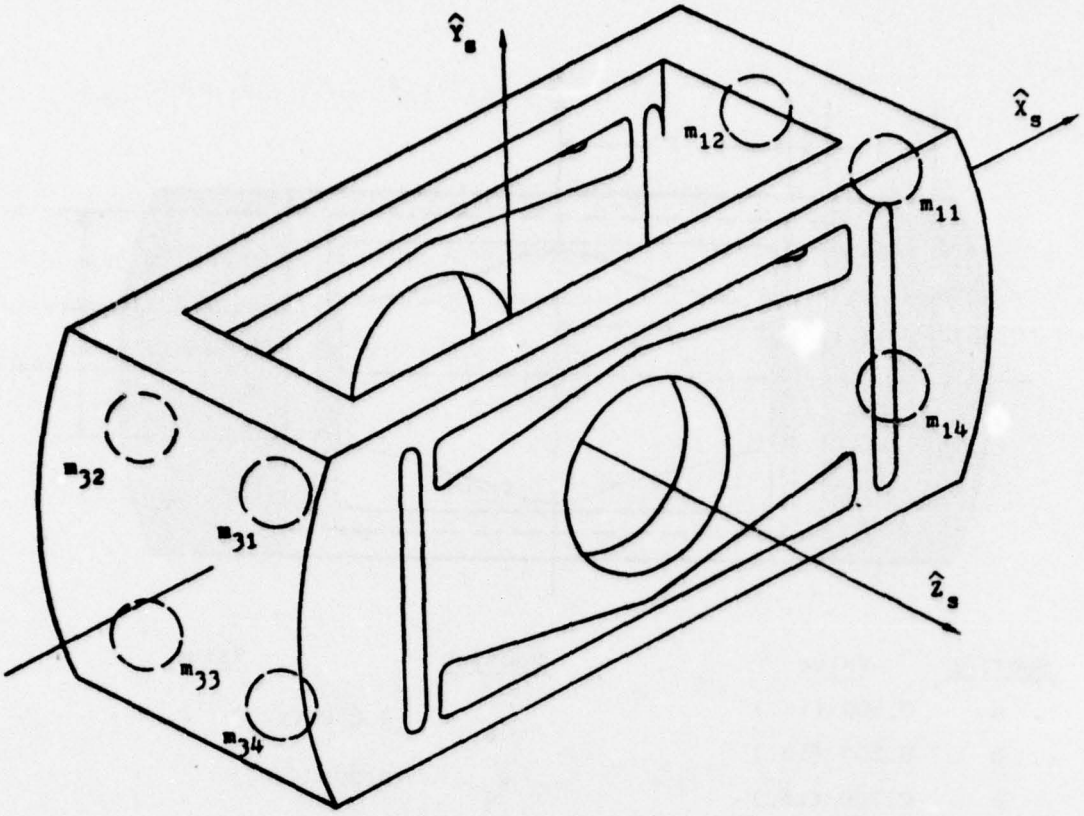


FIG. VIII-3 ISOELASTIC ODD ARM

Arm compliance was calculated using Castigliano's Energy Method [HO-1]. Equations relating straing energy to moment and shear and axial load are given by (8.15 to (8.17).

Bending:
$$U = \frac{1}{2}\int_o^L \frac{m^2}{EI}\,dx \qquad (8.15)$$

Shear:
$$U = \frac{1}{2}\int_o^L \frac{v^2}{GA}\,dx \qquad (8.16)$$

$$\text{Axial:} \qquad U = \frac{1}{2}\int_o^L \frac{P^2}{EA}\,dx \ . \tag{8.17}$$

The terms appearing in (8.21) to (8.23) are defined below:

U total member strain energy

L total member length

M moment acting upon the stressed member

V shear force acting upon the stressed member

P discrete load acting upon the stressed member

A member cross-sectional area

I member area moment of inertia

E member elastic modulus

G member shear modulus.

D. AXIAL ARM COMPLIANCE CALCULATION

The arm loads and support diagram for an arm subject to axial loading is given in Fig. VIII-4.

1. Segment b Strain Energy--Axial Loading

Segment b is assumed subject to axial loading only. Given this assumption, segment b strain energy is

$$U_{ba} = (2)(\tfrac{1}{2})\int_o^b \frac{1}{EA_b}\left[\tfrac{1}{2}P\right]^2 dx \tag{8.18}$$

$$U_{ba} = \frac{1}{4Etw_b}P^2 b \ . \tag{8.19}$$

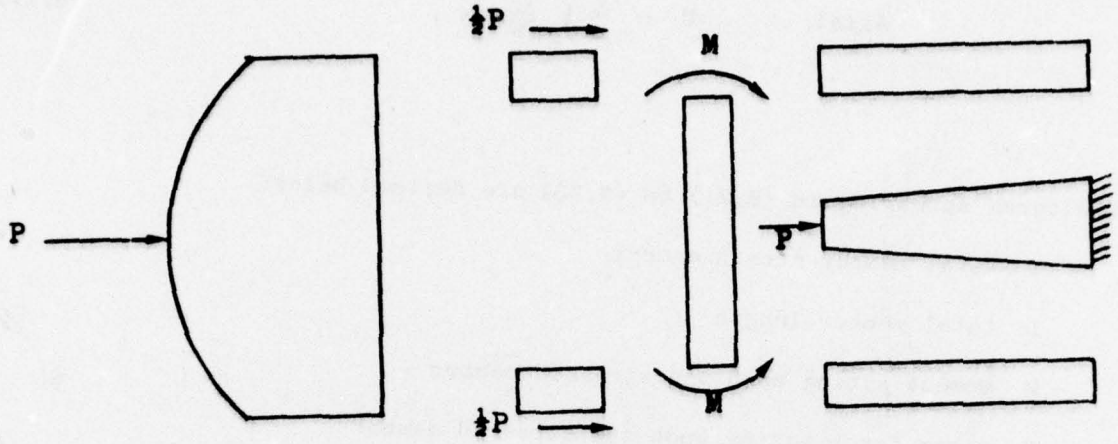


FIG. VIII-4 LOAD AND SUPPORT DIAGRAM FOR AXIALLY LOADED ARM.

2. Segment a Strain Energy--Axial Loading

Under conditions of purely axial arm loading, segment a strain energy is assumed to result from member bending only. Based upon this assumption,

$$U_{aa} = (2)(\tfrac{1}{2}) \int_o^a \frac{1}{EI_a} [\tfrac{1}{2}Px]^2 dx \qquad (8.20)$$

or

$$U_{aa} = \frac{1}{Etw_a^3} P^3 a^3 . \qquad (8.21)$$

3. Segment e Strain Energy--Axial Loading

Segment e has constant thickness t and lateral geometry as shown in Fig. VIII-5 with

$$\rho \triangleq \frac{1}{w_{eo}} (w_{eo} - c) , \qquad (8.22)$$

segment e strain energy is

$$U_{ea} = \frac{1}{2}\int_{o}^{e} \frac{1}{EA} P^2 dx \ . \tag{8.23}$$

Substitution for A as

$$A(x) = t\left[c + \rho \frac{w_{eo}}{e} x\right] \tag{8.24}$$

yields

$$U_{ea} = \frac{1}{2Et}\left(\frac{e}{\rho w_{eo}}\right) P^2[\ell n(c + \rho w_{eo}) - \ell n\ c] \ , \tag{8.25}$$

or

$$U_{ea} = -\frac{P^2}{2Et}\left(\frac{e}{\rho w_{eo}}\right) \ell n(1 - \rho) \ . \tag{8.26}$$

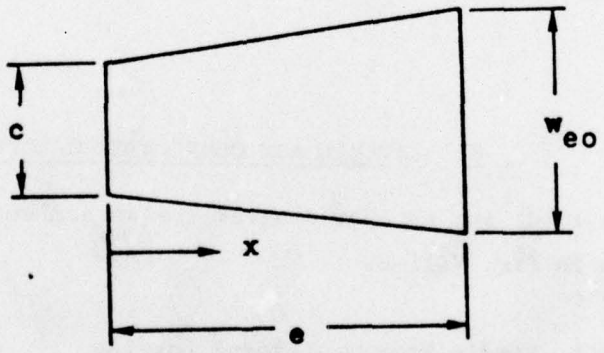


FIG. VIII-5 SEGMENT e LATERAL GEOMETRY

11

4. Total Axial Strain Energy--Axial Loading

The total axial load strain energy introduced into the arm is the summation of (8.19), (8.21), and (8.26).

$$U_a = \left\{ \frac{b}{4Etw_b} + \frac{a^3}{Etw_a^3} - \frac{1}{2Et}\left(\frac{e}{\rho w_{eo}}\right) \ell n(1 - \rho) \right\} P^2 \qquad (8.27)$$

5. Axial Load Compliance

Arm compliance C_a due to an applied axial load is

$$C_a = \frac{\partial U_a}{\partial P} . \qquad (8.28)$$

Hence, from (8.27)

$$C_a = \frac{1}{Et}\left\{ \frac{2a^3}{w_a^3} + \frac{b}{2w_b} - \left(\frac{e}{\rho w_{eo}}\right) \ell n(1 - \rho) \right\} . \qquad (8.29)$$

E. LATERAL ARM COMPLIANCE CALCULATION

The arm loads and support diagram for an arm subject to lateral loading is given in Fig. VIII-6.

1. Segment b Strain Energy--Lateral Loading

Under conditions of lateral arm loading, arm segment b is assumed subject to bending, shear, and axial disturbances. Hence

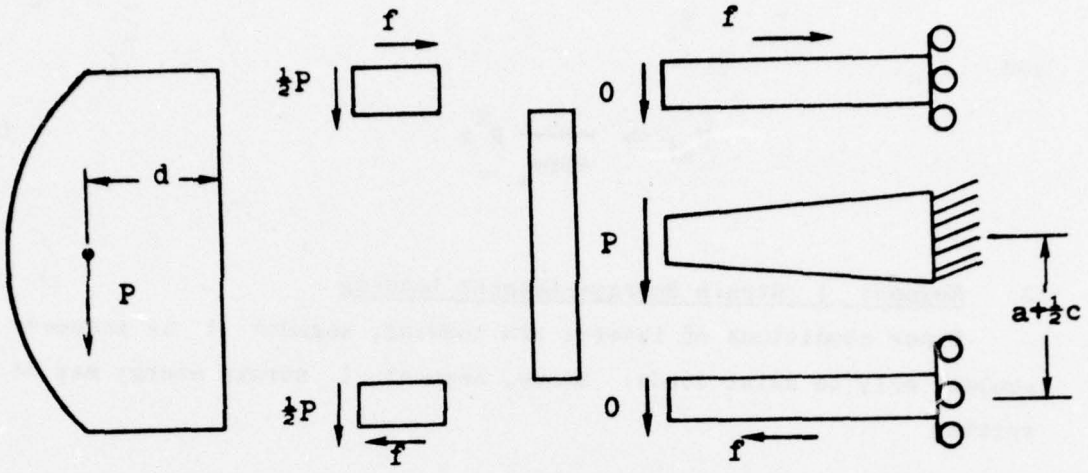


FIG. VIII-6 LOAD AND SUPPORT DIAGRAM FOR LATERALLY LOADED ARM

$$U_{b\ell} = 2(\tfrac{1}{2}) \int_o^b \frac{1}{EI_b} [\tfrac{1}{2}Px]^2 dx + 2(\tfrac{1}{2}) \int_o^b \frac{1}{GA_b} [\tfrac{1}{2}P]^2 dx$$

$$+ 2(\tfrac{1}{2}) \int_o^b \frac{1}{EA_b} \left[\frac{1}{2(a + \frac{c}{2})} Pd \right]^2 dx , \qquad (8.30)$$

and

$$U_{b\ell} = \frac{1}{Et} \left\{ \frac{b^3}{w_b^3} + \frac{bE}{4Gw_b} + \frac{d^2 b}{4w_b (a + \frac{c}{2})^2} \right\} P^2 . \qquad (8.31)$$

2. Segment a Strain Energy--Lateral Loading

Under conditions of lateral arm loading, segment a strain energy is assumed to result from the axial loading of the member only. Therefore

$$U_{a\ell} = 2(\tfrac{1}{2}) \int_o^a \frac{1}{EA_a} [\tfrac{1}{2}P]^2 dx \qquad (8.32)$$

and

$$U_{a\ell} = \frac{1}{4Etw_a} P^2 a \ . \tag{8.33}$$

3. Segment 1 Strain Energy--Lateral Loading

Under conditions of lateral arm loading, segment 1 is assumed subject only to axial loads. Hence, segment 1 strain energy may be written

$$U_{\ell\ell} = 2(\tfrac{1}{2}) \int_o^{\ell} \frac{1}{EA_{\ell}} \left[\frac{1}{2(a + \frac{c}{2})} Pd \right]^2 dx \tag{8.34}$$

or

$$U_{\ell\ell} = \frac{1}{4Etw_{\ell}[a + \frac{c}{2}]^2} P^2 d^2 \ell \ . \tag{8.35}$$

4. Segment e Strain Energy Lateral Loading

Under conditions of purely lateral arm loading, segment e strain energy is assumed due to member bending only. Therefore,

$$U_{e\ell} = \frac{1}{2} \int_o^{e} \frac{\Sigma m^2}{EI_e} dx \tag{8.36}$$

where

$$\Sigma m^2 = p^2 b^2 [1 + (x/b)^2] \ , \tag{8.37}$$

and

$$I_e = \frac{1}{12} t \left[c + \rho \frac{w_{eo}}{e} x \right] \ . \tag{8.38}$$

Defining

$$z \triangleq \frac{b}{Et}(Pb)^2 , \tag{8.39}$$

(8.36) may be rewritten as

$$\frac{u_{e\ell}}{z} = \int_o^e \frac{dx}{[A+Bx]^3} + \frac{1}{b^2}\int_o^e \frac{x^2 dx}{[A+Bx]^3} + \frac{2}{b}\int_o^e \frac{x dx}{[A+Bx]^3} \tag{8.40}$$

where

$$A \triangleq C \tag{8.41}$$

and

$$B \triangleq \rho \frac{w_{eo}}{e} . \tag{8.42}$$

Integration of (8.40) and substitution for A and B yields

$$U_{e\ell} = \frac{3P^2}{Et}\left[\frac{e}{w_{eo}}\right]^3 \left\{ \begin{array}{l} \frac{b}{e}\left(\frac{2}{1-\rho}\right) - \left(\frac{b}{e}\right)^2 \frac{(\rho-2)}{(1-\rho)^2} \\ \\ + \frac{2}{\rho^3}\left[-\ell n(1-\rho)+2(1-\rho)-\frac{(1-\rho)^2}{2} - 1.5\right] \end{array} \right\} \tag{8.43}$$

and with

$$K \triangleq \frac{b}{e}\left(\frac{2}{1-\rho}\right) - \left(\frac{b}{e}\right)^2 \frac{(\rho-2)}{(1-\rho)^2} + \frac{2}{\rho^3}\left[-\ell n(1-\rho)+2(1-\rho)-\frac{(1-\rho)^2}{2} - 1.5\right] \tag{8.44}$$

$$U_{e\ell} = \frac{3P^2}{Et}\left[\frac{e}{w_{eo}}\right]^3 K . \tag{8.45}$$

5. Lateral Load Strain Energy

From (8.30), (8.33), (8.35), and (8.45), the total arm lateral load strain energy is

$$U_\ell = \frac{P^2}{Et}\left\{\begin{array}{l}\left(\frac{b}{w_b}\right)^3 + \frac{bE}{4Gw_b} + \frac{d^2 b}{4w_b\left(a+\frac{c}{2}\right)^2} + \frac{a}{4w_a} \\ \\ \quad + \frac{d^2\ell}{4w_\ell\left[a+\frac{c}{2}\right]^2} + 3\left[\frac{e}{w_{eo}}\right]^3 K\end{array}\right\} \tag{8.46}$$

or

$$U_\ell = \frac{P^2}{Et}\left\{\begin{array}{l}\left(\frac{b}{w_b}\right)^3 + \frac{bE}{4Gw_b} + \frac{d^2(b+\ell)}{4w_b\left(a+\frac{c}{2}\right)^2} \\ \\ \quad + \frac{a}{4w_a} + 3\left[\frac{e}{w_{eo}}\right]^3 K\end{array}\right\}. \tag{8.47}$$

6. Lateral Load Arm Compliance

Since

$$C_\ell = \left.\frac{\partial U_\ell}{\partial P}\right|_{p=1} \tag{8.48}$$

the lateral load arm compliance is

$$C_\ell = \frac{1}{Et}\left\{\begin{array}{l}2\left(\frac{b}{w_b}\right)^3 + \frac{bE}{2GW_b} + \frac{d^2(b+\ell)}{2w_b\left[a+\frac{c}{2}\right]^2} \\ \\ \quad + \frac{a}{2w_a} + 6\left[\frac{e}{w_{eo}}\right]^3 K\end{array}\right\}. \tag{8.49}$$

F. ARM COMPLIANCE CALCULATION

Given the arm dimensions as listed in Fig. VIII-2, the isoelastic nature of the arm can be demonstrated using (8.29) and (8.49). For the case of axial loading, from (8.29),

$$C_a = \frac{1}{Et}\left\{\frac{2a^3}{w_a^3} + \frac{b}{2w_b} - \left(\frac{e}{\rho w_{eo}}\right)\ell n(1-\rho)\right\},$$

and substitution from Fig. VIII-2 yields

$$C_a = \frac{1}{7.5\times10^6}\{10.239 + 0.40 + 1.193\} \tag{8.50}$$

$$C_a = 1.5777 \times 10^{-6}\ \text{ft/lb}_f\ , \tag{8.51}$$

or

$$C_a = 1.0811 \times 10^{-7}\ \text{m N}\ . \tag{8.52}$$

For the case of the laterally loaded arm, from (8.49),

$$C_\ell = \frac{1}{Et}\left\{\begin{array}{l} 2\left(\frac{b}{w_b}\right)^3 + \frac{bE}{2Gw_b} + \frac{d^2(b+\ell)}{2w_b\left[a+\frac{c}{2}\right]^2} \\ \\ \qquad + \frac{a}{2w_a} + 6\left[\frac{e}{w_{eo}}\right]^3 K \end{array}\right\}$$

and

$$C_\ell = \frac{1}{7.5\times10^6}[1.024 + 0.96 + 1.438 + 0.862 + 7.549] \tag{8.53}$$

$$C_\ell = 1.5777 \times 10^{-6}\ \text{ft/lb}_f\ , \tag{8.54}$$

or

$$C_\ell = 1.0811 \times 10^{-7}\ \text{m N.} \tag{8.55}$$

G. OEP FORMULATION IN CONTROL COMPATIBLE FORM

Given the arm mass center and inertia representations presented in Section B, representation of OEP 1 through 12 in control compatible form is complete. The compliances derived for arm axial and lateral loading are interpreted as arm principal axis compliances.

For the odd arm,

$$\psi_{xx} = C_a \tag{8.56}$$

$$\psi_{yy} = \frac{1}{Et}\left(\frac{1}{m_1+m_3}\right)\left(\frac{m_1 d_1^2 + m_3 d_3^2}{2^4 a + \frac{c}{2}]^2}\ \frac{b+\ell}{w_\ell} + (m_1+m_3)\ \mathbb{K}_o\right) \tag{8.57}$$

where

$$\mathbb{K}_o \triangleq 2\left(\frac{b_o}{w_{bo}}\right)^3 + \frac{b_o E_o}{G_o w_{bo}} + \frac{a_o}{2w_{ao}} + 6\left[\frac{e_o}{w_{eo}}\right]^3 K_o \tag{8.58}$$

with K defined by (8.44). ψ_{zz} is defined equal to 1.71 ψ_{xx} based on Ref. AM-1. A precise analytical model for ψ_{zz} is not needed since ψ_{zz} is not a principal contributor to the sensor output torque error.

For the even arm,

$$\psi_{xx} = \frac{1}{Et}\left(\frac{1}{m_2+m_4}\right)\left(\frac{m_2 d_2^2 + m_4 d_4^2}{2[a + \frac{c}{2}]^2}\left[\frac{b+\ell}{w_\ell}\right] + (m_2+m_4)\ \mathbb{K}_e\right) \tag{8.59}$$

where

$$\mathbb{K}_e \triangleq \left(2\ \frac{b_e}{w_{be}}\right)^3 + \frac{b_e E_e}{G_e w_{be}} + \frac{a_e}{2w_{ae}} + 6\left[\frac{e_e}{w_{eo}}\right]^3 K_e\ . \tag{8.60}$$

$$\psi_{yy} = C_a \tag{8.61}$$

$$\psi_{zz} \triangleq 1.71\ \psi_{yy}\ . \tag{8.62}$$

These definitions complete the expression of the OEP vector in control compatible form.

H. COARSE CONTROL OF ARM COMPLIANCES

The error tolerances associated with arm elasticity are minute. Prior to RGG assembly, each instrument arm will be tested in the laboratory to assure both arm-to-arm and axis-to-axis compliance symmetry. Examination of compliance equations (8.29) and (8.29), and Fig. VIII-2 indicate that coarse, preassembly compliance matching can be achieved by mass removal. The dimensions w_a and w_b are the most likely candidates for change by mass removal. Except for mass center distance, d, it will be relatively difficult to modify any of the face dimensions (a, b, c, e, ℓ) once the arm has been machined. The widths, w_a and w_b, however, could be modified by further machining or laser techniques. From (8.29) and (8.49)

$$\frac{\partial C_a}{\partial w_a} = -\frac{ba^3}{Et} w_a^{-4} \tag{8.63}$$

$$\frac{\partial C_a}{\partial w_b} = -\frac{b}{2Et} w_b^{-1} \tag{8.64}$$

$$\frac{\partial C_\ell}{\partial w_a} = -\frac{a}{2Et} w_a^{-1} \tag{8.65}$$

$$\frac{\partial C_\ell}{\partial w_b} = -\frac{6b^3}{Et} w_b^{-4} - \frac{1}{Et}\left(\frac{bE}{2G} + \frac{d^2(b+\ell)}{2\left(a+\frac{c}{2}\right)^2}\right) w_b^{-2}. \tag{8.66}$$

Using the data of Fig. VIII-2, numerical values for these partial derivatives are listed in Table VIII-2.

Table VIII-2

PARTIAL DERIVATIVES OF ARM COMPLIANCE WITH RESPECT TO MEMBER WIDTHS w_a AND w_b

Component	Value $\frac{m/N}{m}$
$\partial C_a/\partial w_a$	-4.577×10^{-4}
$\partial C_\ell/\partial w_a$	-3.101×10^{-7}
$\partial C_a/\partial w_b$	-1.439×10^{-7}
$\partial C_\ell/\partial w_b$	-2.007×10^{-4}

Arm compliances can be changed according to (8.67).

$$\begin{bmatrix} \Delta C_a \\ \Delta C_\ell \end{bmatrix} = \begin{bmatrix} \partial C_a/\partial w_a & \partial C_a/\partial w_b \\ \partial C_\ell/\partial w_a & \partial C_\ell/\partial w_b \end{bmatrix} \begin{bmatrix} \Delta w_a \\ \Delta w_b \end{bmatrix} . \tag{8.67}$$

Since the determinant of the partial derivative is nonzero, the inverse exists, and

$$\begin{bmatrix} \Delta w_a \\ \Delta w_b \end{bmatrix} = \begin{bmatrix} 2261 & -1.566 \\ -3.376 & 4983 \end{bmatrix} \begin{bmatrix} \Delta C_a \\ \Delta C_\ell \end{bmatrix} . \tag{8.68}$$

To first order Δw_a can be used to provide coarse control of C_a while Δw_b can be used to provide coarse control of C_ℓ.

It is also possible to balance compliances by changing the face dimension d, since

$$\frac{\partial C_a}{\partial d} = 0 \tag{8.69}$$

while

$$\frac{\partial C_{\ell}}{\partial d} = \frac{d(b + \ell)}{Etw_b(a + \frac{c}{2})} \quad . \tag{8.70}$$

This control can be used instead of Δw_b, or as a third coarse correction mechanism.

Chapter IX

OUTPUT EFFECTIVE PARAMETER CONTROL USING UNDER-DETERMINED LEAST SQUARES

A. INTRODUCTION

In Ch. VIII the models for a mass motion approach to control by underdetermined least squares were developed. In this chapter the basic control system is configured and simulated.

B. CONTROL CONFIGURATION

The two dominant considerations relative to control system configuration were parameter controllability and arm symmetry. Figure IX-1 displays the nominal positions selected for sensor odd arm control mass placement. The motion of each control mass is independent of the motion of the other controls. The direction of motion for each mass is

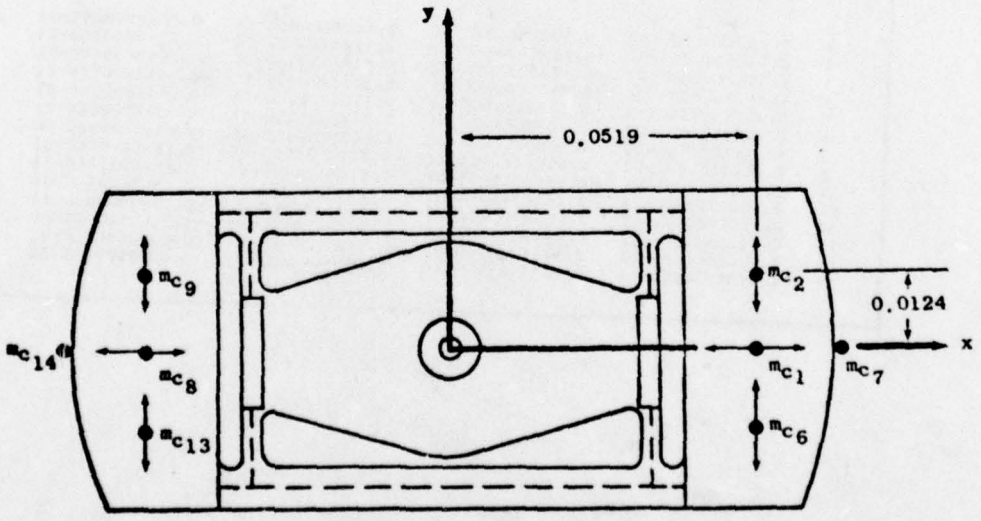


FIG. IX-1 CONTROL MASS PLACEMENT--ODD ARM

PRECEDING PAGE BLANK-NOT FILMED

indicated by the arrows of the figure. Masses 7 and 14 are capable of motion in a direction parallel to the sensor z_s axis (spin axis). Table IX-1 lists nominal mass values and positions relative to sensor axes for each control mass. The control system configurations for both arms are given in Figs. IX-2 and IX-3.

Table IX-1

CONTROL MASS VALUES (grams) AND POSITIONS (meters)

CONTROL MASS DATA -- OCD ARM (SENSOR AXES)

	MASS	X	Y	Z
1	C.2CCCCCCCCD-C2	C.518922CCCD-01	0.CCCCCCCCCD CC	0.254CCCCCCD-01
2	0.1CCCCCCCCD-02	C.518922CCCD-01	0.123E25CCCD-C1	0.254CCCCCCD-01
3	C.1CCCCCCCCD-02	C.518922CCCD-01	0.123825CCCD-01	-0.254CCCCCCD-01
4	C.2CCCCCCCCC-02	C.518922CCCD-01	0.CCCCCCCCCD CC	-0.254CCCCCCD-01
5	C.1CCCCCCCCD-02	C.518922CCCD-01	-0.123825CCCD-01	-C.254CCCCCCD-01
6	C.1CCCCCCCCD-02	C.518922CCCD-01	-0.123825CCCD-01	C.254CCCCCCD-01
7	C.1CCCCCCCCD-02	0.6035040000D-01	0.CCCCCCCCCD CC	0.CCCCCCCCCD CC
8	C.2CCCCCCCC -02	-0.518922CCCD-01	-0.CCCCCCCCCD CC	0.254CCCCCCD-01
9	0.1CCCCCCCC -02	-0.518922CCCD-01	0.123825CCCD-01	0.254CCCCCCD-01
10	C.1CCCCCCCC -02	-0.518922CCCD-01	0.123825CCCD-01	-0.254CCCCCCD-01
11	0.2CCCCCCCCD-C2	-0.518922CCCD-01	-0.CCCCCCCCCD CC	-0.254CCCCCCD-01
12	C.1CCCCCCCCD-02	-0.518922CCCD-01	-0.123825CCCD-01	-0.254CCCCCCD-01
13	0.1CCCCCCCCD-02	-0.518922CCCD-01	-0.123825CCCD-01	0.254CCCCCCD-01
14	0.1CCCCCCCCD-02	-0.6035040000D-01	-0.CCCCCCCCCD CC	-0.CCCCCCCCCD CC

CONTROL MASS DATA -- EVEN ARM (SENSOR AXES)

	MASS	X	Y	Z
1	C.2CCCCCCCCD-02	0.CCCCCCCCCD CC	C.518522CCCD-C1	0.254CCCCCCD-01
2	C.1CCCCCCCCD-02	-0.123825CCCD-01	0.518522CCCD-01	0.254CCCCCCD-01
3	C.1CCCCCCCCD-02	-0.123825CCCD-01	0.518522CCCD-C1	-C.254CCCCCCD-01
4	C.2CCCCCCCCD-02	0.CCCCCCCCCD CC	0.518522CCCD-C1	-C.254CCCCCCD-C1
5	C.1CCCCCCCCD-02	C.123825CCCD-01	0.518522CCCD-01	-0.254CCCCCCD-01
6	C.1CCCCCCCCD-02	0.123825CCCD-01	0.518522CCCD-01	0.254CCCCCCD-01
7	C.1CCCCCCCCD-02	C.CCCCCCCCCD CC	0.6035040000D-01	0.CCCCCCCCCC CC
8	C.2CCCCCCCCD-02	0.CCCCCCCCCD CC	-C.518522CCCD-01	0.254CCCCCCD-01
9	C.1CCCCCCCCD-02	-0.123825CCCD-01	-0.518522CCCD-01	0.254CCCCCCD-01
10	0.1CCCCCCCCD-02	-0.123825CCCD-01	-0.518522CCCD-C1	-C.254CCCCCCD-01
11	0.2CCCCCCCCD-02	0.CCCCCCCCCC CC	-0.518522CCCD-01	-0.254CCCCCCD-01
12	C.1CCCCCCCCD-C2	0.123825CCCD-01	-0.518522CCCD-C1	-0.254CCCCCCC-01
13	0.1CCCCCCCCD-02	0.123825CCCD-01	-0.518922CCCD-01	0.254CCCCCCD-C1
14	0.1CCCCCCCCD-C2	C.CCCCCCCCCD CC	-0.6035040000D-01	-0.CCCCCCCCCC CC

9/2

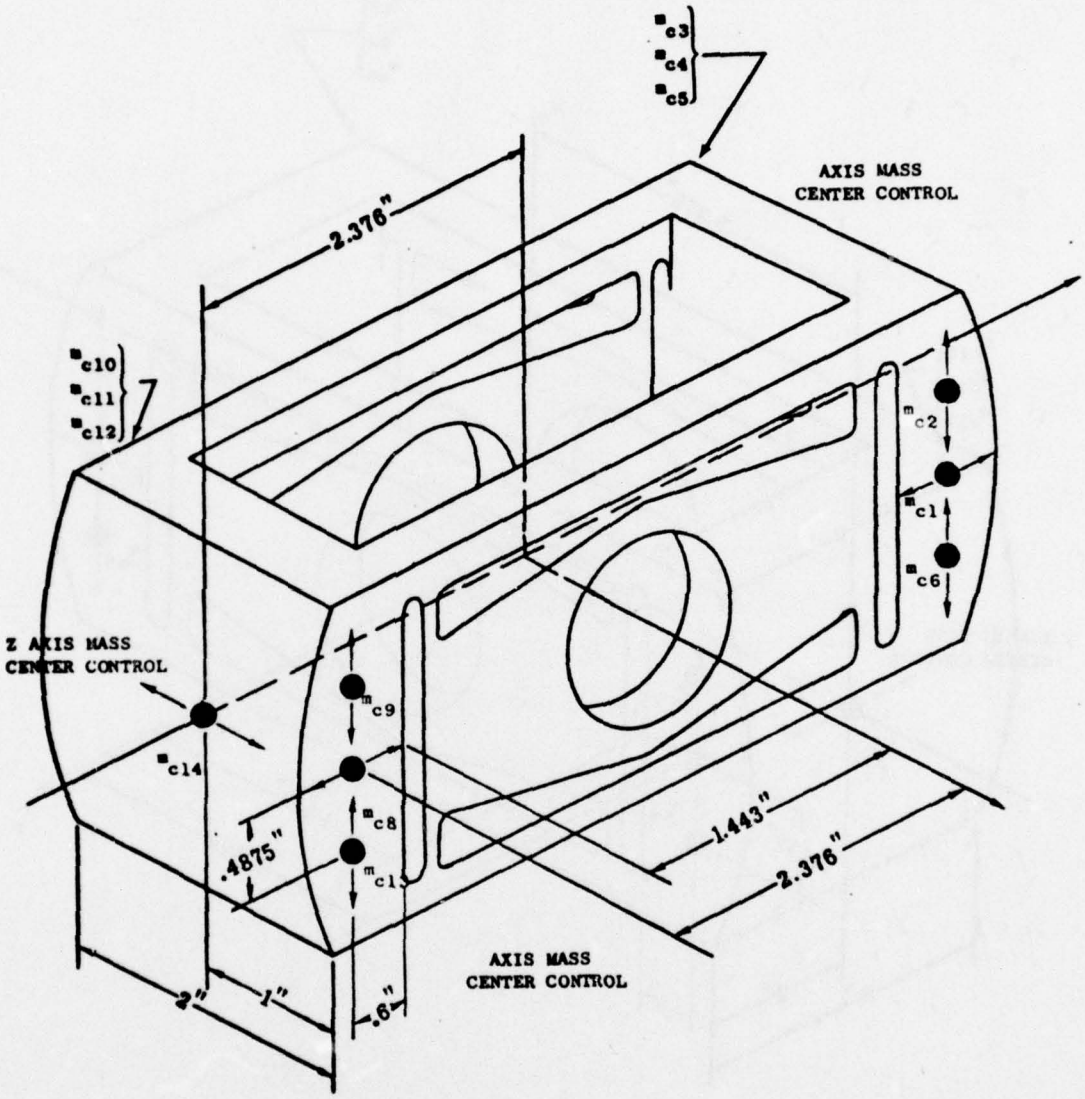


FIG. IX-2 ODD ARM CONTROL SYSTEM NOMINAL CONFIGURATION

9/3

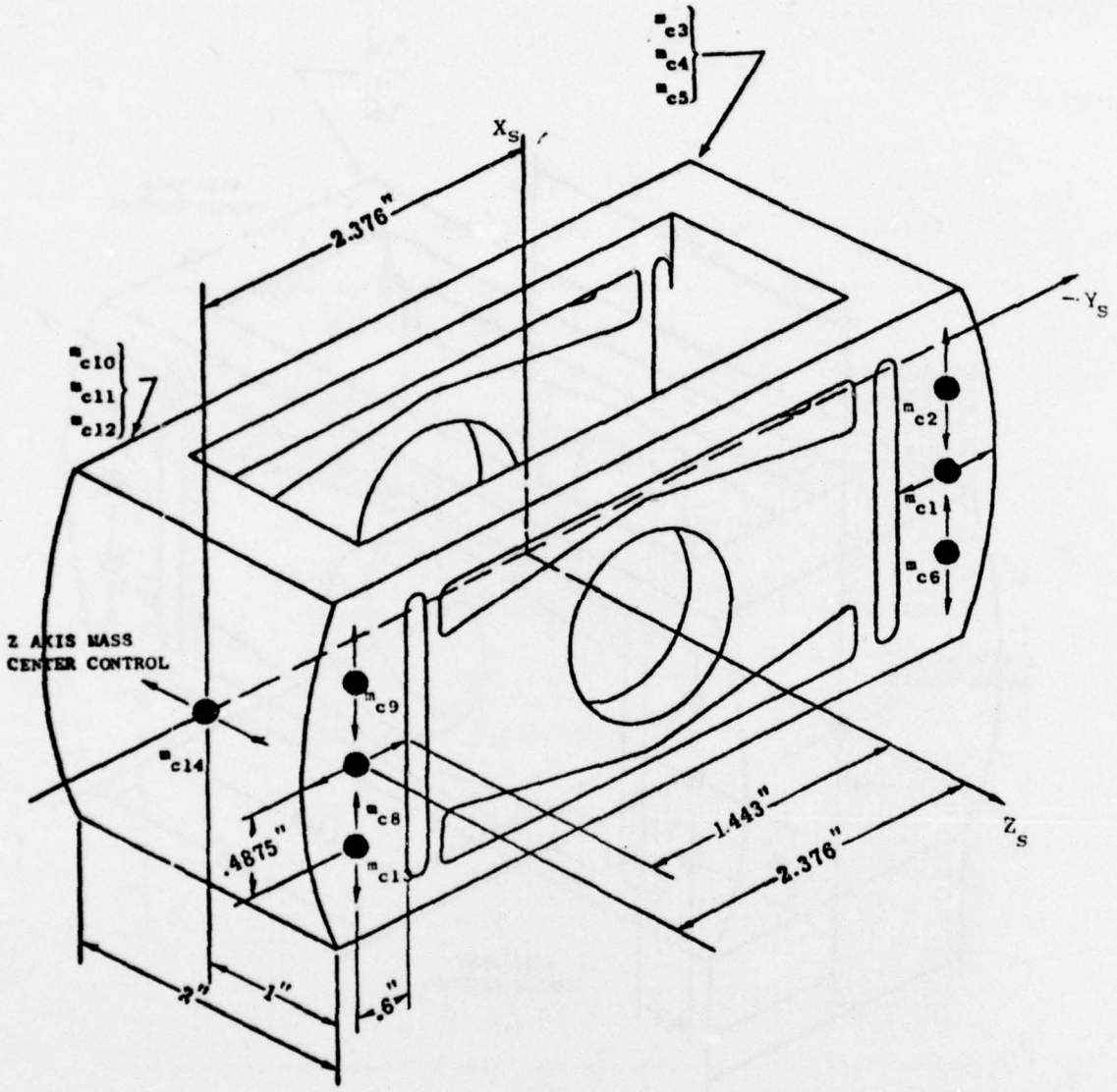


FIG. IX-3 EVEN ARM CONTROL SYSTEM NOMINAL CONFIGURATION

The control vector $\overline{\Delta x}$ is specified in Table IX-2.

Table IX-2

CONTROL VECTOR SPECIFICATION

Vector Position	Description	Dir. of Motion (sensor frame)
1	m_{co1}	x
2	m_{co2}	y
3	m_{co3}	y
4	m_{co4}	x
5	m_{co5}	y
6	m_{co6}	y
7	m_{co7}	z
8	m_{co8}	x
9	m_{co9}	y
10	m_{co10}	y
11	m_{co11}	x
12	m_{co12}	y
13	m_{co13}	y
14	m_{co14}	z
15	m_{ce1}	y
16	m_{ce2}	x
17	m_{ce3}	x
18	m_{ce4}	y
19	m_{ce5}	x
20	m_{ce6}	x
21	m_{ce7}	z
22	m_{ce8}	y
23	m_{ce9}	x
24	m_{ce10}	x
25	m_{ce11}	y
26	m_{ce12}	x
27	m_{ce13}	x
28	m_{ce14}	z

5

1. Arm Physical Characteristics

The inclusion of control masses alters arm physical properties slightly from those listed in Ch. VIII. Arm mass center and inertia tensor components relative to the sensor reference system are given in (9.1) to (9.9) for the sensor odd arm. Comparison with the similar expressions of Ch. VIII indicates the effect of the control masses on the parameters and hence, also reachability.

$$\rho_{xo} = \frac{\Sigma m_{1i} x_{1i} + \Sigma m_{3i} x_{3i} + 3 m_{ci} x_{ci}}{\Sigma m_{1i} + \Sigma m_{3i} + \Sigma m_{ci}} \tag{9.1}$$

$$\rho_{yo} = \frac{\Sigma m_{1i} y_{1i} + \Sigma m_{3i} y_{3i} + \Sigma m_{ci} y_{ci}}{\Sigma m_{1i} + \Sigma m_{3i} + \Sigma m_{ci}} \tag{9.2}$$

$$\rho_{zo} = \frac{\Sigma m_{1i} z_{1i} + \Sigma m_{3i} z_{3i} + \Sigma m_{ci} z_{ci}}{\Sigma m_{1i} + \Sigma m_{3i} + \Sigma m_{ci}} \tag{9.3}$$

$$I_{xxo} = \sum_{i=1}^{4} m_{1i}\left[(y_{1i}-\rho_{yo})^2 + (z_{1i}-\rho_{zo})^2\right] + \sum_{i=1}^{4} m_{3i}\left[(y_{3i}-\rho_{yo})^2 + (z_{3i}-\rho_{zo})^2\right] + \sum_{i=1}^{14} m_{ci}\left[(y_{ci}-\rho_{yo})^2 + (z_{ci}-\rho_{zo})^2\right]; \tag{9.4}$$

$$I_{yyo} = \sum_{i=1}^{4}\left[(x_{ji}-\rho_{xo})^2 + (z_{ji}-\rho_{zo})^2\right] + \sum_{i=1}^{14} m_{ci}\left[(x_{ci}-\rho_{xo})^2 + (z_{ci}-\rho_{zo})^2\right], \qquad j = 1, 3; \tag{9.5}$$

$$I_{zzo} = \sum_{i=1}^{4}\left[(x_{ji}-\rho_{xo})^2 + (y_{ji}-\rho_{yo})^2\right] + \sum_{i=1}^{14} m_{ci}\left[(x_{ci}-\rho_{xo})^2 + (z_{ci}-\rho_{zo})^2\right], \qquad j = 1,3; \tag{9.6}$$

$$I_{xyo} = -\sum_{i=1}^{4} m_{ji}(x_{ji}-\rho_{xo})(y_{ji}-\rho_{yo}) - \sum_{i=1}^{14} m_{ci}\left[(x_{ci}-\rho_{xo})(y_{ci}-\rho_{yo})\right], \quad (9.7)$$

$$j = 1, 3$$

$$I_{xzo} = -\sum_{i=1}^{4} m_{ji}(x_{ji}-\rho_{xo})(z_{ji}-\rho_{z}) - \sum_{i=1}^{14} m_{ci}(x_{ci}-\rho_{xo})(z_{ci}-\rho_{zo}) , \quad (9.8)$$

$$j = 1, 3$$

$$I_{yzo} = -\sum_{i=1}^{4} m_{ji}(y_{ji}-\rho_{yo})(z_{ji}-\rho_{zo}) - \sum_{i=1}^{14} m_{ci}(y_{ci}-\rho_{yo})(z_{ci}-\rho_{zo}), \quad (9.9)$$

$$j = 1, 3 .$$

Equations analogous to (9.1) to (9.9) were developed for the even arm but have not been included. Equations (9.1) to (9.9) indicate the reachability of OEPs 1 through 7, and 11 and 12, since each of these parameters now contains terms which are the products of control mass and control mass position.

2. Elastic Parameter Reachability

Consider the moment producing system depicted in Fig. IX-4 which is composed of two point masses, M and m_c, and the appropriate lever arm having mass m_L. Assume that the original mass center of this system

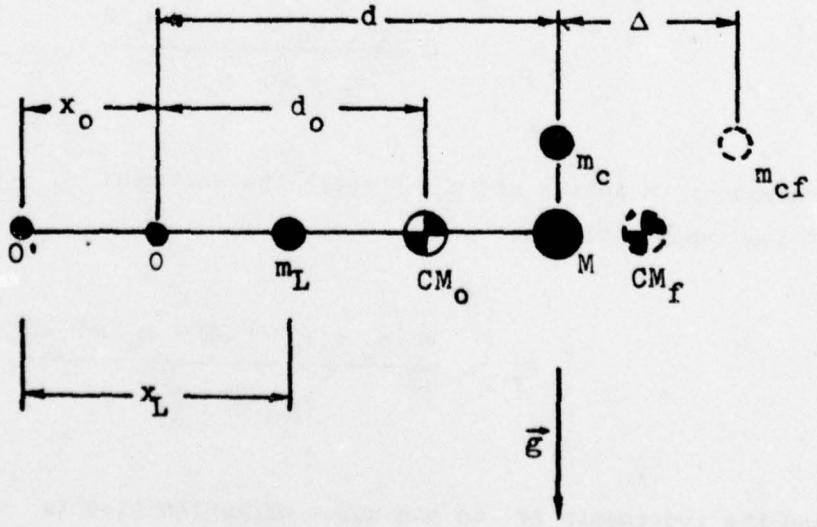


FIG. IX-4 POINT OF APPLICATION INCREMENT EXAMPLE

exists at CM_o and that m_c is perturbed in position from d to $(d + \Delta)$. Under these conditions,

$$CM_o = \frac{m_L x_L + (M + m_c)(x_o + d)}{m_L + M + m_c} \tag{9.10}$$

$$CM_f = \frac{m_L x_L + M(x_o+d) + m_c(x_o+d+\Delta)}{m_L + M + m_c} \tag{9.11}$$

and the change in CM position, $\delta(CM)$ is

$$\delta(CM) = \frac{m_c \Delta}{m_L + M + m_c} . \tag{9.12}$$

In a similar manner, the change in effective point of load application can be calculated relative to point zero of Fig. IX-4. For the unperturbed configuration, the effective point of load application for moment about zero is

$$P_o = \frac{m_L(x_L - x_o) + (M + m_c)d}{m_L + M + m_c} \tag{9.13}$$

Subsequent to motion of m_c through the distance Δ, the effective point of load application is

$$P_f = \frac{m_L(x_L - x_o) + Md + m_c(d + \Delta)}{m_L + M + m_c} \tag{9.14}$$

and the increment δP to the point of application is

$$\delta P = \frac{m_c \Delta}{m_L + M + m_c} \tag{9.15}$$

Hence, comparison of (9.12) and (9.15) yields

$$\delta P = \delta(CM) . \tag{9.16}$$

The significance of this result in light of compliance equations (8.56) and (8.58) is clear--the motion of a control mass along the longitudinal axis of a gradiometer arm affects the lateral compliance of that arm by perturbing the effective point of load application through a distance equal to the change in mass center position of that arm. Therefore, defining

$$\eta_j \triangleq d_j + \Delta\mu_j \tag{9.17}$$

where $\Delta\mu_j \triangleq$ increment to the mass center position of the j^{th} arm relative to sensor axes, the odd arm lateral compliance accounting for control mass relocation along the longitudinal (x) axis is

$$\psi_{yy} = \frac{1}{Et}\left\{\frac{1}{m_1+m_3}\right\}\left\{\frac{m_1\eta_1+m_3\eta_3}{2\left[a+\frac{c}{2}\right]^2}\left[\frac{b+\ell}{w_\ell}\right] + (m_1+m_3)\,\mathbb{K}_o\right\}. \tag{9.18}$$

Similarly, for the even arm,

$$\psi_{xx} = \frac{1}{Et}\left\{\frac{1}{m_2+m_4}\right\}\left\{\frac{m_2\eta_2^2+m_4\eta_4^2}{2\left[a+\frac{c}{2}\right]^2}\left[\frac{b+\ell}{w_\ell}\right] + (m_2+m_4)\,K_e\right\}. \tag{9.19}$$

It is also noted that the lateral compliance of either the odd or even arm may be changed without perturbing the mass center of that arm.

C. THE PARAMETER CONTROL PROBLEM

Having established the reachability of all independent OEPs by the mass repositioning control system, the parameter control problem can be stated as follows:

- given the vector of estimates $\hat{P}$ of the 12 independent OEPs, and
- given the vector P_o of the same 12 independent OEPs for an ideally constructed and operating instrument,
- find the vector of control increments, Δx, which satisfied the under-determined least squares control law developed in Ch. VII-C.

For the Hughes RGG, the parameter vector ΔP is defined by (9.20).

$$\Delta P = \left\{\Delta P_1, \Delta P_2, \Delta P_3, \Delta P_4, \Delta P_5, \Delta P_{11}, \Delta P_{12}, \Delta P_{13}, \Delta P_{14}, \Delta P_{15}, \Delta P_{16}, \Delta P_{17}\right\}^T \tag{9.20}$$

The control vector Δx is defined by Table IX-2, and the matrix F of partial derivatives is

$$F_{12\times 28} = \left\{\frac{\partial \Delta P_i}{\partial \Delta x_j}\right\}_{\substack{j=1,2,\ldots,28 \\ i=1,2,\ldots,12}} . \tag{9.21}$$

The resultant control increment vector, Δx, is specified by (7.10).

D. PARAMETER CONTROLLABILITY

Parameter reachability, which has been demonstrated for all the OEPs is a necessary but not a sufficient condition for parameter controllability. In general, the parameter vector ΔP is controllable if, using unconstrained values for the control Δx, ΔP can be driven to any arbitrary value in a finite number of control iterations. In terms more directly applicable to

OEP control, the vector ΔP is controllable if an only if matrix F has rank 12. If matrix F has rank 12, then $(FF^T)^{-1}$ exists and ΔP can be driven to zero. Note that an additional practical constraint upon ΔP controllability is that the control increments, Δx, required must be physically available to the system. Hence, even though the matrix $(FF^T)^{-1}$ exists, if the value of Δx_1 which results is 10 meters, the system is theoretically controllable but uncontrollable in practice.

Output effective parameter controllability is demonstrated in this chapter using general test case results as validation. The sensitivity or partial derivative matrix F was developed both analytically and numerically. The numerical development used successive perturbations of the individual controls which caused increments to the various OEPs. Controller performance using the numerically determined sensitivity matrix was much superior to that which used analytical partials. The reasons for this improved performance are the systems' nonlinear nature of the system and the fact that the numerical partials include axial misalignment effects. It was also noted that the quality of control system performance was a function of the controller perturbations used to develop the sensitivity matrix F. For best performance, the control perturbations used to develop the matrix of partial derivatives should not differ from the largest actual control increments applied by more than an order of magnitude.

Given the number and locations selected for the control masses, as specified by Table IX-1, qualitative arguments which indicate system controllability can be made. In order to assure parameter controllability from a physical point of view, it is necessary that no control or combination of controls always affect any two parameters in exactly the same way. In this sense the highly nonlinear nature of the system is an aid to controllability. The OEP vector was found to be controllable with 28 control masses available.

E. DIGITAL SIMULATION

A logic flow diagram representing the digital representation of the underdetermined least squares control system is presented in Fig. IX-5. The digital program is "static" in the sense that it does not account for

11

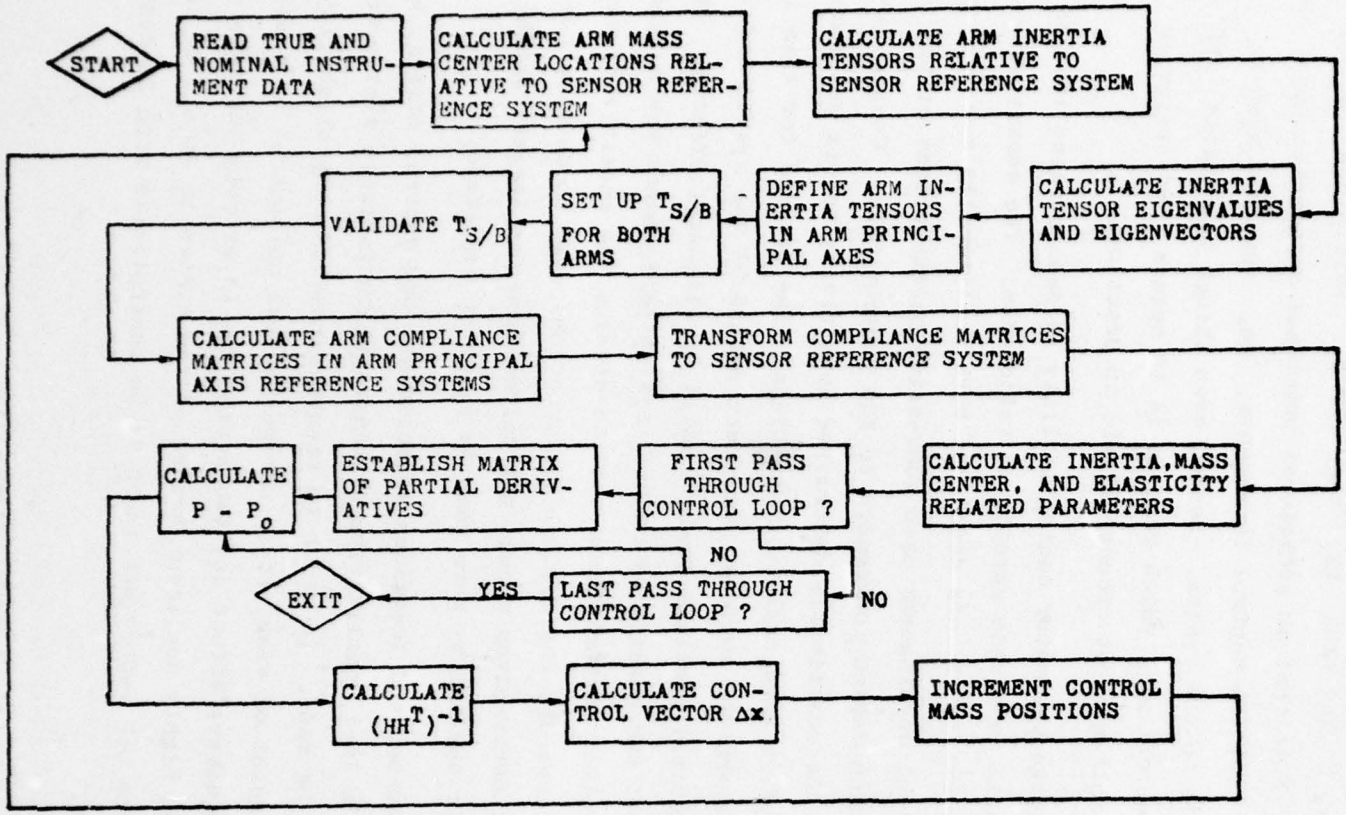


FIG. IX-5 SIMULATION SUMMARY CHART

instrument transient output during control application. This is a negligible effect since both the estimation and control systems are based upon constant parameter values, and quasi-steady state operation. The simulation test program designed to validate the control concept is outlined in the simulation summary chart.

1. Program Checkout

Three test cases were designed and executed to validate the program. For the first of these cases, all control mass values were set to zero and all instrument physical values were nominal. Under these conditions, the resulting instrument physical parameters were expected to match those listed in Table III-1. Simulation output for this test case is listed in Table IX-3. System physical parameters will be given for the remainder of this chapter in the form of Table IX-3. The inertia tensors are printed by row and column as they exist in the program. Hence, the I_{11} term is I_{xx}, I_{12} is I_{xy}, etc. The symbol SA of the computer output refers to the sensor axis system. The symbol BA refers to the principal axis system of the arm specified. TSB is the transformation to the sensor reference system from the arm principal axis reference system. The difference matrices are odd arm minus even arm differences.

Comparison of the simulation printout of Table IX-3 with the ideal system specifications of Table III-1 indicates proper computer modeling of the ideal system. The inertia tensor data are correct to 1 part in 10^8, the accuracy of the input data. Mass center calculations are exact.

The output effective parameter vector calculated for this case is listed in Table IX-4. Note that ideally all 14 OEPs are zero, except for P_5 which is the RGG gradient signal coefficient. The ideal case value for that parameter is 6.122×10^{-3} kg m^2. The P_{14} calculation is in error less than 10^{-16} kg sec^2, and acceptable value based upon the dynamic range involved within the computation of that parameter. The transformations to body from sensor axes remained identity matrices as expected. This test case verified formation of both instrument physical and OEPs.

Table IX-3

IDEAL INSTRUMENT CONFIGURATION

FOUR ARM CONFIGURATION MASSES (KG) AND MASS CENTER (M) SENSOR AXES

ARM	MASS	RHO(X)	RHO(Y)	RHO(Z) SENSOR AXES
1	0.781500000D 00	0.4602567000-01	0.0000000000 00	0.000000000D 00
2	0.781500000D 00	0.000000000D 00	0.4602567000-01	0.000000000D 00
3	0.781500000D 00	-0.4602567000-01	-0.0000000000 00	-0.000000000D 00
4	0.781500000D 00	0.000000000D 00	-0.4602567000-01	-0.000000000D 00

ODD ARM INERTIA TENSOR SA

0.4990017760-03	0.0000000000 00	0.000000000D 00
0.000000000D 00	0.3560001550-02	0.0000000000 00
0.000000000D 00	0.0000000000 00	0.3561000780-02

EVEN ARM INERTIA TENSOR SA

0.3560001550-02	0.0000000000 00	0.0000000000 00
0.0000000000 00	0.4990017760-03	0.0000000000 00
0.0000000000 00	0.0000000000 00	0.3561000780-02

ODD ARM INERTIA TENSOR BA

0.4990017760-03	0.0000000000 00	0.000000000D 00
0.000000000D 00	0.3560001550-02	0.0000000000 00
0.0000000000 00	0.0000000000 00	0.3561000780-02

EVEN ARM INERTIA TENSOR BA

0.3560001550-02	0.0000000000 00	0.0000000000 00
0.0000000000 00	0.4990017760-03	0.0000000000 00
0.0000000000 00	0.0000000000 00	0.3561000780-02

INERTIA TENSOR DIFFERENCE MATRIX SA

-0.3060599770-02	-0.0000000000 00	-0.000000000D 00
-0.0000000000 00	0.3060599770-02	0.0000000000 00
0.0000000000 00	0.0000000000 00	0.000000000D 00

Cont ....

Table IX-3 (Cont)

TSB ODD ARM

0.1000000000D 01 0.0000000000D 00 0.0000000000D 00
0.0000000000D 00 0.1000000000D 01 0.0000000000D 00
0.0000000000D 00 0.0000000000D 00 0.1000000000D 01

TSB EVEN ARM

0.1000000000D 01 0.0000000000D 00 0.0000000000D 00
0.0000000000D 00 0.1000000000D 01 0.0000000000D 00
0.0000000000D 00 0.0000000000D 00 0.1000000000D 01

ODD ARM COMPLIANCE BA

0.3524783460-07 0.0000000000D 00 0.0000000000D 00
0.0000000000D 00 0.3524783460-07 0.0000000000D 00
0.0000000000D 00 0.0000000000D 00 0.6027379720-07

EVEN ARM COMPLIANCE BA

0.3524783460-07 0.0000000000D 00 0.0000000000D 00
0.0000000000D 00 0.3524783460-07 0.0000000000D 00
0.0000000000D 00 0.0000000000D 00 0.6027379720-07

ODD ARM COMPLIANCE SA

0.3524783460-07 0.0000000000D 00 0.0000000000D 00
0.0000000000D 00 0.3524783460-07 0.0000000000D 00
0.0000000000D 00 0.0000000000D 00 0.6027379720-07

EVEN ARM COMPLIANCE SA

0.3524783460-07 0.0000000000D 00 0.0000000000D 00
0.0000000000D 00 0.3524783460-07 0.0000000000D 00
0.0000000000D 00 0.0000000000D 00 0.6027379720-07

COMPLIANCE DIFFERENCE MATRIX SA

-0.1312554230-16 -0.0000000000D 00 -0.0000000000D 00
-0.0000000000D 00 0.1312554230-16 0.0000000000D 00
0.0000000000D 00 0.0000000000D 00 0.0000000000D 00

TWO ARM INSTRUMENT DATA

	ODD ARM	EVEN ARM
MASS	0.1563000000 01	0.1563000000 01
CM(1)	0.0000000000 00	0.0000000000 00
CM(2)	0.0000000000 00	0.0000000000 00
CM(3)	0.0000000000 00	0.0000000000 00

Table IX-4

IDEAL INSTRUMENT OEP CALCULATION FROM DIGITAL SIMULATION

P(1)	0.000000000 00
P(2)	0.000000000 00
P(3)	0.000000000 00
P(4)	0.000000000 00
P(5)	0.512198650-02
P(6)	0.000000000 00
P(7)	0.000000000 00
P(11)	0.000000000 00
P(12)	0.000000000 00
P(13)	0.000000000 00
P(14)	-0.641325860-16
P(15)	-0.000000000 00
P(16)	-0.000000000 00
P(17)	-0.000000000 00

Two additional test cases were devised as a check on control law performance. For the first of these cases, the instrument even arm mass center was offset from the origin of the sensor axis system by 0.989×10^{-5} m. This offset was accomplished by biasing the $\hat{x}_s$ location of each even arm model mass by 1×10^{-5} m as shown in the test input data of Table IX-5. Note that although the position of each even arm model-mass has been perturbed by 1×10^{-5} m, the arm mass center bias is slightly less than that value due to the fact that the positions prescribed for the even arm control masses remained at their nominal values. By seven orders of magnitude the most significantly effected OEP due to this CM shift is P_{11} which is a linear function of ρ_x. The purpose of the test was to check the control as applied by the least square error control law vs the intuitive solution to the problem. A simplified representation of the test case is given in Fig. IX-6.

Based upon the x_s direction of the mass center error and the available directions of motion of the various controls as shown in the figure, it was expected that control masses 1, 4, 8, 11, which are situated upon the instrument odd arm and control masses 16, 17, 19, 20, 23, 24, 26, and 27 on the even arm would exhibit significant motion while the remaining

Table IX-5

INPUT DATA FOR EVEN ARM MODEL MASS x_s POSITION BIAS. POSITION IN MATRIX CORRESPONDS TO MODEL MASS SPECIFICATION

INSTRUMENT SUB-MASS MATRIX

C.1953750 00	0.1953750 00	C.1953750 00	C.1953750 00
C.1953750 00	C.1953750 00	C.1953750 00	C.1953750 00
C.1953750 00	C.1953750 00	C.1953750 00	C.1953750 00
C.1953750 00	C.1953750 00	C.1953750 00	C.1953750 00

FOUR ARM CONFIG. SUB-MASS POSITION VECTORS X,Y,Z (M) SENSOR AXES

ARM 1

C.4602567000-01	0.1264710000-01	C.1262180000-01
C.4602567000-01	0.1264710000-01	-C.1262180000-01
C.4602567000-01	-0.1264710000-01	-0.1262180000-01
C.4602567000-01	-0.1264710000-01	C.1262180000-01

ARM 3

-0.4602567000-01	0.1264710000-01	C.1262180000-01
-0.4602567000-01	0.1264710000-01	-0.1262180000-01
-0.4602567000-01	-0.1264710000-01	-0.1262180000-01
-0.4602567000-01	-0.1264710000-01	C.1262180000-01

ARM 2

-0.1263710000-01	0.4602567000-01	0.1262180000-01
0.1263710000-01	0.4602567000-01	0.1262180000-01
C.1263710000-01	0.4602567000-01	-0.1262180000-01
-0.1263710000-01	0.4602567000-01	-0.1262180000-01

ARM 4

-0.1263710000-01	-0.4602567000-01	0.1262180000-01
0.1263710000-01	-0.4602567000-01	0.1262180000-01
0.1263710000-01	-0.4602567000-01	-0.1262180000-01
-0.1263710000-01	-0.4602567000-01	-0.1262180000-01

FOUR ARM CONFIGURATION MASSES (KG) AND MASS CENTER ARM) SENSOR AXES

ARM	MASS	RHO(X)	RHO(Y)	RHO(Z) SENSOR AXES
1	C.7815000000 00	0.4610316140-01	0.0000000000 00	C.0000000000 00
2	C.7815000000 00	C.9886146010-05	0.4610316140-01	C.0000000000 00
3	C.7815000000 00	-0.4610316140-01	-C.0000000000 00	C.0000000000 00
4	C.7815000000 00	C.9886146010-05	-C.4610316140-01	C.0000000000 00

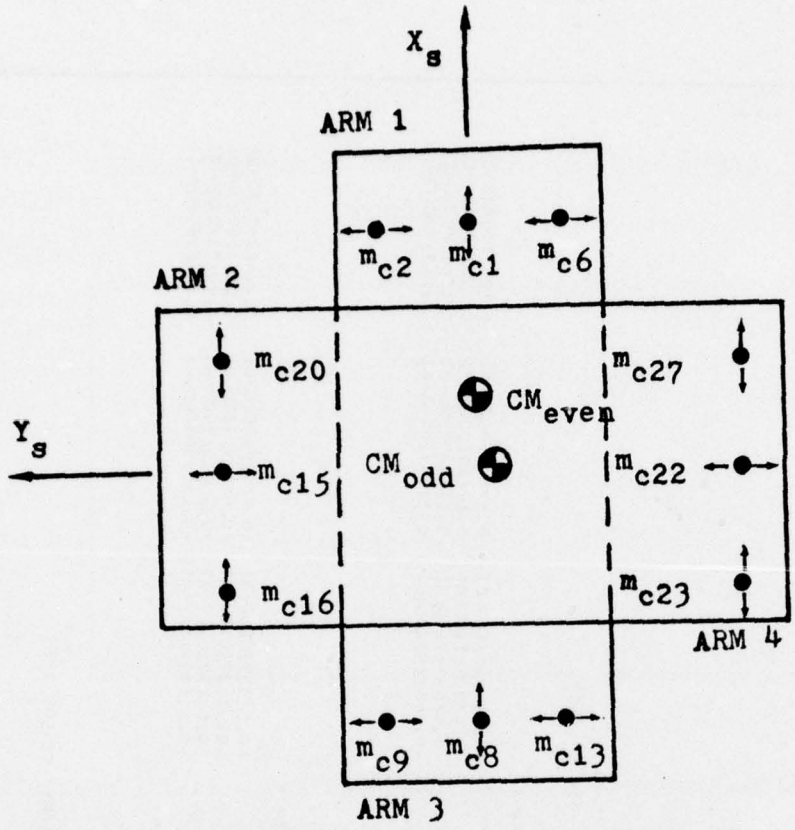


FIG. IX-6 PRECONTROL MASS CENTER AND CONTROL MASS CONFIGURATION FOR P_{11} CONTROL TEST CASE. TEST CASE Oa.

controls would be only slightly effected. This result was verified by the digital simulation. Prescribed control increment magnitudes for this test case are displayed in Fig. IX-7. Results of this test showed even arm mass center not to be driven to zero. This result was also expected. The precontrol and post control instrument physical data are shown in Table IX-6. The precontrol and postcontrol OEP are listed in Table IX-7. Note that P_{11} has been reduced by seven orders of magnitude while all others have assumed nonzero values. Additional control iterations, each following a new parameter estimation exercise, would further reduce the size of the parameter residuals. Since no one control affects only one parameter, mass repositioning for control of P_{11} also changes the values of the other parameters.

/19

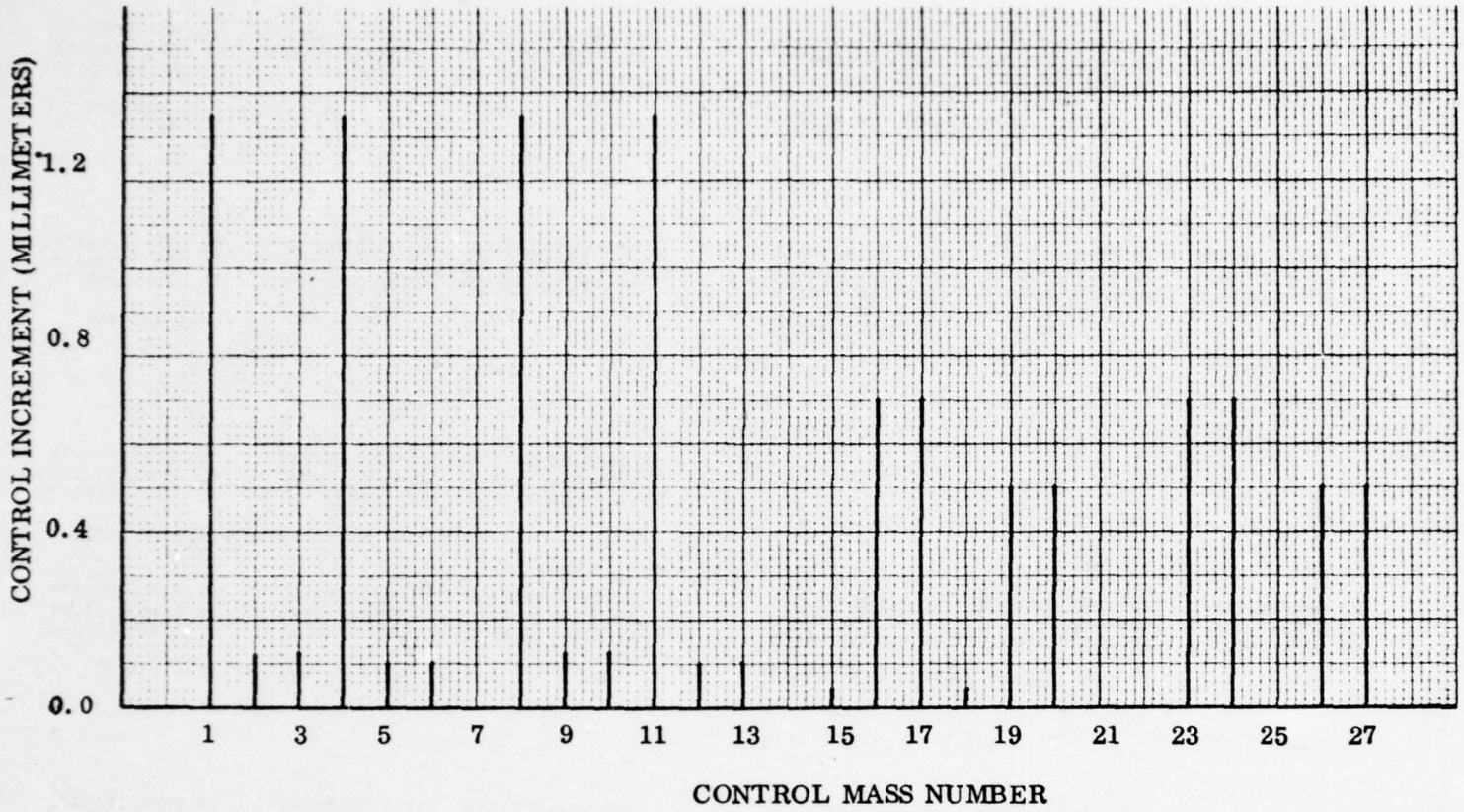


FIG. IX-7 CONTROL SYSTEM RESPONSE TO MASS CENTER OFFSET OF NOMINAL INSTRUMENT IN $\hat{x}_s$ DIRECTION.

Table IX-6

CM OFFSET TEST INSTRUMENT PHYSICAL PROPERTIES. (PRECONTROL)

CCC ARM INERTIA TENSOR SA

0.5105509460-03	0.0000000000 00	0.0000000000 00
0.0000000000 00	0.3620693250-02	0.0000000000 00
0.0000000000 00	0.0000000000 00	0.3612596540-02

EVEN ARM INERTIA TENSOR SA

0.3620693250-02	0.0000000000 00	0.0000000000 00
0.0000000000 00	0.5105509480-03	0.0000000000 00
0.0000000000 00	0.0000000000 00	0.3612596540-02

CCC ARM INERTIA TENSOR BA

0.5105509460-03	0.0000000000 00	0.0000000000 00
0.0000000000 00	0.3620693250-02	0.0000000000 00
0.0000000000 00	0.0000000000 00	0.3612596540-02

EVEN ARM INERTIA TENSOR BA

0.3620693250-02	0.0000000000 00	0.0000000000 00
0.0000000000 00	0.5105509480-03	0.0000000000 00
0.0000000000 00	0.0000000000 00	0.3612596540-02

INERTIA TENSOR DIFFERENCE MATRIX SA

-0.3110142310-02	-0.0000000000 00	-0.0000000000 00
-0.0000000000 00	0.3110142310-02	0.0000000000 00
0.0000000000 00	0.0000000000 00	-0.1779506660-11

TSB CCC ARM

0.1000000000 01	0.0000000000 00	0.0000000000 00
0.0000000000 00	0.1000000000 01	0.0000000000 00
0.0000000000 00	0.0000000000 00	0.1000000000 01

TSB EVEN ARM

0.1000000000 01	0.0000000000 00	0.0000000000 00
0.0000000000 00	0.1000000000 01	0.0000000000 00
0.0000000000 00	0.0000000000 00	0.1000000000 01

CCC ARM COMPLIANCE BA

0.3524783460-07	0.0000000000 00	0.0000000000 00
0.0000000000 00	0.3524783460-07	0.0000000000 00
0.0000000000 00	0.0000000000 00	0.6027379720-07

EVEN ARM COMPLIANCE BA

0.3524783460-07	0.0000000000 00	0.0000000000 00
0.0000000000 00	0.3524783460-07	0.0000000000 00
0.0000000000 00	0.0000000000 00	0.6027379720-07

Cont. ...

Table IX-6 (Cont)

ODD ARM COMPLIANCE SA

0.3524783460-07	0.0000000000 00	0.0000000000 00
0.0000000000 00	0.3524783460-07	0.0000000000 00
0.0000000000 00	0.0000000000 00	0.6027379720-07

EVEN ARM COMPLIANCE SA

0.3524783460-07	0.0000000000 00	0.0000000000 00
0.0000000000 00	0.3524783460-07	0.0000000000 00
0.0000000000 00	0.0000000000 00	0.6027379720-07

THE ARM INSTRUMENT DATA

	ODD ARM	EVEN ARM
MASS	0.1581000000 01	0.1581000000 01
CM(1)	0.0000000000 00	0.9886141000-05
CM(2)	0.0000000000 00	0.0000000000 00
CM(3)	0.0000000000 00	0.0000000000 00

ODD ARM INERTIA TENSOR SA

0.5105653610-03	0.9855769250-12	0.5310342810-13
0.9855769250-12	0.3620724120-02	-0.2639731210-12
0.5310342810-13	-0.2639731210-12	0.3612645820-02

EVEN ARM INERTIA TENSOR SA

0.3620711610-02	0.9855767640-12	-0.1264271310-12
0.9855767640-12	0.5105726880-03	-0.2639826680-12
-0.1264271310-12	-0.2639826680-12	0.3612636630-02

ODD ARM INERTIA TENSOR BA

0.5105653610-03	0.0000000000 00	0.0000000000 00
0.0000000000 00	0.3620724120-02	0.0000000000 00
0.0000000000 00	0.0000000000 00	0.3612645820-02

EVEN ARM INERTIA TENSOR BA

0.3620711610-02	0.0000000000 00	0.0000000000 00
0.0000000000 00	0.5105726880-03	0.0000000000 00
0.0000000000 00	0.0000000000 00	0.3612636630-02

INERTIA TENSOR DIFFERENCE MATRIX SA

-0.3110142250-02	0.1615414750-18	0.1795305590-12
0.1615414790-18	0.3110151430-02	0.9547641880-17
0.1795305590-12	0.9547641880-17	0.9185166500-08

Cont. ...

Table IX-6 (Cont)

TSB ODD ARM

0.1000000000 01	-0.3168901110-09	0.1711888200-10
-0.3168900280-09	-0.1000000000 01	0.3267688120-07
-0.1711888160-10	0.3267688120-07	0.1000000000 01

TSB EVEN ARM

0.1000000000 01	0.3168912770-09	0.1565665450-07
0.3168913460-09	-0.1000000000 01	-0.8509903650-10
-0.1565665450-07	-0.8509904150-10	0.1000000000 01

ODD ARM COMPLIANCE BA

0.3524789460-07	0.0000000000 00	0.0000000000 00
0.0000000000 00	0.3524789360-07	0.0000000000 00
0.0000000000 00	0.0000000000 00	0.6027379720-07

EVEN ARM COMPLIANCE BA

0.3524789750-07	0.0000000000 00	0.0000000000 00
0.0000000000 00	0.3524789460-07	0.0000000000 00
0.0000000000 00	0.0000000000 00	0.6027379720-07

ODD ARM COMPLIANCE SA

0.3524789460-07	0.2164470980-22	0.4284114950-18
0.2164470980-22	0.3524789360-07	0.8177664770-15
0.4284114950-18	0.8177664770-15	0.6027379720-07

EVEN ARM COMPLIANCE SA

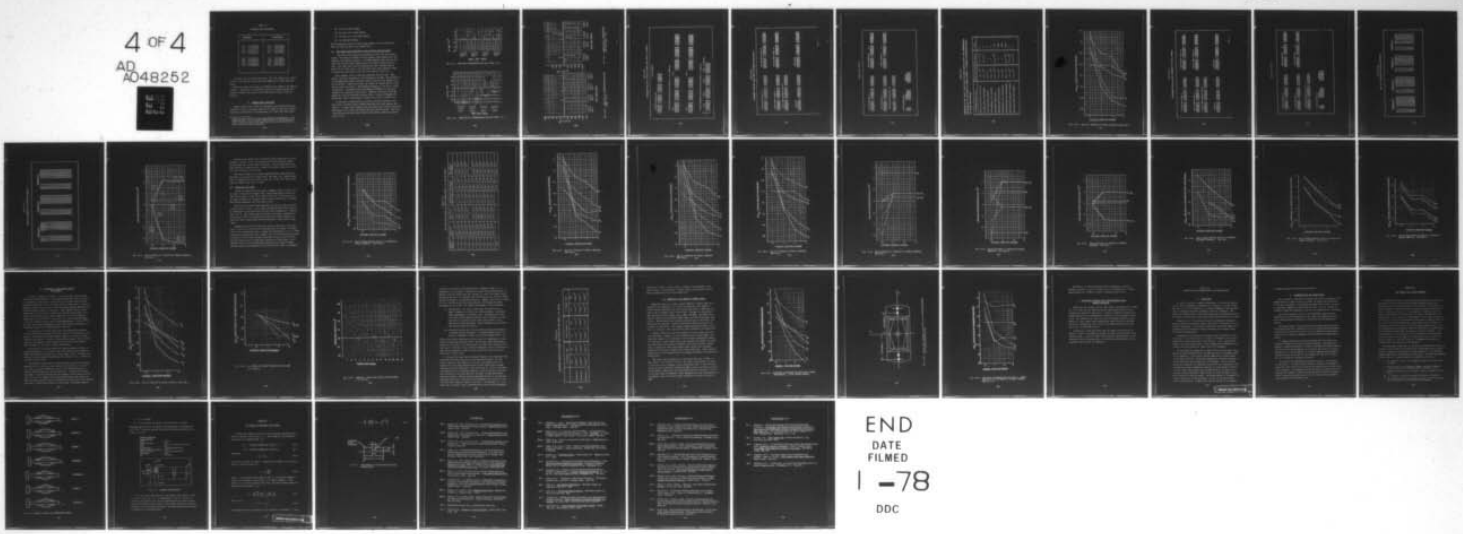
0.3524789750-07	0.2228020710-22	0.3918218650-15
0.2228020710-22	0.3524789460-07	-0.2129685300-17
0.3918218650-15	-0.2129685300-17	0.6027379720-07

TMC ARM INSTRUMENT DATA

	ODD ARM	EVEN ARM
MASS	0.1581000000 01	0.1581000000 01
CM(1)	0.6663902000-05	0.6683960000-05
CM(2)	0.9320765300-07	0.9326764800-07
CM(3)	-0.1599262500-11	-0.1171962800-11

AD-A048 252 STANFORD UNIV CALIF GUIDANCE AND CONTROL LAB F/G 8/5
STUDY TO DEVELOP GRADIOMETER TECHNIQUES.(U)
JUN 77 D B DEBRA, E J PELKA F19628-74-C-0162
UNCLASSIFIED AFGL-TR-76-0297 NL

4 OF 4
AD
AD48252



END
DATE
FILMED
1 -78
DDC

Table IX-7

CM OFFSET TEST OEP VALUES

PRECONTROL		POSTCONTROL	
P(1)	0.0000000000 00	P(1)	0.17953507D-12
P(2)	0.0000000000 00	P(2)	0.9618644990-17
P(3)	-0.1563000000-09	P(3)	0.9139516950-08
P(4)	-0.0000000000 00	P(4)	-0.1844864800-20
P(5)	0.6220284590-02	P(5)	0.6220293370-02
P(6)	0.0000000000 00	P(6)	0.1795350700-12
P(7)	0.0000000000 00	P(7)	-0.9618644990-17
P(11)	-0.1563000000-04	P(11)	0.1109978900-11
P(12)	-0.0000000000 00	P(12)	0.9011837400-14
P(13)	-0.0000000000 00	P(13)	0.0000000000 00
P(14)	-0.6561618700-16	P(14)	-0.3049366500-12
P(15)	-0.0000000000 00	P(15)	-0.9789111810-15
P(16)	-0.0000000000 00	P(16)	0.2049380500-14
P(17)	-0.0000000000 00	P(17)	-0.1986464430-23

A similar test cast which specified a $\hat{y}_s$ mass center inital offset was run. The results of that test were equivalent to those described above.

Based upon these test cases, the simulation was judged to be working properly. Furthermore, the observed control law response agreed with intuitive predictions relative to how the various controls would be applied.

F. GENERAL ERROR CASE TESTS

Several general error cases were defined by perturbing various combinations of the 16 arm model-masses in both position and mass, thereby providing perturbations of the OEP vector ΔP.* The cases tested were:

* Arbitrary specification of model-mass position and magnitude is the mechanism which allows arbitrary specification of the OEP vector ΔP. In all test cases the initial positions of the control masses were their respective nominal positions.

9/2

(1) all arm 4 model masses,

(2) all arm 3 and 4 model masses,

(3) all arm 2, 3, and 4 model masses,

(4) all arm model masses.

The perturbations applied to the 16 model-masses for the various test cases are shown in Figs. IX-8 through IX-11.

F.1 Test Case 4--All Model-Mass Values and Positions Perturbed

Test Case 4 most generally perturbed the input data from nominal values. The errors associated with the separate model masses were independently and randomly selected. Instrument physical data for this test case, prior to any control application, are listed in Tables IX-8 and IX-9. Test case input data are compared with error analysis data of Table III-2 in Table IX-10. The test case error levels generally equal or exceed those specified within the error analysis of Ch. III.

Three separate control iterations comprised the test case. Each control iteration consisted of (1) estimation of the OEP; (2) Calculation of the appropriate control increment vector using the least squares control criterion. Figure IX-12 shows the history of several OEP as a function of control iteration. The parameters reduced by 2.4 to 10 orders of magnitude. Instrument physical parameters subsequent to the third iteration are provided in Table IX-11. Numerical histories of the OEP during the test are tabulated in Table IX-12. Position increments for each control mass at each control iteration are listed in Table IX-13.

In addition to demonstration of overall controller operation, Test Case 4 also indicated certain trends associated with least squares OEP control. Arm mass center location was set by the first control iterations and changed little during the second and third control cycles. Test Case 4 odd and even arm mass center locations vs control iteration are given in Fig. IX-13.

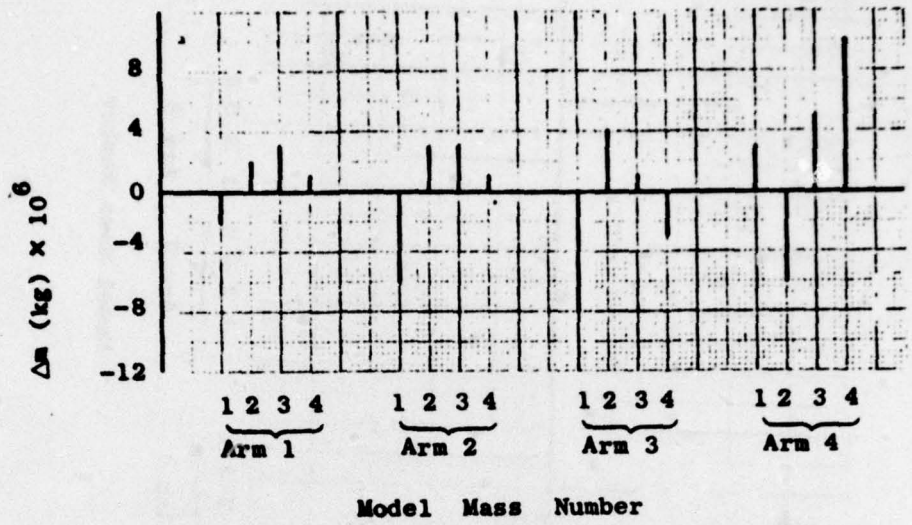


FIG. IX-8 MODEL MASS PERTURBATIONS FOR TEST CASES 1 TO 4.

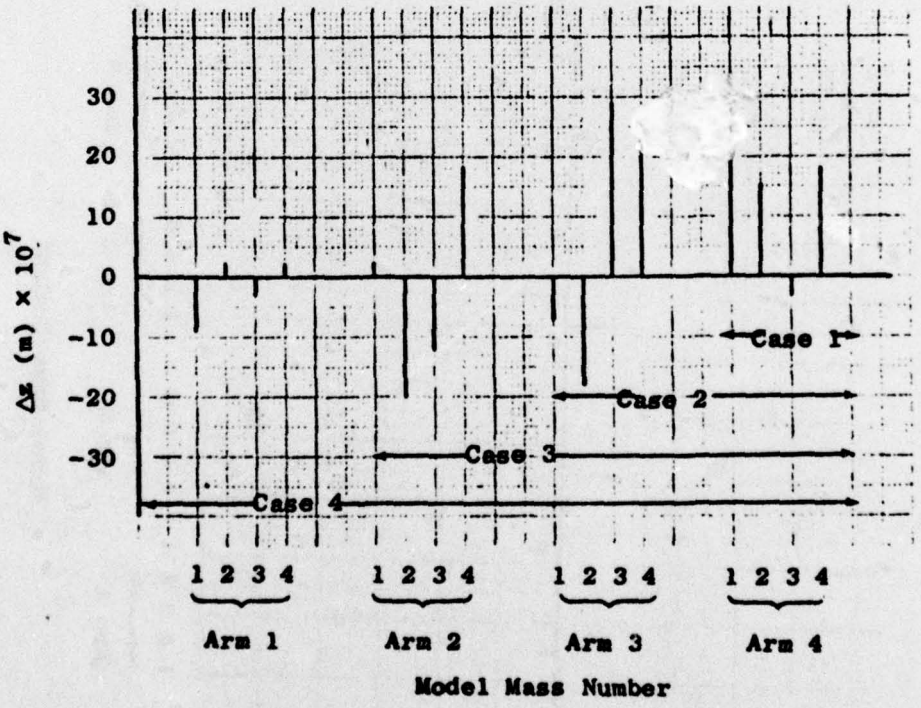


FIG. IX-9. MODEL MASS $\hat{z}_s$ PERTURBATIONS FOR TEST CASES 1 TO 4

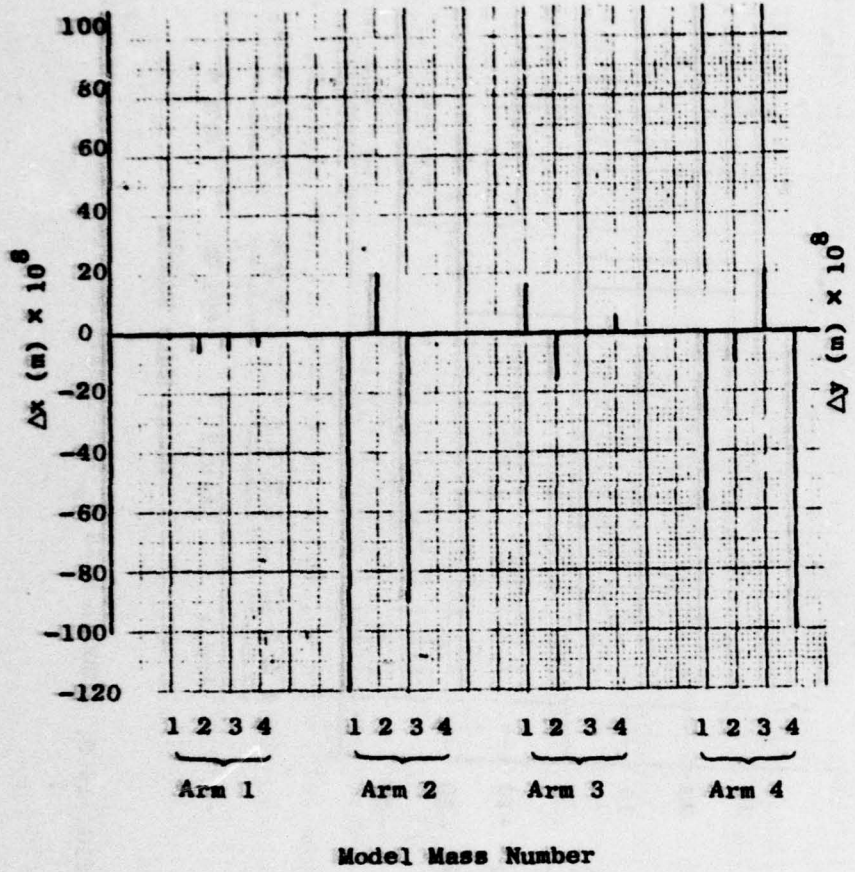


FIG. IX-10 MODEL MASS $\hat{x}_s$ PERTURBATIONS FOR TEST CASES 1 TO 4.

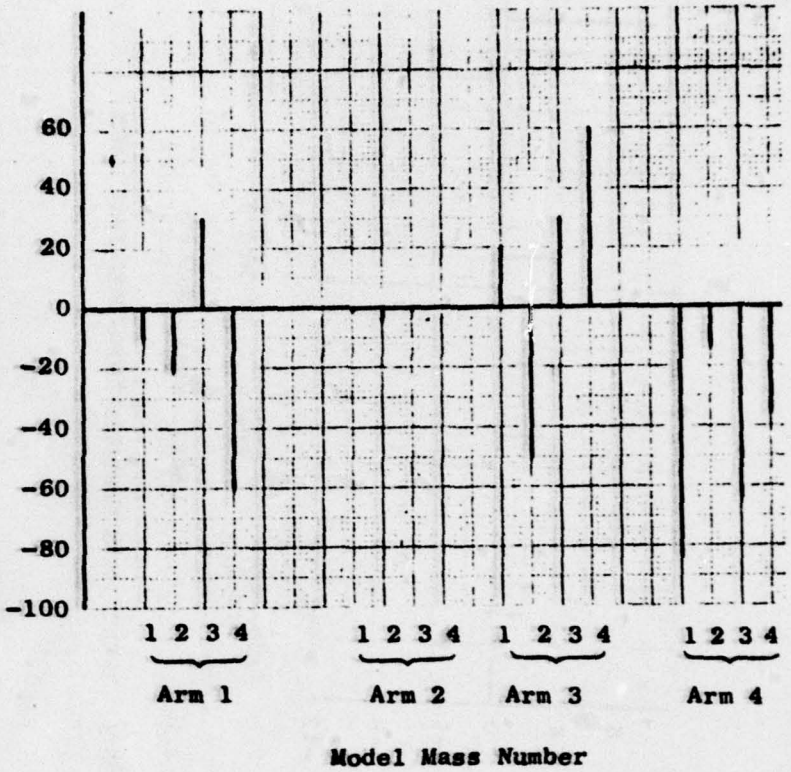


FIG. IX-11 MODEL MASS $\hat{y}_s$ PERTURBATIONS FOR TEST CASES 1 TO 4.

Table IX-8

INSTRUMENT ARM MASS AND MASS CENTER DATA PRIOR TO CONTROL

ACTUAL INSTRUMENT

INSTRUPEAT SUB-PASS MATRIX

C.1953730 00	0.1953770 00	0.1953780 00	0.1953760 00
C.1953690 0C	0.1953780 00	C.1953780 00	0.1953760 00
0.1953670 00	0.1953790 00	0.1953760 00	C.1953720 00
C.1953780 0C	0.1953690 0C	C.19538CC 00	0.1953850 00

FOUR ARM CONFIG. SUB-MASS POSITION VECTORS X,Y,Z (M) SENSOR AXES

ARM 1

0.4602566CCD-01	0.1264700CCD-C1	0.1262090000-01
C.4602561CCD-01	0.1264690000-01	-0.1262160CC0-01
C.4602562CCD-C1	-0.1264680CCD-C1	-0.1262210000-01
C.4602563000-01	-0.1264770CCC-C1	C.1262200CC0-C1

ARM 3

-0.4602551CC0-01	0.1264730000-01	0.1262110000-01
-0.4602583CC0-01	0.1264660000-01	-0.1261890000-01
-0.4602568000-01	-0.1264680000-01	-0.1261930000-01
-0.4602562CC0-01	-0.1264650000-01	0.1262000000-01

ARM 2

-0.1264830000-01	0.4602567000-01	0.1262200000-01
C.1264730C0D-C1	0.4602566CCC-01	0.1261980C00-01
C.1264620000-01	0.4602563CCC-C1	-0.12623CCCC0-01
-C.1264556000-01	0.4602565CCC-C1	-0.1261940000-01

ARM 4

-0.1264770000-01	-0.4602650000-01	0.1262400000-01
0.1264700C00-01	-0.4602580000-01	0.1262330000-01
0.1264730C00-01	-0.4602630000-01	-0.1262210000-01
-0.1264810CCD-01	-0.4602600000-01	-0.1262000000-01

FOUR ARM CONFIGURATION MASSES (KG) AND MASS CENTER (M) SENSOR AXES

ARM	MASS	RHO(X)	RHO(Y)	RHO(Z) SENSOR AXES
1	0.7E1504CCCD CC	0.4610312150-01	-0.2122E84650-C6	-0.2935207160-06
2	C.7815010000 00	0.2987946500-08	0.4610460210-01	-0.2600787370-C6
3	C.7E1496CCCD CC	-0.4610315210-01	0.1162889280-06	0.4613112810-06
4	0.7E15120000 00	-0.5947184860-06	-0.4610363480-01	0.9977985150-06

Table IX-9

INSTRUMENT PHYSICAL DATA PRIOR TO CONTROL APPLICATION

ODD ARM INERTIA TENSOR SA

C.5105C24600-C3	0.1200404870-07	0.2637834420-07
C.1200404870-07	0.3620643110-C2	-C.1120461C80-C8
0.2637834420-07	-0.1120461CEC-C8	0.3612582450-02

EVEN ARM INERTIA TENSOR SA

0.3427C752190-02	-0.2266101440-07	0.2373C46120-07
-0.2266101440-07	0.5105560970-03	0.4564275880-07
0.2373C46120-07	0.4564275880-07	0.3612664370-02

ODD ARM INERTIA TENSOR BA

C.5105C24590-C3	0.C0000000CC 00	0.0000000000 00
C.CCOCC00000 00	0.3620643110-C2	0.0CCCCOCOCCO 00
C.CCOOC00000 00	0.0000000CCC 00	0.3612582450-02

EVEN ARM INERTIA TENSOR BA

0.362C752260-02	0.00C0000000 00	0.0000000000 00
0.0000000000 00	0.5105560960-03	0.0000000000 00
0.000CCCOCCO 00	0.0000000000 00	0.3612664300-02

INERTIA TENSOR DIFFERENCE MATRIX SA

-0.3110249730-C2	0.3466506310-07	0.2647883C30-08
C.3466506310-07	0.3110087C50-02	-0.4676321590-07
0.2647883030-08	-0.4676321550-C7	-C.8191C21480-C7

TSB ODD ARM

C.1C0CCCC000 01	0.3858469240-C5	-C.0503975550-C5
-0.3659E51160-C5	0.9999999900 00	-0.1389857330-03
-C.0503436180-C5	-0.1389897650-C3	-C.9599999500 00

TSB EVEN ARM

0.9999956960 00	-0.7286152660-05	0.2934017690-02
-0.7242591570-05	-0.1000000000 01	-0.1473483430-04
0.2934017800-02	0.1471351990-04	-0.9999956960 00

Cont. ...

Table IX-9 (Cont)

ODD ARM COMPLIANCE BA

0.3515651260-07	0.0000000000 00	0.0000000000 00
0.0000000000 00	0.3524525630-07	0.0000000000 00
0.0000000000 00	0.0000000000 00	0.6011763650-07

EVEN ARM COMPLIANCE BA

0.3525094230-07	0.0000000000 00	0.0000000000 00
0.0000000000 00	0.3533952270-07	0.0000000000 00
0.0000000000 00	0.0000000000 00	0.6043058380-07

ODD ARM COMPLIANCE SA

0.3515651260-07	0.3719181270-15	0.2122687380-12
0.3719181270-15	0.3524525680-07	0.3457005440-11
0.2122687380-12	0.3457005440-11	0.6011763610-07

EVEN ARM COMPLIANCE SA

0.3525115900-07	-0.4431625000-15	-0.7387719570-10
-0.4431625000-15	0.3533952270-07	0.3697129180-12
-0.7387719570-10	0.3697129180-12	0.6043036700-07

COMPLIANCE DIFFERENCE MATRIX SA

-0.9464642030-10	0.8150806270-15	0.7408946450-10
0.8150806270-15	-0.9426587840-10	0.3087292520-11
0.7408946450-10	0.3087292520-11	-0.3177309530-09

TWO ARM INSTRUMENT DATA

	ODD ARM	EVEN ARM
PASS	0.1580598C0 01	0.1580598C0 01
CM(1)	0.2762870D-06	-0.2958720D-06
CM(2)	-0.4799980D-07	-0.5661567D-06
CM(3)	0.8389289E-07	0.3688742D-06

Table IX-10

COMPARISON OF TEST CASE 4 INPUT DATA WITH ERROR ANALYSIS INPUT DATA DEMONSTRATING THE CAPABILITY OF THE SYSTEM TO CONTROL ERRORS IN INSTRUMENT MANUFACTURING WHICH ARE LARGER THAN EXPECTED.

Instrument Error Source	Error Analysis	Test Case 4	Units
Arm-to-arm inertia ratio error	1.0×10^{-4}	1.0×10^{-2}	%
Arm mass center displacement	3.0×10^{-9}	3.0×10^{-7}	m
Pivot compliance mismatch	2.0×10	0	%
Pivot damping ratio mismatch	2.0×10^{-2}	0	%
Spin motor torque error	2.5×10^{-6}	1.0×10^{-4}	N m
Sensor/platform misalignment	5.0×10^{1}	0	μrad
Elastic/Spin axis misalignment	5.0×10^{1}	0	μrad
Spin/Principal axis misalignment	5.0×10^{1}	2.5×10^{3}	μrad
Axis-to-axis compliance mismatch	1.0×10^{-1}	1.0×10^{-1}	%
Arm-to-arm compliance mismatch	1.0×10^{-1}	1.0×10^{-1}	%

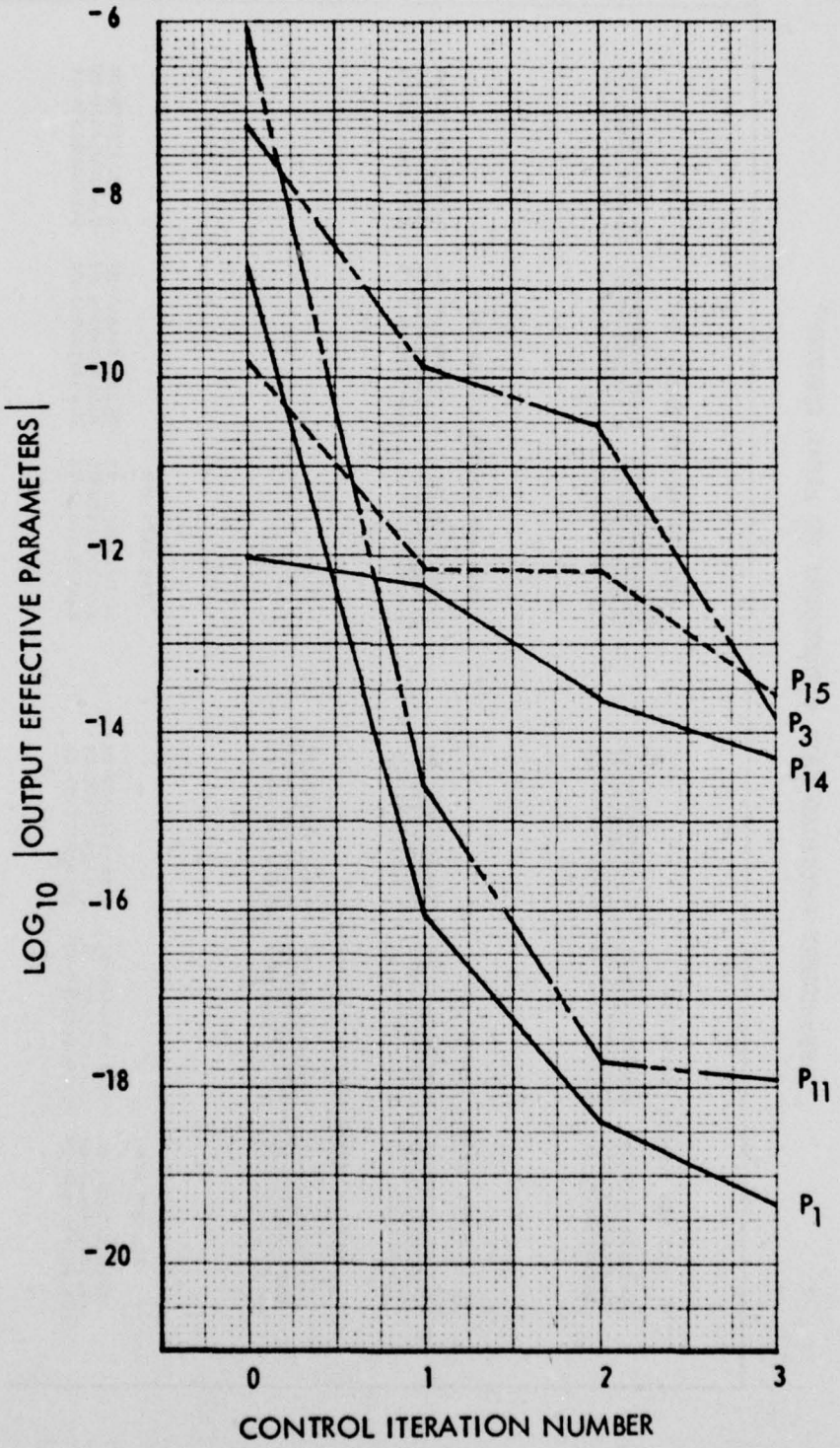


FIG. IX-12 OEPs AS A FUNCTION OF CONTROL ITERATION—TEST CASE 4

Table IX-11

INSTRUMENT PHYSICAL DATA SUBSEQUENT TO FINAL CONTROL

ODD ARM INERTIA TENSOR SA

0.5105111020-03	0.A5C2645870-10	C.2671932790-11
C.E5C2645870-10	0.3620658230-02	-0.1533830190-12
0.2671932790-11	-0.1533830190-12	0.3612EC61CD-C2

EVEN ARM INERTIA TENSOR SA

0.3620693800-02	0.85C2638980-10	0.3507124480-11
0.A502638450-10	0.5105563260-03	-C.1526174880-11
0.3507124480-11	-0.1526174880-11	0.3612606100-02

ODD ARM INERTIA TENSOR BA

C.5105111020-03	0.0000000CCD CC	C.0CCCCCCCOD C0
C.CCOCC0003C 00	0.3620658230-C2	0.00CC00CCOD 00
C.CCOCCCCOCD 00	0.0000000CCD CC	0.3612606100-02

EVEN ARM INERTIA TENSOR BA

0.3620693800-02	0.0000000000 00	0.0000000000 00
0.000COCOCCD 00	0.5105563260-03	0.0000000000 00
0.0000000000 00	0.0000000000 00	0.3612606100-02

INERTIA TENSOR DIFFERENCE MATRIX SA.

-C.511C182700-C2	0.6837481720-16	-0.8351916980-12
C.6837481720-16	0.3110lC15CD-C2	0.1372791EED-11
-C.8351516980-12	0.1372791860-11	-0.1645770110-13

TSB ODD ARM

C.1CCCC00000 01	0.2733840410-07	0.8613322300-09
-C.2733840390-C7	0.10C0000CCD C1	0.1904875190-C7
-0.8613317050-09	-0.1904875790-07	C.100CCCCCCD C1

TSB EVEN ARM

0.100CCCCCOD 01	-0.2733846660-07	-0.4336370870-06
0.2733846690-07	0.1000000000 01	-0.4920010510-09
0.4336370870-06	0.4919891960-09	0.1000000000 01

Cont. ...

Table IX-11 (Cont)

ODD ARM COMPLIANCE BA

0.3515E5126D-07	0.0000000000 00	0.0000000000 00
0.0000000000 00	0.3524530420-07	0.0000000000 00
0.0000000000 00	0.0000000000 00	0.6011726350-07

EVEN ARM COMPLIANCE BA

0.3525073270-07	0.0000000000 00	0.0000000000 00
0.0000000000 00	0.3533952270-07	0.0000000000 00
0.0000000000 00	0.0000000000 00	0.6043058380-07

ODD ARM COMPLIANCE SA

0.3515E5126D-07	0.2427428100-17	0.2145982050-16
0.2427428100-17	0.3524530420-07	0.4737870360-15
0.2145982050-16	0.4737870360-15	0.6011726350-07

EVEN ARM COMPLIANCE SA

0.3525073270-07	-0.2427358810-17	-0.1091891730-13
-0.2427358810-17	0.3533952270-07	-0.1234482950-16
-0.1091891730-13	-0.1234482950-16	0.6043058380-07

COMPLIANCE DIFFERENCE MATRIX SA

-0.5422013870-10	0.4854786910-17	0.1094041710-13
0.4854786910-17	-0.9421847860-10	0.4861318660-15
0.1094041710-13	0.4861318660-15	-0.3125412240-09

T&C ARM INSTRUMENT DATA

	ODD ARM	EVEN ARM
MASS	0.1580998CD 01	0.1580988CD 01
CM(1)	0.2091233?D-05	0.2091246?D-05
CM(2)	-0.3437328?C-05	-0.3437350?0-05
CM(3)	0.1001426?0-06	0.3527536?0-06

Table IX-12

OEPs AS A FUNCTION OF CONTROL ITERATION

Iteration 0		Iteration 1		Iteration 2		Iteration 3	
P(1)	0.264767380-08	P(1)	-0.865869700-16	P(1)	-0.431064180-18	P(1)	0.42[illegible]237230-19
P(2)	-0.467635440-07	P(2)	-0.463483590-16	P(2)	-0.613665850-19	P(2)	0.95[illegible]44393D-19
P(3)	-0.119167360-07	P(3)	0.139576750-09	P(4)	0.198315110-10	P(3)	-C.16[illegible]55870-13
P(4)	C.346653450-07	P(4)	-0.155543650-15	P(4)	-C.711110880-17	P(4)	-0.35[illegible]82C950-17
P(5)	0.522033680-02	P(5)	0.622028240-02	P(5)	0.[illegible]22028520-02	P(5)	0.6[illegible]C28460-02
P(6)	C.264767380-08	P(6)	-0.869869700-16	P(6)	-0.431064180-18	P(6)	0.42[illegible]237230-19
P(7)	0.467635440-07	P(7)	0.463483590-16	P(7)	0.613665850-19	P(7)	-0.95[illegible]44393D-19
P(8)	0.154821940-07	P(8)	-0.264C55140-1C	P(8)	-0.753483060-11	P(8)	0.31[illegible]280280-14
P(9)	0.000000000 00	P(9)	-C.0CCC00C0D 00	P(9)	-0.000000000 00	P(9)	0.000000000 00
P(10)	C.000000000 00	P(10)	-0.0CC000C0D 00	P(10)	-0.000000000 00	P(10)	C.000000000 00
P(11)	C.904575530-06	P(11)	0.232302810-14	P(11)	C.2C8708920-17	P(11)	0.11[illegible]53870-17
P(12)	0.819199350-06	P(12)	0.321911930-14	P(12)	0.163392660-17	P(12)	C.85[illegible]C19870-18
P(13)	0.000000000 00	P(13)	0.000000000 00	P(13)	0.000000000 00	P(13)	C.000000000 00
P(14)	-0.953575260-12	P(14)	-0.6CC575470-12	P(14)	-0.323023180-13	P(14)	-0.69[illegible]981C-14
P(15)	0.185188330-09	P(15)	-0.794192240-12	P(15)	0.790463740-12	P(15)	0.27345E250-13
P(16)	C.771686820-11	P(16)	-0.446681810-13	P(16)	0.365505150-13	P(16)	0.12[illegible]12E0-14
P(17)	0.203732460-14	P(17)	0.280398950-14	P(17)	-0.162767870-16	P(17)	C.12134729D-16

Table IX-13

CONTROL INCREMENTS BY ITERATION NUMBER (m)

Iteration 1		Iteration 2		Iteration 3	
DELX(1)	0.5146910-03	DELX(1)	-0.6491890-04	DELX(1)	0.1818280-05
DELX(2)	-0.4314790-03	DELX(2)	-0.1754170-03	DELX(3)	-0.1431510-04
DELX(3)	-0.4204020-03	DELX(3)	-0.1755740-03	DELX(3)	-0.1426760-04
DELX(4)	0.3618800-03	DELX(4)	-0.6374930-04	DELX(4)	0.1253860-05
DELX(5)	-0.8290440-03	DELX(5)	0.1704990-03	DELX(5)	-0.2521750-05
DELX(6)	-0.8401560-03	DELX(6)	0.1706290-03	DELX(6)	-0.2566090-05
DELX(7)	0.1031610-03	DELX(7)	-0.3803630-06	DELX(7)	0.4711550-06
DELX(8)	0.3971310-03	DELX(8)	0.1535180-04	DELX(8)	0.5486420-05
DELX(9)	-0.3746000-03	DELX(9)	-0.2706140-03	DELX(9)	-0.1335460-04
DELX(10)	-0.3835330-03	DELX(10)	-0.2706800-03	DELX(10)	-0.1330790-04
DELX(11)	0.2443250-03	DELX(11)	0.1652170-04	DELX(11)	0.4922060-05
DELX(12)	-0.7921750-03	DELX(12)	0.7528250-04	DELX(12)	-0.1561970-05
DELX(13)	-0.8032780-03	DELX(13)	0.7543220-04	DELX(13)	-0.1605570-05
DELX(14)	-0.7837130-04	DELX(14)	0.1009330-05	DELX(14)	-0.1993030-06
DELX(15)	-0.4098740-03	DELX(15)	-0.8586230-04	DELX(15)	-0.9681750-05
DELX(16)	0.3371300-03	DELX(16)	0.1956270-03	DELX(16)	0.9464370-05
DELX(17)	0.1023710-03	DELX(17)	0.1581820-03	DELX(17)	0.8526980-05
DELX(18)	-0.6732150-03	DELX(18)	-0.8992190-04	DELX(18)	-0.5654580-05
DELX(19)	0.4442850-03	DELX(19)	-0.1494300-03	DELX(19)	-0.3709840-05
DELX(20)	0.6787710-03	DELX(20)	-0.1507720-03	DELX(20)	-0.2721190-05
DELX(21)	0.1441270-03	DELX(21)	-0.2716690-06	DELX(21)	-0.1505880-06
DELX(22)	-0.3456470-03	DELX(22)	-0.1016560-04	DELX(22)	-0.6220130-05
DELX(23)	0.5409660-03	DELX(23)	0.1003790-03	DELX(23)	0.1042410-04
DELX(24)	0.3062960-03	DELX(24)	0.1030270-03	DELX(24)	0.9487520-05
DELX(25)	-0.6089970-03	DELX(25)	-0.1022700-04	DELX(25)	-0.6193470-05
DELX(26)	0.6482080-03	DELX(26)	-0.2445840-03	DELX(26)	-0.2749320-05
DELX(27)	0.8826080-03	DELX(27)	-0.2460190-03	DELX(27)	-0.1761410-05
DELX(28)	-0.1687290-03	DELX(28)	-0.3434080-06	DELX(28)	-0.1188720-06

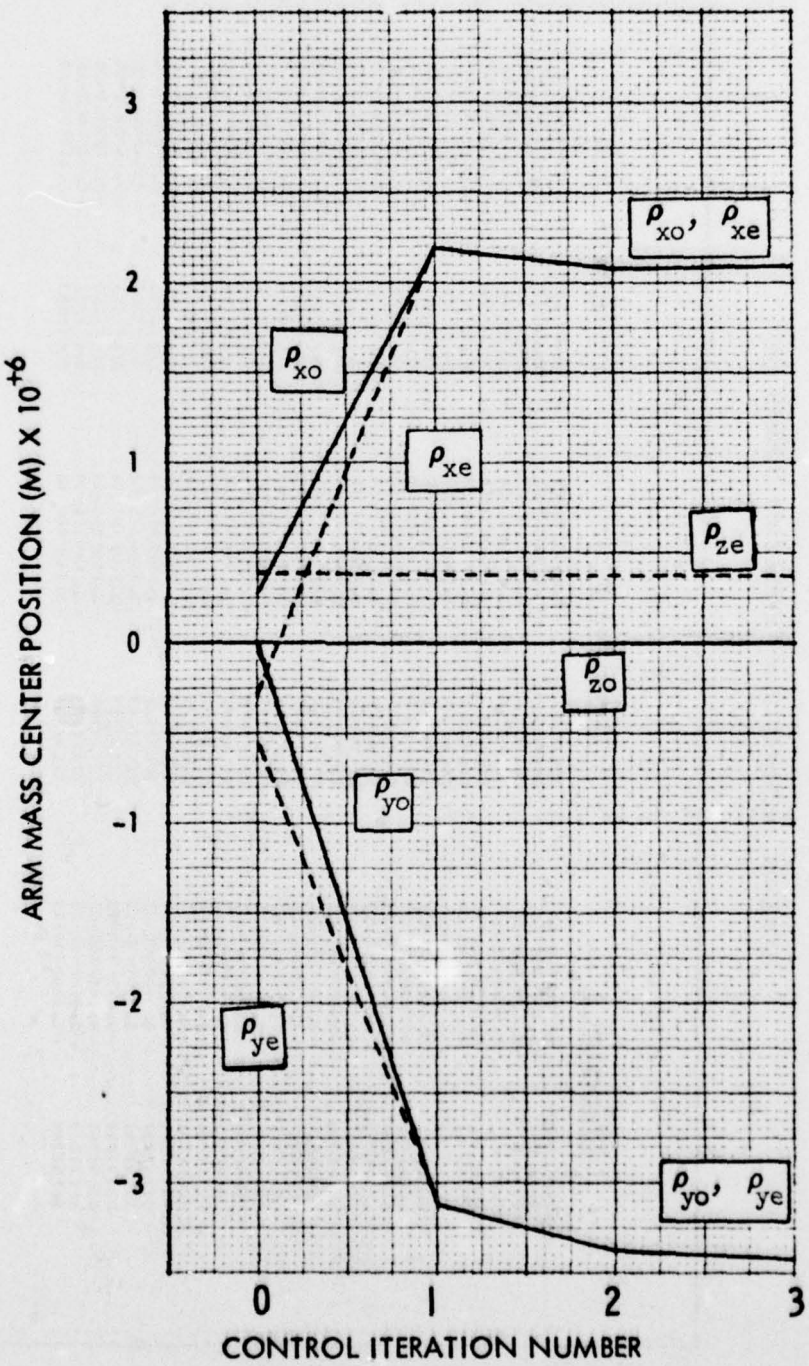


FIG. IX-13 ARM CM LOCATION AS A FUNCTION OF CONTROL ITERATION, TEST CASE 4.

The second and third control iterations trim the OEP which are less strongly a function of CM. In particular, the third iteration aligns arm principal axes to the sensor axis system. Arm principal axis rotations relative to sensor axes as a function of control iteration for this test case are shown in Fig. IX-14.

The overall effect of the control upon RGG error torque output for Test Case 4 is calculated in Table IX-14. The total $2\omega_s$ output torque error is reduced from its precontrol value of 10^4 E.U. to a postcontrol value of slightly less than 0.10 E.U.

F-2 Additional Test Cases

Graphical results from Test Cases 1 through 3 cited in Section IX-D are shown in Figs. IX-15 through IX-23. The OEP magnitude histories for these cases appear in Figs. IX-15, IX-16, and IX-17. The controller in all cases performed in a manner similar to that of Test Case 4, although OEP absolute magnitudes very from case to case.

Histories of arm mass center positions for the test cases are given in Figs. IX-18 to IX-20. In all cases, the terminal mass center position is determined to within 5% after the first control application. Furthermore, arm $\hat{z}_s$ mass center position is seen to be almost incidental and uncontrolled. This is reasonable since this mass center component is never more than a second order small contributor to sensor error torque output.

Figures IX-21 to IX-23 display the iteration histories of arm principal to sensor axis rotations for the additional test cases. The magnitude of each misalignment angle is reduced by approximately 4 to 6 orders of magnitude through each test. However, the zero slope situation between iterations 1 and 2--which is quite noticeable in Figs. IX-14 and IX-23 for Test Cases 4 and 3--is much less significant in Test Cases 1 and 2. Absolute values of the transformation angles tend to posses a greater terminal value as the complexity of the initial error state is increased.

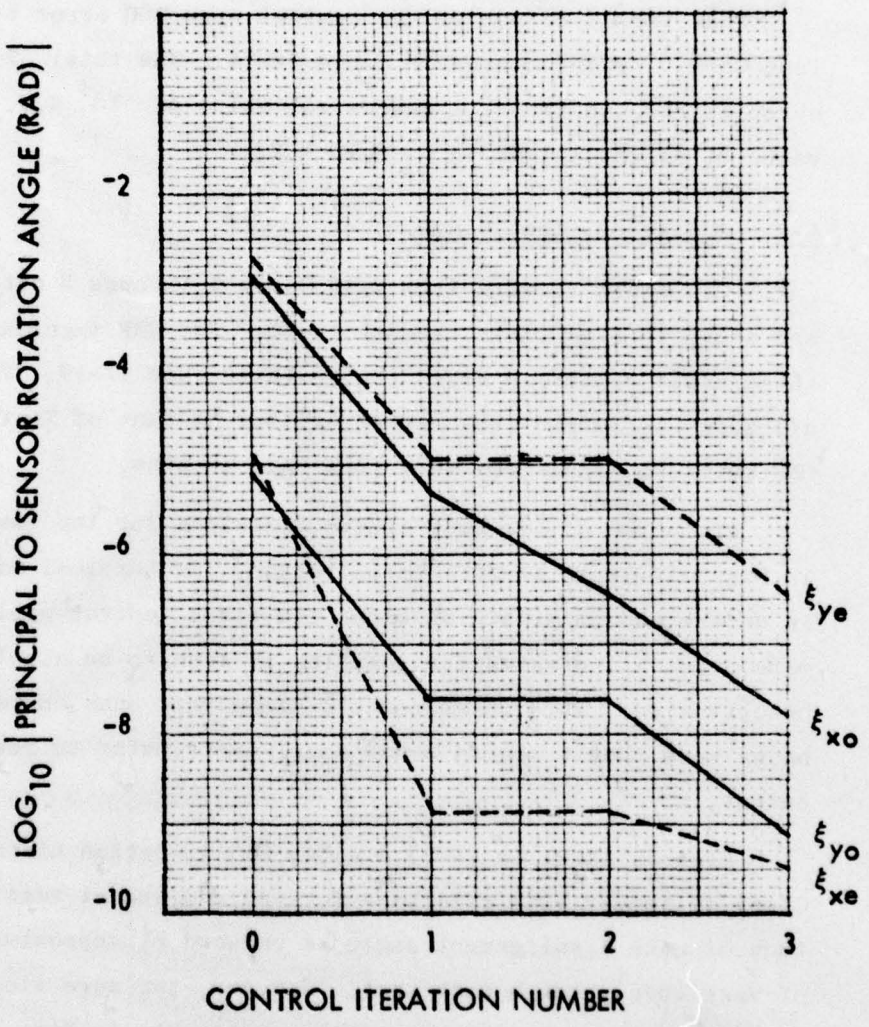


FIG. IX-14 ARM TO SENSOR ROTATION ANGLES AS A FUNCTION OF CONTROL ITERATION; TEST CASE 4.

TABLE IX-14

PRE- AND POST-CONTROL RGG OUTPUT TORQUE ERROR (N m) FOR TEST CASE 4

Parameter Number	Pre-Control Value	Post-Control Value	Relevant Dynamic State	Pre-Control 2ws Torque	Post-Control 2ws Torque
1	0.265×10^{-8}	0.426×10^{-19}	1.0×10^{-2}	0.265×10^{-10}	0.426×10^{-21}
2	0.468×10^{-7}	0.959×10^{-19}	1.0×10^{-2}	0.468×10^{-9}	0.959×10^{-21}
3	0.819×10^{-7}	0.168×10^{-13}	4.4×10^{-1}	0.360×10^{-7}	0.739×10^{-14}
4	0.347×10^{-7}	0.357×10^{-17}	4.0×10^{-9}	0.138×10^{-15}	0.142×10^{-25}
5	0.522×10^{-7}	0	4.0×10^{-9}	0.209×10^{-15}	0
11	0.905×10^{-6}	0.120×10^{-17}	1.0×10^{-4}	0.905×10^{-10}	0.120×10^{-21}
12	0.819×10^{-6}	0.890×10^{-18}	1.0×10^{-4}	0.819×10^{-10}	0.890×10^{-22}
14	0.954×10^{-12}	0.696×10^{-14}	4.8×10^{1}	0.458×10^{-10}	0.334×10^{-12}
15	0.185×10^{-9}	0.273×10^{-13}	4.9×10^{-4}	0.907×10^{-13}	0.134×10^{-16}
16	0.772×10^{-11}	0.122×10^{-14}	4.9×10^{-4}	0.378×10^{-14}	0.598×10^{-18}
17	0.204×10^{-14}	0.121×10^{-16}	4.8×10^{1}	0.979×10^{-13}	0.581×10^{-15}
RSS				0.360×10^{-7}	03.34×10^{-13}

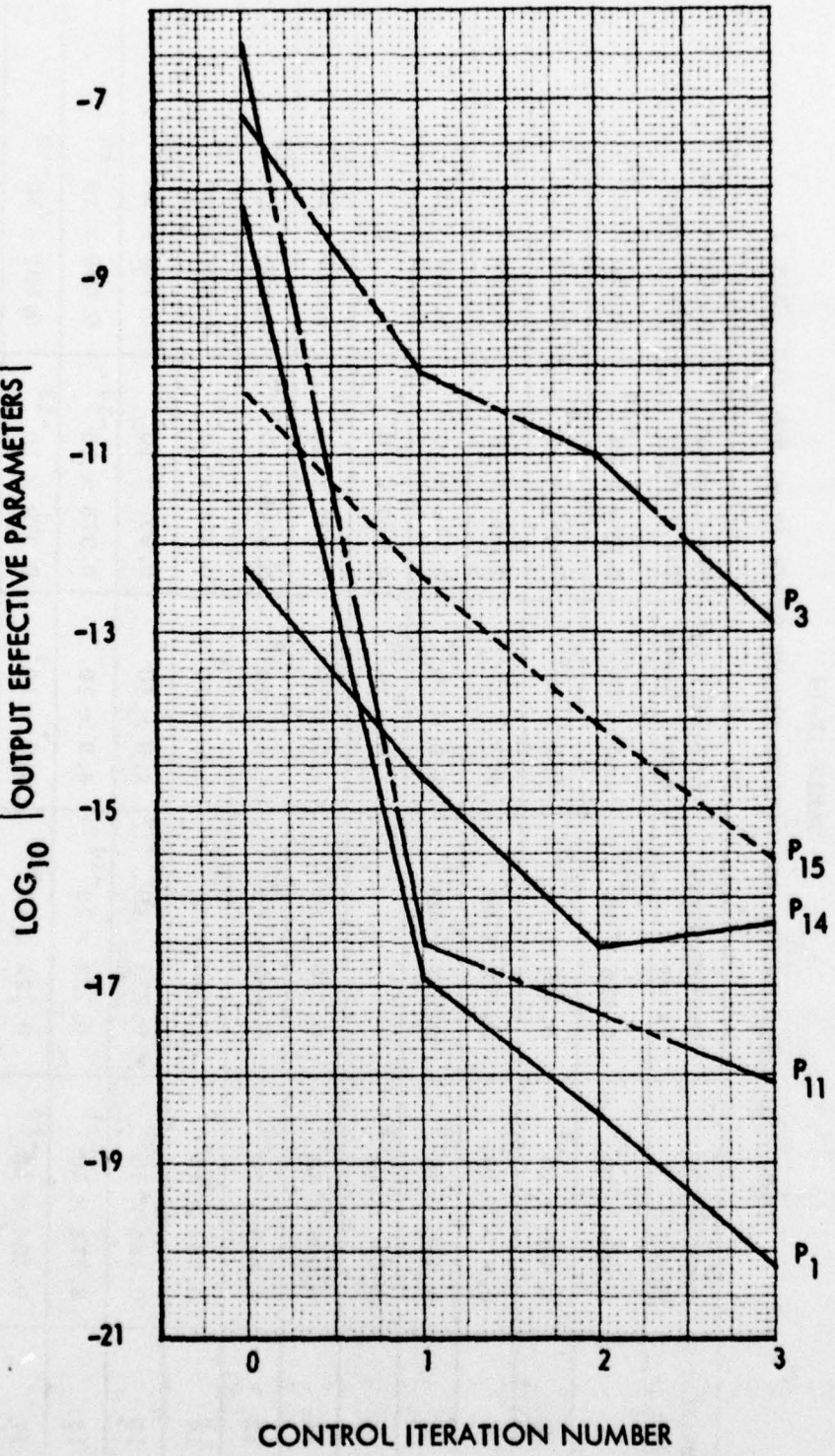


FIG. IX-15 OEP AS A FUNCTION OF CONTROL ITERATION. TEST CASE 1.

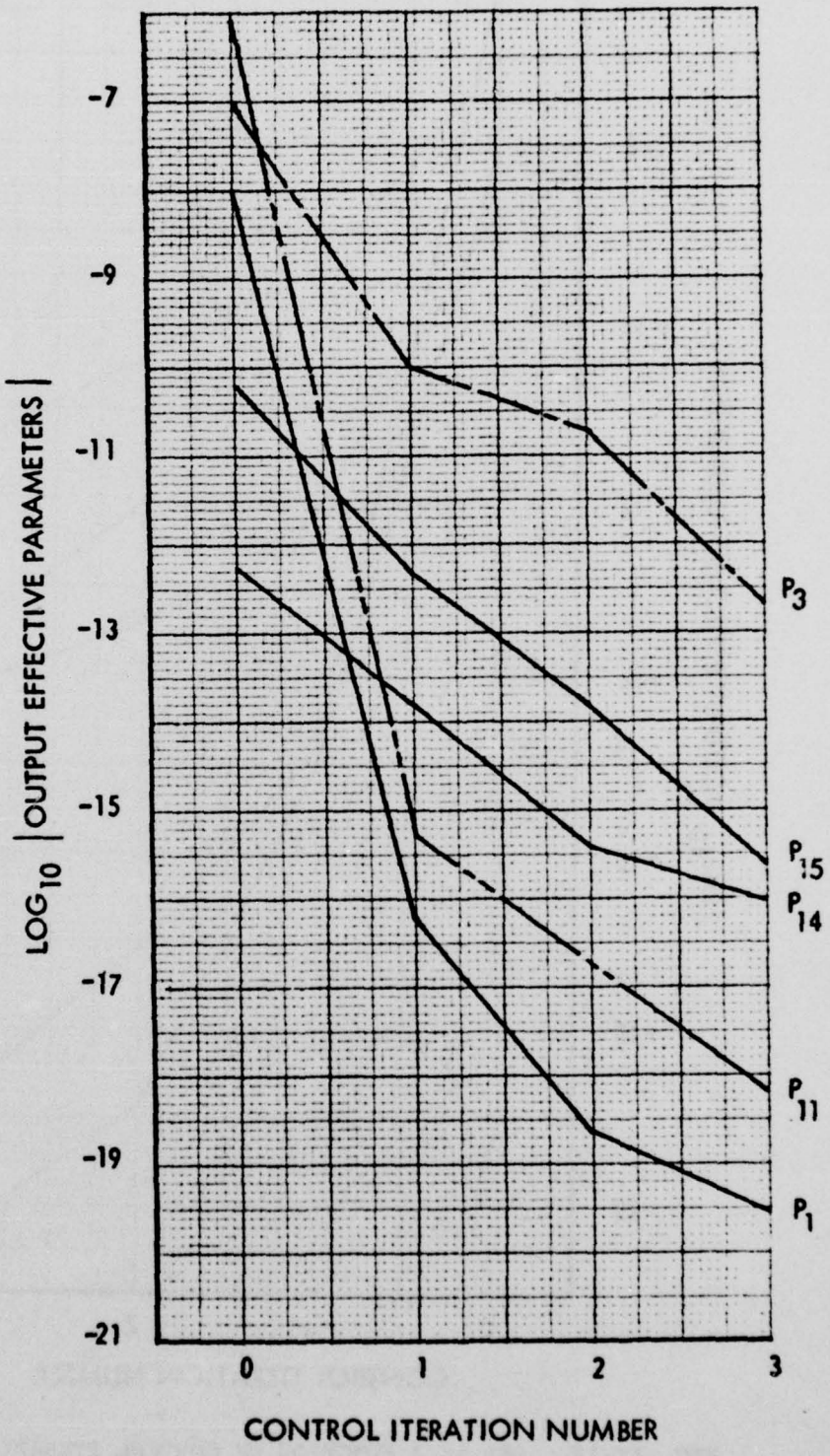


FIG. IX-16 OEP AS A FUNCTION OF CONTROL ITERATION. TEST CASE 3.

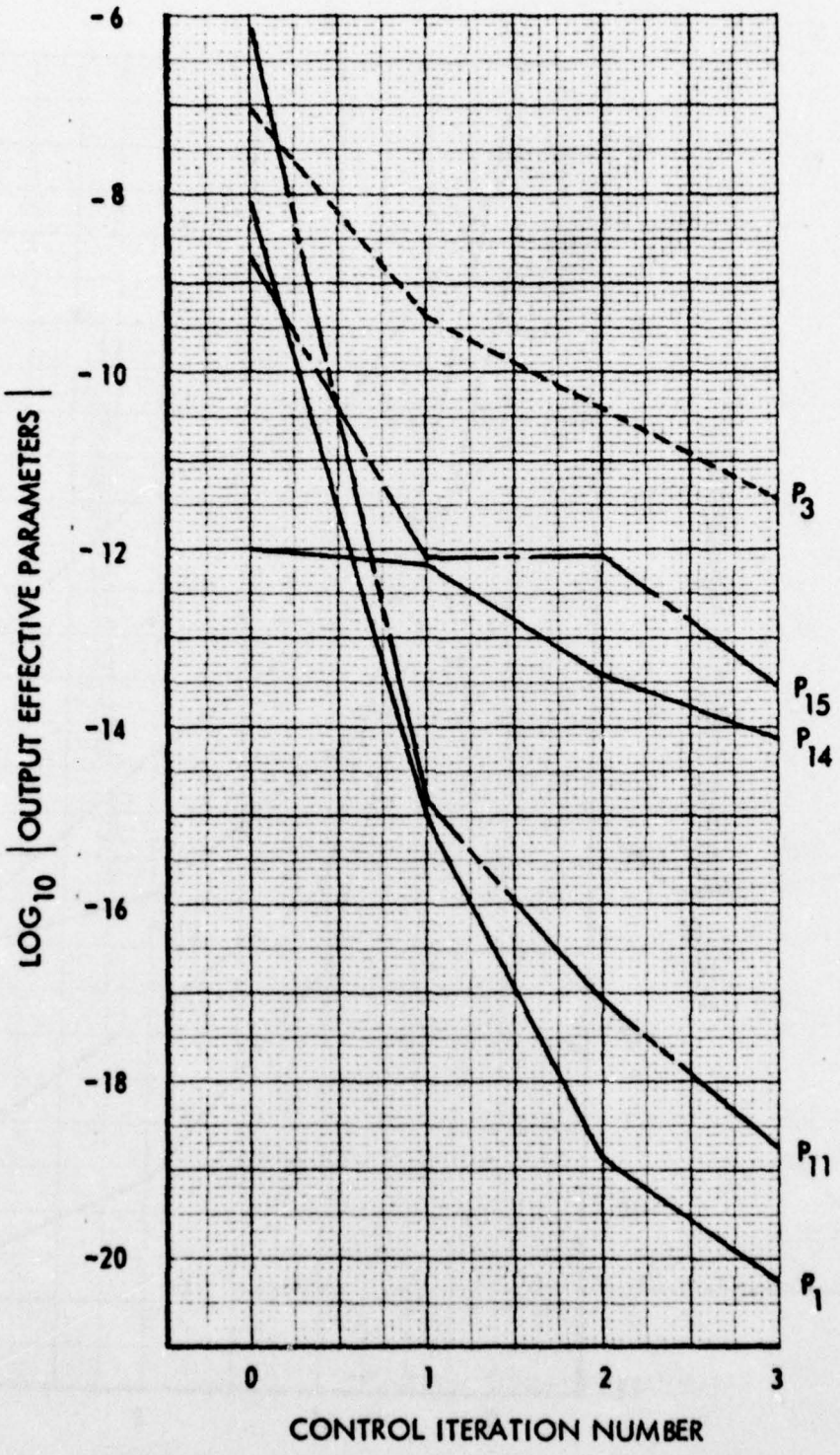


FIG. IX-17 OEP AS A FUNCTION OF CONTROL ITERATION. TEST CASE 3.

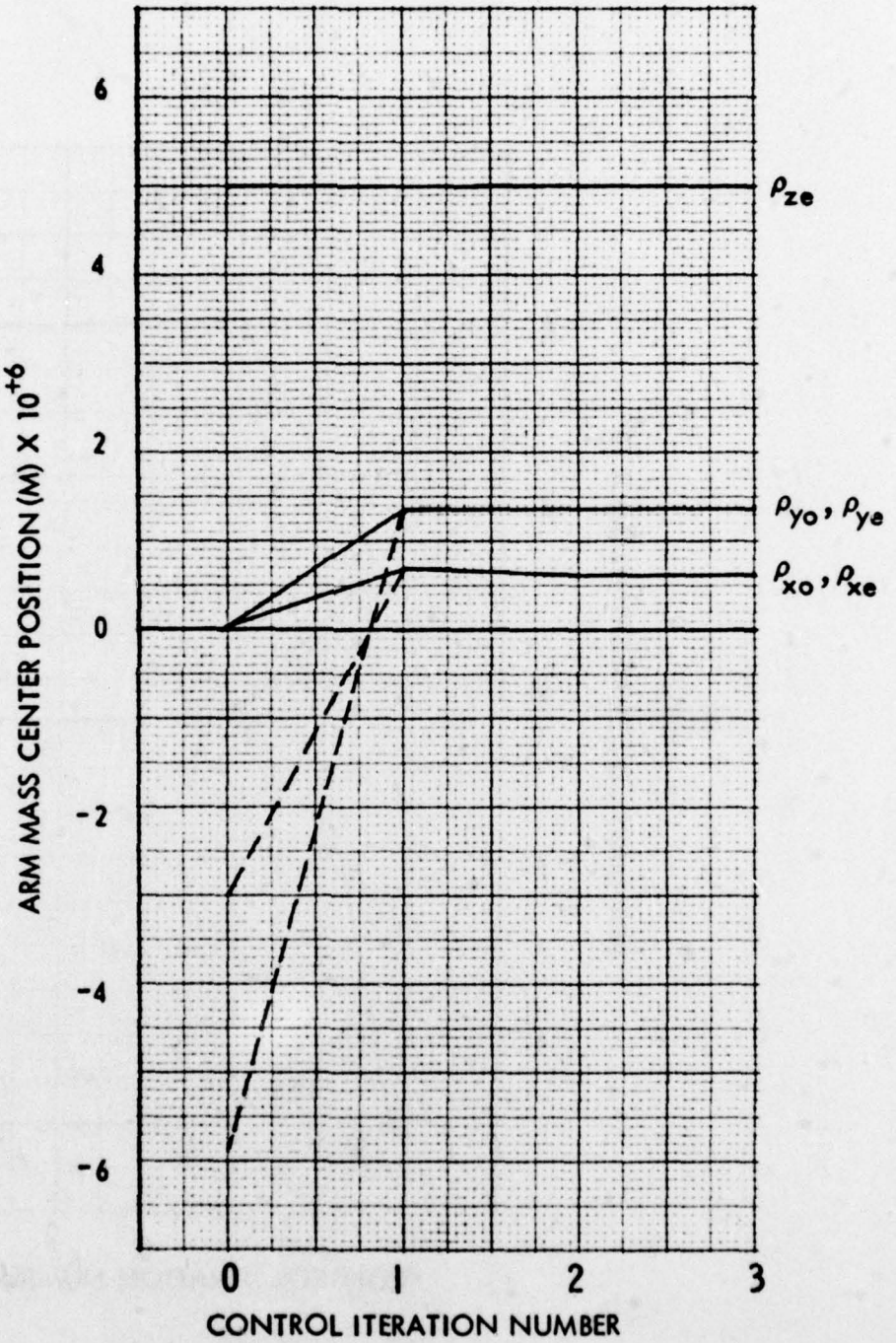


FIG. IX-18 ARM CM LOCATION AS A FUNCTION OF CONTROL ITERATION, TEST CASE 1.

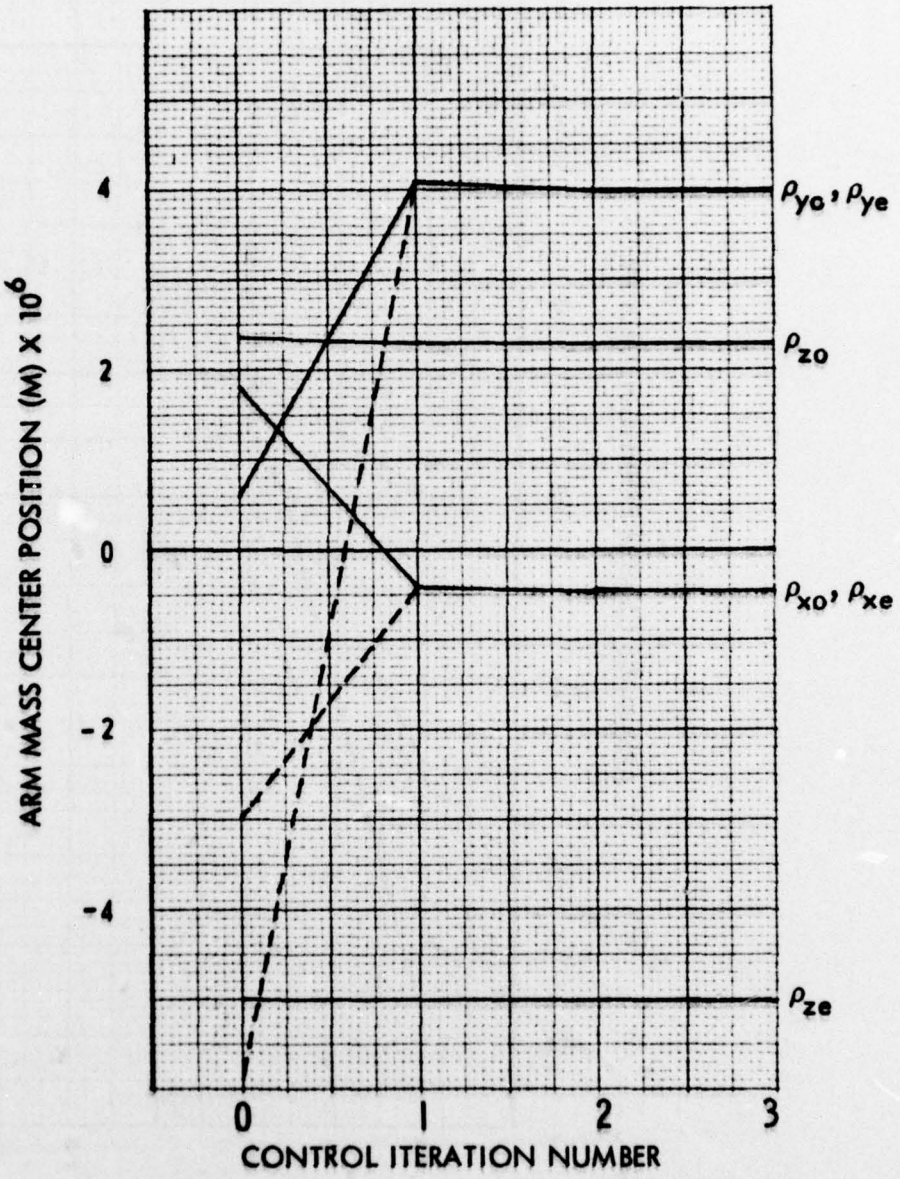


FIG. IX-19 ARM CM LOCATION AS A FUNCTION OF CONTROL ITERATION, TEST CASE 2.

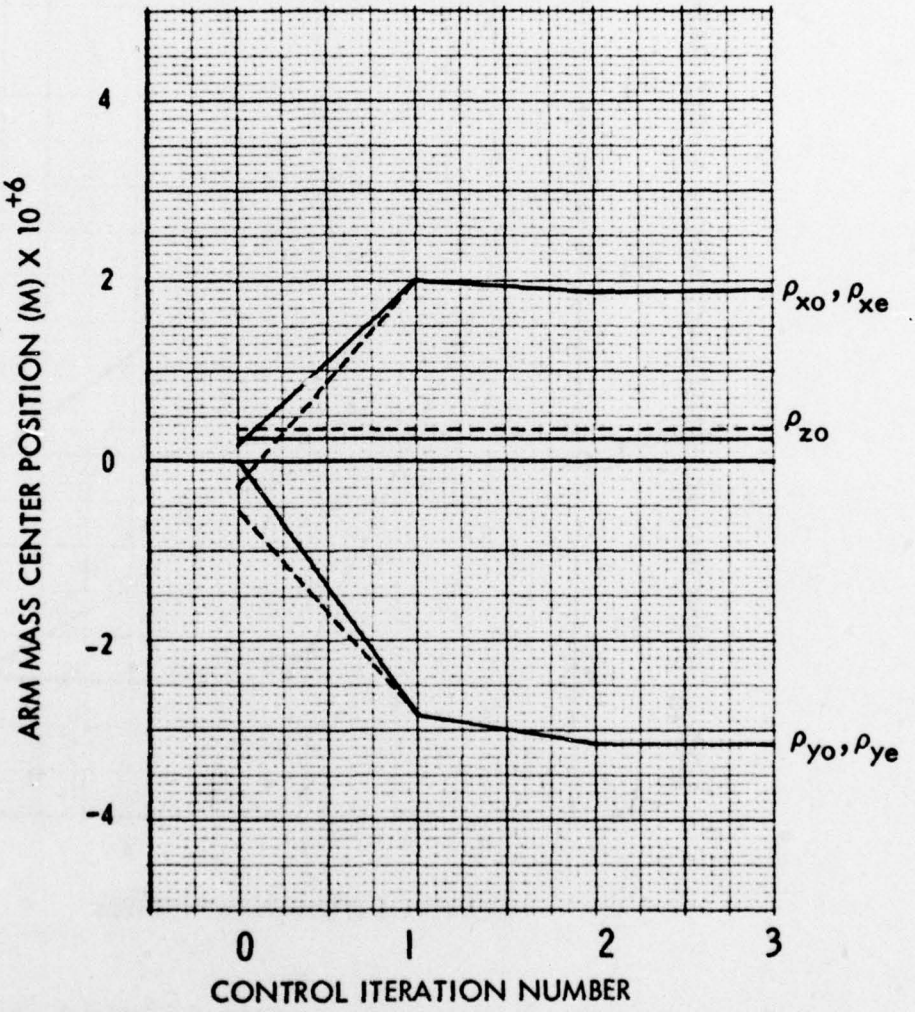


FIG. IX-20 ARM CM LOCATION AS A FUNCTION OF CONTROL ITERATION. TEST CASE 3.

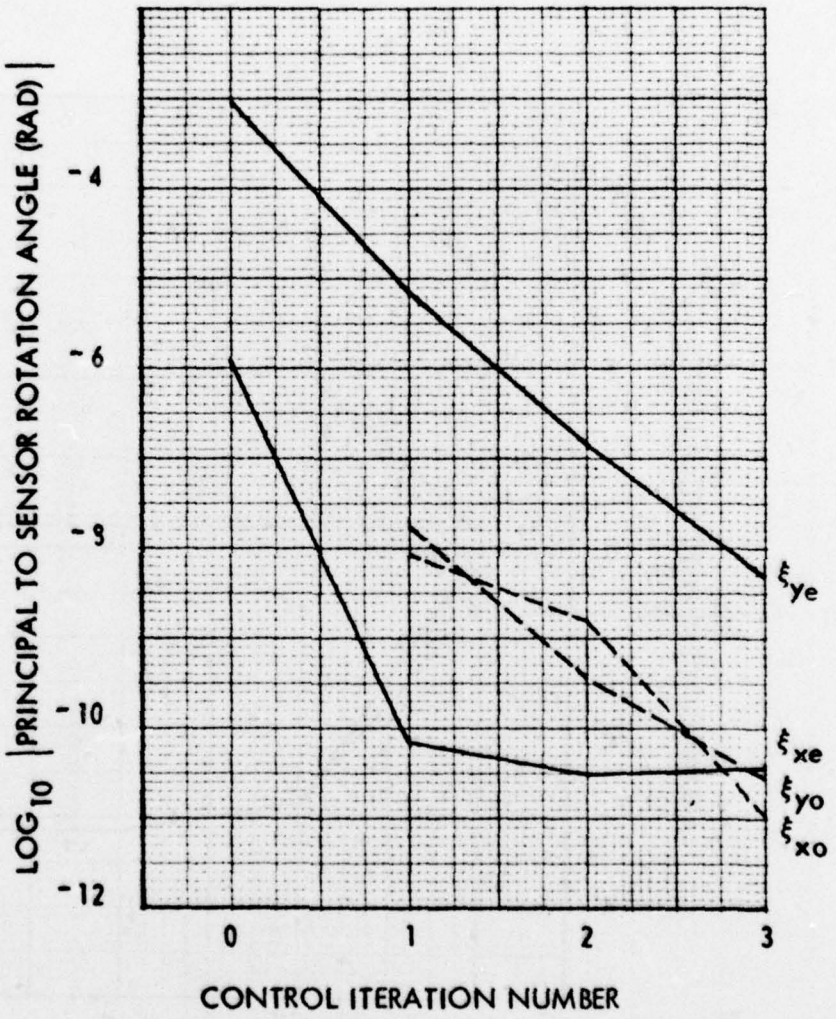


FIG. IX-21 ARM TO SENSOR ROTATION ANGLES AS A FUNCTION OF CONTROL ITERATION. TEST CASE 1

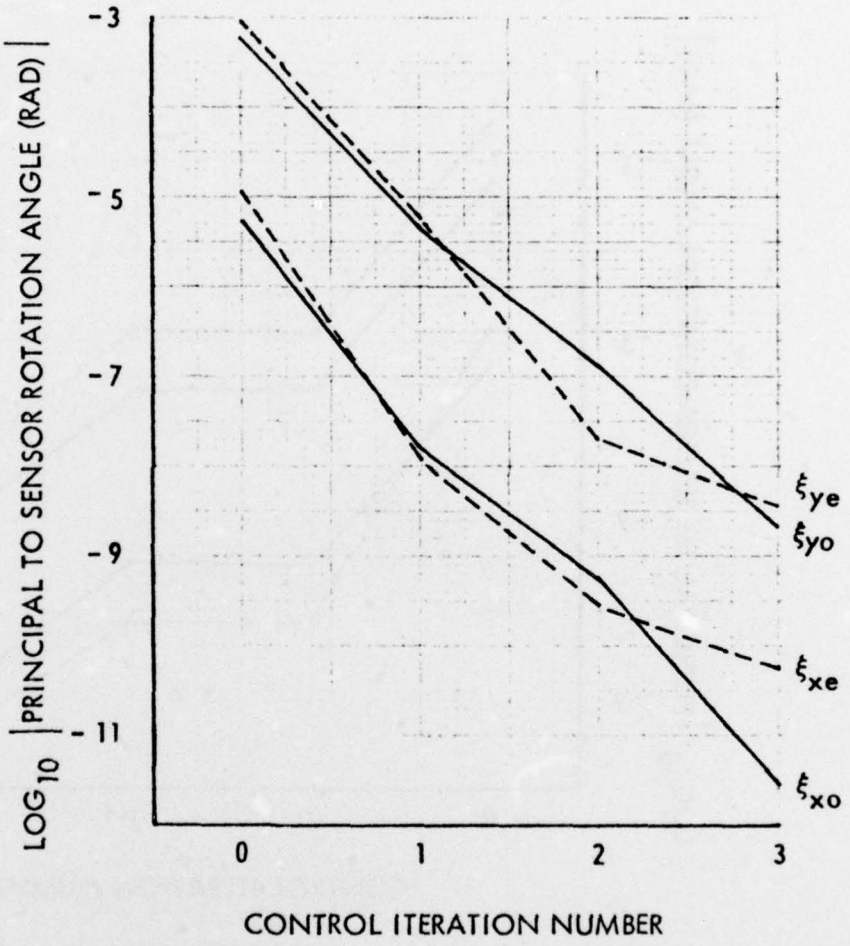


FIG. IX-22 ARM TO SENSOR ROTATION ANGLES AS A FUNCTION OF CONTROL ITERATION. TEST CASE 2.

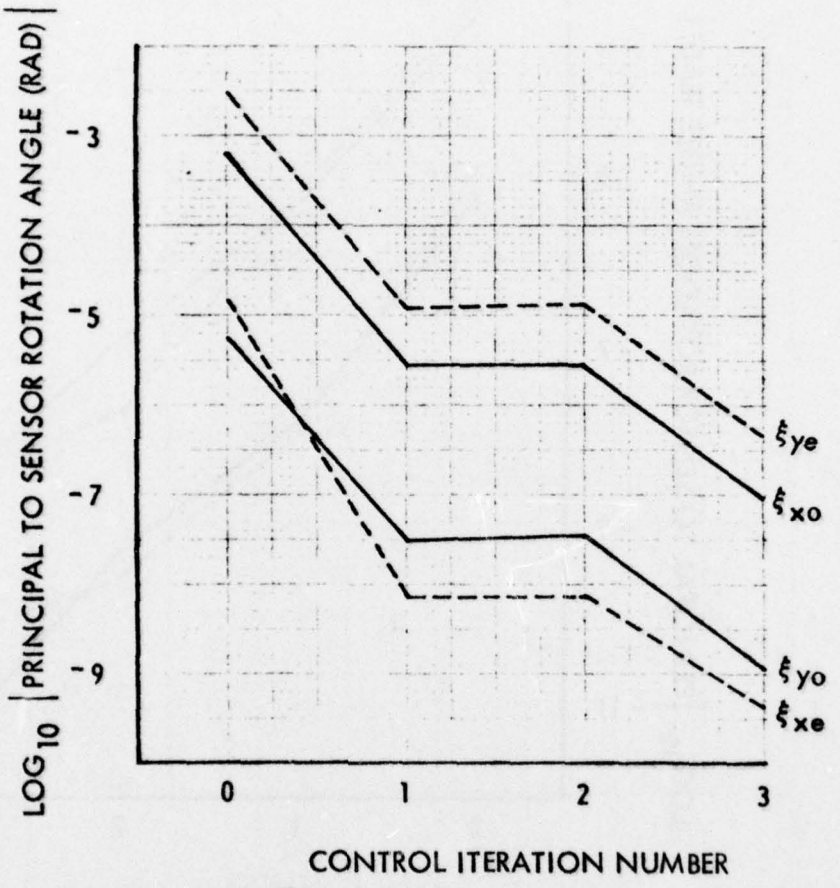


FIG. IX-23 ARM TO SENSOR ROTATION ANGLES AS A FUNCTION OF CONTROL ITERATION. TEST CASE 3.

G. VARIATIONS IN THE NOMINAL CONTROL MASS VALUES

In order to evaluate the effect of using different control masses upon controller performance, an additional general test case, Test Case 5, was defined. Test Case 5, with nominal 1 and 2 gram control masses mounted as described in Sect. IX-B was similar to Test Case 4 in that the parameter errors included within this case exceeded design specifications by approximately 2 orders of magnitude. Least squares control system performance for this case is displayed for several selected OEP in Fig. IX-24. The precontrol $2\omega_s$ output torque error for this system was approximately 5.35×10^{-9} N m, while the $2\omega_s$ error torque subsequent to the last (third) control iteration was approximately 4.90×10^{-14} N m. The $2\omega_s$ error torque subsequent to the third iteration corresponds to a gradient signal error of approximately 0.014 E.U.

Two variations of control mass values were defined for Test Case 5 and are referred to as Cases 5a and 5b. The first of these cases, Test Case 5a, was executed with control masses equal to 0.5 and 1.0 grams instead of the nominal 1.0 and 2.0 gram control masses. For the second case, 5b, the nominal 1.0 and 2.0 gram control masses of Test Case 5 were increased to 2.0 and 4.0 grams respectively.

Test Cases 5, 5a, and 5b yielded the results expected in terms of control mass motion. In all three cases, OEP reduction was adequate to assure RGG operation at signal error levels below 1 E.U. Of particular interest was the controller performance with respect to P_{14} control, as displayed in Fig. IX-25.

The parameter values of Fig. IX-25 correspond to RGG error signals between 0.07 E.U. (for P_{14} control during Test Case 5a) to 1.8×10^{-5} E.U. (for P_{14} control during Test Case 5). Fig. IX-26 displays the control mass increments for control iteration 1, for each of the three test cases. The solid and open crosses represent control mass motion for the 2 x and 1/2 x nominal control mass cases respectively, while the solid triangles represent control mass motion for Test Case 5 which assumed the nominal control mass values of 1 and 2 grams. The figure supports

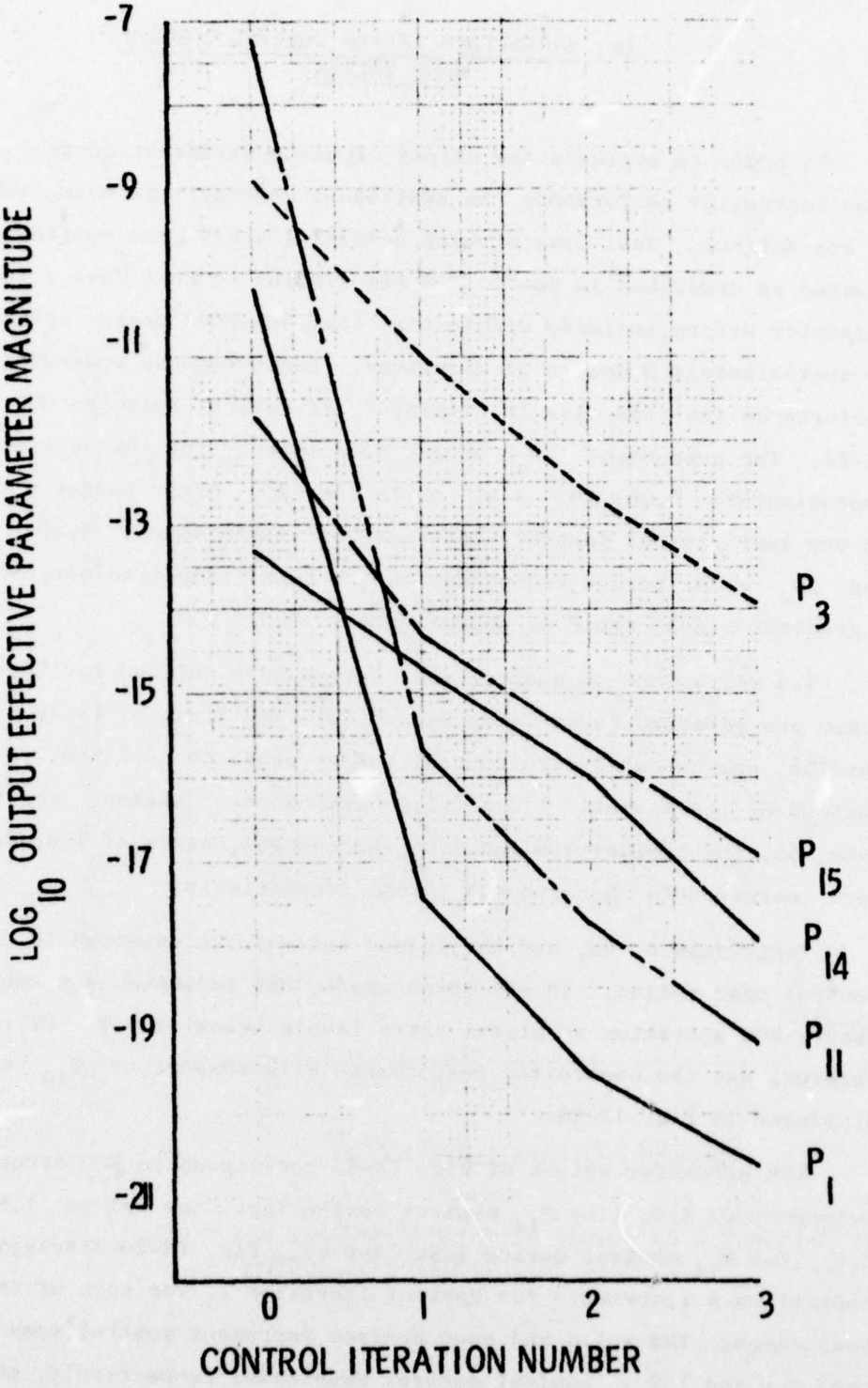


FIG. IX-24 OEP AS A FUNCTION OF CONTROL ITERATION, TEST CASE 5.

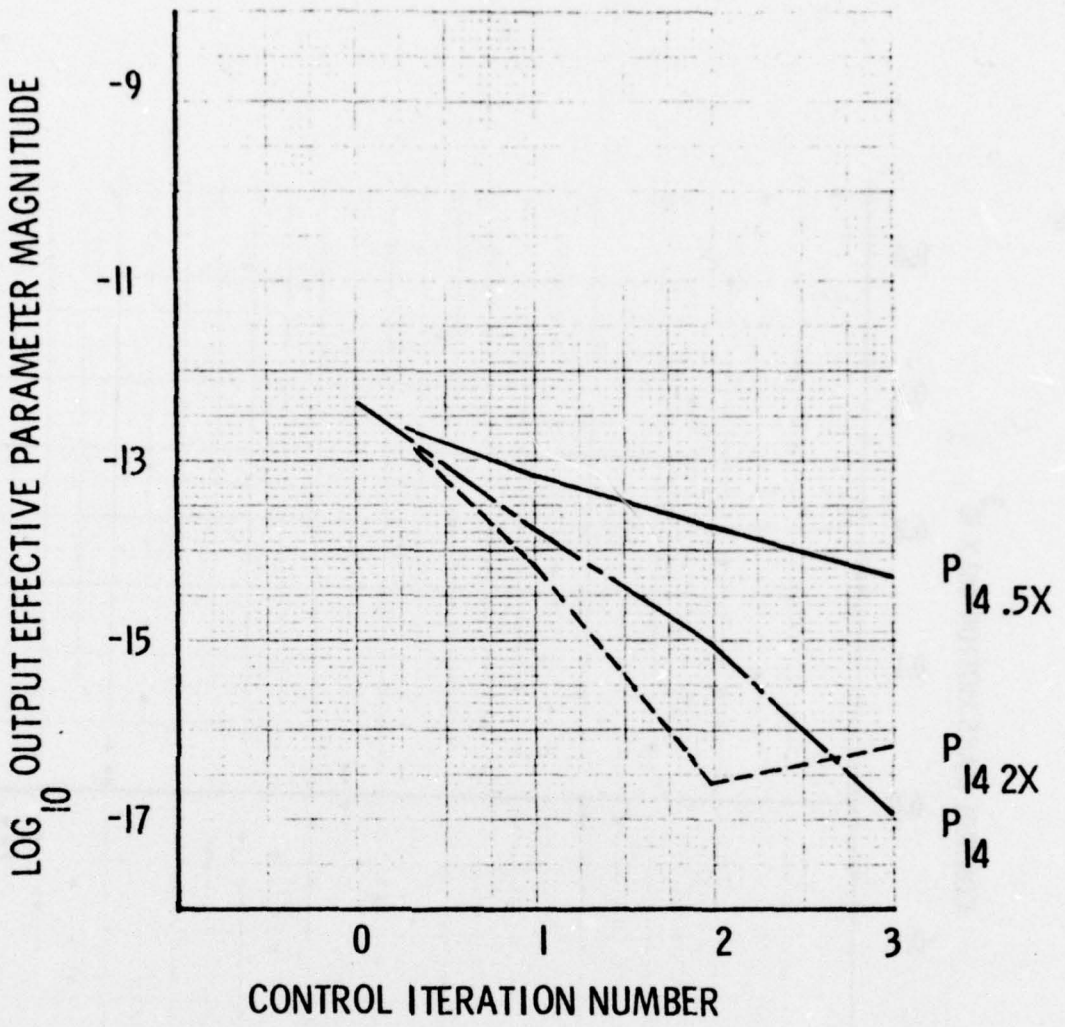


FIG. IX-25 P_{14} CONTROL VS CONTROL ITERATION FOR TEST CASES 5, 5a, AND 5b.

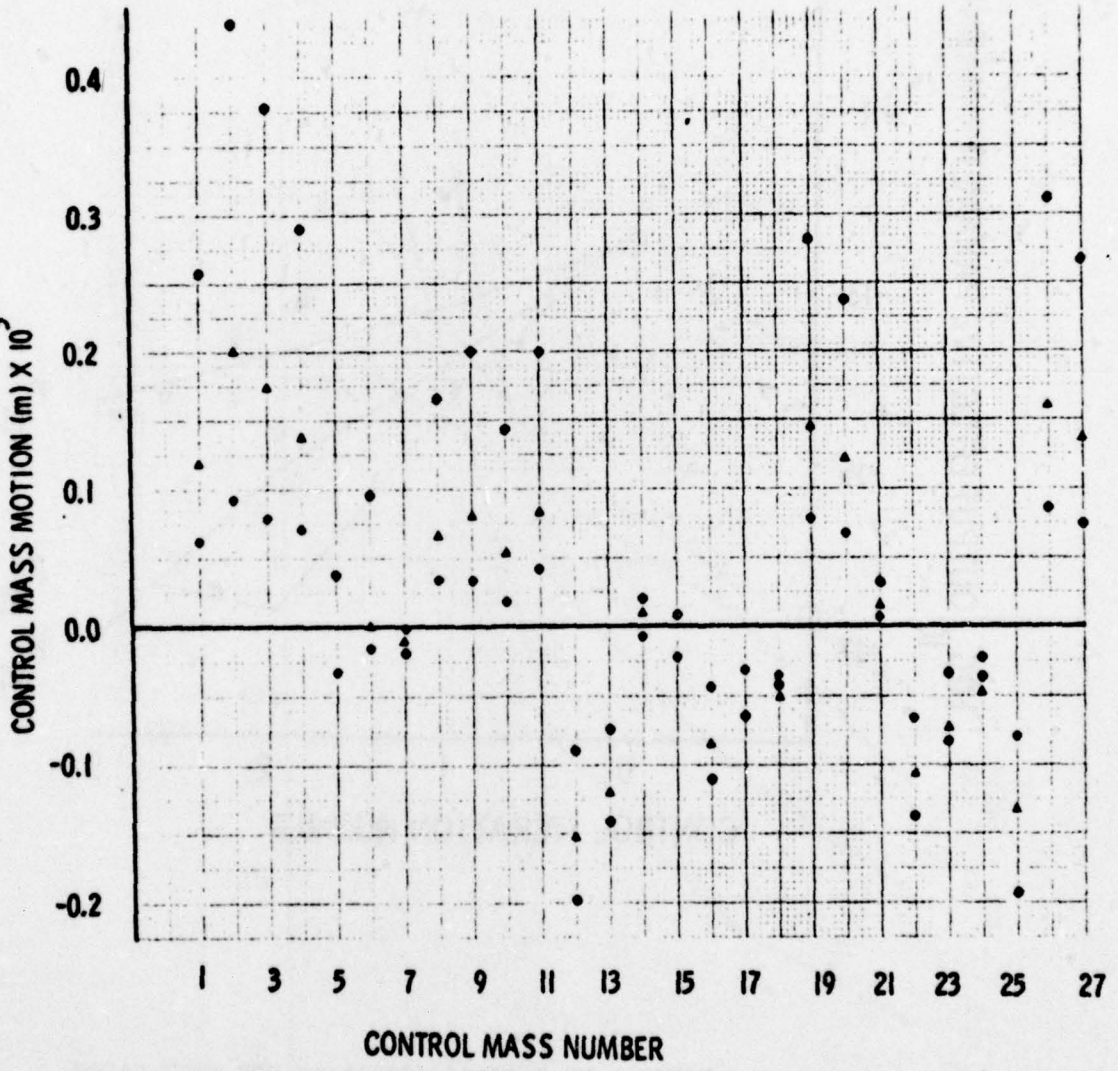


FIG. IX-26 ITERATION 1 CONTROL MASS MOTION FOR TEST CASES 5, 5a, AND 5b.

intuition with respect to the mass motion, although a linear 1, 2, 4 progression is not evident. Examination of Fig. IX-26 indicates that, in general, when the control mass was one-half (or twice) the nominal value, the motion was twice (or one-half) the nominal motion, and that both these motions occurreed in a consistent direction. However, the motions of masses 5, 6, 14, and 15 did not follow this pattern. The reasons for these deviations are not clear. Two likely contributors to the problem are:

(1) The quadratic cost function upon which the control law is based , weights all control mass motions equally, and weights them independently of algebraic sign. By changing the motion of a control which moves relatively little from plus to minus, the motion of a second control which moves farther in the nominal case could be reduced. Such a situation would decrease the value of the cost function;

(2) Since the controls are of nonzero mass, they are contributors to system initial conditions. An altered system initial condition is expected to result in an altered control vector Δx.

Control mass motion associated with Test Case 5a is substantially larger than that associated with Test Case 5, while control mass motion associated with Test Case 5b is substantially less than that associated with Test Case 5. The data of Fig. IX-26 and subsequent control iterations are most easily evaluated in terms of overall motion from the statistical tabulation of Table IX-15.

In Table IX-15, mean (μ) and standard deviation (σ) values have been calculated based upon the motion of all 28 control masses, for each control iteration, for Cases 5, 5a, and 5b. From Table IX-15, it is apparent that the larger control masses of Test Case 5b move through consistently smaller distances. Only the iteration 1 data of the Table are significant for case-tocase comparison since the motions associated with iterations 2 and 3 are generally one order of magnitude smaller than the iteration 1 motion, and are described relative to the previous iteration conditions. The control motion sequence for cases 5a, 5, and 5b, based upon iteration 1 data is 3.6, 2.2, 1 as compared to 4, 2, 1 based upon a strictly linear interpretation of control mass performance

Table IX-15

STATISTICAL ANALYSIS OF CONTROL MASS MOTION FOR TEST CASES 5, 5a, AND 5b.

	$\frac{1}{2}$ × Masses (5a)		Nominal Masses (5)		2 × Masses (5b)	
	$\mu(m)$	$\sigma(m)$	$\mu(m)$	$\sigma(m)$	$\mu(m)$	$\sigma(m)$
Iteration 1	8.19×10^{-5}	1.81×10^{-4}	1.12×10^{-5}	1.21×10^{-4}	7.14×10^{-6}	5.54×10^{-5}
Iteration 2	1.29×10^{-5}	2.37×10^{-5}	8.56×10^{-7}	3.94×10^{-6}	1.01×10^{-7}	8.9×10^{-7}
Iteration 3	3.56×10^{-6}	6.52×10^{-6}	4.37×10^{-8}	2×10^{-7}	1.97×10^{-9}	7.14×10^{-9}

sensitivity. Hence, to first order, a change in the magnitude of the control masses can be expected to change linearly and inversely the distances through which the control masses move.

H. REDUCTION IN THE NUMBER OF CONTROL MASSES

Using Test Case 5 as a datum, several additional control mass configurations were defined in an attempt to reduce the total number of control masses employed by the least squares controller. Based upon the control mass increments noted in Test Cases 1 through 5 it was evident that the z-axis controls--MCO_7, MCO_{14}, MCE_7, and MCE_{14} (see Table IX-2)--could be removed with negligible effect upon controller performance (Test Case 6). These controls were removed from the system of Test Case 5 and the system was exercised. Figure IX-27 displays OEP vs controller performance for Test Case 6. The results closely approximate those of Test Case 5 as expected. The z-axis controls were concluded to be unnecessary.

Further reductions in the total number of control masses were much less successful. Analysis of the instrument/control system design indicated that removal of any additional control masses required the removal of 8 additional control masses due to the asymmetrical effects of control mass removal upon the separate instrument arm inertia tensors. Significantly asymmetrical arms would require large control mass increments and would be expected to saturate the control mechanisms. This situation amounts to practical uncontrollability although the system is theoretically controllable.

The control mass placement for a 16 control mass test is shown in Fig. IX-28. With the basic system of Test Case 5 restructured to conform to the control mass placement of Fig. IX-28 (Test Case 7), the controller system was again exercised, yielding the OEP vs control iteration histories of Fig. IX-29. Based upon system performance between iterations 0 and 1, it is clear that all parameters remain reachable with this reconfiguration, as expected, since 16 controls remain available for control of only 12 OEPs.

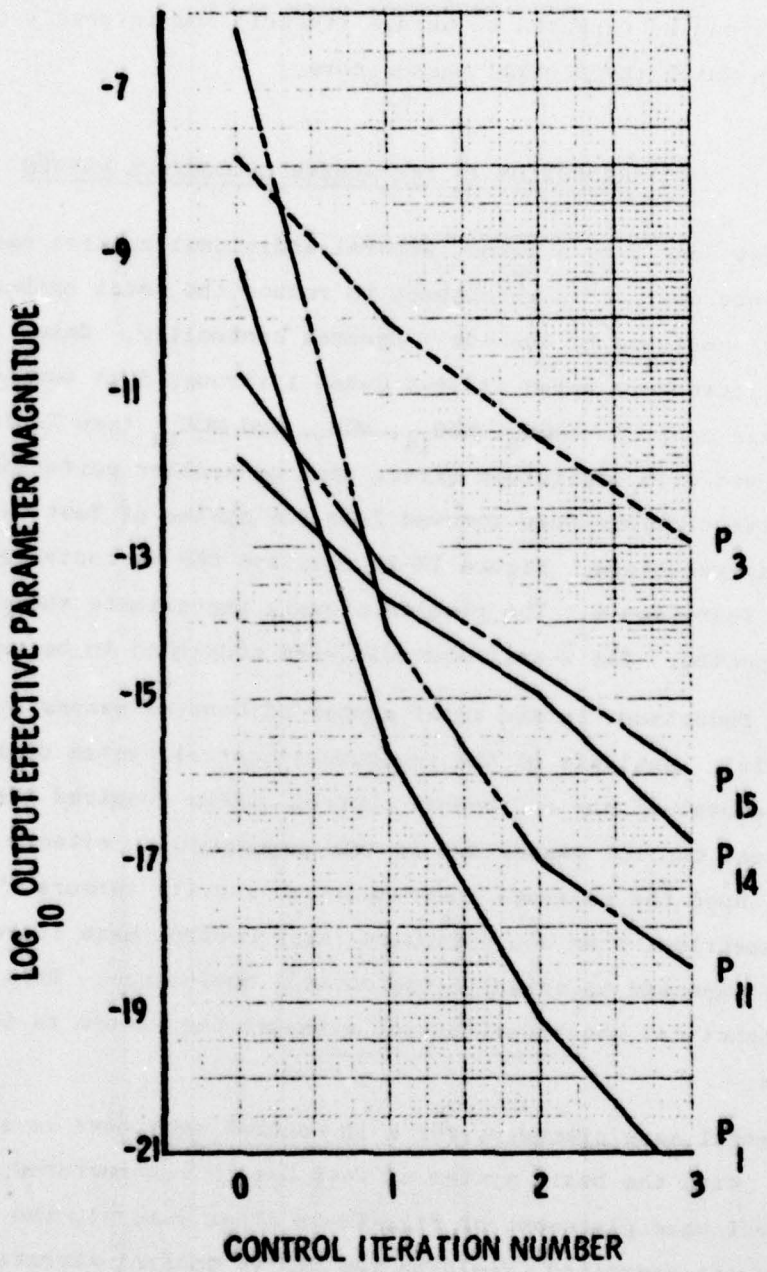


FIG. IX-27 CONTROLLER PERFORMANCE FOR TEST CASE 6 SYSTEM CONFIGURATION. z-AXIS CONTROL REMOVED.

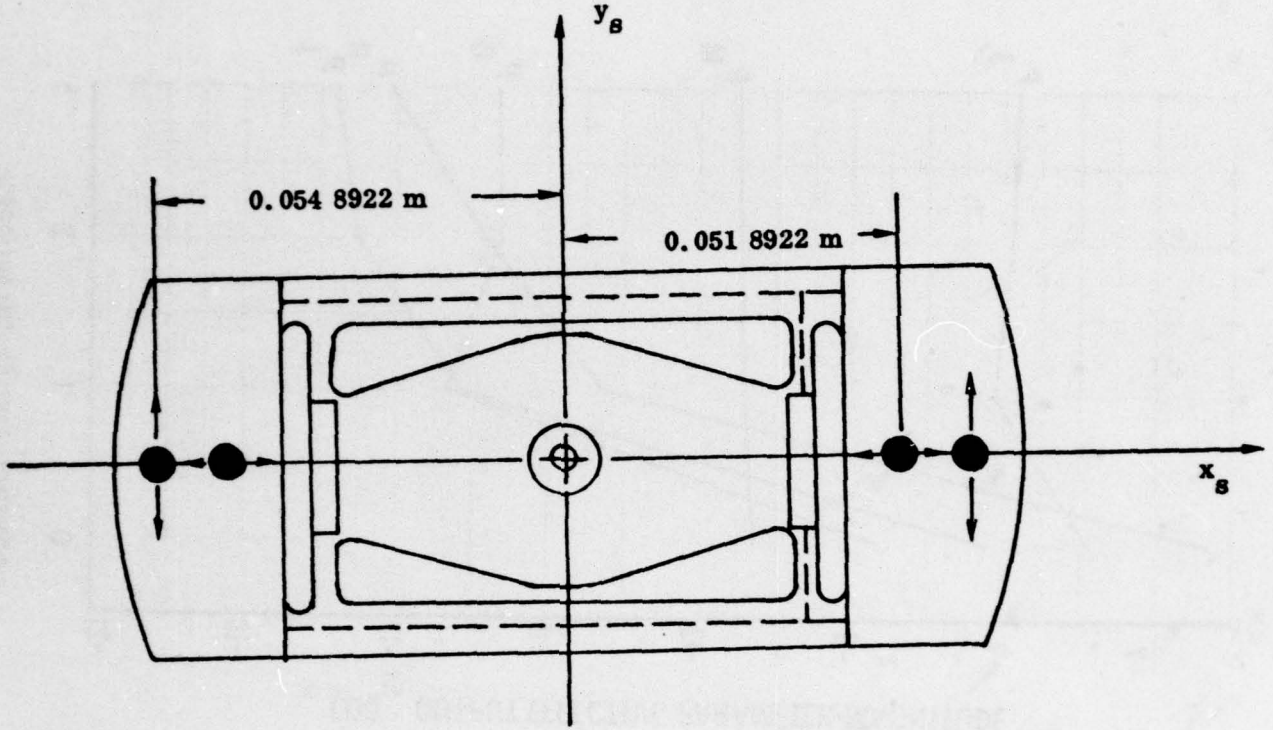


FIG. IX-28 CONTROL MASS PLACEMENT FOR ODD ARM WITH SYSTEM RECONFIGURED TO 8 CONTROL MASSES PER ARM.

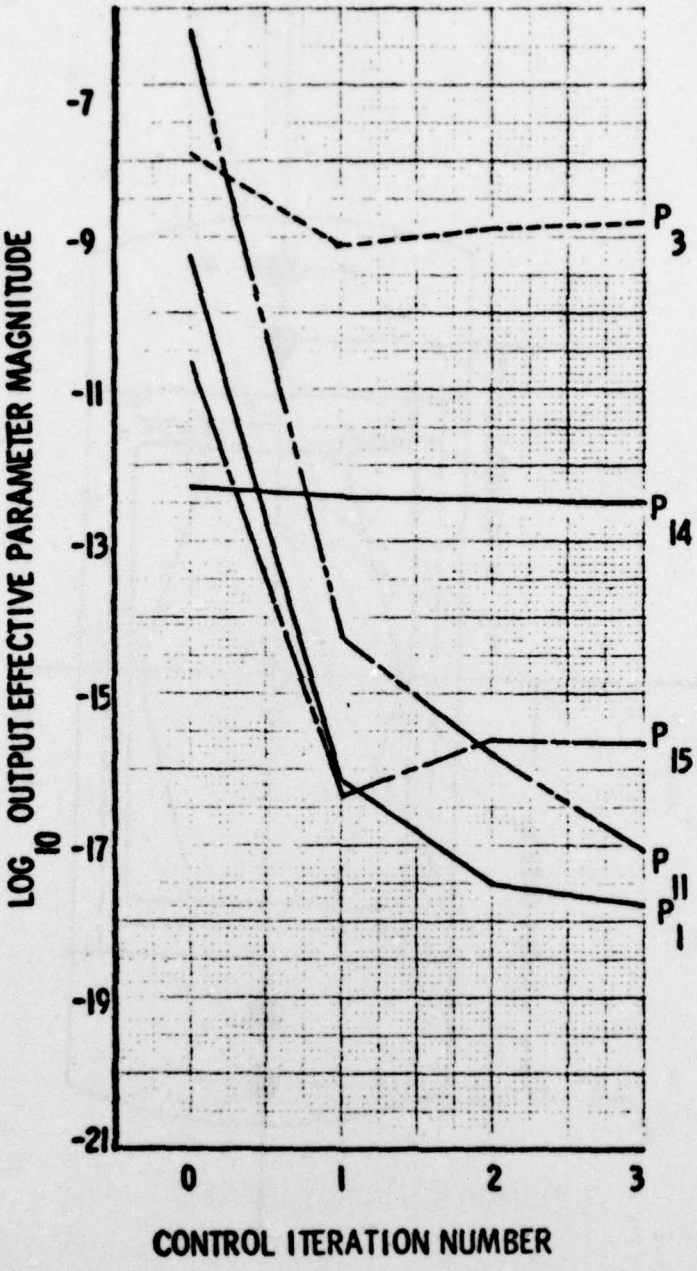


FIG. IX-29 CONTROLLER PERFORMANCE FOR TEST CASE 7. SYSTEM CONFIGURATION WITH NUMBER OF CONTROLS REDUCED FROM 28 to 16.

Observation of system performance during subsequent iterations, however, indicates a lack of available control configurations to reduce simultaneously all 12 OEPs to levels of operation below 1 E.U.

I. CONCLUSIONS REGARDING THE UNDER-DETERMINED LEAST SQUARES CONTROLLER

Based upon the analyses and test case results of Chapters VII through IX, it is clear that the under-determined least squares control law is an effective approach to OEP control. Digital simulations indicate that manufacturing errors corresponding to 60,000 E.U. can be reduced to below 1 E.U. This reduction in output error can be achieved using 24 control masses of 1 and 2 grams placed symmetrically about the arms of the RGG. For such a configuration, each control mass requires less than 0.50 mm of motion to provide OEP control.

Furthermore, it has been shown that the amount of mass motion required to control the parameters changes "linearly" with the size of the control masses. It was also shown that using the identity matrix as the parameter control weighting matrix, mass motion control parallel to the instrument spin axis was not required.

Chapter 10

CONCLUSIONS AND RECOMMENDATIONS FOR FURTHER STUDY

A. CONCLUSIONS

In order to provide a complete measurement of the gravity gradient tensor, three independent gradiometers are required. In order to minimize the error in the estimates of the tensor components, the sensitive axes of the Hughes and Bell instruments should be orthogonal. The between-the-weights axes of the Draper Labs spherical gradiometer should lie along the diagonals of three planes which form the corner of a cube.

Production of a 1 EU moving base gravity gradiometer represents a quantum jump in the precision levels required for the manufacture of an inertial instrument. It is nearly certain that analytical output compensation will be required if these instruments are to achieve their 1 EU accuracy design goal.

Estimation of the separate instrument physical parameters is not required. It is necessary only to estimate the composite of all parameters which effect the output in the same way; ie.e., groups which modulate the same dynamic input. These composites were defined as the 'output effective parameters' (OEPs) and can be estimated.

Several different approaches to OEP estimation can be used. Phase sensitive signal demodulation is the approach which is recommended due to its simplicity. This method requires application of known inputs to the sensor platform. Based upon compensation technique analysis, an active parameter control mechanism is recommended. Active parameter control can compensate for modeling errors which are undetected if only an analytical output compensation approach to sensor signal correction is used. Small masses which can be repositioned on the arms of the rotating gravity gradiometer (RGG) provide an effective means of parameter control for this instrument. Using mass motion it is possible to control compliance related parameters, as well as inertia and mass center related terms. A simple least squares control law is adequate

PRECEDING PAGE BLANK-NOT FILMED

for specifying mass repositioning requirements.

B. RECOMMENDATIONS FOR FURTHER STUDY

The mechanisms of parameter estimation and control developed for the Hughes RGG do not apply directly to either the Draper Labs gradiometer or the Bell gradiometer. The methods developed could, however, be used to synthesize compensation algorithms for both. In fact, the Bell instrument already uses parameter control as an integral part of its design.

The actual frequency content of the gradiometer signal will be significant in the determination of the inputs to be applied for parameter identification and should be evaluated as the instruments are tested.

The output spectra of the platform forcing mechanism and the platform sensors will play a significant role in overall system performance. Investigations into these areas will involve tradeoffs between the designs of jitter isolation equipment and the sensing and compensation required.

A complete simulation and testing program will be necessary for parameter estimation and control system validation. The significant expense of digital simulation (including noise models and high frequency effects) must be traded against the relatively low accuracy of analog implementation. The feasibility of a hybrid implementation should be considered as an alternative to this tradeoff for the initial stages of final compensation technique validation.

The size of the gradiometers prevents the use of a large number of instruments. At least a fourth instrument should be considered as a consistency check and a way of reducing the expected value of the errors in the gradient. An optimum orientation should be calculated and it is expected that complete gradient information would be available from any three, though the expected values of the variances would be somewhat larger than the four-instrument case.

Appendix A

THE CONTROL MASS MOTION MECHANISM

The mass motion devices currently under consideration for use with the RGG are the mercury mass balance tubes discussed in Ref. AM-1. This device was the first mass motion control device considered but it has limitations. Recent experiments with the mechanisms indicate difficulty of operation within a 2 g environment. A simple calculation shows the centripetal accelerations at the ends of the RGG arms to be approximately 50 g. Hence, it was advisable to seek another source of mass motion, one which provided enough output force to operate under the 50 g constraint while maintaining a wide enough range of motion to accommodate the required shift in control masses (upper bound of 1 mm). One mechanism which exceeds both these specifications is a piezoelectric device produced by Burleight Instruments called the 'Inchworm'. The standard device, which incorporates three separate but attached piezoelectric crystals, can provide 5-lb through distances of up to 25 mm with an accuracy of 6×10^{-9} m [BU-1]. The speed of the motion is variable from 0.3 μm/minute to 10 mm/minute.

The principle of operation of the device is demonstrated in Fig. A-1. Crystals 1 and 3 operate as clamps during voltage application, whereas crystal 2 extends linearly during voltage application. The following example demonstrates the simplicity of operation. The operating sequence shown in Fig. A-1 causes the shaft to be pulled to the left.

a) At time zero, crystal 1 is clamped, locking the control shaft in place;

b) While crystal 1 (c1) remains clamped, a voltage is applied across crystal 2 (c2) causing a linear extension of c2;

c) Following extension of c2, crystal 3 (c3) is clamped onto the shaft;

d) c1 is opened to allow free motion of the shaft through c1;

e) The voltage across c2 is removed, causing a contraction which pulls the shaft to the left since c3 is clamped;

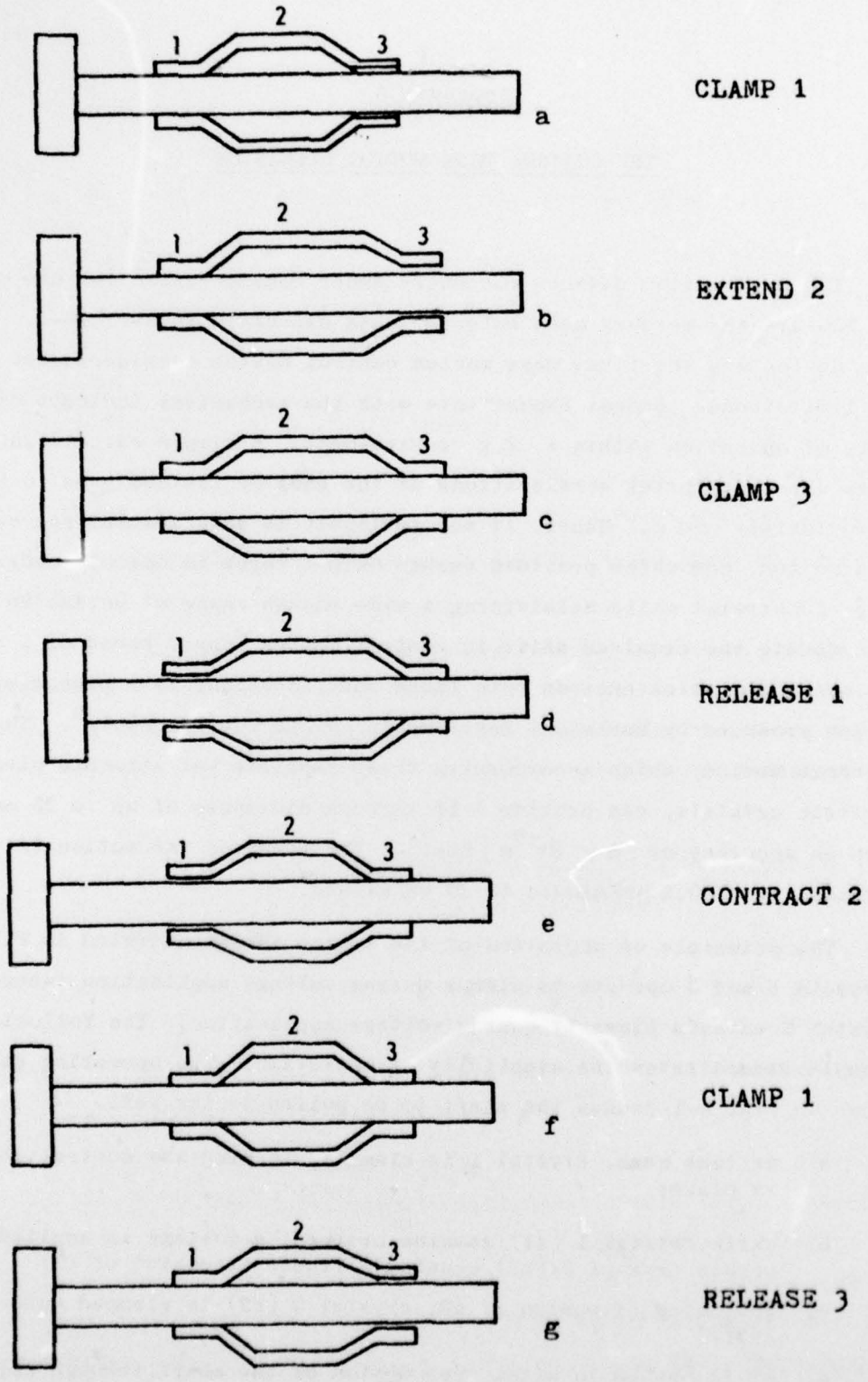


FIG. A-1 CLAMPING SEQUENCE FOR INCHWORM MASS MOTION

f) c1 is clamped;

g) c3 is released and another iteration may be initiated.

Repeated application of the sequence provides motion in increments of 6×10^{-9}m. Controller physical characteristics and specifications are shown in Fig. A-2.

SPECIFICATIONS

Inchworm: PZ-500

Travel	0-25mm
Resolution of Travel	6nm
Speed	0.3μm per minute to 20 mm per minute
Load	5 lbs.
Housing Material	Chrome Plated Stainless Steel
Spindle and Spindle Tip Material	Invar 36
Electrical Connector	Viking Thorkom II TKP07-102
Cable Length	6 feet
Size	(See below.)

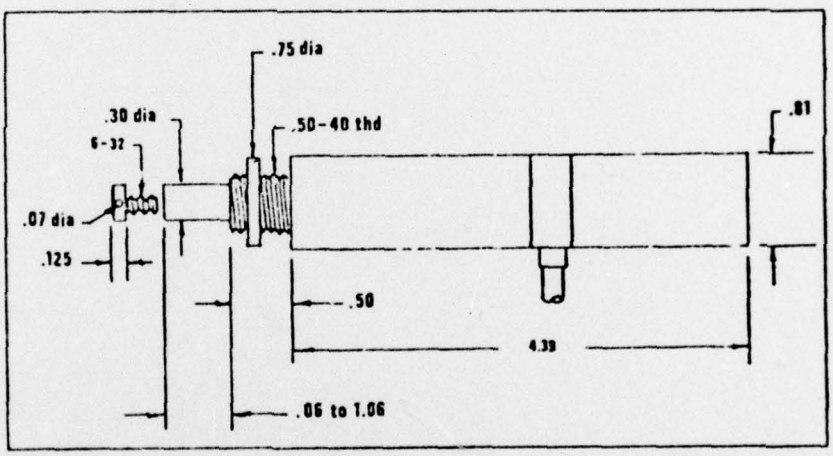


FIG. A-2 INCHWORM SPECIFICATIONS

A 2 gram mass acted upon by a centripetal acceleration of 50 g results in a force of 1 N, or approximately 0.23 lb. Hence, the controller described in Fig. IX-5 is approximately one order of magnitude "overdesigned" both in terms of force output capability and motion capability in the arm axial direction. The operating principle, however is applicable to RGG application.

Appendix B

AN APPROACH TO COMPLIANCE FINE TUNING

The RGG high compliance pivots are solid aluminum cylinders with a length to diameter ration equal to 1. The method for fine tuning two such pivots is straightforward. Let

$$C_1 \triangleq \text{torsional compliance of pivot 1 ,} \tag{B.1}$$

$$C_2 \triangleq \text{torsional compliance of pivot 2 ,} \tag{B.2}$$

and assume

$$C_1 > C_2 \, . \tag{B.3}$$

For a solid cylinder of length L subjected to a torque T, the strain energy U may be written as

$$U = \frac{1}{2} \frac{T^2 L}{G I_p} \tag{B.4}$$

where G is the member shear modulus, and I_p is the polar moment of inertia of the member cross section. If a groove of depth δ and width d is cut into the pivot, Fig. IX-1, the strain energy within the pivot due to the torque T is

$$U = \frac{1}{2} \frac{T^2}{G} \left\{ 4 \frac{L-d}{\pi r^4} + \frac{4d}{\pi (r - \delta)^4} \right\} \, . \tag{B.5}$$

Hence with

$$\Delta C \triangleq C_1 - C_2 \, , \tag{B.6}$$

the compliances can be matched by a cut of width d and depth δ, where

PRECEDING PAGE BLANK-NOT FILMED

$$\delta = r\left\{1 - \left[\frac{\pi G r^4}{4d}(\Delta C) + 1\right]^{-1/4}\right\} . \qquad (B.7)$$

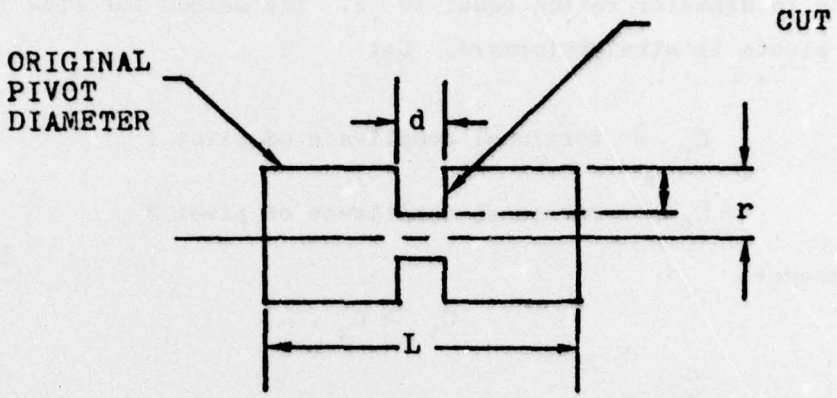


FIG. B-1 HIGH COMPLIANCE PIVOT MODIFIED FOR COMPLIANCE MATCH.

REFERENCES

AM-1 Ames, C.B., R.L. Forward, et al., "Prototype Moving Base Gravity Gradiometer," R&D Design Evaluation Report, Hughes Research Labs, Malibu, Calif., Jan 1973.

AM-2 Ames, C.B., R.L. Forward, et al., " Prototype Moving Base Gravity Gradiometer," Semiannual Tech. Rept. No. 1, Hughes Research Labs., Malibu, Calif., Aug 1972.

AM-3 Ames, C.B., R.L. Forward, et al., "Prototype Moving Base Gravity Gradiometer," Technical Proposal, Hughes Research Labs, Malibu, California, Sept 1971.

BE-1 Beyer, L.A., "Proposed Development of a Gravity Gradiometer for Energy Resource Exploration and Exploitation," U.S. Dept. of the Interior, Geological Survey Branch; Memo to R.P. Sheldon, Chief Geologist, Menlo Park, Calif., 22 jan 1973.

BEL-1 Bell, C.C., R.L. Forward, and H.P. Williams, "Simulated Terrain Mapping With the Rotating Gravity Gradiometer," from, Advances In Dynamic Gravimetry, Wilbur T. Kattner, editor; Proceedings of the Symposium on Dynamic Gravimetry, Fort Worth, Texas, Mar 1970.

BEL-2 Bell, C.C., R.L. Forward, and J.R. Morris, "Mass Detection by Means of Measuring Gravity Gradients," AIAA Second Annual Meeting, San Francisco, Calif., July 1965.

BR-1 Britting, K.R., S.J. Madden, and R.A. Hildebrandt, "Assessment of the Impact of Gradiometer Techniques on the Performance of Inertial Navigators," Air Force Cambridge Research Labs, AFCRL-71-0465, Bedford, Mass., Sept 1971.

BRY-1 Bryson, A.E., and Y.C. Ho, Applied Optimal Control, Blaisdel Publishing Co., Waltham, Mass., 1969.

BRY-2 Bryson, A.E., and W.E. Hall, "Optimal Control and Filter Synthesis By Eigenvector Decomposition," Stanford University, SUDAAR No. 436, Nov 1971.

BU-1 Burleigh Instruments, Inc., East Rochester, New York.

CA-1 Cannon, R.H., Dynamics of Physical Systems, McGraw Hill, New York, 1967.

REFERENCES (Cont)

CO-1 Colombo, G., et al., "Shuttle Borne 'Skyhook': A new Tool For Low-Orbital-Altitude Research," Smithsonian Institute Astrophysical Observatory, Cambridge, Mass., Sept 1974.

DEB-1 DeBra, D.B., J.C. Harrison, and P.M. Muller, "A Proposed Lunar Orbiting Gravity Gradiometer Experiment," from, The Moon, H. Alfven, Z. Kopal, and H.C. Uray, editors, Vol. 4, Nos. 1 and 2, Apr 1972.

DEB-2 DeBra, D.B., Private communication to Phil LaHue, Hughes Research Labs, 19 Apr 1976.

DEB-3 DeBra, D.B., and E.J. Pelka, "Study To Develop Gradiometer Compensation Techniques," Stanford University, AFCRL Rpt. TR-74-0114, 1 Feb 1973.

DEU-1 Deutsch, R., Estimation Theory, Prentice Hall, Inc., Englewood Cliffs, N.J., 1965.

FO-1 Forward, R.L., "Geodesy With Orbiting Gravity Gradiometers," from, The Use of Artificial Satellites for Geodesy, Geophysical Monograph Series, Vol 15, American Geophysical Union, Washington, D.C.,

HA-1 Hammond, J.A., "Results of Absolute Gravity Determinations At a Number of Different Sites," Journal of Geophysical Research, Vol 76, No. 32, American Geophysical Union, Washington D.C., Nov 1971.

HE-1 Heller, W.G., "Gradiometer Aided Inertial Navigation," The Analytic Sciences Corp., TR-312-5, Reading, Mass., Apr 1975.

HO-1 Hoff, N.J., The Analysis of Structures, John Wiley & Sons, Inc., Englewood Cliffs, N.J., 1965.

IV-1 Ivey, K.A., A-C Carrier Control Systems, John Wiley & Sons, Inc., New York, New York, 1947.

JO-1 Jordan, S.K., "Effects of Geodetic Uncertainties on a Damped Inertial Navigation System," IEEE Transactions on Aerospace and Electronic Systems, Vol, AES-9, No.5, New York, New York, Sept 1973.

KA-1 Karamcheti, K., Vector Analysis and Cartesian Tensors, Holden-Day, Inc., San Francisco, Calif., 1967.

REFERENCES (Cont)

LI-1 Likeness, B.K., "Flotation Technique Testing of Low Level Accelerometers," Ph.D. Dissertation, Dept. Aeronautics and Astronautics, Stanford University, Guidence and Control Lab., Stanford Calif., SUDAAR No. 399, May 1970.

LO-1 Loomis, A.A., "Earth and Ocean Physics Planning Applications Study," Jet Propulsion Lab., Calif., Institute of Technology, Pasadena, Calif., May 1972.

LOR-1 Lorell, K.R., and B.O. Lange, "Precision Attitude Control of Symmetric Spinning Bodies," Ph.D. Dissertation, Stanford University, Dept. of Aeronautics and Astronautics, SUDAAR 422, Stanford, Calif., Apr 1971.

MC-1 McKinley, H.L., "The Stability and Control of The Principal Axes of Almost Spherical Bodies," Ph.D. Dissertation, Stanford University Dept. of Aeronautics and Astronautics, SUDAAR 325, Stanford, Calif., Feb 1968.

ME-1 Metzger, E.H., and A. Jircitano, "Analysis of Real Time Mapping of Horizontal and Vertical Gravity Anomalies Aboard a Moving Vehicle Such as an Aircraft," International Symposium on Applications of Marine Geodesy, Colombus, Ohio, Jun 1974.

ME-2 Metzger, E.H., and A. Jircitano, "Inertial Navigation Performance Improvement Using Gravity Gradient Matching Techniques," AIAA Guidance and Control Conference, Boston, Mass., Aug 1975.

MU-1 Muller, P. and W. Sjorgen, "Mascons: Lunar Mass Concentrations," Science, Vol.161, No. 3842, Aug 1968.

PE-1 Peters, R.C., "Preliminary Gravity Gradiometer Error Models," The Aerospace Corp., Rept. No. TOR-0074(4113)-2, El Segundo, Calif., Jun 1974.

PO-1 Powell, J.D., and B.O. Lange, "Control of a Spinning Drag-Free Satellite With an Application of Estimation Theory," Stanford University, Dept. of Aeronautics and Astronautics, SUDAAR 402, Stanford, Calif., May 1970.

RE-1 Reid, D.B., "Optimal Inputs for System Identification," Ph.D. Dissertation, Stanford University Dept. of Aeronautics and Astronautics, SUDAAR 440, Stanford, Calif., May 1972.

REFERENCES (Cont)

SA-1 Sakuma, A., "Recent Developments in the Absolute Measurement of Gravity," Proceedings of the International Conference on Precision Measurement and Fundamental Constants, National Bureau of Standards Spec, Publ. 343, D.N. Langenberg and B.N. Taylor, editors; U.S. Govt. Printing Office, Washington, D.C., 1971.

TE-1 Terman, F.E., Radio Engineering, McGraw Hill Book Co., Inc., New York, New York, 1947.

TR-1 Trageser, M.B., "A Gradiometer System for Gravity Anomaly Surveying," from, Advances in Dynamic Gravimetry, Wilbur T. Kattner, editor; Proceedings of the Symposium on Dynamic Gravimetry, Fort Worth, Texas, Mar 1970.

TR-2 Trageser, M.B., "Feasibility Model Gravity Gradiometer Test Results," Paper No. 75-1093, AIAA Guidance and Control Conference, Boston, Mass., Aug 1975.

WI-1 Williams, O.P., " Gradiometry: An Assessment of the State-of-the-Art," Defense Mapping Agency, Washington, D.C., Sept 1974.